UNIVERSITY OF CALIFORNIA,
IRVINE

Unveiling the Cosmos: Insights from Big Bang Nucleosynthesis, Dark Matter Modeling, and Studies in Quantum Gravity

DISSERTATION

submitted in partial satisfaction of the requirements
for the degree of

DOCTOR OF PHILOSOPHY

in Physics

by

Anne-Katherine Burns

Dissertation Committee:
Professor Timothy M.P. Tait, Chair
Professor Nathaniel Craig
Professor Kevork N. Abazajian

2024

DEDICATION

To the women and gender-nonconforming folks of the physics community:
past, present, and future.

TABLE OF CONTENTS

LIST OF FIGURES

LIST OF TABLES

ACKNOWLEDGMENTS

There are so many people for whom I feel so much gratitude.

First and foremost, I want to extend my heartfelt appreciation to my advisor, Tim for his unwavering kindness, guidance, and belief in my potential as a physicist. Thank you to the students and professors in the UCI physics community for providing such a supportive and safe learning environment that fosters both collaboration and friendship. Thank you to Nathaniel and his entire research group at KITP for warmly welcoming me during my stay there and creating a culture of active engagement across diverse research domains. Thank you to the wonderful mentors I've had the privilege of learning from during my time at UCI. Especially to Jessica, whose dedication both to science and to helping others serves as a constant source of inspiration and whose support has been invaluable in my research journey. I am also grateful to my own students and mentees - Raynah and others, whose enthusiasm for learning and exploration has kept my own passion for discovery always top of mind.

To my best friends: Haley, Holly, Reb, Kerin, and Minna, thank you for always having my back and making me laugh - it is legal to be silly after all. Thank you to my mom, for fostering my love of learning from the time I was little and launching me into the career path I'm on today. Thank you to my dad for always reminding me to take the high road. Thank you to my sisters, Josephine and Elizabeth for being my lifelong friends and confidants. Thank you to my friends in Santa Barbara for reminding me of the value of community. Lastly, thank you to Ibs, whose unwavering support, encouragement, and companionship has been a constant source of strength and inspiration. You are my number one cheerleader and my knight of cups, and I will forever be grateful to you for all the ways in which you've supported me throughout my PhD.

Chapter 2 of this dissertation is a reprint of the material as it appears in [19], used with permission from Physics Review D. The co-authors listed in this publication are Max Fieg and Christopher M. Karwin, and Arvind Rajaraman. Chapter 3 of this dissertation is a reprint of the material as it appears in [20], used with permission from Physics Review D. The co-authors listed in this publication are Chris Karwin, Simona Murgia, Igor Moskalenko, Sean Fillingham, and Max Fieg. Chapter 4 of this dissertation is a reprint of the material as it appears in [21]. The co-authors listed in this publication are David E. Kaplan, Tom Melia, and Surjeet Rajendran. Chapter 5 of this dissertation is a reprint of the material as it appears in [22], used with permission from European Physics Journal C. The co-authors listed in this publication are Tim M. P. Tait, and Mauro Valli. Chapter 6 of this dissertation is a reprint of the material as it appears in [17], used with permission from Physical Review Letters. The co-authors listed in this publication are Tim M. P. Tait, and Mauro Valli. Chapter 7 of this dissertation is a reprint of the material as it appears in [23], used with permission from Physics Review D. The co-authors listed in this publication are Venus Keus, Marc Sher, and Tim M. P. Tait.

VITA

Anne-Katherine Burns

EDUCATION

Doctor of Philosophy in Physics and Astronomy **2024**
University of California, Irvine *Irvine, California*

Bachelor of Science in Physics **2019**
College of William and Mary *Williamsburg, Virginia*

RESEARCH EXPERIENCE

Graduate Research Assistant **2019–2024**
University of California, Irvine *Irvine, California*

Graduate Research Fellow **2023**
University of California, Santa Barbara *Santa Barbara, California*

TEACHING EXPERIENCE

Teaching Assistant **2019–2024**
University of California, Irvine *Irvine, California*

REFEREED JOURNAL PUBLICATIONS

Dark matter interpretation of the Fermi-LAT observations toward the outer halo of M31 **2021**
Phys.Rev.D 103 (2021) 2, 023027

Dark matter explanations of the gamma-ray excesses from the Galactic Center and M31 **2021**
Phys.Rev.D 103 (2021) 6, 063023

Indications for a Nonzero Lepton Asymmetry from Extremely Metal-Poor Galaxies **2023**
Phys.Rev.Lett. 130 (2023) 13, 131001

PRyMordial: the first three minutes, within and beyond the standard model **2024**
Eur.Phys.J.C 84 (2024) 1, 86

Constraints on Variation of the Weak Scale from Big Bang Nucleosynthesis **2024**
Phys.Rev.D 109 (2024) 12, 123506

SOFTWARE

PRyMordial `https://github.com/vallima/PRyMordial`
A package dedicated to efficient computation of observables in the Early Universe with the focus on the cosmological era of Big Bang Nucleosynthesis.

ABSTRACT OF THE DISSERTATION

Unveiling the Cosmos: Insights from Big Bang Nucleosynthesis, Dark Matter Modeling, and Studies in Quantum Gravity

By

Anne-Katherine Burns

Doctor of Philosophy in Physics

University of California, Irvine, 2024

Professor Timothy M.P. Tait, Chair

While the Standard Model of particle physics and the ΛCDM model of cosmology have been celebrated for their explanatory prowess, many phenomena remain unexplained. In this dissertation, we explore several methods of inquiry into these enigmas. In Chapters 2 and 3, we scrutinize signals that may hint at the presence of dark matter, and develop models through which these signals can be explained. Next, in Chapter 4, we employ well developed tools such as the path integral to formulate a new method for determining time evolution in cosmology. Finally, in Chapters 5 through 7, we use precise observations of primordial light elements to constrain theories beyond both the Standard Model and ΛCDM. Together, these investigations shed light on some of the mysteries of the cosmos and will hopefully inspire future avenues of exploration.

Chapter 1

Introduction

The ΛCDM model is a powerful theory that describes the history of our universe from times less than one second after the Big Bang to today. This model, in combination with the Standard Model (SM) of particle physics and cosmological inflation can account for observations ranging from the Cosmic Microwave Background (CMB), to the distribution of Large Scale Structure (LSS), to the formation of light elements such as Helium and Lithium. Together, ΛCDM and cosmological inflation predict that at very early times the universe went through a period of rapid expansion, known as inflation, and has been expanding and cooling ever since. According to the model, the rate of this expansion can be predicted by considering three components of energy density: radiation, matter (including both visible matter and cold dark matter), and dark energy.

While both ΛCDM and the Standard Model have had much success in their abilities to correctly predict observables now measured by experiments, there are intriguing mysteries that remain unexplained. These mysteries lead us to questions such as, *Why is there more matter in the universe than anti-matter? What is the nature of dark matter? How does gravity fit into our understanding of the universe on the smallest measurable scales?* and

so many more. Today, experimentalists and theorists across sub-fields seek the answers to these questions and cross disciplinary research is crucial to increasing our understanding of the universe.

Of particular relevance to the work discussed here is the sub-field of astroparticle physics. It is the goal of this sub-field to study the interactions and properties of elementary particles through the lens of astrophysics and cosmology. In recent years, astroparticle physics has gained attention and popularity, in part due to the fact that we have only recently entered a new era in physics research: that of precision cosmology. Precise cosmological observables such as CMB temperature data and measurements of the primordial abundances of light nuclei are newly available to us through ingenious advances in technology and data analysis. These and other early universe observables allow particle physicists to "see" back to times before the formation of stars and galaxies. Using this data we are able to probe times in cosmological history in which the universe was extraordinarily hot and dense. These high temperature environments are the same environments that we endeavor to create on earth using particle colliders like the Large Hadron Collider (LHC) at CERN. For this reason, collider phenomenology research is compatible and at times directly comparable to the research done by astroparticle physicists.

The purpose of this introduction is to provide background knowledge necessary to understand subsequent chapters. I will begin by discussing the known properties of and evidence for dark matter (DM) and potential detection methods. Next, I will give a brief overview of the current status of research in quantum gravity. Finally, I will further discuss the formation of light nuclei in the universe, known as Big Bang Nucleosynthesis (BBN).

1.1 Dark Matter: Known Properties and Detection Methods

Evidence for the existence of DM is broad, robust, and spans a wide range of energy scales. While we know little about its nature, the most widely accepted theory of DM is that it must be some type of subatomic particle who's mass can be as small as 10^{-22} eV and as large as 10^{19} GeV. According to the ΛCDM model, DM makes up about 85% of the matter content in the universe, and 26.8% of the total energy density. Based on this overarching theory, we are able to calculate the DM density today, also known as the relic abundance. While we have yet to observe any interactions between DM and SM particle via strong or electroweak interactions, the existence of DM is implied by many examples of gravitational phenomena that cannot be explained by our modern theory of gravity without the presence of additional unseen matter.

One of the most famous of these phenomena is galaxy rotation curves. The visible matter density of spiral galaxies decreases radially outwards from their centers. If visible matter made up the entirety of the matter in these galaxies, we would expect the rotation velocity of the arms of the galaxy to decrease with increased radius. What we observe, however, is that the rotation curves of spiral galaxies flatten out with increased radius - the velocity of luminous matter in spiral galaxies does not decrease with increased radius. This feature is well explained by the presence of non-luminous matter at large radii. This phenomenon was observed by Dr. Vera Rubin in the early 1970's and while its significance was debated by the community at the time, is known to be the first discovered evidence for the existence of DM.

In the realm of early universe cosmology and astroparticle physics, further evidence for DM can be gleaned in observations of the CMB. Averaged over the sky, the CMB is a perfect blackbody. Precision observations show very small temperature anisotropies at the level of a

few parts in 100,000. In order to analyze these anisotropies, we decompose the temperature map into an angular power spectrum. The height of each of the peaks of this angular power spectrum can be predicted using some set of cosmological parameters using programs such as CAMB [24]. The third peak in the spectrum is particularly sensitive to the density of DM, and by comparing data to simulation, we have been able to verify the value of DM density predicted by ΛCDM, further supporting the existence of some type of DM.

Research groups around the world have made it their primary objective to attempt to detect interactions between DM and SM particles. This is generally done in one of three ways, illustrated in Figure 1.1. The first method is known as direct detection. Direct detection experiments aim to measure interactions of DM and SM particles via scattering. One of the most famous of these experiments is the XENON experiment, located at the Italian Gran Sasso National Laboratory. Since the start of its operation in 2006, the XENON collaboration has been searching for DM weak interactions with Xenon atoms in a liquid Xenon target chamber. The collaboration has collected nearly 20 years of data, actively searching for nuclear recoils in the Xenon which could be evidence of DM scattering. Through these efforts, they have been able to place extremely competitive bound on the DM mass and coupling to SM particles.

The LZ Experiment is another such direct detection expierment, also using liquid Xenon, located at the Sanford Underground Research Facility (SURF) in South Dakota. In July 2023, the LZ experiment and XENON experiment published results on the same day. The LZ experiment was able to exclude cross sections above $9.2\times10^{-48}\text{cm}^2$ at 36 GeV at the 90% confidence level [25] and the XENON experiment was able to exclude cross sections above $2.58\times10^{-47}\text{cm}^2$ at 28 GeV at the 90% confidence level [26].

Figure 1.2, taken from [1] shows the most current bounds on DM mass and coupling from spin-independent elastic WIMP-nucleus scattering searches at a variety of direct detection experiments, including the bounds from XENON, shown in black. The orange dotted line

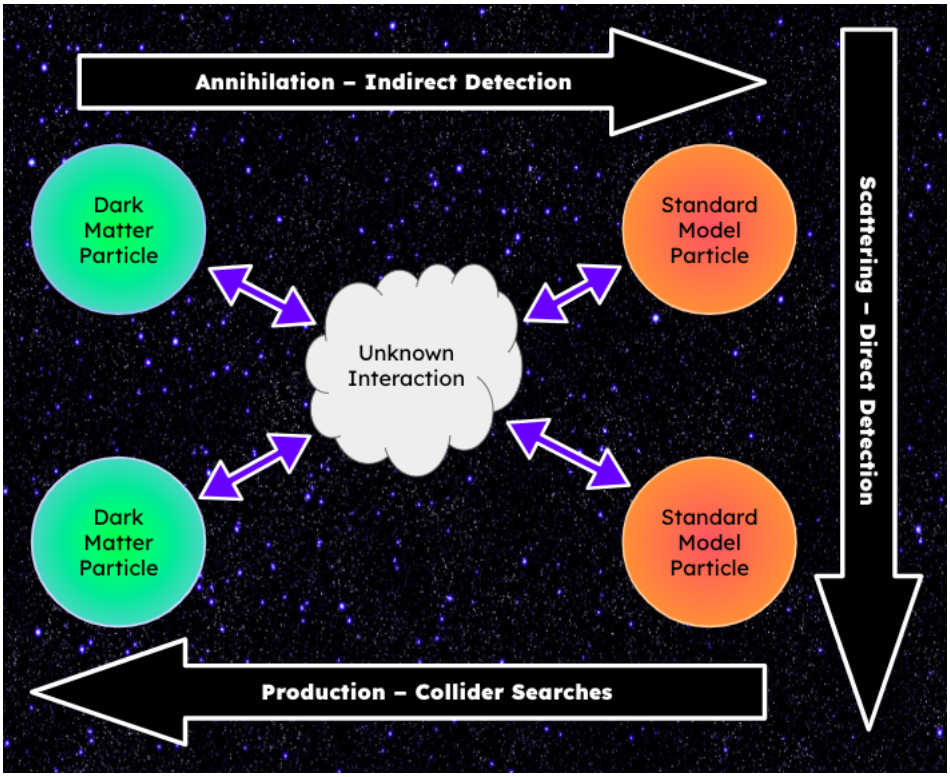

Figure 1.1: This figure shows the three main categories of DM search. The first is indirect detection searches, in which physicists hope to observe the SM products of DM annihilation. The second is direct detection searches, in which physicists hope to observe scattering of a DM particle off of a SM particle. Finally, the third is collider searches, in which physicists hope to observe the production of DM particles from SM particles.

on the plot corresponds to the "neutrino floor", a theoretical limit on the sensitivity of direct detection experiments due to an irreducible background of astrophysical neutrinos. As collaborations push exclusion limits down into smaller cross sections, experiments are getting closer to entering the region of parameter space in which the expected rate of DM interactions is comparable to the rate of neutrino interactions. While the neutrino floor poses a significant experimental design challenge to direct detection collaborations, strides have been made to mitigate this challenge and more and more, the neutrino floor is being demoted to a "neutrino fog" [27].

The second way that particle physicists attempt to search for DM is via collider searches in which SM particles annihilate and produce DM. There are many model dependent and inde-

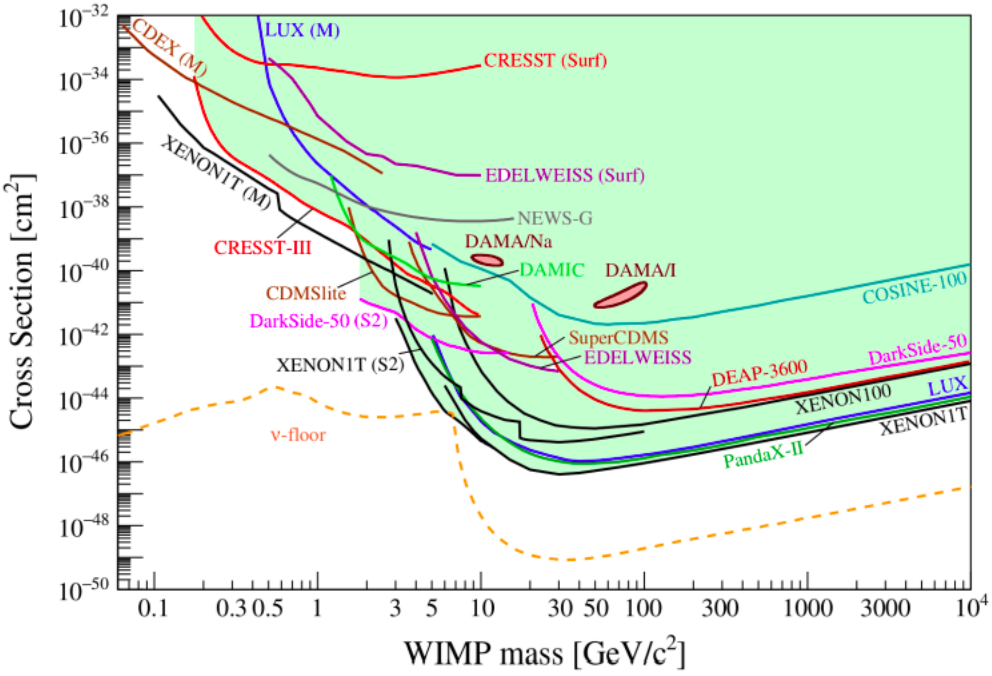

Figure 1.2: Current bounds on DM mass and coupling from spin-independent elastic WIMP-nucleus scattering searches at a variety of direct detection experiments. Exclusion limits were created assume the following parameters for an isothermal WIMP halo: local DM density, $\rho_0 = 0.3$ GeV/cm^3, local DM velocity, $v_0 = 220$ km/s, and DM escape velocity, $v_{esc} = 544$ km/s. The M label corresponds to results obtained assuming the Migdal effect. The Surf label corresponds to results obtained from experiments not operated underground. Figure taken from [1].

pendent search strategies, the majority of which rely on searching for an absence of expected energy in collider data. An example of one search of this type is the search for dark photons with the FASER detector [2]. The FASER experiment, located at the LHC, is designed to search for light particles produced by proton-proton collisions at the ATLAS interaction point in the far-forward direction. In their 2023 paper, cited above, the collaboration used data from FASER to search for dark photons decaying to an electron and positron. Their analysis is almost entirely free of backgrounds, and through this analysis they were able to put extremely competitive bonds on the dark photon mass and kinetic mixing. Figure 1.3, taken from their paper, shows their constraints.

The final way in which experimentalists and phenomenologists search for DM is through a

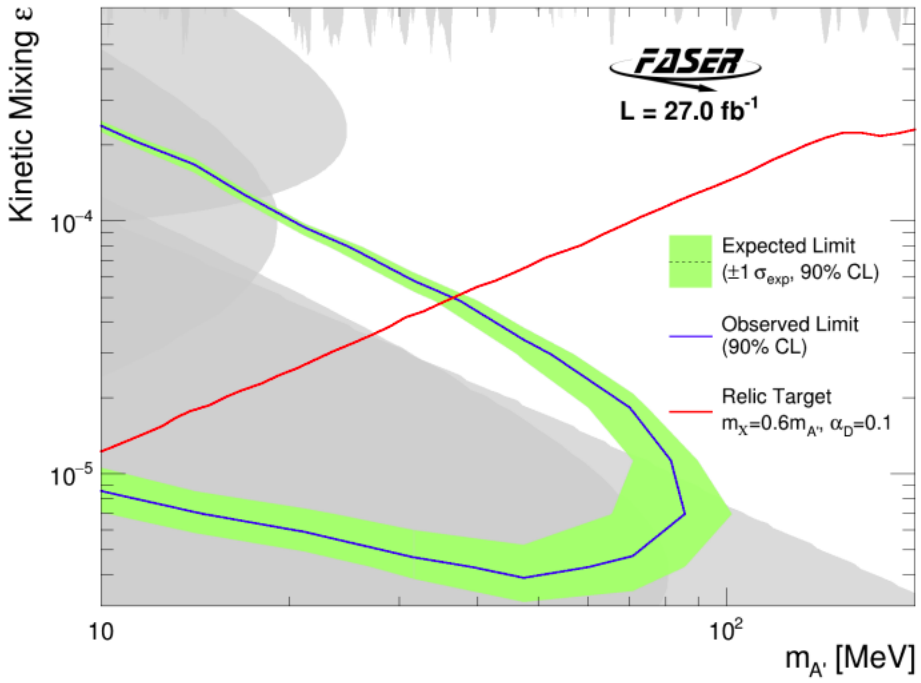

Figure 1.3: In this figure, the grey region correspond to regions previously excluded by other experiments. The green region is the result of thier search: a 90 percent confidence level exclusion contour in dark photon mass and kinetic mixing parameter space. The red line corresponds to the region of parameter space for which the dark photon would yield the correct relic density of DM. Figure taken from [2].

method known as indirect detection. The goal of indirect detection searches is to discover the SM particle products of DM annihilation or decay. Throughout the years, there have been many potential signals from a variety of astrophysical sources, some of which continue to be a topic of debate today. One of these potential signals is an excess of positrons seen in cosmic rays by the AMS-02 experiment [28]. As primary cosmic rays composed of predominantly protons and alpha particles travel through the Milky Way, they are expected to scatter off of interstellar gas, a process which produces positrons, electrons, and photons. These particles constitute so-called secondary cosmic rays. The following diffusion equation describes the approximate evolution of the number density field of cosmic rays, ψ, at a given energy,

$$\frac{\partial \psi}{\partial t} = Q(\vec{x}, E, t) + D(E)\nabla^2\psi + \frac{\partial}{\partial E}(b(E)\psi). \tag{1.1}$$

In this equation, $Q(\vec{x}, E, t)$ represents the sources of the cosmic rays and $b(E)$ describes the energy loss of the studied cosmic ray species. $D(E)$ is the diffusion coefficient and is often parameterized in the following way: $D(E) = D_0(E/E_0)^\delta$. Here, $D_0 \sim$ few $\times 10^{28}$ cm^2/s and $E_0 = 1$ GeV. Discussion of the different possible values that δ can take is beyond the scope of this thesis, but can be found in Dr. Tracy Slatyer's "Les Houches Lectures on Indirect Detection of Dark Matter" [29].

Primary cosmic rays have, on average, harder energy spectrums than secondary cosmic rays, and their energy spectrums are expected to differ by a factor of E^δ. It follows that the ratio of primary to secondary cosmic rays is expected to increase with increasing energy. It was therefore a suprise to the community when, in 2008, the PAMELA experiment observed an excess of positrons at high energies [30]. This result was confirmed with smaller errors by the AMS-02 experiment [28]. While PAMELA observed an excess of positrons at energies of O(10 GeV), AMS-02 saw the positron fraction continue to increase up to energies of about 300 GeV. The discovery of this excess was particularly exciting for DM phenomenologists, as the excess can be well explained by the annihilation or decay of a heavy DM particle. Recently, other explanations for this excess, i.e. positron production by pulsars [31], have been favored due to the fact that the required parameters for the aforementioned DM model are in tension with bounds from the CMB. While alternative explanations have gained popularity, there continue to be models hypothesized in which DM could produce the positron excess and avoid constraints from other observations. Figure 1.4 is taken from Ref [3] and shows the expected positron excess from one such DM model compared to the AMS-02 data. In this model, DM annihilates into a long-lived unstable state which later decays into electron-positron pairs.

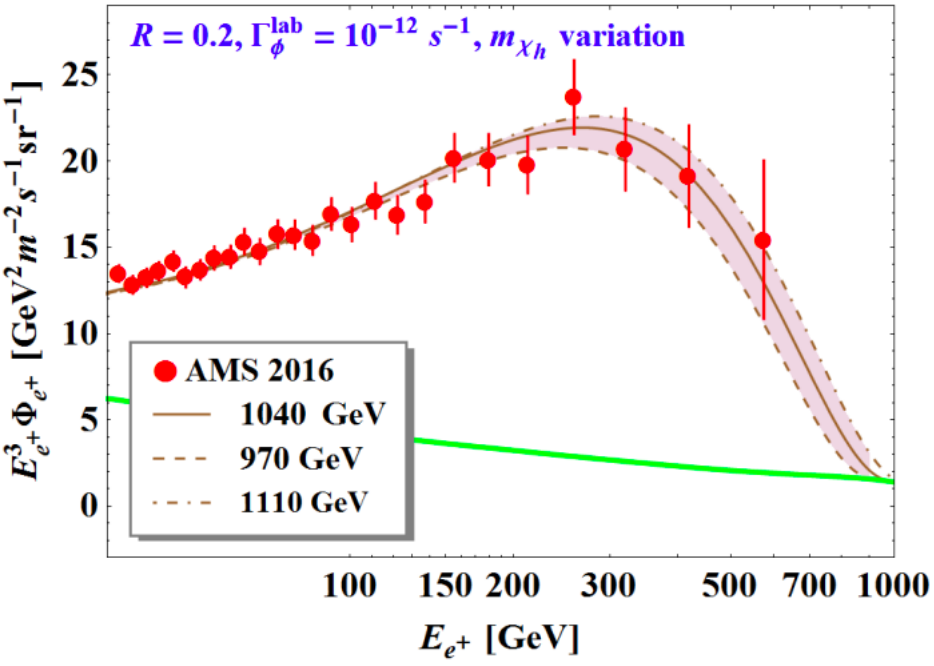

Figure 1.4: This figure shows the fit results of the DM model proposed by Kim, et al with the positron spectrum reported by the AMS-02 Collaboration for varying DM mass. Here, R is the ratio of the DM mass to the mass of the unstable state and Γ_ϕ^{lab} is the decay rate of the unstable particle, ϕ, in the lab frame. The green line represents the theoretically expected positron spectrum. Figure taken from [3].

Other potential signals have been observed as well, including cosmic ray antiprotons and anti-helium from the AMS-02 experiment [32, 33], the 3.5 keV line [34], 21cm absorption [35], and the Galactic Center excess [36]. The Galactic Center excess is the subject of Chapters 2 and 3 of this thesis and will be discussed in further detail there.

1.2 Quantum Gravity

The subfield of quantum gravity has a rich history dating back to the 1930s. The overarching goal of quantum gravity research is to find a consistent and measurable theory of gravity that can describe gravitational dynamics on all scales, from the motion of planets down to the Planck scale. This objective is particularly relevant to the themes of this thesis because

of the role a quantum theory of gravity must play in the very early universe. This topic is also pertinent to Chapter Four of this thesis, where we delve deeper into a specific method of calculating time evolution in the context of quantum cosmology.

The Planck scale, characterized by the Planck units, is the scale at which quantum effects of gravity are expected to become relevant. Planck scale energy is of the order 10^{19} GeV and Planck scale time is of the order 10^{-44} s. For early universe cosmologists, this means in practice that until we have a theory of quantum gravity, times earlier than 10^{-44} s will remain a mystery.

Currently, our understanding of gravity is derived from the theory of General Relativity which describes gravity as a geometrical property of spacetime, and relates the curvature of spacetime to the energy density of matter, radiation, and dark energy. This description of gravity is fundamentally different than our descriptions of the three other known fundamental forces: the strong force, weak force, and electromagnetic interaction. The dynamics and kinematics of these forces are governed by the SM, the underlying mathematical framework of which is a quantum field theory. The SM Lagrangian, in which each particle is included as a dynamical field, can be constructed by first writing down the set of symmetries that govern the system and then writing down the most general renormalizable Lagrangian which includes all of the SM particles and respects the aforementioned set of symmetries. The SM set of symmetries includes global Poincaré symmetry and local $\mathrm{SU}(3)\times\mathrm{SU}(2)\times\mathrm{U}(1)$ gauge symmetry. It is the hope of the majority of theorists who work on quantum gravity to include the gravitational force into this model of particle physics.

Since the strong force, weak force, and electromagnetic interaction all have at least one force carrier particle or gauge boson, it is logical to assume that gravity must have one as well. The theoretical gauge boson for gravity is known as the graviton. It has been known since the 1950s that, taking into account some light assumptions, the graviton should be a massless particle with spin-2 [37].

One of the fundamental challenges in quantum gravity research is that when gravity is treated as a quantum field, the resulting theory is nonrenormalizable. In short, this means that in order for a quantized theory of gravity to make finite predictions at energies beyond the Planck scale, experimentalists would need to measure infinitely many parameters that would then serve as the inputs for the theory. With this challenge in mind, many ideas and theories have been explored, including, famously, string theory in which theorists hope that underlying symmetries of the fundamental theory will reduce the number of parameters in the theory to be finite.

1.3 Big Bang Nucleosynthesis

BBN is the theory of the production of light nuclei in the early universe. The resulting abundance value of each of the light nuclei at the end of BBN is summarized in Table 1.1. These abundance values correspond to the mass fractions of each of the nuclei, i.e. about 24.7% of the baryonic mass that existed in the universe at the end of BBN was in helium-4 nuclei. While some light elements have been produced in stars since the time of BBN, it is believed that the majority of each of these elements that exists in the universe today was created during BBN. This calculation was first done in 1966 [38] and has since been greatly refined and improved upon.

Nuclei	Theoretical Abundance Value
^{4}He	0.24689
D/H	2.4583×10^{-5}
^{3}He/H	1.0414×10^{-5}
^{7}Li/H	5.4432×10^{-10}

Table 1.1: Theoretical Abundance values of the light nuclei produced during BBN, calculated using the PRyMordial code and reported to five significant figures [17].

BBN is of particular interest to cosmologists for two main reasons. The first is that the theory is known to be "parameter free", by which theorists mean that every parameter that goes

into the standard BBN calculation, without taking into account any new physics effects, has been measured.[1] For this reason, theorists are able to place extremely powerful constraints on new physics scenarios which have some effect on this era of the early universe using the observations of primordial light element abundances. These constraints are so powerful both because of the parameter free nature of the theory, and because our observation and theory matches up to an incredible level of precision. The second reason that BBN is considered to be unique is that it is the first event that cosmologists have direct evidence for in the early universe. In addition, we know the temperature, and thereby the time, at which it must have happened. While there are many theories about events that took place in the universe prior to BBN, the light element abundances are our earliest direct observation.

There are three important temperature eras, each with unique physical phenomena, that are important to our understanding of the production of light elements, as shown in Figure 1.5. The first era corresponds to temperatures below the QCD phase transition, at which point protons and neutrons were formed from quarks, and above temperatures of about 1 MeV. During this time, electrons, positrons, photons, and neutrinos were coupled in a plasma. In addition, three reactions converting protons to neutrons and neutrons to protons were in chemical equilibrium and conversion happened freely and regularly.

Around temperatures of about 1 MeV, two important events occurred. The first is that neutrinos decoupled non-instantaneously from the plasma. After this decoupling, the temperatures of the photon bath and the neutrino bath evolved independently. In addition, the reactions governing neutron to proton conversion and vice versa fell out of chemical equilibrium due to the neutron-proton conversion rate, $\Gamma_{n\leftrightarrow p} \sim G_F^2 T^5$ falling faster than the expansion rate of the universe, $H \sim \sqrt{g_* G_N} T^2$ where g_* is the effective number of relativistic degrees of freedom in the early universe. At this point the ratio of neutrons to protons got

[1] It should be noted that historically this was not the case. Before the baryon density was measured using the CMB, it was accurately predicted by comparing the theoretical value of the deuterium abundance to observations [39].

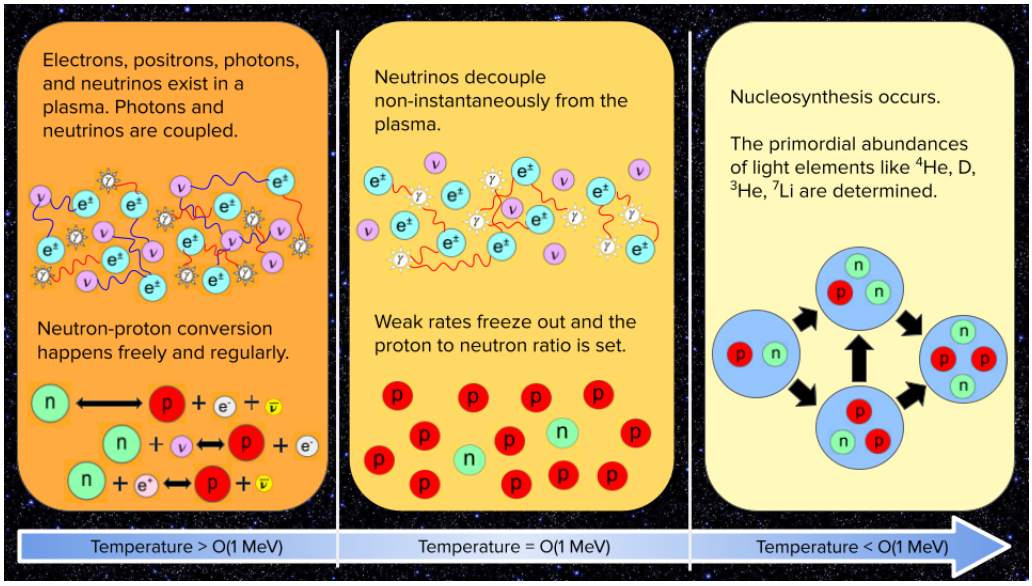

Figure 1.5: This figure shows the three most important temperature eras in the production of light elements. The first is temperatures below the QCD phase transition and above 1 MeV in which photons and neutrinos are coupled and neutron-proton conversion happens freely and regularly. The second is the time at which the universe has a temperature of O(1 MeV). At this time neutrinos decoupled non-instantaneously from the plasma and proton-neutron conversion freezes out. Finally, at temperatures below 1 MeV, BBN occurs.

set at about 1:6. At temperatures below about 1 MeV, the process of nucleosynthesis began with neutrons and protons fusing to form deuterium nuclei plus a photon. It is important to note that during this time the average temperature of photons in the bath was higher than the deuterium binding energy. As a result, almost immediately after deuterium formed in the aforementioned process, it would photodissociate. This time period is known as the "deuterium bottleneck" and until the photon bath cooled below the deuterium binding energy, BBN was unable to proceed. During this time, the neutron to proton ratio declined due to beta decay, in which neutrons decay into protons, electrons, and electron-antineutrinos causing the final ratio of neutrons to protons to be about 1:7. This parameter, the neutron to proton ratio, is extremely important in determining the final abundance values, and in particular, the final abundance value of helium-4 as the majority of the neutrons in the universe at the time end up in these nuclei.

Another important parameter that plays a role in the BBN calculation is the baryon to

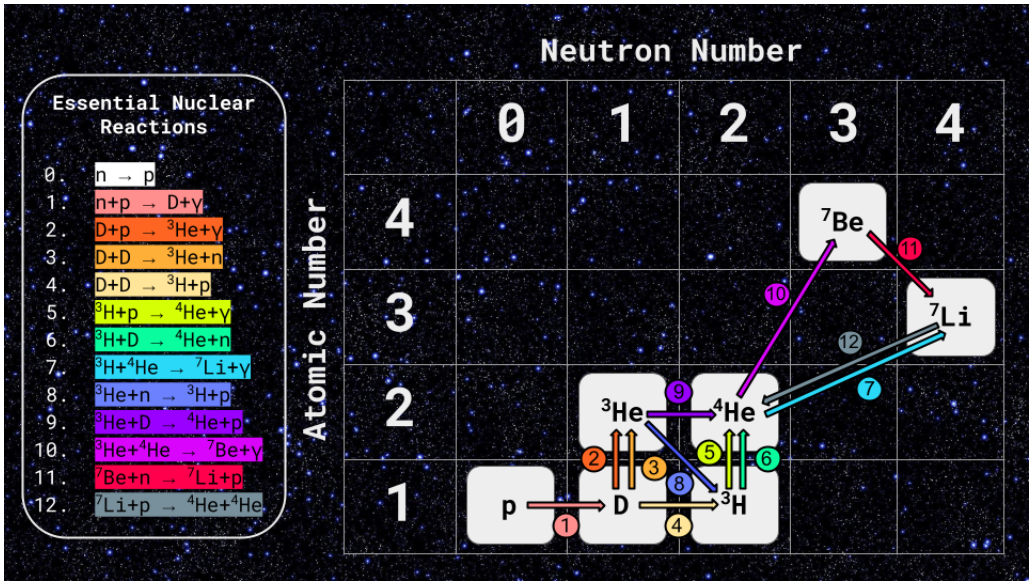

Figure 1.6: This graphic shows the 12 most essential nuclear reactions in the production of light nuclei during BBN. Rows represent the number of protons per nuclei and columns represent the number of neutrons.

photon ratio, η_B which has been measured to be about 6×10^{-10}. η_B controls the rate at which nuclei collide and react in thermonuclear reactions during BBN, which ultimately determines their final abundance values. There are hundreds of these thermonuclear reactions which play a role, the twelve most essential of which have been summarized in Figure 1.6. This is discussed in further detail in Chapter 5 and Figure 5.2 shows the way in which abundance values vary with varied η_B.

Theorists predict that by 180 seconds after the Big Bang the abundances of deuterium, helium-3, helium-4 and lithium-7 leveled out to their final predicted primordial values. At this time in the early universe, photons were not yet free streaming, and thus, experimentalists are unable to directly observe times this early. Instead, observational astrophysicists seek out regions of space which are known to be primarily composed of hydrogen and helium to observe the abundances of these elements. This is because the production of heavier elements such as carbon, nitrogen, and oxygen alters the abundances of light elements, especially those of helium and deuterium. By seeking out environments with low metallicity, astrophysicists ensure that the values of the element abundances that they are measuring

are as close as possible to the true primordial values.

Observational astrophysicists measure primordial deuterium using spectroscopy, specifically by looking at the absorption spectra from young, low-metallicity galaxies backlit by quasars. Deuterium is measured in absorption spectra by observing the spectra's isotope-shifted Lyman-α features. Deuterium is known to be entirely destroyed during stellar processing, so observing sufficiently high-redshift galaxies is crucial to this measurement. In addition, for this reason along with the fact that BBN is the only known significant source of deuterium in the universe, our measurements of the primordial deuterium abundance are lower bounds. The weighted average of the 11 most precise measurements of deuterium is the following [40]:

$$\mathrm{D/H} \times 10^5 = (2.547 \pm 0.025). \tag{1.2}$$

The primordial abundance of ^{4}He is also measured via spectroscopy using the emission lines of both helium and hydrogen in metal poor galaxies. In these galaxies primordial interstellar gas is ionised by photons emitted from young stars. A number of strong emission lines can be observed as a result of this gas cooling. It has been confirmed using that with these galaxies that an increase in helium abundance is correlated with increased production of heavier elements, so it is therefore necessary to extrapolate any measurements of helium abundance down to zero metallicity to access the primordial value. The electron density and temperature of the interstellar gas in question has a measurable effect on the observed abundance value. In 2015 it was demonstrated that by including the He λ10830 infrared emission line in the determination of the ^{4}He abundance, systematic uncertainties on the measurement could be significantly lowered due to the dependence on the He λ10830 emission line with the electron density [41]. The recommended value from the PDG for the primordial ^{4}He abundance is

[40]:

$$Y_p = 0.245 \pm 0.003. \tag{1.3}$$

In 2022 the EMPRESS collaboration published a new value for the primordial ^{4}He abundance, arguing that this value is more accurate than previously accepted values due to the inclusion of measurements from newly observed extremely metal poor galaxies [42]. This result is discussed in further detail in Chapters 6 and 7.

While there is some data on the primordial abundance of ^{3}He, the PDG does not recommend using it as a cosmological probe due to the limited available data and uncertainty in the expected abundance of ^{3}He from stellar production. The limited available data on the primordial abundance of ^{3}He comes from our own solar system and regions of ionized gas in the Milky Way with similar levels of metallicity as are found in the sun [43].

Unlike the other light element abundances, the primordial abundance of ^{7}Li is measured in the atmospheres of metal-poor stars [44]. The observational value reported by the PDG is [40]:

$$\mathrm{Li/H} = (1.6 \pm 0.3) \times 10^{-10} \tag{1.4}$$

the uncertainty on which is more than an order of magnitude larger in comparison to the value than the uncertainty on the deuterium or ^{4}He abundances. This measurement is in tension with the theoretically determined value of the ^{7}Li abundance at the level of about 5σ. This tension has historically been known as the "Lithium Problem." While many solutions to the Lithium Problem have been proposed, one of the recent and most convincing solutions comes from Brian Fields and Keith Olive in their 2022 paper [4].

Under the assumption that ^{7}Li is not significantly depleted in stars, the observed value of

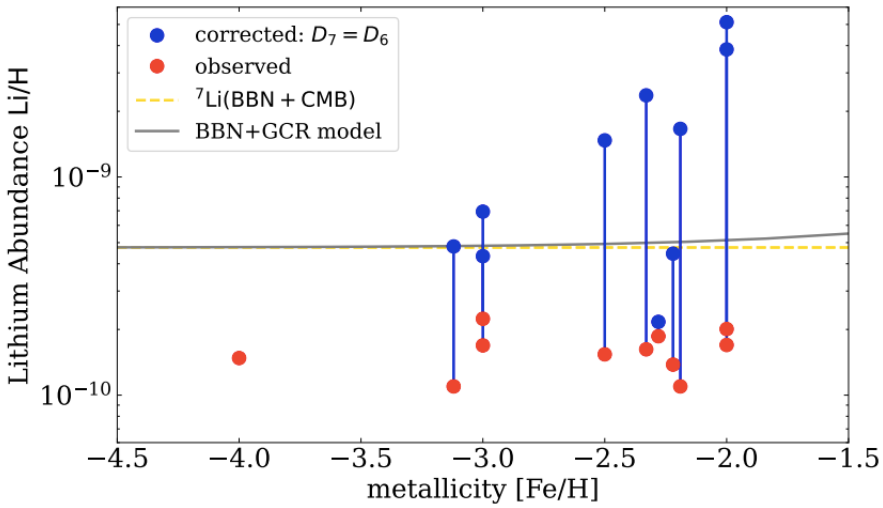

Figure 1.7: In this figure, the red points are the observed values of (^{6}Li + ^{7}Li)/H and the blue points are the values of (^{6}Li + ^{7}Li)/H with corrections for stellar depletion included. The yellow line shows the theoretically predicted value of (^{6}Li + ^{7}Li)/H and the black line shows the author's model for BBN+CMB evolution. It is clear from this figure that if ^{7}Li is depleted in stars to the extent that ^{6}Li is depleted, the result is an over correction to the Lithium Problem. Figure taken from [4].

the ^{7}Li abundance is significantly below the theoretically predicted value. Ref. [4] proposes a solution to the Lithium Problem by calling this assumption into question. The authors cite two pieces of evidence in recent observations of metal poor stars to back up their argument. The first is that the values of the ^{7}Li abundance in observed stars differ significantly between stars. Second, in recent data there is no evidence of previously reported ^{6}Li abundance, and the authors of these studies have produced tight new upper limits on the the ^{6}Li/^{7}Li ratio in the observed stars [45]. These new observations imply that the original abundance of ^{6}Li has depleted significantly over time. The authors of Ref. [4] argue that if the abundance of ^{7}Li has depleted as significantly as that of ^{6}Li, then the tension between the theory value of the ^{7}Li abundance and the observed value will be alleviated. Figure 1.7 shows the main results of their paper.

Chapter 2

On Dark Matter Explanations of the Gamma-Ray Excesses from the Galactic Center and M31

This chapter is heavily based on work previously published in collaboration with Max Fieg, Christopher M. Karwin, and Arvind Rajaraman [19].

2.1 Introduction

There is now overwhelming evidence that most of the matter in the universe is composed of dark matter (DM) [46, 47, 48, 49, 50, 51, 52, 53, 54]. However, despite much experimental effort for many decades now, the nature of DM still remains elusive. Determining the characteristics of DM is one of the most important outstanding problems in particle physics.

One of the most promising approaches for detecting DM is indirect detection. DM particles can annihilate or decay to Standard Model (SM) particles, which can be detected in astro-

physical searches. In particular, annihilation or decay into photons gives a striking signal, since their direction of arrival is correlated with their annihilation location, and because photons can travel over large distances.

Simulations predict that the highest DM density should be near the Galactic center (GC), though models differ on the exact profile shape. Since the annihilation signal goes as the square of the density, the GC is thus expected to be one of the brightest sources of γ-rays from DM annihilation, and this makes it is an important target for indirect searches.

It has now been well established that there exists an excess of γ-rays toward the GC (as compared to the expected background) [55, 56, 57, 58, 59, 60, 61, 62, 63, 5, 64, 65, 66, 67, 68, 69, 70, 71]. Intriguingly, the signal is found to be broadly consistent with having a DM origin, in regards to the energy spectrum and morphology. However, there are other plausible interpretations of the excess, including mis-modeling of the foreground emission from the Milky Way (MW), and an un-resolved population of point sources, such as millisecond pulsars [72, 73, 74, 75, 76]. These other possibilities make it very difficult to extract a DM signal with a high degree of confidence.

Determining whether or not the GC excess does in fact have a DM origin (at least in part) will likely require complementarity with other targets, as well as other search methods (e.g. direct detection). For γ-ray searches, the MW's dwarf spheroidal (dSph) satellite galaxies offer another promising target, as they are expected to be dominated by DM, with very little astrophysical background. However, thus far there has been no global signal detected, a result that is in tension with the DM interpretation of the GC excess [77, 78]. However, it is important to note that the limits from the dSphs are subject to systematic uncertainties relating to their DM content, and this prohibits their ability to robustly constrain the GC excess [79, 80, 81].

Looking beyond the MW, the Andromeda galaxy (also known as M31) is the closest large

spiral galaxy to us and is predicted to be the brightest extragalactic source of DM annihilation [82, 83]. Recently, observations towards M31's outer halo reported evidence for an excess signal, with a peak in the γ-ray spectrum at an energy similar to the GC excess [6]. Moreover, the analysis is based on the outer regions of M31 where backgrounds from standard astrophysical emission are less dominant. It is thus plausible that both these signals result from DM annihilation.

In this work we perform a simultaneous analysis of the GC and M31 to determine if these two excesses are consistent with having a DM origin. We first examine the two spectra and see if they are consistent with each other once J-factors are taken into account. This turns out to be the case; furthermore, the required scaling turns out to be within the allowed range from a recent analysis of the M31 J-factor [20].

We then compare these spectra to various models of DM annihilation. We first consider 2-body final states, such as DM annihilating to bottoms and taus. It is also interesting to consider four-body final states, which are motivated in models where DM is coupled to the SM through pseudoscalar mediators [84, 85, 86, 87] (such models avoid direct detection constraints). We therefore consider a few motivated examples of annihilation to four final-state particles. As we shall show, both two-body annihilations and four-body annihilations can produce good fits to the observed spectra.

The chapter is organized as follows. In section 2.2 we review the observational data leading to the GC excess, and the more recent signal towards the outer halo of M31. We also review the current bounds on the J-factors of the two signal regions. In the following section, Section 2.3, we compare the M31 and GC spectra and examine whether they are consistent with the allowed J-factors. We then, in Section 2.4, consider the spectra from specific DM models and find the best fit to the observations. We end with a summary of our results. In Appendix A, we present results for other two-body and four-body annihilation channels, along with a table summarizing all our results.

2.2 Review of GC and M31 Observations

2.2.1 GC

For the GC excess we use data from Ref. [5]. Here we summarize a few main aspects of the analysis. The observations are based on approximately 5.2 years of *Fermi*-LAT data, with energies between 1–100 GeV, in 20 logarithmically spaced energy bins.

A majority of the diffuse emission in the Galaxy is due to the interaction of cosmic rays (CRs) with the interstellar gas and radiation fields. Indeed, the emission toward the GC is dominated by standard astrophysical processes, and the GC excess only amounts to a small fraction of the total emission. To quantify the uncertainty in the foreground/background emission, Ref. [5] employs the CR propagation code GALPROP[1] [88, 89, 90, 91, 92, 93, 94, 95, 96, 97, 98] to build four different interstellar emission models (IEMs), corresponding to two main systematic variations.

First, Galactic CRs are thought to be accelerated primarily from supernova remnants (SNRs) via diffusive shock acceleration (see Ref. [5] and references therein). However, the distribution of SNRs is not well determined due to the observational bias and the limited lifetime of their shells, and so other tracers are often employed. Ref. [5] uses two possible tracers, namely, the distribution of OB-type stars, which are progenitors of supernovae, and pulsars, which are the end states of supernovae.

The second main variation comes from the tuning of the IEMs to the γ-ray data. This was done outside of the signal region, working from the outer Galaxy inward, with two variations in the fit. In the intensity-scaled variation, only the normalizations of the IEM components were left free to vary. In the index-scaled variation, additional degrees of freedom were

[1] Available at `https://galprop.stanford.edu`

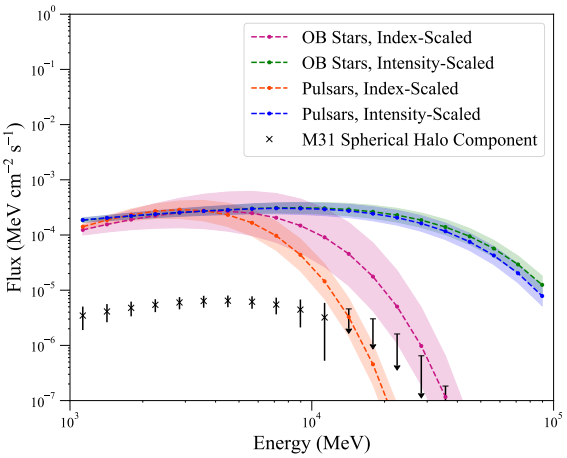

Figure 2.1: The colored dashed lines show the spectra of the GC excess for different IEMs, based on Ref. [5]. The bands show the 1σ uncertainty. Black points show the spectrum for M31's spherical halo component, based on Ref. [6].

given to the gas-related components interior to the Solar circle by also freely scaling the spectral index.

Combining the variations in the CR density and the tuning procedure gives four possible IEMs which quantify the uncertainty in the foreground/background emission. We shall denote these four IEMs as (a) OB Stars, index-scaled (b) OB Stars, intensity-scaled (c) Pulsars, index-scaled; and (d) Pulsars, intensity-scaled. Figure 2.1 shows the spectra for the GC excess, corresponding to the four IEMs. Note that the intensity-scaled models have a high-energy tail which is not present in the index-scaled models.

2.2.2 M31

For the M31 analysis we follow Ref. [6]. The analysis employs 7.6 years of *Fermi*-LAT data, with energies between 1–100 GeV, in 20 logarithmically spaced energy bins. Similar to the GC, the foreground emission from the MW is the dominant component when looking towards M31's outer halo, and Ref. [6] again used GALPROP to build specialized IEMs to

characterize the emission.

Evidence for an excess signal was found, having a radial extension of $\sim 120 - 200$ kpc from the center of M31. To characterize the excess, three additional signal components were added to the model (i.e. in addition to the IEM). For the inner galaxy a 0.4° disk was used, consistent with what has previously been reported [99, 100, 101]. A second concentric ring was also added, extending from 0.4° to 8.5° (corresponding to a projected radius of ∼120 kpc); this is referred to as the spherical halo component. Finally, a third concentric ring was added, extending from 8.5° and covering the remaining extent of the field (corresponding to a projected radius of ∼200 kpc); this is referred to as the far outer halo component.

Here, we only use data from the spherical halo region, and the corresponding spectrum is shown in Figure 2.1. The inner galaxy is problematic for two reasons. First, it is difficult to disentangle a possible DM signal from standard astrophysical emission. Secondly, there still remains a high systematic uncertainty to the actual γ-ray signal that is detected [6, 20]. This is due to an uncertainty in the underlying H I gas maps that are used for the Milky Way (MW) foreground. We also ignore the far outer halo region because it begins to approach the MW disk toward the top of the field, which significantly complicates the analysis. If the excess γ-ray emission observed toward M31's outer halo does in fact have a physical association with the M31 system, then it is particularly important to establish this in the spherical halo region [20].

2.2.3 J-factors

The greatest uncertainty for the DM interpretation of M31's outer halo comes from the J-factor. This is covered in extensive detail in Ref. [20]. Here, we use results from that study to quantify the full uncertainty range, and below we summarize the key points.

The J-factor characterizes the spatial distribution of the DM, and is given by the integral of the mass density squared, over the line of sight. When describing the DM distribution as an ensemble of disjoint DM halos, the J-factor is:

$$J = \sum_i \int_{\Delta\Omega} d\Omega \int_{\mathrm{LoS}} ds \rho_i^2(\mathbf{r}_i(s, \mathbf{n})), \tag{2.1}$$

summed over all halos in the line of sight (LoS), where $\rho_i(\mathbf{r})$ is the density distribution of halo i, and $\mathbf{r}_i(s, \mathbf{n})$ is the position within that halo at LoS direction $\mathbf{n}$ and LoS distance s.

J-factors determined from these spherically-averaged profiles are an underestimate of the total J-factor because of the effect of the non-spherical structure. This underestimate is typically encoded with a boost factor. The substructure component is very important for indirect detection, as it enhances the overall signal, since the predicted γ-ray flux scales as the mass density squared. This is especially true for MW-sized halos and toward the outer regions.

The main uncertainties in the boost factor include the minimum subhalo mass, the subhalo mass function, the concentration-mass relation, the distribution of the subhalos in the main halo, the mass distribution of the subhalos themselves, and the number of substructure levels. In Ref. [20] these physical parameters are varied within physically motivated ranges (as representative of the current uncertainty found in the literature) in order to quantify the uncertainty in the substructure boost. Additionally, there is also an uncertainty in the halo geometry, which is quantified by calculating J-factors for the different experimental estimates found in the literature.

In addition to the substructure and halo geometry, another primary driver of the J-factor uncertainty for obervations toward M31's outer halo is the contribution to the signal from the MW's DM halo along the line of sight, which is also accounted for in Ref. [20]. Including all these uncertainties, the J-factor integrated over the spherical halo region, (which we will

henceforth denote as J_{M31}) is found to range from $(2.0 - 31.1) \times 10^{20}$ GeV^2 cm^{-5}, with a geometric mean of 7.9×10^{20} GeV^2 cm^{-5}. We emphasize that this range accounts for the contribution from the MW's halo along the line of sight.

For the GC we use the J-factor from Ref. [5] that was used to extract the excess signal (which is consistent with the data that we use in this analysis). This corresponds to a Navarro-Frenk-White (NFW) density profile with a slope $\gamma = 1$, a scale radius $r_{\rm s} = 20$ kpc, and local DM density $\rho_\odot = 0.3$ GeV cm^{-3}. The J-factor integrated over the $15^\circ \times 15^\circ$ GC region (which we will henceforth denote as J_{GC}) has a value of 2.2×10^{22} GeV^2 cm^{-5}. We note that there is an uncertainty in the GC J-factor due to the value of the local DM density, as well as the other parameters in the density profile. However, in this work we consider just the uncertainty in the M31 J-factor, since it is dominant.

As described in more detail in the next section, a particularly important quantity in our analysis will be the ratio of the J-factors:

$$J_r \equiv J_{GC}/J_{M31} \tag{2.2}$$

For the values of J_{M31} between $(2.0-31.1)\times 10^{20}$ GeV^2 cm^{-5} for the spherical halo component of M31, and $J_{GC} = 2.2 \times 10^{22}$ GeV^2 cm^{-5} we find that J_r lies between $J_{r,low} = 7.07$ and $J_{r,high} = 110.0$. Using the geometric mean of $J_{M31} = 7.9 \times 10^{20}$ GeV^2 cm^{-5}, we define $J_{r,mid} = 28.17$.

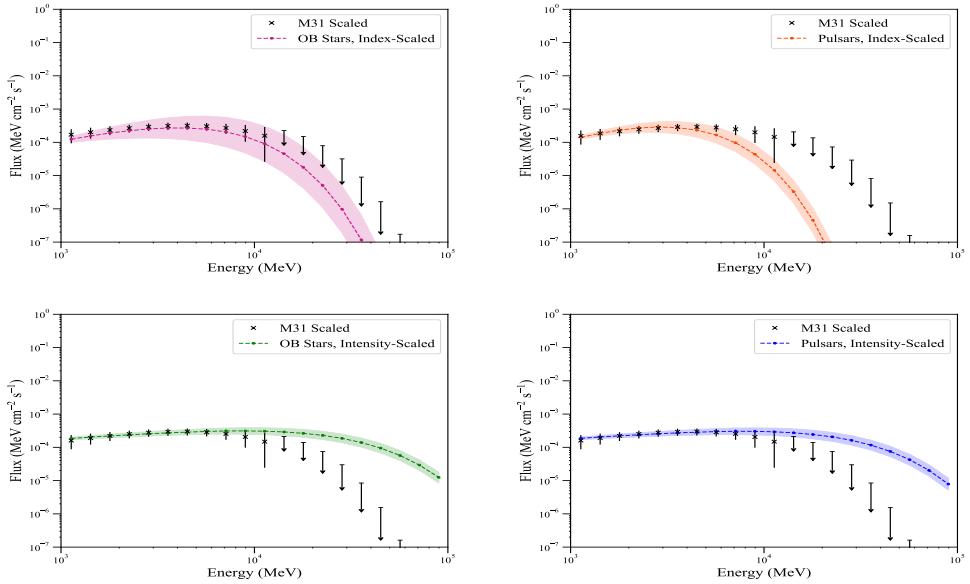

Figure 2.2: Comparison of GC spectra (colored bands) to scaled M31 spectra (black data points). The bands and error bars give the 1σ statistical error. The top two panels show the index-scaled IEMs, and the bottom two panels show the intensity-scaled IEMs. In each case the M31 data is scaled by the appropriate J-factor for the IEM.

2.3 Spectral Comparison of the GC and M31 Excesses

2.3.1 Best-fit J-factor ratios

The flux observed from M31 is much lower than that of the GC excess. If the excesses are indeed from an underlying DM model, then the underlying cross-section for DM annihilation to photons should be the same. The difference in the spectra would then be attributable mostly to the ratio between J_{M31} and J_{GC}. We note, however, that there may be some differences that arise from secondary emission, which depends on the particular astrophysical backgrounds in each respective targets (i.e. the gas and interstellar radiation fields) [102]. For simplicity these effects are not considered in this analysis.

To test the agreement between the two spectra we multiply the M31 data by a scaling factor. This factor is then the ratio J_r. Since the four GC background models yield significantly

different spectra, we fit the scaling factor independently for each of them.

The best-fit scaling factor is determined using a χ^2 fit. We account for upper limits (ULs) in the data by including an error function in the χ^2 definition [103, 104, 20]

$$\chi^2 = \sum_{i=1}^{m} w_i^2 - 2 \sum_{i=m+1}^{20} \ln \frac{1 + \mathrm{erf}(w_i/\sqrt{2})}{2} \tag{2.3}$$

where

$$w_i = \frac{(\frac{y_i}{z_i} - J)}{\sigma_i^r} \qquad \text{and} \qquad \mathrm{erf}(z) = \frac{2}{\sqrt{\pi}} \int_0^z e^{-t^2}\, \mathrm{d}t \tag{2.4}$$

The first term on the right-hand side of Eq. (2.3) is the classic definition of χ^2, and the second term introduces the error function to quantify the fitting of ULs. The number of good data points is given by m, and the sum is over the 20 energy bins. Here y_i is the flux from the GC and z_i is the flux from M31, for the ith energy bin.

The error on the flux ratio J_r is taken to be

$$\sigma_i^r = \frac{\sigma_i^y}{z_i} \tag{2.5}$$

where we use just the statistical error on the GC data, which we assume to be symmetric. This allows for a reasonable spectral comparison, and is further justified by the fact the uncertainty in the GC excess is dominated by the systematics. We note that in general a more sophisticated treatment of the errors may be appropriate (e.g. [103, 20]). However, we have tested different prescriptions for handling the error and in all cases we find that the results are qualitatively consistent.

We minimize the χ^2 with respect to J, and identify the minimum with the optimized rescaling factor. The second column of Table 2.1 shows the best-fit results for each IEM. We note

IEM	J_r
Pulsars, intensity-scaled	48.96 ± 2.31
Pulsars, index-scaled	36.63 ± 3.37
OB Stars, intensity-scaled	48.76 ± 2.22
OB Stars, index-scaled	41.24 ± 5.75

Table 2.1: J-factor ratio for each IEM.

that the best-fit J-factor ratios are well within the bounds from section 2.2.3. There is a preference for smaller values of $J_r \sim 40$, corresponding to larger values of J_{M31}. We will refer to these as the *model-independent* J_r values (as these are found without reference to a specific DM annihilation model).

2.3.2 Spectral Comparisons

We further examine the agreement between the M31 spectrum and the GC excess by scaling the M31 data by the best-fit J-ratio found above, and comparing the two spectral shapes. These comparisons are shown in Fig. 2.2. The top panel shows the rescaled M31 data compared to the GC excess for the index-scaled IEMs. As can be seen, the spectra show excellent agreement.

The bottom panel shows the intensity-scaled IEMs. As can be seen, there is a strong tension between the GC and M31 spectra at high energy (above $\sim$10 GeV). This is due to the existence of the so-called "high-energy tail" in the intensity-scaled IEMs. The nature of the high-energy tail of the GC excess has been investigated in numerous studies (e.g. [5, 105, 106, 107]). It remains uncertain whether this feature is a true property of the signal or if it is due to mis-modeling of the background. When comparing the GC excess to the M31 excess, it is important to note that the two signals are extracted from very different regions

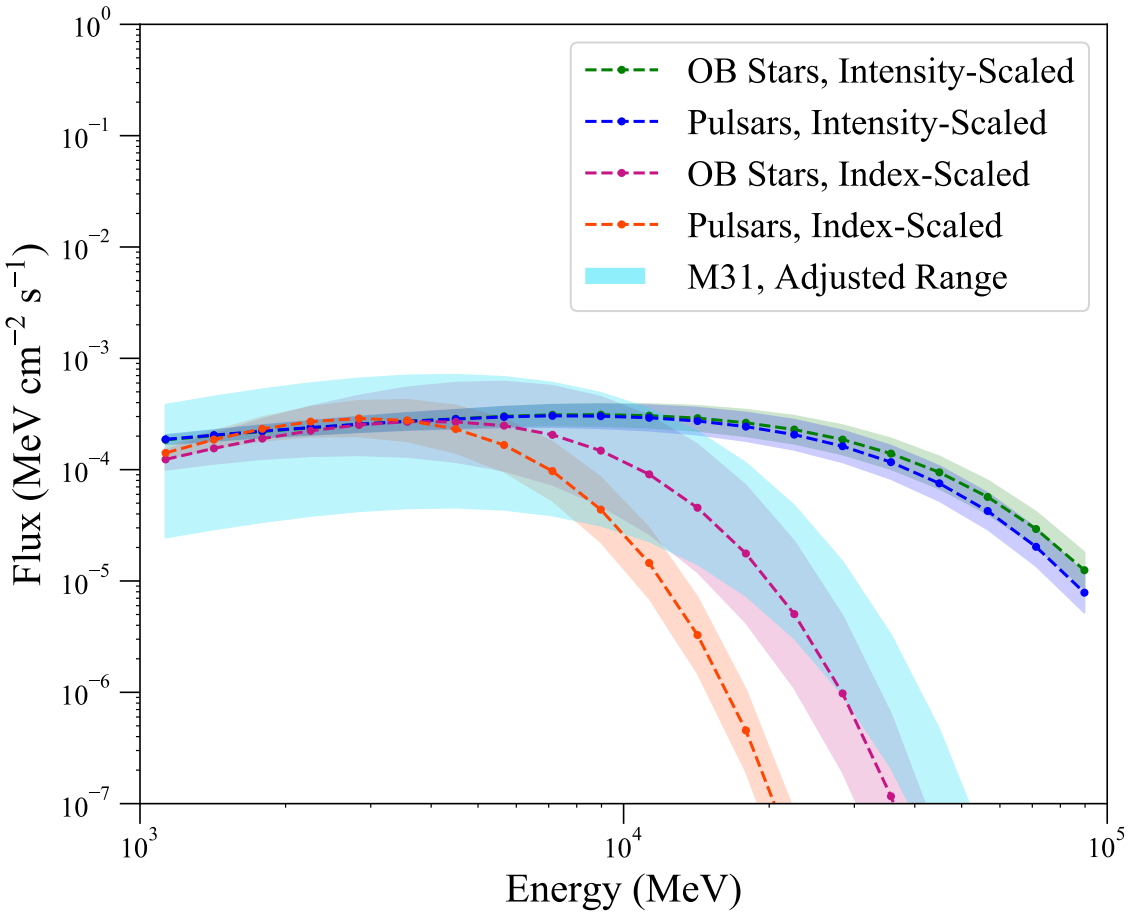

Figure 2.3: The blue band shows the range of M31 flux values scaled up by a J-factor ratio between 7.7 and 110. Dashed lines show the four different GC IEMs with one sigma error bands.

of the galaxy, and thus they may not be directly comparable. In particular, this is the case when considering secondary emission, which depends on the astrophysical backgrounds. With that said, the M31 data does not possess a high-energy tail, and so seems to be in strong tension with those models. Indeed, this would be in general agreement with previous studies which have found that the high-energy tail is not very compatible with having a pure DM explanation [106, 107].

One can also examine whether a different choice of J-factor could ameliorate the tension at high energies between the M31 excess and the intensity scaled GC excesses. To examine this, we find the range of possibilities for the M31 flux, by rescaling it by the maximum and minimum J-factors allowed from Ref. [20]. Figure 2.3 shows the scaled M31 data compared to the GC excess for the four IEMs. As can be seen, the M31 data shows good agreement with the index-scaled IEMs, whereas there is still tension with the intensity-scaled IEMs.

2.4 Dark Matter Models

In this section we perform a DM fit simultaneously to both signals. We will take a model where DM is a real scalar field χ of mass m_χ, and consider various possibilities for the dominant annihilation process; specifically, we will consider both two-body and four-body final states. For the standard WIMP models the DM spectra were generated using PPPC [108]. For the four-body annihilations the spectra were produced using FeynRules [109] and MadGraph [110], and showered with Pythia 8 [111]. The photons were binned in 20 logarithmically-spaced bins from $1-100$ GeV, just as for the GC and M31 data.

The predicted γ-ray flux from DM annihilation is given by

$$E^2 \frac{d\Phi}{dE}\bigg|_{GC} = \mathcal{N}_{GC}(E^2 \frac{dn}{dE}) \qquad E^2 \frac{d\Phi}{dE}\bigg|_{M31} = \frac{\mathcal{N}_{GC}}{J_r}(E^2 \frac{dn}{dE}) \tag{2.6}$$

Here

$$\mathcal{N}_{GC} = J_{GC} \frac{\langle \sigma v \rangle}{4\pi \eta m_\chi^2} \tag{2.7}$$

where $\langle \sigma v \rangle$ is the velocity averaged cross section, η is 2 (4) for conjugate (non-self conjugate) DM, m_χ is the DM mass, and dn/dE is the number of γ-ray photons per annihilation.

We perform a χ^2 fit as in Eqs. 2.3-2.4. The main difference is the definition of w_i. This quantity is defined separately for the GC and M31. For the GC:

$$w_i = \frac{y_i - N E^2 \frac{dn}{de}}{\sigma_i^y} \tag{2.8}$$

where σ_i^y is the 1-sigma error on the GC flux and y_i is the best fit value of the GC flux for a given IEM. Similarly for M31 we have

$$x_i = \frac{z_i - J^{-1} N E^2 \frac{dn}{de}}{\sigma_i^z} \tag{2.9}$$

where the error σ_i^z is the 1-sigma error on the M31 flux and z_i is the best fit value of the M31 flux.

Finally, we define the total chi-squared as

$$\chi^2_{tot} = \chi^2_{GC} + \chi^2_{M31} \tag{2.10}$$

We marginalize over N in order to minimize this quantity with respect to $J_{\rm r}$ and m_χ. This is done separately for each GC IEM.

Figure 2.4 shows the results for the two-body annihilation to bottom quarks with the OB Stars, index-scaled IEM. The color scale indicates the value of $\Delta\chi^2$. The best-fit is shown with a red point, and also overlaid are the 1σ, 2σ, and 3σ confidence contours, correspond-

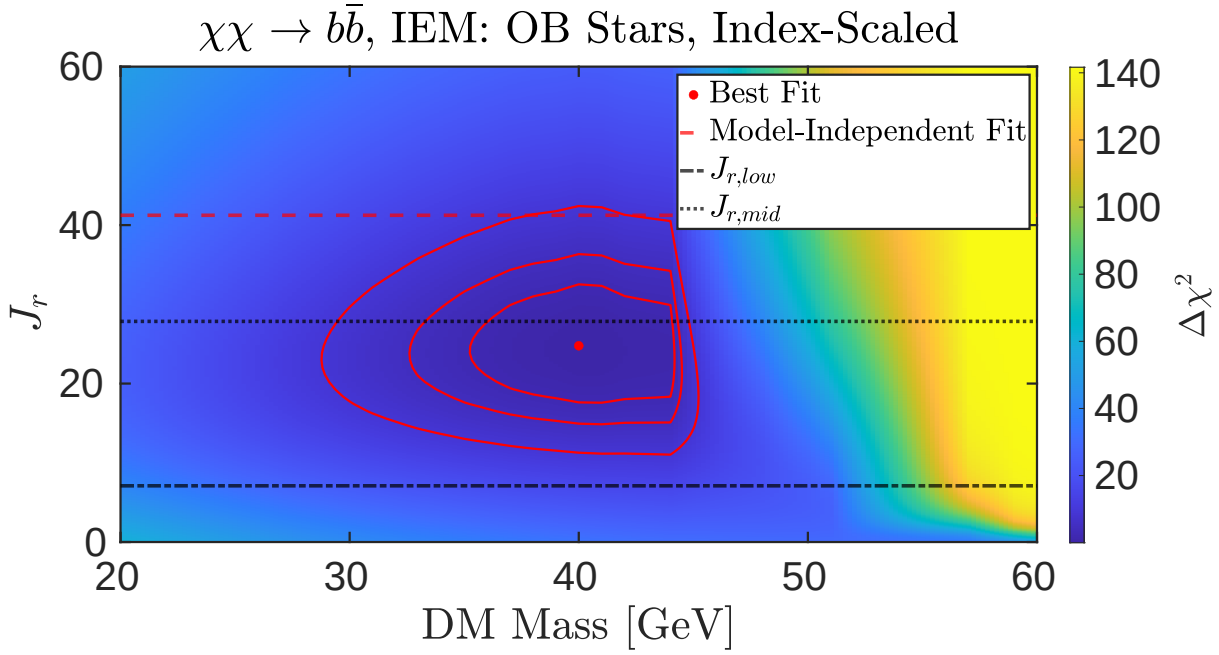

Figure 2.4: $\Delta\chi^2$ for $\chi\chi \to b\bar{b}$, for the OB Stars index-scaled IEM. The red dot indicates the best fit point, and the contours are 1,2, and 3 σ contours. The dashed red line shows the model independent J_r value. Dash-dotted and dotted black lines show high and mean values of J_r from section 2.2.3.

ing to $\Delta\chi^2 = 2.30, 4.61$ and 9.21, respectively. For comparison, we also show the model-dependent J_r value from Table 1 and $J_{r,low}, J_{r,mid}$ from Section 2.2. As can be seen, the J_r corresponding to the DM fit is in good agreement with the range found in Ref. [6]. In Figure 2.5 we show the corresponding best-fit DM spectrum compared to the GC and scaled M31 data.

We have also extended our analysis to other possible annihilation modes; these results are presented in the Appendix. Specifically, we first considered other two-body annihilations where the DM annihilates to two tau leptons, and the case where the DM annihilates to two light quarks, which we take to be down quarks for concreteness. Figure 2.6 shows the results for these annihilation channels.

As mentioned above, direct detection and collider searches significantly constrain DM couplings. This has motivated the study of models where the DM is coupled to the SM quarks

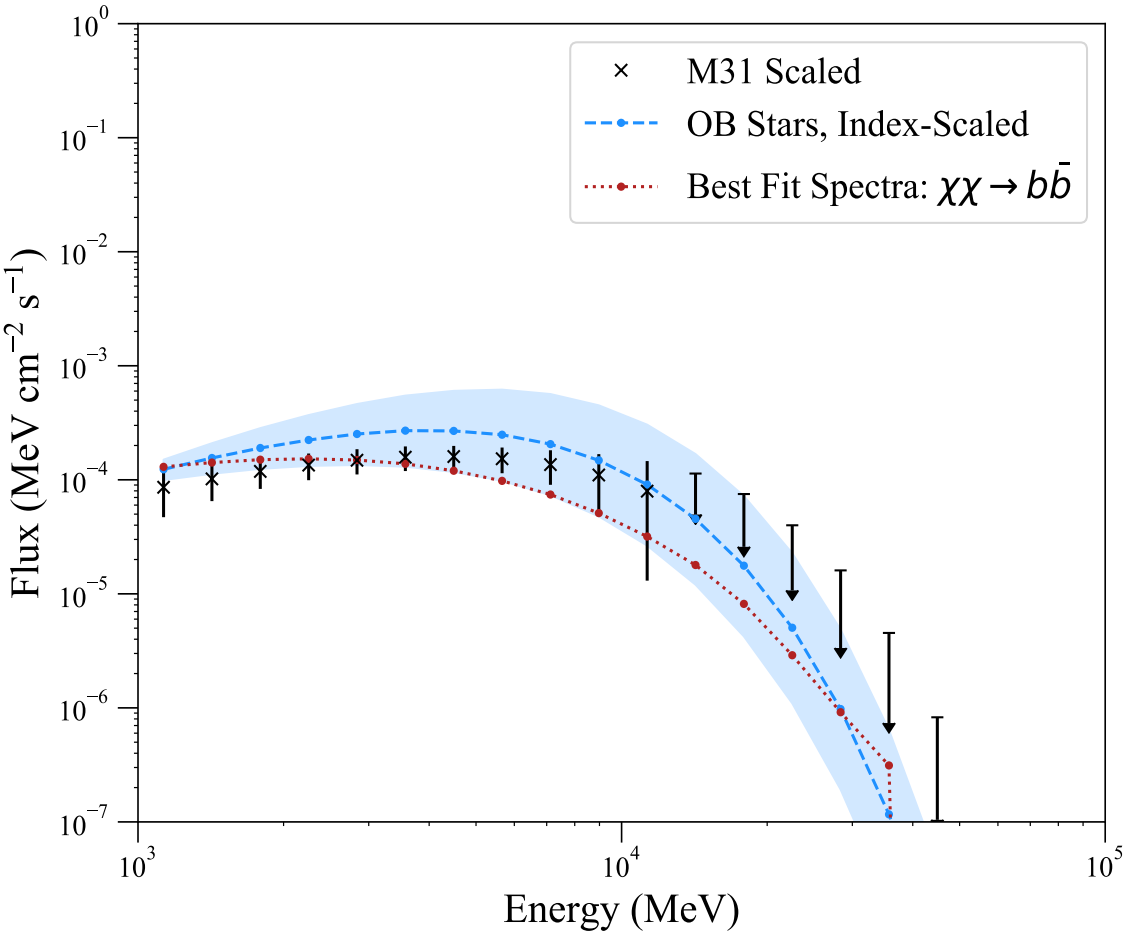

Figure 2.5: Dashed lines show the GC excess with the OB Stars, index-scaled IEM. Black points show the M31 flux data scaled up by the appropriate ratio J_r taken from Table 2.2. The dotted line shows the corresponding best-fit model spectra for $\chi\chi \to b\bar{b}$.

through a pseudoscalar mediator [84, 85, 86, 87]. For example, one can consider a model with a mediator ϕ and the interactions

$$\mathcal{L}_{int} = \chi^2\phi^2 + \phi\bar{b}b \tag{2.11}$$

In this model, DM primarily annihilates to four b-quarks. The precise annihilation mode depends on the coupling, for example if the mediator coupled as $\phi\bar{d}d$, there would be a annihilation to four d quarks. Generically we get a four-body annihilation.

Results for some possible 4-body final states are shown in Figure 2.7. We note that the best fit DM mass increases for the four body annihilation mode; this is expected because each quark has less energy.

The corresponding best-fit parameters for all models are summarized in Table 2.2. We also show the fits for the $b\bar{b}$ annihilation mode for all 4 IEM's in Figure 2.8.

Lastly, we note that there has recently been reports of evidence for an excess in the flux of antiprotons [112]. Specifically, Ref. [113, 114] find an excess signal that is consistent with having a DM origin, compatible with the GC excess. Within systematic uncertainties, there is some overlap between our best-fit DM parameters and those corresponding to the antiproton excess. On the other hand, we note that Ref. [115] takes a less optimistic view of the antiproton excess, reporting a non-detection (although the upper limits still clearly show an anomaly around the signal region).

2.5 Conclusion

The GC excess, an excess of γ-ray photons from the GC, has been a long-standing potential signal of DM annihilation. However, the large astrophysical background and the potential

existence of new sources makes it difficult to make definitive statements about the origin of this excess. On the other hand, the M31 excess is from a region where astrophysical backgrounds (not associated with the conventional interstellar emission from the MW foreground) are not expected to be large, and hence lends credence to the possibility that the excess is indeed associated with DM annihilation, rather than an unknown astrophysical background.

We have further examined these two excesses, to see if their magnitudes and spectral shapes are consistent with DM annihilation. The two signals are expected to be related by the ratio of the two J-factors. The recent analysis of the M31 J-factor allows us to check this relation, and we have found that indeed the excesses are consistent with the determined J-factors. The spectral shapes for the index-scaled IEMs are also in very good agreement. On the other hand, there is tension with the intensity-scaled IEMs due to the so-called high-energy tail.

We also fit the excesses to a number of DM models, where the DM annihilates to either two or four SM particles. We found that excellent fits can be achieved both in two-body and four-body annihilations, as can be seen in the Appendix.

In summary, we have found that the M31 excess and the GC excess are mutually consistent with a DM origin. The DM models prefer a somewhat higher value for the M31 J-factor, and prefer a particular IEM (the index-scaled models) for the GC. Currently, several DM models are consistent with the excesses.

Future prospects to confirm the excess toward the outer halo of M31, and to better understand its nature, will crucially rely on improvements in modeling the interstellar emission towards M31. For the GC, the excess has been under investigation for many years now, and further improvements in the IEM will continue to play a significant role in better understanding the nature of the signal. Additionally, working towards a better understanding of the possible point-like nature of the excess will be key. Improved sensitivity from other indirect

detection constraints will also continue to play an important role in DM interpretations of the two signals, and likewise for constraints from direct detection. Further analysis of these complementary signals would be extremely interesting, and could shed light on the nature of DM.

Acknowledgements and Author Contributions Statement

We are grateful to Simona Murgia for many detailed explanations of how to interpret and analyze the published data from *Fermi*-LAT, and for feedback on our analysis.

Using the CASRAI CRediT Contributor Roles Taxonomy: Conceptualization, A.K.B., M.F., C.K., A.R.; Data curation, A.K.B., M.F., C.K.; Formal analysis, A.K.B., M.F., C.K.; Funding acquisition, C.K., A.R.; Investigation, A.K.B., M.F., C.K., A.R.; Methodology, A.K.B., M.F., C.K., A.R.;Project administration, A.R.; Software, A.K.B., M.F., C.K.; Supervision, C.K., A.R.; Validation, A.K.B., M.F., C.K., A.R.; Visualization, A.K.B., M.F., C.K.; Writing – original draft, A.K.B., M.F., C.K., A.R.; Writing – review and editing, A.K.B., M.F., C.K., A.R.

Appendix 2A: Other Annihilation Channels

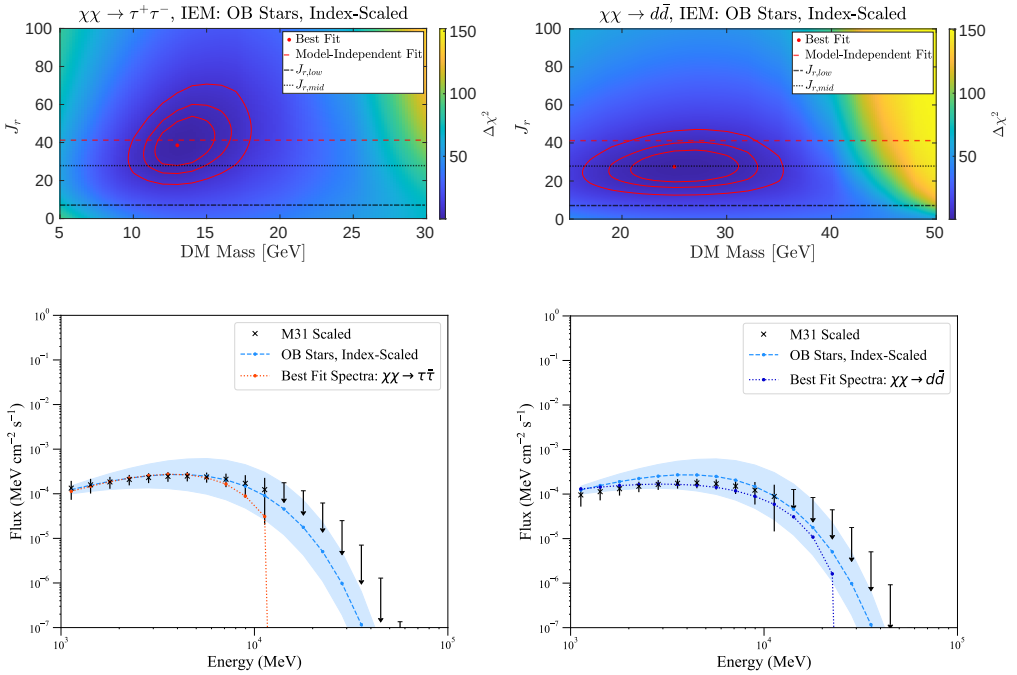

Figure 2.6: The left panels are similar to Figures 2.4 and 2.5 for $\chi\chi \to \tau\bar{\tau}$, and the right panels are similar to Figures 2.4 and 2.5 for $\chi\chi \to d\bar{d}$

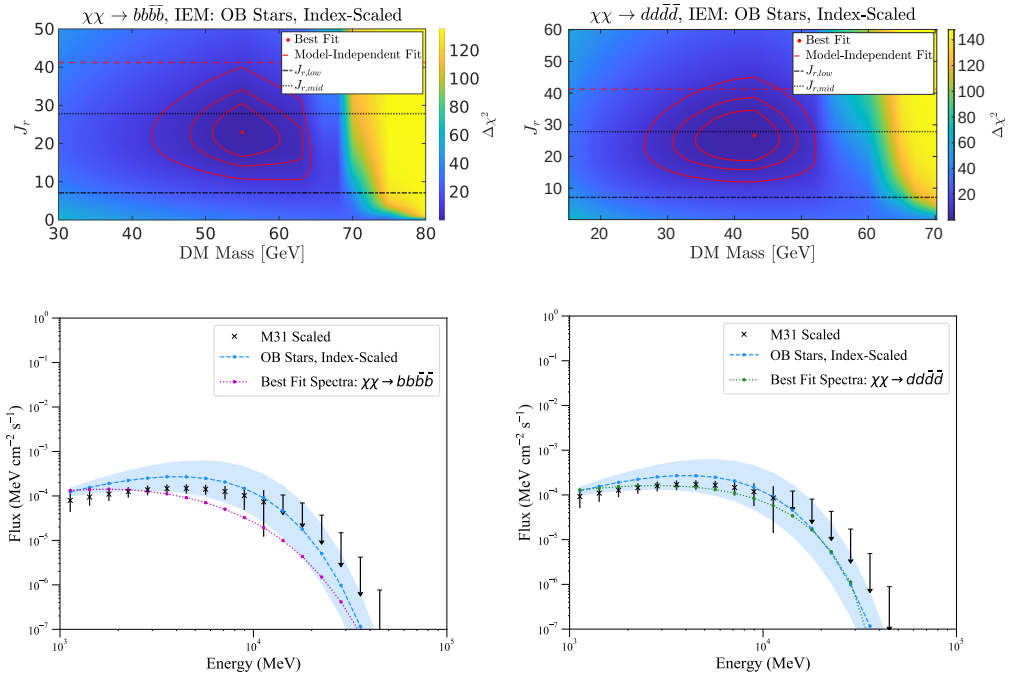

Figure 2.7: Similar to Fig 2.6, but for $\chi\chi \to bb\bar{b}\bar{b}$ and $\chi\chi \to dd\bar{d}\bar{d}$ respectively.

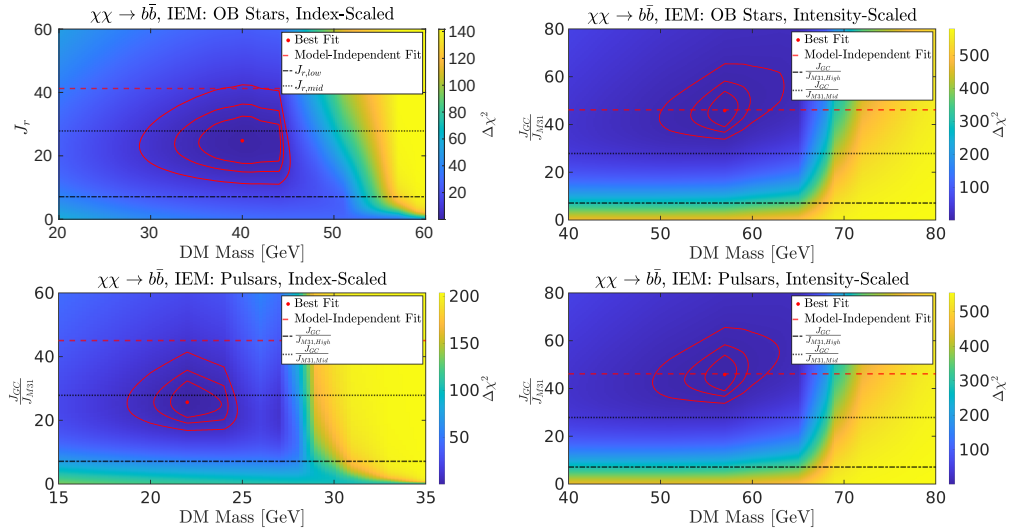

Figure 2.8: $\Delta\chi^2$ for $\chi\chi \to b\bar{b}$, for all 4 IEM's. The red dot indicates the best fit point, and the contours are 1,2, and 3 σ contours. The dashed red line shows the model independent J_r value. Dash-dotted and dotted black lines show high and mean values of J_r from section 2.2.3.

DM Model	IEM	m_χ [GeV]	$\mathcal{N}_{GC} \times 10^8$ [cm^{-2} s^{-1}]	J_r	χ^2_{red}
$b\bar{b}$	Pulsars, intensity-scaled	$57^{+1.3}_{-2.1}$	$2.6^{+0.14}_{-0.14}$	$45.9^{+8.1}_{-6.9}$	2.00
	Pulsars, index-scaled	$22^{+1.9}_{-0.9}$	$3.9^{+0.31}_{-0.31}$	$25.7^{+6.7}_{-4.8}$	1.72
	OB Stars, intensity-scaled	$57^{+1.3}_{-1.7}$	$2.7^{+0.16}_{-0.16}$	$45.9^{+8.0}_{-6.9}$	2.4
	OB Stars, index-scaled	$40^{+4.1}_{-4.7}$	$2.1^{+0.10}_{-0.10}$	$24.8^{+7.8}_{-7.2}$	1.01
$d\bar{d}$	Pulsars, intensity-scaled	$43^{+3.7}_{-4.9}$	$3.6^{+0.16}_{-0.16}$	$51.4^{+9.8}_{-7.2}$	1.43
	Pulsars, index-scaled	$17^{+1.3}_{-1.3}$	$5.0^{+0.24}_{-0.24}$	$29.4^{+6.5}_{-5.4}$	0.99
	OB Stars, intensity-scaled	$45^{+3.1}_{-5.5}$	$3.6^{+0.17}_{-0.17}$	$53.2^{+9.9}_{-7.7}$	1.72
	OB Stars, index-scaled	$25^{+6.1}_{-4.1}$	$3.3^{+0.01}_{-0.01}$	$27.5^{+8.3}_{-8.0}$	0.81
$bb\bar{b}\bar{b}$	Pulsars, intensity-scaled	$81^{+0.3}_{-3.0}$	$1.76^{+0.11}_{-0.11}$	$42.2^{8.4}_{-5.8}$	2.40
	Pulsars, index-scaled	$36^{+1.1}_{-3.5}$	$2.4^{+0.19}_{-0.19}$	$24.8^{+5.9}_{-5.1}$	1.92
	OB Stars, intensity-scaled	$81^{+0.3}_{-2.5}$	$1.8^{+0.12}_{-0.12}$	$42.2^{+8.4}_{-5.7}$	2.85
	OB Stars, index-scaled	$55^{+4.9}_{-4.1}$	$1.4^{+0.01}_{0.01}$	$22.9^{+7.6}_{-6.3}$	1.19
$dd\bar{d}\bar{d}$	Pulsars, intensity-scaled	$67^{+3.9}_{-6.7}$	$2.2^{+0.1}_{-0.1}$	$50.5^{+9.1}_{-7.5}$	1.57
	Pulsars, index-scaled	$25^{+1.3}_{-2.3}$	$3.1^{+0.18}_{-0.18}$	$27.5^{+6.6}_{-5.0}$	1.24
	OB Stars, intensity-scaled	$67^{+4.3}_{-5.1}$	$2.2^{+0.11}_{-0.11}$	$50.5^{+9.0}_{-7.5}$	1.89
	OB Stars, index-scaled	$43^{+3.7}_{-8.7}$	$1.9^{+0.01}_{-0.01}$	$26.6^{+8.0}_{-7.8}$	0.87
$\tau^+\tau^-$	Pulsars, intensity-scaled	$15^{+1.1}_{-1.7}$	$15.7^{+1.03}_{-1.03}$	$52.3^{+9.7}_{-7.3}$	2.51
	Pulsars, index-scaled	$12^{+0.5}_{-1.5}$	$15.7^{+0.53}_{-0.53}$	$43.1^{+9.3}_{-7.7}$	0.63
	OB Stars, intensity-scaled	$15^{+1.5}_{-1.1}$	$15.6^{+1.1}_{-1.1}$	$52.3^{+9.1}_{-7.7}$	2.90
	OB Stars, index-scaled	$13^{+2.3}_{-1.5}$	$15.5^{+1.14}_{-1.14}$	$38.5^{+12.6}_{-10.6}$	0.78

Table 2.2: Best-fits for m_χ, $\mathcal{N}_{GC}$, and the ratio J_r for various annihilation channels.

Chapter 3

Dark matter interpretation of the Fermi-LAT observations toward the outer halo of M31

This chapter is heavily based on work previously published in collaboration with Christopher M. Karwin, Simona Murgia, Igor Moskalenko, Sean Fillingham, and Max Fieg [20].

3.1 Introduction

Observational evidence for dark matter (DM) in M31 comes from measurements of its rotational velocity curve [116, 117, 118, 119, 120]. These observations provide coarse-grained properties of the DM distribution near the central regions of the halo where the galaxy resides. With the existing data, the fine-grained structure of DM and its distribution outside of the galaxy is primarily inferred from simulated halos. Within the standard cosmological paradigm, M31's DM halo is expected to extend well beyond the galactic disk, and it is also

expected to contain a large amount of substructure. However, there is currently a high level of uncertainty regarding the exact nature of the halo properties, i.e. the geometry, extent, and substructure content, especially on galactic scales [121, 122, 123, 10, 124, 125, 126, 127, 128, 129, 130, 131, 132, 133, 134, 135, 136, 137, 138, 139, 140, 141, 142, 143, 7, 144, 12].

Due to its mass and proximity, the detection sensitivity of M31 to DM searches with γ-rays is competitive with the Milky Way (MW) dwarf spheroidal galaxies, particularly if the signal is sufficiently boosted by substructures [145, 146, 147, 148, 149, 150]. Moreover, M31 is predicted to be the brightest extragalactic source of DM annihilation [82, 83].

A detailed study of the γ-ray emission observed towards M31's outer halo has recently been made in Ref. [12]. In that study evidence is found for an excess signal that appears to be distinct from the conventional MW foreground, having a total radial extension upwards of $\sim$120–200 kpc from the center of M31. One possible explanation for the signal is that it arises from cosmic rays (CRs) which have escaped the galactic disk and are interacting with the gas of M31's circumgalactic medium [151]. However, the spectral properties of the observed emission do not seem to be consistent with standard CR scenarios [12]. The other main physical interpretation is that the signal arises from DM, which is thought to be the dominant component in the outer regions of the galaxy.

γ-ray emission from M31's inner galaxy has also been detected, but the exact nature of the emission still remains an open question, as the morphology of the signal doesn't appear to trace regions rich in gas and star formation [99, 100, 101, 152, 153, 12, 13, 154]. On the other hand, the total γ-ray luminosity is found to be in general agreement with the well-known scaling relationship between the γ-ray luminosity and infrared luminosity (8–1000 μm) for star-forming galaxies [155]. Ultimately, a better determination of the γ-ray signal from M31's inner region is still needed, which will require a refinement of the underlying gas maps (HI) used to model the Galactic foreground emission, as the current maps may be holding a fraction of gas that actually resides in the M31 system [12]. The Doppler-shifted

velocity of the gas, together with the Galactic rotation curve, is used to separate the MW and M31 gas. The uncertainty arises from two main conditions. First, there is a partial overlap of the rotational velocities for M31 and the MW. Second, M31 is at a fairly high latitude where there is an increased uncertainty in the rotational speed of the MW gas, which is measured in the Galactic disk.

In this work we interpret the excess γ-ray emission observed towards M31's outer halo in the framework of DM annihilation. We consider WIMP (i.e. weakly interacting massive particle) DM, and focus the analysis on the uncertainties associated with the properties of the DM halo. Moreover, we consider a realistic observational perspective, in which the line of sight towards M31's outer DM halo naturally extends through a similar DM halo around the MW. In general, this is not directly accounted for when modeling the MW foreground γ-ray emission, and can significantly impact the results.

The chapter is organized as follows. In Section 3.2 we give a qualitative description of M31's outer halo. In Section 3.3 we present the M31 data, DM fit, and analytical J-factor calculations. In Section 3.4 we present results for our best-fit models, and we consider these results in the context of the Galactic center (GC) excess, and more generally, in the context of the current status of DM indirect detection. In Section 3.5 we conclude. Additional details for the complementary DM searches we consider are given in Appendix 3.5.

3.2 M31's Outer Halo

For observations of γ-ray emission arising from DM annihilation towards M31's outer halo, the total signal would ostensibly contain emission from the MW's DM halo along the line of sight, emission from the local filamentary structure connecting the MW and M31 [156], and emission from the entire DM halo of M31, plus any secondary emission (from M31 and

the MW). For the MW halo, a DM signal should be pretty bright, but since the observation occurs from within the halo, the emission can be easily confused with the isotropic component (and other components of the MW interstellar emission model (IEM)). For M31, we observe the entire halo from the outside, and therefore we see the total integral signal. Thus M31 is advantageous for halo searches with γ-rays because it breaks the observational degeneracy.

Figure 3.1 provides a qualitative description of M31's outer halo, including an accounting of some notable structures along the line of sight that may provide hints of the DM distribution. The γ-ray counts map (shown in black and white) is from Ref. [12]. The bright emission along zero degree latitude is the plane of the MW. The size of M31's DM halo is indicated with a dashed cyan circle, which corresponds to a projected radius of 300 kpc, for an M31-MW distance of 785 kpc. The dash-dot lime-green circle shows the outer boundary of the spherical halo (SH) region, which we use for the DM fit, as discussed in Section 3.3. M31's satellite population is shown with open red circles. A subset of the satellites in M31 (which are thought to reside within DM substructures) are known to be positioned within a large thin plane (The Great Plane of Andromeda, GPoA); and likewise, a subset of the MW satellites are known to be part of a large planar structure as well (The Vast Polar Structure of the Milky Way) [157, 158, 159, 160, 161, 162, 163]. In addition, the satellite system of M31 is highly lopsided, as about 80% of its satellites lie on the side closest to the MW [159, 164]. For members of the GPoA, those to the north of M31 recede from us, and those to the south of M31 move toward us, in the plane of rotation.

Also shown in Figure 3.1 are two notable, highly extended gas clouds in the direction of M31, namely, Complex H [165, 123, 166, 167] and the M31 cloud [123, 168]. The gas contours show HI emission from the HI4PI all-sky survey (based on EBHIS and GASS) [169]. The M31 cloud is a highly extended lopsided gas cloud centered in projection on M31, originally reported in Ref. [123]. It remains uncertain whether the M31 cloud resides in M31 or the MW. Most recently Ref. [168] has argued that M31's disk is physically connected to the

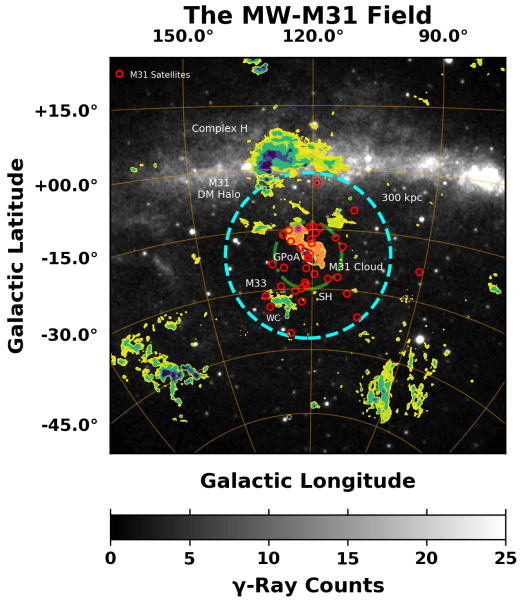

Figure 3.1: The line of sight looking towards M31's outer halo. The size of M31's DM halo is indicated with a dashed cyan circle, which corresponds to a projected radius of 300 kpc, for an M31-MW distance of 785 kpc. The dash-dot lime-green circle shows the outer boundary of the SH region ($r_{\rm tan} = 117$ kpc), which we use for the DM fit. M31's population of satellite galaxies is shown with red open circles. M33 can be seen in the lower left corner. Also plotted are some notable gas clouds in the region, namely, the M31 cloud (orange region surrounding the M31 disk), Wright's cloud (WC), and Complex H. See text for more details.

M31 cloud. If at the distance of M31 ($\sim$785 kpc) the total gas mass is estimated to be $\sim 10^8$–10^9 $M_\odot$. Complex H can be seen toward the top of M31's DM halo. The distance of Complex H from the MW is uncertain, although its likely distance has been estimated to be $\sim$30 kpc from the GC, which corresponds to the cloud having a diameter of about $\sim$10 kpc and an HI mass of $\sim 10^7$ $M_\odot$ [123, 166, 167]. Complex H does not appear to contain any stars, and it has been postulated to be either a dark galaxy of the Local Group or an example of a cold accretion flow [167].

Figure 3.1 also shows HI emission contours corresponding to M33. γ-ray emission from M33 has recently been detected [12, 170, 171], making it the only extragalactic satellite galaxy to be detected in γ rays. The total HI mass of the M33 disk is $\sim 10^9$ $M_\odot$. The hook-shaped gas cloud to the right of M33 is Wright's cloud, first reported in Ref. [172]. The distance

of Wright's cloud remains uncertain [125]. The HI mass of Wright's cloud at the distance of M33 is $\sim 4.5 \times 10^7$ $M_\odot$ [173]. Although no contours are shown, we note that below M33 is "the dark companion to M33", which is another highly extended gas cloud originally reported in Ref. [174], and labeled as a compact high-velocity cloud. If at the distance of M33, Ref. [173] estimates the HI mass to be $\sim 10^7$ $M_\odot$, and the size to be $\sim 18.2 \times 14.6$ kpc. See Ref. [173] for details of the cloud.

The main objective of Figure 3.1 is to provide a qualitative summary of some well-known objects in the line of sight towards M31's outer halo. In particular, for the M31 satellites we do not necessarily expect to detect them individually in γ rays (aside from M33). For the gas clouds, any γ-ray emission would depend on the actual location of the cloud, along with the CR density in the region. To investigate this in depth would require a detailed modeling which is beyond the scope of this analysis.

3.3 Analysis

3.3.1 Gamma-Ray Data for M31

To determine whether the excess γ-ray emission observed towards M31's outer halo is consistent with a DM interpretation, we employ the best-fit γ-ray spectra from Ref. [12]. The analysis uses 7.6 years of *Fermi*-LAT data, with energies between $1-100$ GeV, in 20 logarithmically spaced energy bins. The foreground emission from the MW is the dominant component when looking towards M31's outer halo, and GALPROP is employed to build specialized IEMs to characterize the emission, including a self-consistent determination of the isotropic component. The parameters of the GALPROP model are tuned to the measured local interstellar spectra of CRs, including the latest AMS-02 measurements. An in-depth analysis of the systematic uncertainties related to the observations is performed, and an

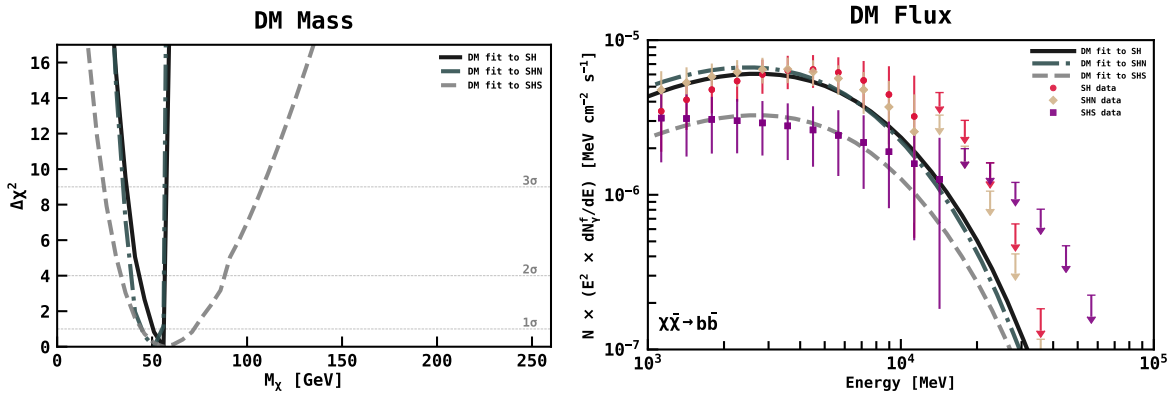

Figure 3.2: **Left panel**: $\Delta\chi^2$ profile for the three different fit variations: spherical halo (SH): solid black curve; spherical halo north (SHN): dash-dot turquoise curve; spherical halo south (SHS): dashed grey curve. The light grey dotted lines show the 1, 2, and 3 sigma contour levels, for 1 degree of freedom. **Right panel**: Best-fit spectra overlaid to the corresponding data. Arrows give the 1σ upper limits.

excess signal is detected. It is important to note that in Ref. [12] the excess emission is characterized with a power-law with exponential cutoff spectral model, as this was found to provide a good fit. Thus the data that we fit to in this analysis corresponds to the assumption of the same particular spectral model.

M31's halo is characterized in Ref. [12] using three symmetric components centered at M31 labeled as: inner galaxy (IG; r $\leq$ 0.4°), spherical halo (SH; 0.4° $>$ r $\leq$ 8.5°), and far outer halo (FOH; r $>$ 8.5°). For an M31-MW distance of 785 kpc, the IG, SH, and FOH correspond to projected radii of 5.5 kpc, 117 kpc, and ∼200 kpc, respectively. In this chapter we only consider the SH component. The IG component is complicated by uncertainty in the expected γ-ray emission from standard astrophysical processes. The FOH component overlaps with the MW plane at the top of the field, which significantly complicates the interpretation of the emission from this region. In addition, properly modeling the FOH will require a thorough treatment of secondary emission from DM, which we leave for a future study.

Two different fit variations were performed in Ref. [12] to determine the spectrum of the SH component. In the main variation (full) the entire template was used. In an alternative

variation (north and south) the template was separated into north and south components. In this case the spectral parameters for the two halves are allowed to vary independently, although they are fit simultaneously. This results in three different determinations of the spectrum, which we label as spherical halo (SH), spherical halo north (SHN), and spherical halo south (SHS). We use these variations to quantify the systematic uncertainty of the signal related to modeling the MW foreground, which differs in the two regions.

It is important to emphasize that the line of sight towards M31 extends through the MW DM halo, in addition to the M31 DM halo. However, the potential γ-ray contribution from the MW component is not explicitly accounted for when determining the M31 contribution. Some of the MW halo component would likely be attributed to the isotropic component, as well as to the other components of the IEM; however, it is unclear the extent to which this would occur. This is partly due to the fact that the absorption of a MW DM halo signal by other MW components in large part depends on the actual halo geometry and substructure content in the direction of the M31 field. Thus the spectra for the M31-related components from Ref. [12] contain the total excess emission along the line of sight, which may also include some significant contribution from the MW's extended DM halo. This is taken into account in our J-factor calculations.

3.3.2 Dark Matter Fit

As our representative DM model we consider annihilation into bottom quarks. This channel has been shown to provide a good fit to the γ-ray GC excess. The DM spectra[1] are obtained from PPCC 4 DM ID [102, 175], and they include electroweak corrections. We scan DM masses from 6 GeV to 256 GeV, using a 5 GeV spacing. Note that we choose a binning of 5 GeV since it gives 20 mass bins between 1-100 GeV, which is the same number of bins as the data.

[1] available at `http://www.marcocirelli.net/PPPC4DMID.html`

The γ-ray flux for DM annihilation is given by

$$\frac{d\Phi}{dE} = \frac{<\sigma_f v>}{4\pi\eta m_\chi^2}\frac{dN_\gamma^f}{dE}J, \tag{3.1}$$

where $<\sigma_f v>$ is the velocity averaged annihilation cross-section for final state f, m_χ is the DM mass, $\eta = 2$ (4) for self-conjugate (non-self-conjugate) DM, dN_γ^f/dE is the number of γ-ray photons for annihilation into final state f, and J is the astrophysical J-factor, which will be discussed in Section 3.3.3. In general Eq. (3.1) is summed over all final states f. In this analysis we use $\eta = 2$.

By multiply each side of Eq. (3.1) by the energy squared we obtain units of MeV cm^{-2} s^{-1}:

$$E^2\frac{d\Phi}{dE} = \frac{<\sigma_f v>}{4\pi\eta m_\chi^2}(E^2\frac{dN_\gamma^f}{dE})J.$$

To fit to the γ-ray data we freely scale the quantity in parentheses by a normalization factor N, using a χ^2 fit. This then implies:

$$N = \frac{<\sigma_f v>}{4\pi\eta m_\chi^2}J. \tag{3.2}$$

The M31 data contains upper limits which need to be accounted for in the fit procedure. For n measurements of x_i with uncertainties σ_i and m upper limits with $x_j < n\sigma_j$ (nth confidence level), the χ^2 can be defined as [176, 104]

$$\chi^2 = \sum_i^n z_i^2 - \sum_j^m 2\ln\frac{1+\mathrm{erf}(z_j/\sqrt{2})}{2}, \tag{3.3}$$

where

$$z_i = \frac{x_i - \hat{x}_i(\theta)}{\sigma_i}, \tag{3.4}$$

and

$$\mathrm{erf}(x) = \frac{2}{\sqrt{\pi}} \int_0^x e^{-t^2} dt. \tag{3.5}$$

The first term on the right-hand side in Eq. (3.3) is the classic definition of chi-squared, and the second term introduces the error function to quantify the fitting of upper limits. The quantity $\hat{x_i}(\theta)$ in Eq. (3.4) is the modeled value. We also calculate the reduced chi-squared:

$$\chi^2_{\mathrm{red}} = \frac{\chi^2}{\nu}, \tag{3.6}$$

with the degrees of freedom $\nu = 20 - 1 = 19$, corresponding to 20 energy bins and 1 free parameter in the fit.

Results for the fit are shown in Figure 3.2. The left panel shows the $\Delta\chi^2$ profile for the three different fit variations. Dashed grey lines show the 1,2, and 3 sigma contour levels (for 1 degree of freedom), corresponding to $\Delta\chi^2$ values of 1, 4, and 9, respectively. The best-fit mass for the SH model is $56^{+0.2}_{-5.5}$ GeV, with $\chi^2_{\mathrm{red}} = 0.97$, and $N = (5.4 \pm 0.5) \times 10^{-10}$. The best-fit mass for the SHN model is $51^{+4.3}_{-6.5}$ GeV, with $\chi^2_{\mathrm{red}} = 0.9$, and $N = (6.6 \pm 0.5) \times 10^{-10}$. And the best-fit mass for the SHS model is $56^{+16.1}_{-11.5}$ GeV, with $\chi^2_{\mathrm{red}} = 0.5$, and $N = (3.0 \pm 0.4) \times 10^{-10}$. The corresponding best-fit spectra are plotted in the right panel of Figure 3.2, overlaid to the corresponding data. We note that the data for the SH and SHN quickly falls off above $\sim$40 GeV, as can be seen in the upper limits. Additionally, the DM spectra have an intrinsic kinematic cutoff at the value of the DM mass. This results in the steep $\Delta\chi^2$ profile above the minimum, as the higher masses get severely penalized in the fit.

3.3.3 Analytical Determination of the J-Factor

For the best-fit models the corresponding annihilation cross-section is calculated using Eq. (3.2). This requires knowledge of the J-factor, which is the greatest uncertainty in the analysis. The J-factor characterizes the spatial distribution of the DM, and is given by the integral of the mass density squared, over the line of sight. When describing the DM distribution as an ensemble of disjoint DM halos, the J-factor is:

$$J = \sum_i \int_{\Delta\Omega} d\Omega \int_{\mathrm{LoS}} ds \rho_i^2(\mathbf{r}_i(s, \mathbf{n})), \tag{3.7}$$

summed over all halos in the line of sight (LoS), where $\rho_i(\mathbf{r})$ is the density distribution of halo i, and $\mathbf{r}_i(s, \mathbf{n})$ is the position within that halo at LoS direction $\mathbf{n}$ and LoS distance s.

J-factors determined from these spherically-averaged profiles are an underestimate of the total J-factor because of the effect of the non-spherical structure. This underestimate is typically encoded with a boost factor. To calculate J-factors we use the CLUMPY[2] code [177, 178, 179]. For a detailed discussion of the boost factor calculation see the CLUMPY papers/website, as well as Refs. [10, 133, 139, 140, 7] and references therein. Here we summarize the key points. The main parameters for the boost factor are the following:

- minimum subhalo mass
- mass-concentration relationship
- subhalo mass function (index and normalization), i.e. the number of subhalos per volume in a given mass range
- mass distribution of subhalos
- distribution of subhalos in the main halo

[2]available at `https://clumpy.gitlab.io/CLUMPY/`

Since the γ-ray flux from DM annihilation scales as the square of the DM density, the effect of substructure is very important for indirect detection, as it provides a boost to the total flux. The flux enhancement is most significant for larger halos, since they enclose more levels of hierarchical formation. The size of the smallest DM subhalo is determined by the free streaming scale of the DM particles [180, 140, 8]. This depends on the specific particle physics and cosmological models, and in general it is highly uncertain. In this study we consider minimum subhalo masses in the range $M_{\rm min} = 10^{-6} - 10^{6}\ M_{\odot}$. The lower limit is typically expected for thermal WIMP DM with a mass of $\sim$100 GeV [180], and the upper limit reflects the typical resolution power of DM simulations.

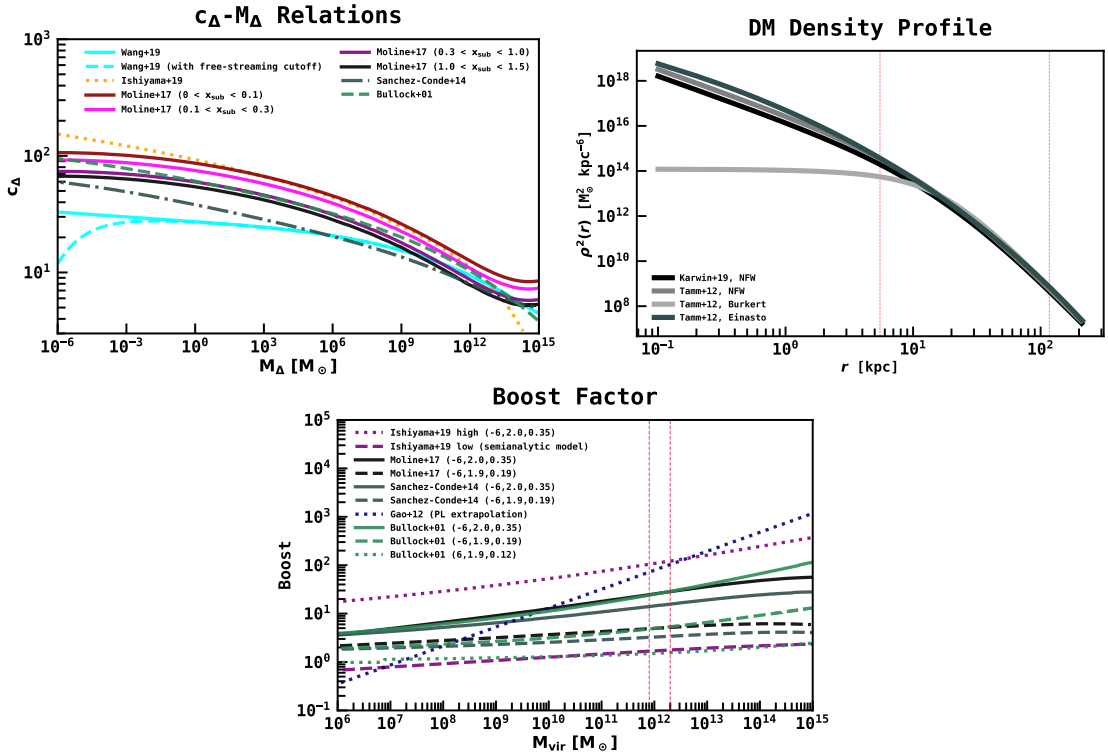

Figure 3.3: **Top panel:** Concentration-mass relations from Refs. [7, solid black, purple, magenta, and red], [8, dotted yellow], [9, dash-dot grey], [10, dashed green], and [11, solid and dashed cyan]. **Middle panel:** Different DM density profiles for M31. The region bounded by the red dashed lines corresponds to the SH. **Bottom panel:** Mass dependence of the boost factor for different parameters. The name in the legend specifies the model of the concentration-mass relation, and in parentheses the numbers give (in order) the power of the minimum subhalo mass, the PL index of the subhalo mass function, and the fraction of the halo resolved in substructure. The red dashed lines correspond to the mass range for M31 and the MW.

The concentration parameter c_Δ, at a given characteristic overdensity Δ, can be defined as

$$c_\Delta = \frac{R_\Delta}{r_{-2}}, \tag{3.8}$$

where R_Δ is the radius of the DM halo corresponding to the overdensity Δ, and r_{-2} is the position where the slope of the DM density profile reaches -2. The boost factor is highly sensitive to the concentration parameter, as it scales as the concentration to the third power [177, 178, 179]. In general the concentration is a function of halo mass and redshift. In the top panel of Figure 3.3 we plot different determinations of the concentration-mass relation at z=0. The solid lines (black, purple, magenta, and red) are from Ref. [7], which is based on two N-body cosmological simulations of MW-sized haloes: VL-II [134] and ELVIS [141]. These results summarize some of the main properties of the concentration parameter; namely, for a given halo the concentration decreases with increasing radius, and the concentration of subhalos is higher than that of field halos. In particular, the solid lines in Figure 3.3 are for different radial bins defined in terms of $x_{\rm sub} \equiv R_{\rm sub}/R_\Delta$. The solid black line is calculated outside of the virial radius, and it gives an approximation for field halos (see [7] for further details). For simplicity, in our benchmark model we use the relation from Ref. [10], plotted with a dashed green line in the top panel of Figure 3.3. As can be seen, this serves as a good intermediate model between the different estimates. Note that we have also tested the model from Ref. [9] and the results are qualitatively consistent.

The boost factor also depends on the subhalo mass function, which specifies the number of subhalos at a given mass. This function is given by a simple power law (PL), having an index of ~ -1.9 to -2.0 [133, 7]. The normalization of the PL is chosen so that the mass of the DM halo resolved in substructure is a specified amount. To bracket the uncertainty in the J-factor for both M31 and the MW, we vary the index of the subhalo mass function (α) and the fraction of the halo resolved in substructure ($f_{\rm sub}$) in the ranges $1.9-2.0$ and $0.12-0.35$, respectively. These values are representative of the current uncertainty [133, 181, 13].

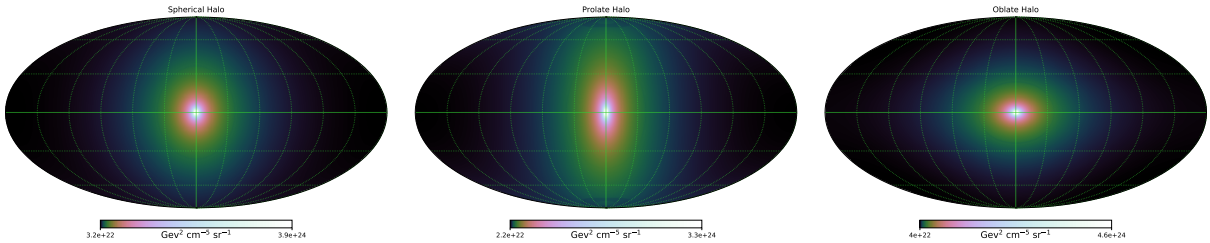

Figure 3.4: MW J-factors for three different geometries, as indicated above each map. Maps are shown in Galactic coordinates with a Mollweide projection. The corresponding axis ratios are given in Table 3.1. For the prolate halo q=1.67, and for the oblate halo q=0.6. The color scale ranges from the minimum halo value to 1/10 the maximum halo value. The DM model is "Einasto high" from Table 3.2. Note that these particular maps don't show individually resolved substructures, although they are included in the analytical model.

The middle panel of Figure 3.3 shows different DM density profiles for M31. The region bounded by the dashed red lines corresponds to the SH, where the fit to the γ-ray data is performed. The solid black curve is from Ref. [12], and the other curves are from Ref. [182]. For our J-factor calculations we test two profiles. We use the NFW profile from Ref. [12], which has corresponding halo properties of $R_{\rm vir} = 210$ kpc, $R_{\rm s} = 18.9$ kpc, and $\rho_{\rm s} = 2 \times 10^6\ M_\odot\ {\rm kpc}^{-3}$. In CLUMPY this corresponds to the kZHAO profile with parameters $\alpha, \beta, \gamma = 1,3,1$. We also use the Einasto profile from Ref. [182], which has the corresponding halo properties of $R_{\rm vir} = 210$ kpc, $R_{\rm s} = 178$ kpc, and $\rho_{\rm s} = 8.12 \times 10^3\ M_\odot\ {\rm kpc}^{-3}$. In CLUMPY this corresponds to the kEINASTO_N profile with the parameter n=6. The overdensity factor is set to $\Delta = 200$. We use an M31-MW distance of 785 kpc.

Other major uncertainties in the boost factor calculation are the spatial distribution of subhalos in the main halo, as well as the mass distribution of the subhalos themselves. We assume that the density profile and the spatial distribution of the subhalos are the same as the density profile of the main halo for both the NFW and Einasto distributions. Note that both the spatial distribution of subhalos and their density profiles have been found to prefer an Einasto distribution compared to an NFW, although both profiles provide a good fit (see [133] and references therein). Additionally, it's found that within $\sim$25 kpc from the center of MW-sized halos there is a depletion of the subhalo population due to tidal disruption from

the galactic disk [144].

In principle each DM halo of a given mass is a hierarchical structure, so that even subhalos have subhalos themselves. For simplicity we set the number of substructure levels to 2. We have also tested including higher substructure levels, but we find that they do not make a significant difference for our J-factor calculations, as has been previously found [7].

The bottom panel of Figure 3.3 shows the mass dependence of the boost factor for different choices of the minimum subhalo mass, the subhalo mass function, and the fraction of the halo mass resolved in substructure. Within the uncertainties we have considered, the overall boost factor ranges from $\sim$1.5–26.0 (for an NFW density profile). Note that this is the value reported by CLUMPY for the entire halo, which we report here for easy comparison with different values from the literature.

3.3.4 Halo Geometry

Another important systematic uncertainty for determining the J-factor for the M31 field is the halo geometry, for both M31 and the MW. Indirect DM searches typically assume spherical symmetry for the halo shape, however, in the standard DM paradigm (ΛCDM), DM halos are expected to be very non-spherical, and in fact, spherical halos are rare (see [128] and references therein).

For the MW, numerous studies have been done to infer the DM halo geometry, but differing conclusions have been reached. The halo has been found to be spherical [183], prolate [184, 138, 185], oblate [186], triaxial (including the so-called "Gaia sausage") [137, 187, 188], and even lopsided [136]. Further complicating the matter is that the halo geometry may have a radial dependence [189, 190]. Moreover, it's found in both simulations and observations that for galaxy pairs (similar to M31 and the MW) the halos tend to bulge toward their

respective partners [159, 164].

In general the halo geometry can be described with an ellipsoid, with the axes a, b, and c. The shape is characterized by the axis ratios, with the normalization condition abc = 1 (see the CLUMPY code for more details). For describing the MW halo, the a-axis corresponds to the Galactic x-axis (connecting the Sun to the Galactic center), the b-axis corresponds to the Galactic y-axis, and the c-axis corresponds to the Galactic z-axis (perpendicular to the Galactic plane). We use the references cited above to calculate J-factors for different MW halo geometries. Note that we also consider a triaxial halo geometry modeled after the Gaia sausage. Although the evidence indicates that this structure may be a subdominant component of the halo, for simplicity we test a more extreme scenario where the entire halo follows this geometry. Figure 3.4 shows the three main halo shapes that we test, and the specific axis ratios for all geometries are summarized in Table 3.1.

In the top panel of Figure 3.5 we show the J-factor ratio ($J/J_{\rm Sph}$) for the Einasto high DM model, where J is for the alternative geometry, and $J_{\rm Sph}$ is for the spherical halo. The ratio range for all DM models is given in Table 3.2. We find that at most the halo shape may increase or decrease the MW J-factor (with respect to spherical geometry) by factors of 2.29 and 0.34, respectively.

To test how the MW J-factor varies with Galactic latitude we repeat the calculations with the line of sight centered at latitudes of -50° and 0°, with longitude = 121°. Note that $b = -50^\circ$ corresponds to the region used in Ref. [12] for tuning the isotropic spectrum, which we refer to as the tuning region (TR). Results for this test are shown in the middle panel of Figure 3.5 (for the Einasto high model), where we plot the J-factor ratio with respect to the value obtained in the TR. In all cases a gradient can be seen, with the amplitude of the variation dependent on the halo geometry. This is even true for a spherical halo, due to our position in the Galaxy at $\sim$8.5 kpc from the Galactic center. The range of gradient ratios for all DM models is given in Table 3.2. In going from high latitude to low latitude, the J-factors

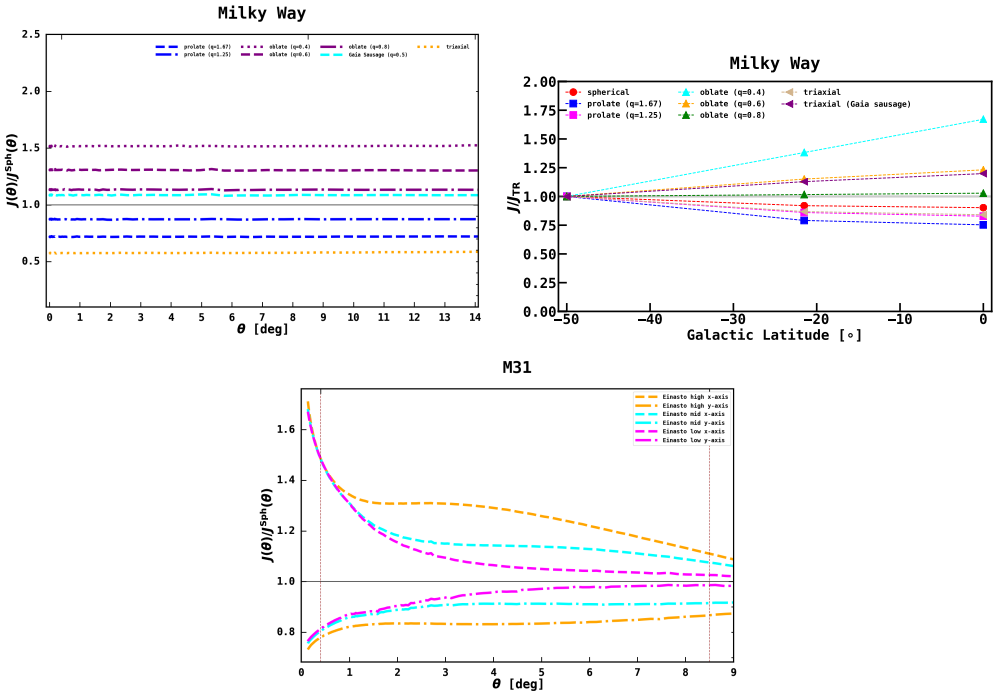

Figure 3.5: **Top:** Ratio of the J-factor (J) for different MW halo geometries compared to a spherical halo ($J^{\rm Sph}$), for an Einasto density profile. **Middle:** Gradient ratio for the J-factor calculated with the line of sight centered at three different Galactic latitudes (with $l = 121°$). The ratio is calculated with respect to a latitude of $b = -50°$ ($J_{\rm TR}$), which is comparable to the region used for tuning the isotropic spectrum in Ref. [12]. The middle data points at $l = --21.5°$ correspond to the M31 field. In all cases the J-factors are integrated over the region 0.4° to 8.5°, using the Einasto high model from Table 3.2. **Bottom:** Ratio of the J-factor (J) for different M31 halo geometries compared to a spherical halo ($J^{\rm Sph}$), for an Einasto density profile.

Table 3.1: MW Halo Geometry

Halo Geometry	Axes (a,b,c)
Spherical	1, 1, 1
Prolate (q=1.67)	0.84, 0.84, 1.41
Prolate (q=1.25)	0.93, 0.93, 1.16
Oblate (q=0.4)	1.36, 1.36, 0.54
Oblate (q=0.6)	1.19, 1.19, 0.71
Oblate (q=0.8)	1.08, 1.08, 0.86
Triaxial	0.67, 1.34, 1.113
Triaxial (Gaia Sausage, $\alpha = 70°$)	1.38, 1.06, 0.69

Note: The axes are normalized so that abc=1. In general, prolate halos have a=b<c, and oblate halos have a=b>c. For convenience we also give the ratio q=c/a. The specific axis ratios come from the literature, as discussed in the text. For visualization purposes, the different geometries are plotted in Figure 3.4.

for the spherical and prolate halos decrease by a minimum factor of 0.77. Alternatively, the J-factors for the oblate and triaxial (Gaia sausage) halos increase by a maximum factor of 1.38. Since Ref. [12] tunes the isotropic spectrum in a region below the M31 field (consistent with $l = -50°$), these results show that it is not necessarily the case that the MW DM halo component would be fully absorbed by the isotropic template. Moreover, even a gradient of $\sim$20$-$40% (as is found in the gradient calculation) would be a significant contribution to the total J-factor for the M31 field.

We also test how the J-factor depends on the M31 halo geometry, with the main goal of estimating the full uncertainty range. For simplicity we test two different geometries. In each case the minor-to-major axis ratio is 0.4 (with a>b=c). This represents a highly flattened halo, but it has also been found for M31 in particular [132]. We test two different orientations, one with the major axis pointing along the line of sight connecting M31 and the MW (x-axis), and the other with the major axis pointing perpendicular to the line of sight (y-axis), running from left to right in the field of view. Note that results for the z-axis orientation are similar to those of the y-axis orientation. The bottom panel of Figure 3.5 shows the ratio of the J-factor for these different geometries compared to a spherical geometry (for the Einasto

Table 3.2: J-Factors and Cross Sections

Model	$\alpha_{\rm sub}$	$f_{\rm sub}$	$M_{\rm min}$ [$M_\odot$]	$J_{\rm MW}$ ($\times 10^{20}$) [GeV^2 cm^{-5}]	$J_{\rm M31}$ ($\times 10^{20}$) [GeV^2 cm^{-5}]	$J/J_{\rm Sph}$ (MW)	$J/J_{\rm Sph}$ (M31)	$J_{\rm MW}/J_{\rm TR}$	$<\sigma v>_{\rm I}$ ($\times 10^{-26}$) [cm^3 s^{-1}]	$<\sigma v>_{\rm II}$ ($\times 10^{-26}$) [cm^3 s^{-1}]
Einasto high	2.0	0.35	10^{-6}	27.5	3.6	0.57, 1.52	0.82, 1.32	0.79, 1.38	1.4	11.8
NFW high	2.0	0.35	10^{-6}	15.0	1.8	0.57, 1.51	0.82, 1.33	0.79, 1.38	2.5	23.6
Einasto mid	1.9	0.19	10^{-6}	4.6	0.6	0.49, 1.81	0.88, 1.24	0.79, 1.34	8.2	70.9
NFW mid	1.9	0.19	10^{-6}	3.3	0.3	0.45, 1.86	0.87, 1.25	0.79, 1.34	11.8	141.9
Eiansto low	1.9	0.12	10^{6}	1.94	0.1	0.35, 2.29	0.90, 1.21	0.78, 1.29	20.9	425.6
NFW low	1.9	0.12	10^{6}	1.90	0.1	0.34, 2.19	0.89, 1.22	0.77, 1.30	21.3	425.6
Einasto smooth	–	–	–	1.50	0.05	–	–	–	27.5	851.2
NFW smooth	–	–	–	1.6	0.05	–	–	–	25.8	851.2

Note: J-factors are integrated over the spherical halo component (0.4° to 8.5°). The largest subhalo mass is taken to be 10% the mass of the host halo. The calculations include 2 levels of substructure. For the M31 NFW profile $R_{\rm vir} = 210$ kpc, $R_{\rm s} = 18.9$ kpc, and $\rho_{\rm s} = 2.0 \times 10^6\ M_\odot$ kpc^{-3}. For the M31 Einasto profile $R_{\rm vir} = 210$ kpc, $R_{\rm s} = 178$ kpc, and $\rho_{\rm s} = 8.12 \times 10^3\ M_\odot$ kpc^{-3}. The MW profiles have the same parameters except we use the local DM density $\rho_\odot = 0.4$ GeV^2 cm^{-3}, with a solar distance $R_\odot = 8.5$ kpc. The overdensity factor is set to $\Delta = 200$. We use an M31-MW distance of 785 kpc. The spatial distribution of subhalos and the density profile of the subhalos is the same as the density profile of the main halo for both NFW and Einasto distributions. Columns 7 and 8 give the average uncertainty range (low, high) on the J-factor due to the halo geometry, with respect to a spherical halo ($J_{\rm Sph}$). Column 9 shows the J-factor gradient (low, high) with respect to the tuning region (TR) used in Ref. [12], which is centered at $b = -50°$. Cross-sections are given for the SH data. Using Eq. 3.2 and the best-fit parameters from the respective fits, the cross-sections for the SHN and SHS data can be obtained by the following ratios: SH/SHS = 1.8 and SH/SHN = 1.0. Subscript I on the cross-section indicates case I, where $J_{\rm total} = J_{\rm M31} + J_{\rm MW}$, and subscript II on the cross-section indicates case II, where $J_{\rm total} = J_{\rm M31}$. Corresponding curves are plotted in Figure 3.6.

high model). The uncertainty range for all DM models is given in Table 3.2. The M31 halo geometry introduces an uncertainty in the range $0.82 - 1.32$, where the increase is seen for the major axis aligned with the x-axis and the decrease is seen for the major axis aligned along the perpendicular axes.

3.3.5 J-Factor Uncertainty from the Milky Way Foreground

In the context of the J-factor uncertainty from the MW foreground, we consider two extreme cases. For case I we assume that none of the MW halo signal along the line of sight has been absorbed by the isotropic component (and other components of the IEM), and thus the total J-factor is the sum of the J-factors for the MW and M31. For case II we assume that the MW halo signal along the line of sight has been completely absorbed, and so the total J-factor is due only to M31. In actuality, if the observed excess is in fact related to DM then the true case is likely somewhere between the two extremes.

3.3.6 Total J-Factor Uncertainty

Figure 3.6 shows the different J-factors as a function of radial distance from the center of M31. The grey band is the J-factor uncertainty for M31 from this work. The blue band is the J-factor uncertainty for the MW from this work. The markers are the M31 calculations for the NFW (squares) and Einasto (circles) profiles, with the boost factor, corresponding to the values in Table 3.2. The dash-dot lines towards the bottom show the smooth M31 profiles corresponding to the markers. As can be seen, the smooth profiles are anti-correlated to the total profiles, i.e. as the boost factor increases, the fraction of DM resolved in substructure also increases, and the fraction of the smooth DM component decreases. The solid curves are independent calculations for M31 from Ref. [12] (extending to 14 degrees) and Ref. [13] (extending to 10 deg). Likewise the dashed lines are independent calculations for the MW.

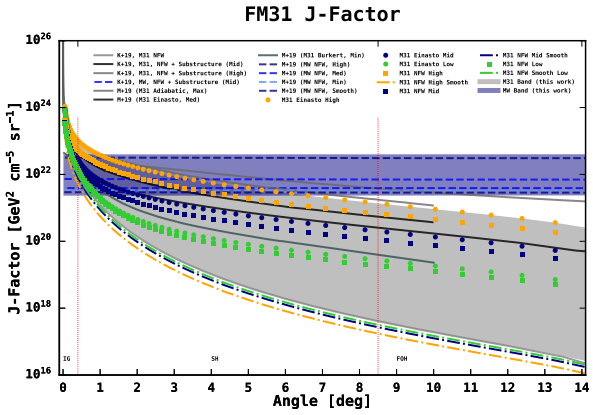

Figure 3.6: J-factors for M31 and the MW. The grey band is the J-factor uncertainty for M31 from this work. The blue band is the J-factor uncertainty for the MW from this work. The markers are the M31 calculations for the NFW (squares) and Einasto (circles) profiles, with the boost factor. Parameters for the different variations are given in Table 3.2. The solid curves are independent calculations for M31 from Ref. [12] (extending to 14 degrees) and Ref. [13] (extending to 10 deg). Likewise the dashed lines are independent calculations for the MW. The dash-dot lines towards the bottom show the smooth M31 profiles corresponding to the markers. The vertical dotted red lines show the boundaries of M31's IG, SH, and FOH (the fit is performed over the SH).

As can be seen, there is good consistency between the different estimates. Our resulting models are summarized in Table 3.2.

We note that Ref. [82] reports an M31 J-factor (integrated within the scale radius) of $(6.2^{+7.9}_{-3.5}) \times 10^{19}$ GeV^2 cm^{-5}, corresponding to a boost factor of 2.64 and a scale radius of 2.57°. The uncertainty in their calculation comes from the uncertainty in $M_{\rm vir}$ and $c_{\rm vir}$. Their boost factor is comparable to our low and mid models (with an NFW profile). When integrating over the same scale radius, we obtain J-factor values in the range $2.2 \times 10^{19} - 17.0 \times 10^{19}$ GeV^2 cm^{-5}, in agreement with the values reported in Ref. [82].

3.4 Results

We calculate annihilation cross-sections using Eq. (3.2) with the values obtained from following the procedure described in Sec. 3.3, and results are given in Table 3.2. The reported values are for the SH data. The cross-sections for the SHN and SHS data can be obtained by the following ratios: SH/SHS = 1.8 and SH/SHN = 1.0. In Figure 3.7 we plot the corresponding best-fit DM parameters. The red data point corresponds to case I, for which $J = J_{\rm MW} + J_{\rm M31}$. The coral data point is for case II, for which $J = J_{\rm M31}$. The best-fit values for the three fit variations are all very similar, so for visual clarity we plot the mean, and the error bars show the full systematic range. Note that the error bars in the cross-section assume that the minimum subhalo mass is $10^{-6}\ M_\odot$, and they include the uncertainty due to the halo geometry outlined in Sec. 3.3. We compare the data points from M31's outer halo to numerous complementary targets for indirect DM searches. Details for all of the overlays are given in Appendix 3.5.

Broadly speaking, contours for the GC excess are shown in black, and contours for the antiproton excess are shown in teal. As can be seen, there is a rather large range in the different determinations. This is due to the different assumptions that are made in each analysis. Generally speaking, these results can be interpreted collectively as defining the currently explored systematic uncertainties in the respective signals. In the case of the GC excess, the uncertainty range in the cross-section spans roughly 1.5 orders of magnitude. This is because the GC excess is only a small fraction of the total emission in the region, and thus it has a strong dependence on the treatment of the IEM, which in general is difficult to accurately model due to the complexity of the GC region. Moreover, the inferred DM parameters also have a strong dependence on the halo assumptions, such as the local DM density, which may span between $\sim$0.3-0.6 GeV/cm^3 [191, 188]. In the case of the antiproton excess, Refs. [192, 193] report detection contours, whereas Ref. [194] takes a less optimistic view, reporting upper limits (although the limits still clearly show an anomaly around the

signal region).

Another important constraint is the upper limits from the MW dwarfs. Here too there is a fairly large uncertainty range. Compared to the limits reported in Ref. [77], the latest limits from Ref. [78] are less constraining. These limits of course have a strong dependence on the assumptions made for the J-factors, and by employing semi-analytic models of DM subhalos to derive realistic satellite priors on the J-factor (for the ultrafaint dwarfs), Ref. [79] has recently shown that the limits may be even weaker, by a factor of $\sim$2–7. Correspondingly, if the halos are non-spherical then the limits may be weakened as well, as discussed in Refs. [80, 81].

As can be seen in Figure 3.7, the limits coming from M31's inner galaxy are competitive with the limits from the MW dwarfs. In this case, however, the difficulty is in accurately separating a DM signal from the standard astrophysical emission. The limits shown in Figure 3.7 are from Ref. [13], and they are for the most conservative case, i.e. they assume that all of the observed emission is from standard astrophysical processes, and thus model it using a 0.4° disk, as determined from the emission itself. Upper limits for a DM signal are then calculated in addition to the disk. While this is definetly a very conservative choice to make, it is by no means preferred, as the γ-ray emission from M31's inner galaxy has actually been found to not correlate with regions rich in gas and star formation.

The data points for M31's outer halo have a large overlap with the DM interpretations of both the GC excess and the antiproton excess, while also being compatible with the limits from the MW dwarfs. However, this requires that the J-factor be towards the higher end of the uncertainty range. Correspondingly, this has two main implications. First, the minimum subhalo mass must be $\lesssim 10^{-6}\ M_{\odot}$. Second, the signal must have some contribution from the MW's DM halo along the line of sight, i.e. the J-factor must correspond to case I, as it cannot be due to M31 alone.

3.5 Summary, Discussion, and Conclusion

An excess γ-ray signal towards the outer halo of M31 has recently been reported [12]. In this work we interpret the excess in the framework of DM annihilation. As our representative case we use WIMP DM annihilating to bottom quarks, and we fit the DM mass and annihilation cross-section to the observed γ-ray spectra from Ref. [12]. In that study M31's halo is characterized using three symmetric components centered at M31, namely, the IG ($r \leq 0.4^\circ$), SH ($0.4^\circ > r \leq 8.5^\circ$), and FOH ($r > 8.5^\circ$). Here we fit just to the SH component. The IG and FOH components are difficult to disentangle from standard astrophysical processes and are not considered in this study.

The greatest uncertainty in our analysis is the determination of the J-factor, which we calculate using the CLUMPY code. This uncertainty arises from two main factors. First, there is a high uncertainty in the substructure nature of the DM halo's for both M31 and the MW, as well as an uncertainty in the halo geometries. To bracket the substructure uncertainty we vary the subhalo mass function, the fraction of the halo resolved in substructure, and the minimum subhalo mass in the ranges $1.9 - 2.0$, $0.12 - 0.35$, and $10^6 - 10^{-6}$ $M_\odot$, respectively. For the concentration-mass relation we adopt the model from Ref. [10]. The largest subhalo mass is taken to be 10% the mass of the host halo. The calculations include 2 levels of substructure. For the underlying smooth density profiles we test both an NFW profile and an Einasto profile. The spatial distribution of subhalos and the density profile of the subhalos are assumed to be the same as the density profile of the main halo. All calculations are made self-consistently for M31 and the MW (i.e. they have the same halo paramaters). Our calculated total boost factor ranges from $\sim$1.5$-$26.0 (for an NFW density profile). Note that this is the value reported by CLUMPY for the total halo, which we report here for easy comparison with other studies.

We have also characterized how the halo geometry impacts the J-factor for the M31 field.

To do this we have used the range of different halo shapes found in the literature. For the MW we find that the halo shape may change the J-factor in the range $J/J_{\rm Sph} = 0.34 - 2.3$. The corresponding range for M31 is found to be 0.8–1.3. Thus the impact is more significant for the MW, due to our position within the halo.

The other main uncertainty in the J-factor for the M31 field is the contribution from the MW's DM halo along the line of sight. In Ref. [12] a detailed modeling of the foreground emission was performed, as well as an in-depth analysis of the corresponding systematic uncertainties. However, the model does not explicitly account for a potential contribution from the MW's extended DM halo. It is likely that such a signal could be (partially) absorbed by the isotropic component. The magnitude of this effect, however, depends on the specific halo geometry and substructure properties of the MW DM halo in the M31 field, which are not well constrained. In order to help control this, Ref. [12] used a region below the M31 field to tune the isotropic normalization. Here, we improve on this determination by considering variations of the MW DM component in the M31 field and in the tuning region due to different halo geometries. We find that the ratio is significant and, more specifically, in the range of $J_{\rm MW}/J_{\rm TR} = 0.8 - 1.4$. Thus even in the ideal case where the isotropic component is able to perfectly absorb the emission from the MW's DM halo, there could still be a gradient in the M31 field that is not included in the foreground model and is likely to be a significant component in this region. Since the uncertainty in the J-factor due to the contribution from the MW's DM halo along the line of sight is significant but cannot be precisely constrained, here we consider the two extreme cases: one where none of the MW halo component has been absorbed by the isotropic component, and so $J_{\rm total} = J_{\rm M31} + J_{\rm MW}$ (case I); the other where the MW component has been completely absorbed so that $J_{\rm total} = J_{\rm M31}$ (case II).

When these uncertainties are taken into account, we find that the observed excess in the outer halo of M31 favors a DM particle with a mass of $\sim$45–72 GeV. The full systematic uncertainty in the cross-section currently spans 3 orders of magnitude, ranging from $\sim$

$5 \times 10^{-27} - 5 \times 10^{-24}$ cm^3 s^{-1}. We compare the best-fit DM parameters for M31's outer halo to numerous complementary targets. We conclude that for the DM interpretation of the M31 outer halo excess to be compatible with the GC excess, antiproton excess, and current indirect detection constraints, it requires the J-factor to be towards the higher end of the uncertainty range. This in turn has two main implications. First, the minimum subhalo mass must be $\lesssim 10^{-6}\ M_\odot$. And in fact this is expected in the standard DM paradigm (ΛCDM). Second, the signal must have a significant contribution from the MW's DM halo along the line of sight, i.e. it is too bright to be originating from M31 alone. This condition cannot be ruled out, and it is in fact likely that some fraction of the MW DM halo emission is embedded in the signal toward M31. This is a feature of the methodology employed to tune the MW foreground, as discussed in this chapter. Given these conditions hold, we find that there is a large overlap with the DM interpretations of both the GC excess and the antiproton excess, while also being compatible with the limits from the MW dwarfs. Although the uncertainty in the current measurements is clearly far too large to make any robust conclusions (either positive or negative), this region in parameter space still remains viable for discovery of the DM particle.

Future prospects to confirm the excess toward the outer halo of M31, and to better understand its nature, crucially rely on improvements in modeling the interstellar emission towards M31. Furthermore, observations of the halos of other galaxies, e.g. M33, could provide a confirmation of this type of signal, provided sufficient data is available since the signal is predicted to be fainter there. Other prospects may include a study of the distribution of properties of the isotropic background around the direction to M31 and further out with a goal to see the distortions in the MW DM halo. Alternatively, constraints on the subhalo population by other astrophysical probes and, in turn, on their contribution to the M31 signal, might also provide a further test of the viability of the DM interpretation.

Acknowledgements and Author Contributions Statement

C.K. is pleased to acknowledge conversations with Daniel McKeown and James Bullock.

Using the CASRAI CRediT Contributor Roles Taxonomy: Conceptualization, C.M.K., S.M., I.M., S.F.; Data curation, A.K.B., C.M.K., S.M., I.M., S.F., M.F.; Formal analysis, A.K.B., C.M.K., S.M., I.M., S.F., M.F.; Funding acquisition, C.M.K., S.M., I.M., S.F.; Investigation, A.K.B., C.M.K., S.M., I.M., S.F., M.F.; Methodology, A.K.B., C.M.K., S.M., I.M., S.F., M.F.; Project administration, C.M.K., S.M., I.M., S.F.; Software, A.K.B., C.M.K., S.M., I.M., S.F., M.F.; Supervision, C.M.K., S.M.; Validation, C.M.K., S.M., I.M., S.F.; Visualization, A.K.B., C.M.K., S.M., I.M., S.F., M.F., C.K.; Writing – original draft, C.M.K., S.M., I.M., S.F.; Writing – review and editing, A.K.B., C.M.K., S.M., I.M., S.F., M.F.

Appendix 3A: DM Parameter Space

Here we summarize all of the results overlaid in Figure 3.7. The black data points (furthest four to the right) are for a DM interpretation of the GC excess, as presented in Ref. [195]. The two points at lower energy are for two of the models employed for the fore/background γ-ray emission from the MW, *OB stars index-scaled*, and the points at higher energy are for the other two models, *pulsars index-scaled*. The NFW profile has $\gamma = 1.0$ (upper) and $\gamma = 1.2$ (lower). In addition, the NFW profile has $R_s = 20$ kpc and $\rho_\odot = 0.4$ GeV cm^{-3}. Note that the annihilation final state preferred by the fit to the data favors mostly bottom-type quarks, with a small fraction of leptons. Thus this model is not directly comparable to the other overlays which generally assume annihilation into a single final state.

The black contour that is highly elongated in the y-direction is for the GC excess from Ref. [191]. The contour represents the total uncertainty (3σ statistical + systematic). The

uncertainty is dominated by the systematics, and in particular, the value of the local DM density (this study also considers uncertainties due to the index and scale radius of the DM profile, γ and R_s). The upper region of the contour corresponds to $\rho_\odot = 0.28$ GeV cm^{-3} (which is taken as the benchmark value), and the lower region of the contour corresponds to $\rho_\odot = 0.49$ GeV cm^{-3}. The shift occurs at a cross section value of $\sim 6 \times 10^{-26}$ cm^3 s^{-1}. See Ref. [191] for details. Also plotted in Figure 3.7 is the best-fit point from Ref. [196] (the black data point to the far left).

Other contours for the GC excess are also shown with different shades of grey. The lowest and darkest contour (2σ) is from Ref. [105], then above that is the contour (2σ) from Ref. [197], and above that is the contour from Ref. [198]. The NFW profiles for all of these contours have $\gamma = 1.2$, $R_s = 20$ kpc, and $\rho_\odot = 0.4$ GeV cm^{-3}.

The two lowest purple curves show limits for the MW satellite galaxies. The dashed curve is from Ref. [77] and results from the combined analysis of 15 dwarf spheroidal galaxies using Pass-8 data. The solid curve is from Ref. [78] and results from the combined analysis of 45 stellar systems, including 28 kinematically confirmed DM-dominated dwarf spheroidal galaxies, and 17 recently discovered systems that are dwarf candidates. Note that the dwarf limits are obtained by assuming spherical symmetry of the DM halos; however, if the halos are non-spherical then the limits may be weakened, as discussed in Refs. [80, 81]. We also plot the limits from Ref. [79] ($V_{50} = 10.5$ km s^{-1}), which employs semi-analytic models of DM subhalos to derive realistic satellite priors on the J-factor (for the ultrafaint dwarfs). This result explicitly exemplifies the uncertainty range associated with limits from the MW dwarfs.

The two highest purple curves are for the LMC and SMC. The dash-dot curve shows 2σ limits from the LMC from Ref. [199], based on Pass-7 data. The dotted curve shows 2σ limits from the SMC from Ref. [200].

The tan band shows the 2σ upper-limit from the extragalactic γ-ray background (EGB) from Ref. [201]. The band reflects the uncertainties related to the modeling of DM subhalos. This analysis shows that blazars, star-forming galaxies, and radio galaxies can naturally account for the amplitude and spectral shape of the EGB over the energy range 0.1–820 GeV, leaving only modest room for other contributions.

The blue curve shows γ-ray limits (3σ) from the MW halo from Ref. [202]. This is the limit obtained with modeling the MW diffuse emission using GALPROP, for an NFW profile, with $\gamma = 1$ and a local DM density of 0.43 GeV cm^{-3}. The limits are generally weaker without modeling the diffuse emission, and they have a strong dependence on the local DM density.

The light purple curve is for DM subhalos from Ref. [203]. These limits are based on DM subhalo candidates from the unassociated point sources detected by *Fermi*-LAT. In total there are 19 subhalo candidates. The minimum subhalo mass for the upper limit calculation is assumed to be 10^{-5} M$_\odot$.

The upper gray band in Figure 3.7 shows radio constraints for the GC from Ref. [204]. The limits are derived using VLA observations at 330 MHz of the central 0.04° around Sgr A*. An NFW profile is used with $\gamma = 1.26$, R$_s$ = 20 kpc, a local DM density of 0.3 GeV cm^{-3}, and a flat density core of 2 pc. The limits include energy losses due to IC and convection. The lower limit is for $V_C = 0$ km s^{-1}, and the upper limit (not shown) is for $V_C = 1000$ km s^{-1}. The limits can be much stronger (up to 3 or 4 orders of magnitude) when not including IC and convection, or for a core radius closer to zero. There is also a high uncertainty of the magnetic field strength in the innermost region of the GC.

The lower gray band shows radio limits from the central region of M31 ($\sim$1 kpc) from Ref. [205]. The band represents joint constraint from four different surveys: VLSS (74 MHz), WENSS (325 MHz), NVSS (1400 MHz), and GB6 (4850 MHz). An M31 signal is detected for all surveys but VLSS. The highest region is for a central magnetic field strength

$B_0 = 5$ μG and DM concentration of $c_{100} = 12$, the middle region is for $B_0 = 50$ μG and DM concentration of $c_{100} = 20$, and the lowest region is for $B_0 = 300$ μG and DM concentration of $c_{100} = 28$. An NFW profile is used for the DM density, with $\gamma = 1$, and a flat core for r<50 pc. The limits have a large uncertainty due to the uncertainties in the DM profile and magnetic field strength in the inner regions of M31. The magnetic field is modeled with an exponential dependence in galactocentric radius and height above the galactic plane. The analysis accounts for leptonic energy losses due to IC emission, synchrotron emission, Bremsstrahlung, and Coulomb scattering, with synchrotron emission being the dominant loss mechanism over most of the energy range. We note, however, that uncertainties in the astrophysical modeling of these processes may weaken the limits even further. In particular, the limits have a strong dependence on the relative strength of the inverse Compton losses compared to the synchrotron losses, which in turn depends on the energy density of M31's interstellar radiation field.

Also shown are contours for a recently reported excesses in the flux of antiprotons. The upper light teal contour (2σ) is from Ref. [192]. The lower dark contour (2σ) is from Ref. [193]. The NFW profiles for these contours have $\gamma = 1.0$, $R_s = 20$ kpc, and $\rho_\odot = 0.4$ GeV cm^{-3}. The teal curve shows upper-limits from Ref. [194], where a less optimistic view of the excess is given (although the limits still clearly show an anomaly around the signal region).

The red curve is for M31's inner galaxy from Ref. [13]. These limits are obtained by assuming that all of the observed γ-ray emission from M31's inner galaxy arises from standard astrophysical emission, and therefore including a 0.4° disk template (which is derived directly from the bright γ-ray emission that is observed) in the DM fit. In addition, to account for the foreground/background emission, the standard IEM is fit directly to the γ-ray data in the signal region.

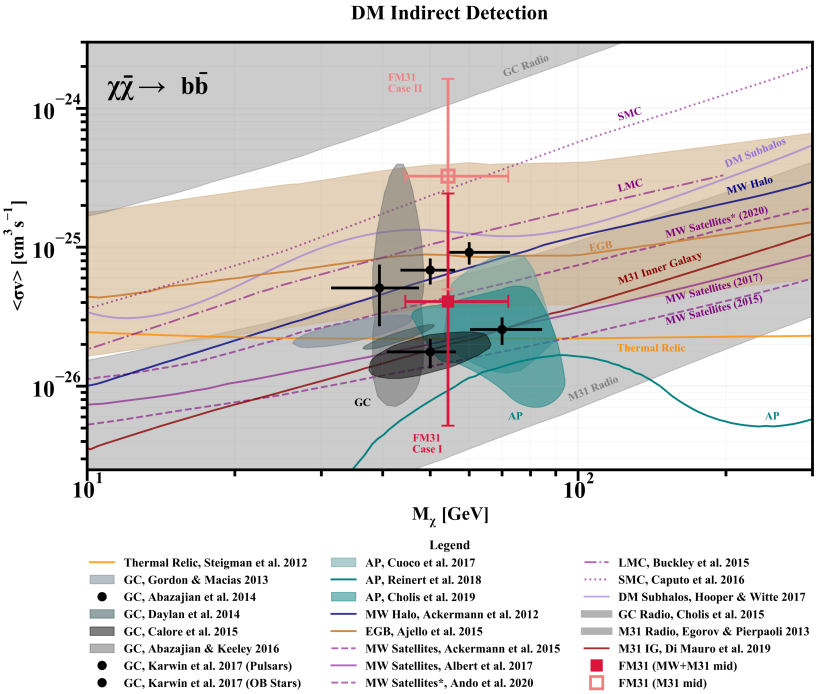

Figure 3.7: DM parameter space. The red and coral data points are for M31's outer halo. The red data point corresponds to case I, for which $J = J_{\rm MW} + J_{\rm M31}$. The coral data point is for case 2, for which $J = J_{\rm M31}$. The best-fit values for the three fit variations used in this analysis are all very similar, so here we plot the mean, and the error bars show the full systematic uncertainty range. Note that the error bars in the cross-section assume that the minimum subhalo mass is 10^{-6} $M_\odot$, and they include the uncertainty due to the halo geometry. Contours for the GC excess are shown in black, and contours for the antiproton excess are shown in teal. Numerous limits from other targets are also overlaid, including the MW satellites shown with purple curves, and M31's inner galaxy shown with a red curve. See Section 3.4 for more details, as well as Appendix 3.5.

Chapter 4

Time Evolution in Quantum Cosmology

This chapter is heavily based on work previously published in collaboration with David E. Kaplan, Tom Melia, Surjeet Rajendran [21].

4.1 Introduction

Quantum Mechanics and General Relativity are the two great pillars of modern physics. Together, they describe phenomena ranging from sub-nuclear scales to the size of the universe, spanning nearly 45 orders of magnitude in energy and time scales. While the ultra-violet nature of gravity is unknown, there is no doubt that its infrared behavior is governed by General Relativity. It is thus important to quantize classical General Relativity *i.e.* develop a framework where the gravitational degrees of freedom evolve quantum mechanically as opposed to their evolution via the equations of motion of classical General Relativity. This is important both to ensure the basic consistency of these two theories with each other and

to identify potentially new dynamics that may be present in the quantum theory.

This program has been successfully implemented in the perturbative regime where the phenomena of interest are restricted to the quantum mechanics of gravitons *i.e.* fluctuations around a classical background [206]. But, it is important to understand the quantum mechanical behavior of gravitation in the non-linear regime where the gravitational dynamics cannot be described solely as fluctuations around a classical background. This non-linear regime describes the behavior of gravitation around black holes and the cosmos. Unfortunately, the application of quantum mechanical principles to derive the correct quantum dynamics of non-linear gravitational systems has been plagued by a number of confusions.

These confusions arise since gravitation is a gauge theory. Canonical quantization requires the identification of the physical degrees of freedom and a suitable elimination of the gauge degrees of freedom [207]. The direct application of the procedure to quantize electromagnetism on gravitation results in a trivial Hamiltonian [207, 208]. Since this procedure is unable to eliminate the gauge degrees of freedom without trivializing the theory, it was suggested that the gauge degree of freedom can be eliminated by restricting the Hilbert space of the theory to only include the energy eigenstates of the Hamiltonian. If this were to be true, the time evolution of physical states would be trivial. While some measure of time evolution can be recovered in asymptotically flat space-times, this procedure does not work for cosmological space-times. This confusion is also tied to the definition of time. The Hamiltonian describes time evolution. In General Relativity, due to general covariance, there is no universal notion of time. One thus needs to recognize that time evolution should be identified as the relative evolution between the gravitational states and other states in the theory, with one of the states acting as a clock to keep track of the relative evolution. While this point is well known, the insistence that the universe is in an energy eigenstate implies that the dynamical world can be explained only if the universe was placed in an enormous superposition over all time [209]. Such a state is not normalizable. Moreover, the clock state

needs to be integrated over all time in order to create this state. But, it is difficult to see how such a clock can be constructed to monotonically track relative evolution over all time using systems with bounded Hamiltonians with quantum states that span a finite range of energies [210].

In light of the above confusions, there has been considerable interest in developing a path integral approach to quantizing non-linear gravitational states [211]. This path integral formalism needs to handle the gauge redundancy in the system. Unfortunately, this problem has not been properly handled in existing work. Current approaches to this problem are focused on maintaining all of the classical equations of motion of General Relativity. This prevents these approaches from performing a sensible gauge fixing procedure. Without gauge fixing, the procedure yields divergent answers.

The intent of this chapter is to clarify these confusions and present a path integral approach to quantizing General Relativity. We focus our attention on the simplest scenario - namely mini-superspace quantum cosmological models where we only consider homogeneous cosmological evolution [211]. We show that a suitably gauge fixed path integral yields finite transition amplitudes. We find that the gauge fixing procedure is necessary not only to get finite transition amplitudes but also to define the notion of co-ordinate time. The general covariance of the theory implies that this procedure maintains physical correlations between gravitational states and the matter states in the universe. As a virtue of the path integral procedure, via the Schwinger-Dyson procedure, we show that the dynamical equations of motion of Einstein are automatically obeyed at the level of expectation values of the field operators. Our analysis shows that the Hamiltonian constraint equation that emerges in classical General Relativity is not a requirement of the quantum dynamics. But, this is not a problem since these classical constraints only need to be obeyed by the classical (*i.e.* coherent) states of the theory. We construct such states and a corresponding Hamiltonian that can be used to describe non-trivial time evolution of this gravitational system. This

procedure also clarifies the role of the classical constraint equation in the dynamics of the quantum system.

The rest of this chapter is organized as follows. In section 4.2, we describe the general principles of quantizing a theory using the path integral, the construction of a Hamiltonian and classical coherent states consistent with this path integral. In section 4.3, we apply this path integral approach to quantizing mini-superspace cosmology. Using this formalism, we construct the corresponding Hamiltonian in section 4.4. In section 4.5, we apply these principles to an explicit model of a cosmology with a rolling scalar field. We then conclude in section 4.6.

4.2 Quantization

Given a physical system whose classical dynamics are known, how does one derive the appropriate quantum mechanical evolution? Since the classical dynamics are a subset of the overall quantum dynamics, it is not possible to derive the quantum mechanical evolution solely from the classical equations. The process of quantization requires us to make certain axiomatic assumptions. For example, in the canonical quantization procedure, this requires making assumptions about commutation (or anti-commutation) relations between fields and their conjugate momenta. We then assume that the time evolution of quantum states is governed by the Schrodinger equation, with a Hamiltonian constructed from the field operators. Ultimately, the only logical requirement of this procedure is that the time evolution of a subset of quantum states that correspond directly to classical states should automatically satisfy the classical equations of motion whenever such states obey the quantum equations of motion. In addition, one might also expect that the classical equations of motion hold in some "average" sense since the average behavior of a large number of quantum systems should resemble classical dynamics.

We review how these issues are addressed in the path integral formulation of quantum mechanics. Given a classical Lagrangian $\mathcal{L}(\phi, \partial_\mu \phi)$ for some scalar field ϕ, instead of the Schrodinger equation, the path integral formulation makes an axiomatic assumption about the time evolution of field basis states. That is, given the field operator $\phi(x)$, we consider its eigenstates $|\phi_e\rangle$ *i.e.* $\phi(x)|\phi_e\rangle = \phi_e|\phi_e\rangle$. The time evolution of these states is defined to be:

$$\langle \phi_f | T(t_2; t_1) | \phi_i \rangle = \int_{\phi(t_1)=\phi_i}^{\phi(t_2)=\phi_f} D\phi \, e^{i \int_{t=t_1}^{t=t_2} d^4x \, \mathcal{L}(\phi, \partial_\mu \phi)} \tag{4.1}$$

This defines the transition matrix element of the time evolution operator of an initial basis state $|\phi_i\rangle$ at time t_1 with the basis state $|\phi_f\rangle$ at time t_2. This axiomatic assumption leads to an immediate consequence. The path integral (4.1) should not change when the variable of integration ϕ is shifted to $\phi + \delta\phi$. Demanding the invariance of the path integral under variable redefintion, we obtain the so called Schwinger-Dyson relations which yield the analogs of the field equations. In the Heisenberg picture, this yields the equations[1]:

$$\langle \Psi | \frac{\delta S}{\delta \phi(t)} | \Psi \rangle = 0 \tag{4.2}$$

where S is the classical action $S = \int_{t_1}^{t_2} d^4x \mathcal{L}(\phi, \partial_\mu \phi)$. This procedure is the analog of Ehrenfest's theorem in quantum field theory and it shows that the classical equations are obeyed at the level of expectation values of normal ordered operators $\frac{\delta S}{\delta \phi}$. In proving the above, we assume that variations vanish at the boundaries. We also confess to an abuse of notation. Throughout this chapter, we will discuss objects such as the expectation value described in (4.2). In such expressions, objects such as $\frac{\delta S}{\delta \phi}$ are normal ordered operators and not classical fields.

[1]One can also construct analogous equations in the Schrodinger picture where now the derivatives in the field equations will act on the expectation values of the fields

An important subtlety rises in the case of gauge theories. In such theories, the path integral (4.1) yields a finite answer only after gauge fixing. Thus the Lagrangian in (4.1) is the gauge fixed Lagrangian $\mathcal{L}_F$. The Schwinger-Dyson procedure is still valid but the identity (4.2) it generates will involve the gauge fixed action S_F as opposed to the classical action S. This identity can be different from the classical relation. There is nothing inconsistent about this since the quantum relations supersede classical equations. All that can be required is that for classical states, these relations reproduce the classical equations of motion.

What are these classical states? To understand these, it is useful to switch from the path integral to the Hamiltonian formulation which more readily deals with states and their evolution. Before describing classical states, let us first address how one might obtain the corresponding Hamiltonian H from the path integral. The path integral is defined in terms of the classical Lagrangian $\mathcal{L}(\phi, \partial_\mu \phi)$ where the fields and their derivatives are commuting classical fields. The Hamiltonian though is a function of non-commuting field operators and their conjugate momenta. The procedure for computing the classical Hamiltonian from the classical Lagrangian thus yields a problem of ordering due to the non-commuting nature of the field operators.

For a bosonic theory, we can resolve the issue of defining classical states and identifying the ordering of the Hamiltonian by making the following observation. We want the quantum theory to retain the symmetries of the classical theory. That is, we want the symmetries of the classical Hamiltonian to also be symmetries of the quantum Hamiltonian. To accomplish this, express the field and its conjugate momentum in terms of canonical creation and annihilation operators. Construct coherent states $|\Psi_c\rangle$ of these creation and annihilation operators - these are the classical states of this theory. Coherent states have the property that for any operator O, specification of the diagonal matrix elements $\langle \Psi_c | O | \Psi_c \rangle$ completely specifies the operator (for example, see [212]). Thus, the Hamiltonian H is completely determined by the expectation values $\langle \Psi_c | H | \Psi_c \rangle$. For coherent states $|\Psi_c\rangle$ one can show [213, 214]:

$$\langle \Psi_c | : H : | \Psi_c \rangle = H_c \left(\langle \Psi_c | \Pi | \Psi_c \rangle, \langle \Psi_c | \phi | \Psi_c \rangle \right) \tag{4.3}$$

Here $: H :$ and H_C are, respectively, the normal ordered and classical Hamiltonian obtained from the classical Lagranian $\mathcal{L}$. That is, the expectation value of the normal ordered Hamiltonian $: H :$ in a coherent state $|\Psi_c\rangle$ is equal to the classical Hamiltonian evaluated on the coherent state expectation values of the field and its conjugate momenta. From this construction, it is clear that time evolution generated by $: H :$ preserves the symmetries of the corresponding classical theory. Thus, as long as the quantum dyanmics is generated by $: H :$, the symmetries of the classical theory are also maintained at the quantum level.

The above statements about coherent states are likely more familiar to the reader in the context of field theories where the kinetic terms of the Hamiltonian are those of a free theory. But, this construction and result also applies for general field theories where the kinetic terms of the Hamiltonian are non-quadratic. To see this, suppose we have a Hamiltonian with non-quadratic kinetic terms in the field ϕ and its conjugate momentum Π. Now ϕ and Π are simply operators on a Hilbert space. We can trivially imagine a free field theory constructed with ϕ and Π and for this free field theory, we can define creation and annihilation operators using ϕ and Π and construct a Fock space. This Fock space is an orthonormal basis on this Hilbert space. Now, consider the original non-linear theory. Even though the Fock space states constructed with the canonical creation and annihilation operators are not energy eigenstates of the non-linear theory, these Fock space states are still an orthonormal basis on the Hilbert space. When the canonical creation and annihilation operators act on these Fock space states, they will have the same algebra as the case of the free field theory since the operator algebra is independent of the underlying Hamiltonian. The construction and properties of coherent states simply relies on this operator algebra. Since this algebra also

holds in the case of the non-linear Hamiltonian, we can use the creation and annihilation operators of the free field theory to define coherent states. The resultant statements about expectation values of normal ordered operators thus applies to these non-linear theories as well. The above construction will be central to our discussions about the Hamiltonian for General Relativity. We will use the requirement that the quantum evolution of coherent states reproduce the symmetries of classical General Relativity to resolve operator ordering problems in quantum General Relativity.

We have now described two different ways to time evolve a quantum state: the first using the path integral (4.1) and the second using the Schrodinger equation employing the normal ordered Hamiltonian (4.3). It can be shown that these two procedures yield the same time evolution using the conventional derivation of the path integral from the Schrodinger equation [214]. Henceforth, in this chapter, when we refer to the Hamiltonian, we will always mean this normal ordered Hamiltonian and simply denote it as H instead of $:H:$.

In the following sections, we employ the above principles to obtain the time evolution of quantum cosmology.

4.3 Quantum Cosmology

We describe the quantum mechanical evolution of a scalar field ϕ with potential $V(\phi)$ in General Relativity. We work in mini-superspace where we restrict our attention to the homogeneous evolution of $\phi(t)$ and the metric $g_{\mu\nu}(t)$. In this limit, the metric $g_{\mu\nu}$ is:

$$g_{\mu\nu} \rightarrow ds^2 = -N(t)^2 dt^2 + a(t)^2 \left(dx^2 + dy^2 + dz^2\right) \tag{4.4}$$

To describe quantum evolution, we need to know the physical degrees of freedom. In this system, these are $\phi(t)$ and $a(t)$, with $N(t)$ being a gauge degree of freedom.

We formulate the quantum theory via the path integral formulation. In the path integral formulation what we wish to compute is the transition matrix element:

$$\langle \phi_f, a_f | T\left(t_2; t_1\right) | \phi_i, a_i \rangle \tag{4.5}$$

where $T\left(t_2; t_1\right)$ is the propagator that propagates an initial basis state $|\phi_i, a_i\rangle$ of the scalar field ϕ and the scale factor a at time t_1 to a final basis state ϕ_f and a_f at time t_2.

There are two interrelated issues that arise when defining this path integral and they have a common resolution. The first issue is that since $N\left(t\right)$ is a gauge degree of freedom, the path integral can only be defined by gauge fixing $N\left(t\right)$. For this metric ansatz, a convenient gauge to use is the gauge $\dot{N}\left(t\right) = 0$. The second issue arises from the definition of time. In General Relativity, time is simply a parameter - it can be redefined at will and thus one has to confront the question of what is meant by the definition of the propagator $T\left(t_2; t_1\right)$ since the values $t_{1,2}$ can clearly be redefined.

To resolve these issues, let us simply write down the standard formula for the gauge fixed path integral that yields the matrix elements of $T\left(t_2; t_1\right)$:

$$\langle \phi_f, a_f | T\left(t_2; t_1\right) | \phi_i, a_i \rangle = \int_{\phi(t_1)=\phi_1, a(t_1)=a_1, N(t_1)=N_1}^{\phi(t_2)=\phi_2, a(t_2)=a_2, N(t_2)=N_2} DN\, D\phi\, Da\, D\lambda\, e^{i \int_{t=t_1}^{t=t_2} d^4x \left(\mathcal{L} - \lambda \dot{N}\right)} \tag{4.6}$$

In the above, we should also include Gibbons-Hawking-York boundary terms to define the variational calculus for manifolds with a boundary. These will not be relevant for our discussion and thus we do not explicitly write them. In (4.6), we have introduced a Lagrange multiplier λ to enforce the gauge condition $\dot{N} = 0$. The gauge condition also restricts the initial conditions of the function $N\left(t_1\right) = N\left(t_2\right) = N_0$. Setting $\dot{N} = 0$, the integral over N is trivial, with N fixed at the boundary; in this case the condition $\dot{N} = 0$ fully fixes the gauge.

We are thus reduced to evaluating:

$$\langle \phi_f, a_f | T\left(t_2; t_1\right) | \phi_i, a_i \rangle = \int_{\phi(t_1)=\phi_1, a(t_1)=a_1, N(t_1)=N_0}^{\phi(t_2)=\phi_2, a(t_2)=a_2, N(t_2)=N_0} D\phi \, Da \, e^{i \int_{t=t_1}^{t=t_2} d^4x \tilde{\mathcal{L}}} \tag{4.7}$$

Here $\tilde{\mathcal{L}}$ is the gauge fixed Lagrangian after the path integral over N and λ have been performed. This path integral is dominated by paths near the classical paths that are extrema of the action *i.e.* paths that satisfy the classical equations of motion:

$$\partial_t \left(\frac{\partial \tilde{\mathcal{L}}}{\partial \dot{\phi}} \right) - \frac{\partial \tilde{\mathcal{L}}}{\partial \phi} = 0 \tag{4.8}$$

$$\partial_t \left(\frac{\partial \tilde{\mathcal{L}}}{\partial \dot{a}} \right) - \frac{\partial \tilde{\mathcal{L}}}{\partial a} = 0 \tag{4.9}$$

It is easily checked that (4.8) produces the usual second order differential equation for a scalar field ϕ while (4.9) yields the second (or spatial, $G_{ii} = -8\pi G T_{ii}$) Friedman equation *i.e.* a second order differential equation for $a\left(t\right)$. Since both of these equations are second order differential equations, given the boundary conditions $\left(\phi\left(t_1\right) = \phi_i, a\left(t_1\right) = a_i\right)$ and $\left(\phi\left(t_2\right) = \phi_f, a\left(t_2\right) = a_f\right)$, we can find a classical solution. It can be shown that the path integral (4.7) is finite [211] and thus defines a sensible propagator $T\left(t_2; t_1\right)$.

What would happen if we picked a different value for the gauge parameter N *i.e.* set $N_0 \to \tilde{N}_0$ in the path integral (4.7)? From the metric (4.4), a redefinition $N_0 \to \tilde{N}_0$ is a redefinition of the time co-ordinate. Now consider a path $\left(\phi\left(t\right), a\left(t\right)\right)$ from $\left(\phi\left(t_1\right) = \phi_i, a\left(t_1\right) = a_i\right)$ to $\left(\phi\left(t_2\right) = \phi_f, a\left(t_2\right) = a_f\right)$ in the $a - \phi$ plane. When we set $N_0 \to \tilde{N}_0$, this is simply a reparameterization $\left(\phi\left(\tilde{t}\right), a\left(\tilde{t}\right)\right)$ of the same physical path in the $a - \phi$ plane where we get $\tilde{t}$ from the reparameterization determined by $N_0 \to \tilde{N}_0$. Since the action of General Relativity

is invariant under time re-parameterization, we then have:

$$\langle \phi_f, a_f | \tilde{T}\left(\tilde{t_2}; \tilde{t_1}\right) | \phi_i, a_i \rangle = \langle \phi_f, a_f | T\left(t_2; t_1\right) | \phi_i, a_i \rangle \tag{4.10}$$

That is, the transition matrix element of the propagator between the physical states $|\phi_i, a_i\rangle$ and $|\phi_f, a_f\rangle$ are the same as long as the time co-ordinates in the propagator are suitably rescaled. Thus, the time evolution of the basis state $|\phi_i, a_i\rangle$ is:

$$|\phi_i, a_i\rangle \rightarrow \sum_{\phi_f, a_f} c_{\phi_f, a_f}\left(t_2, t_1\right) |\phi_f, a_f\rangle = \sum_{\phi_f, a_f} \tilde{c}_{\phi_f, a_f}\left(\tilde{t_2}, \tilde{t_1}\right) |\phi_f, a_f\rangle \tag{4.11}$$

where the coefficients $c_{\phi_f, a_f}\left(t_2, t_1\right)$ and $\tilde{c}_{\phi_f, a_f}\left(\tilde{t_2}, \tilde{t_1}\right)$ are the transition matrix elements (4.10). Given this time evolution of the basis states, we see that the initial quantum state $|\Psi\left(t_1\right)\rangle = |\tilde{\Psi}\left(\tilde{t_1}\right)\rangle = |\Sigma\rangle$ becomes the final state $|\Psi\left(t_2\right)\rangle = |\tilde{\Psi}\left(\tilde{t_2}\right)\rangle = |\Omega\rangle$.

This clarifies the issue of time that has plagued discussions about quantum cosmology. Time evolution is the statement that a given initial quantum state $|\Sigma\rangle$ evolves to a state $|\Omega\rangle$. This evolution takes a certain co-ordinate time. But, co-ordinate time by itself is meaningless in General Relativity. The co-ordinate time can be changed simply by picking a different value of N_0. What does this time evolution in co-ordinate time mean? In the above, we have shown the following. Let us pick some value of N_0. This defines a co-ordinate time t. We can pick an initial quantum state $|\Psi\left(t_1\right)\rangle = |\Sigma\rangle$. Using the path integral, we can now compute the final state $|\Psi\left(t_2\right)\rangle = |\Omega\rangle$. Instead of N_0, suppose we pick a different value $\tilde{N_0}$. This picks a different definition of the co-ordinate time $\tilde{t}$. As long as we rescale the times suitably $t_1 \rightarrow \tilde{t_1}$ and $t_2 \rightarrow \tilde{t_2}$, we have the same physical effect: $|\Psi\left(t_1\right)\rangle = |\tilde{\Psi}\left(\tilde{t_1}\right)\rangle = |\Sigma\rangle \rightarrow |\Psi\left(t_2\right)\rangle = |\tilde{\Psi}\left(\tilde{t_2}\right)\rangle = |\Omega\rangle$. We thus learn that no matter what value of N_0 is chosen, the physical evolution of the quantum states in the $a - \phi$ Hilbert space is the same - the time co-ordinate is just a convenient parameterization of this evolution.[2]

[2]In a deeper sense, time evolution should be regarded as the relative evolution between different quantum states. In general, one could try to formulate time evolution without co-ordinate time by writing the laws of

It is important to note that even though the co-ordinate time label that is used to define time evolution can be changed by picking a different value of N_0, for any given N_0, the co-ordinate label is extremely meaningful. Time evolution, by its very definition, is the notion that an initial quantum state $|\Sigma\rangle$ changes over a certain co-ordinate time to become a different state $|\Omega\rangle$. We see that the gauge fixing that is necessary to perform the path integral (*i.e.* picking a value of N_0) fixes the meaning of the co-ordinate time that appears in the time evolution operator. Without a definition of a co-ordinate time, this time evolution operator is meaningless.

This is the key difference between our treatment of the path integral and the conventional approach. In the conventional approach, once the finite path integral over the dynamical degrees of freedom ϕ and a is performed, an integral is performed over all possible values of N_0. This makes the path integral independent of the gauge fixing parameter N_0 while yielding a divergent answer. But, this is hardly surprising - N is a gauge degree of freedom and an integration over a gauge degree of freedom is expected to be divergent. This integral over N should not be performed. In physical terms, when a sum over all N is performed, the question that is being asked is: if the quantum state is initially in the basis state $|\phi_i, a_i\rangle$, what is the transition matrix element for the state to become the basis state $|\phi_f, a_f\rangle$ over **all** time? It is unsurprising that this answer is ill defined and divergent - the basis states have a wide spread of conjugate momenta and thus when integrated over all time, they can transition into each other in infinitely many ways. The physical meaning of time evolution is not the amplitude for transitioning from an initial quantum state to some final quantum state over the entire history of the universe. Rather, the physical meaning of time evolution is the actual path taken by the quantum state in Hilbert space to go from an initial state to some final state. Time is a parameterization of this path. It is thus fully appropriate for the path integral, which in fact describes this evolution in a particular choice of time

nature in terms of partial derivatives of various fields. Since the motion is along a complicated Hilbert space, such an equation is likely to be complex. It is easier to describe this motion using a simple parameterization, namely, time.

co-ordinate, to depend on this choice via the gauge parameter N_0. We have seen that despite this dependence, the physical outcomes are independent of the choice of N_0.

Another major difference between our approach and the conventional approach is that the procedure outlined above does not involve the constraint equation obtained from the first (or temporal,[3] $G_{tt} = -8\pi G T_{tt}$) Friedman equation.[4] In the conventional approach, since the path integral over $N(t)$ is retained, the constraint equation is required to hold, resulting in the Wheeler-DeWitt equation. In our procedure, the path integral over N is trivial due to the gauge choice $\dot{N}(t) = 0$ and the fixed boundary conditions (or) choice of time coordinate. The classical paths from $(\phi(t_1) = \phi_i, a(t_1) = a_i)$ to $(\phi(t_2) = \phi_f, a(t_2) = a_f)$ are not required to satisfy this constraint equation and thus we do not require the Wheeler-DeWitt equation to hold. In classical General Relativity, the constraint equation restricts the initial conditions for the second order dynamical equation for the scale factor – the second/spatial Friedman equation. Classically, this implies that in this system, we are only allowed to specify $\phi(t_1) = \phi_1, \phi(t_2) = \phi_2$, and $a(t_1) = a_i$. Due to the constraint equation, there is no freedom to specify $a(t_2) = a_f$ and the scale factor $a(t_2)$ is dynamically determined. In quantum evolution, due to the absence of this constraint, one in general gets a spread of metric states $a(t_2)$ correlated with the scalar field state $\phi(t_2)$ as opposed to the unique correlation between $\phi(t_2)$ and $a(t_2)$ in the classical case.

Let us now comment on the connection between this quantization procedure and the classical field equations. The path integral, as a virtue of the Schwinger-Dyson procedure discussed

[3]Note we have used Weinberg's convention in defining the Riemann tensor, which we adopt for this chapter.

[4]The analogous approach in electromagnetism would be not to invoke the requirement that physical states obey Gauss' law, $\nabla.E\,|\Psi\rangle_{\text{physical}} = 0$. The unconstrained theory has a classical non-zero background charge density that is conserved because $[H, \nabla.E] = 0$. We will see below that the counterpart of this background in the gravity theory is a pressureless dark matter component.

above, guarantees the following identities [5]:

$$\langle\Psi|\left(\partial_t\left(\frac{\partial\mathcal{L}}{\partial\dot{\phi}}\right)-\frac{\partial\mathcal{L}}{\partial\phi}\right)|\Psi\rangle=0$$
$$\langle\Psi|\left(\partial_t\left(\frac{\partial\mathcal{L}}{\partial\dot{a}}\right)-\frac{\partial\mathcal{L}}{\partial a}\right)|\Psi\rangle=0 \tag{4.12}$$

The equations (4.12) are the analogs of Ehrenfest's equations that correspond to the second order field equations for ϕ and a. However, when we perform the variation δN on N, we get the equation:

$$\langle\Psi|\left(\frac{d\lambda}{dt}-\frac{\partial\mathcal{L}}{\partial N}\right)|\Psi\rangle=0 \tag{4.13}$$

This is not a constraint on $\langle\Psi|\frac{\partial\mathcal{L}}{\partial N}|\Psi\rangle$ - rather, it describes the evolution of the Lagrange multiplier λ in the path integral. There is thus no physics associated with this equation. We thus see that the Wheeler-DeWitt equation does not follow from the path integral and is thus not an actual requirement of the quantum dynamics (see [215**?**] for similar phenomena in the Euclidean path integral).

The fact that (4.13) is not of the form $\langle\Psi|\frac{\partial\tilde{\mathcal{L}}}{\partial N}|\Psi\rangle=0$, the quantum analog of the classical first order constraint $\frac{\partial\tilde{\mathcal{L}}}{\partial N}=0$ that arises from classical General Relativity, should not bother us. In a typical quantum theory, since the Schrodinger equation is a first order differential equation, the quantum state of the physical degrees of freedom can be freely specified as initial conditions. The Schrodinger equation then yields the dynamical evolution of this initial state. The imposition of the constraint $\langle\Psi|\frac{\partial\tilde{\mathcal{L}}}{\partial N}|\Psi\rangle=0$ is a restriction on the allowed initial state. But, there do not appear to be any inconsistencies in the quantum theory by relaxing this constraint since gauge fixing the gauge degree of freedom N can be done

[5] We write these in the Heisenberg picture for notational simplicity. In the Schrodinger picture, the derivatives act on expectation values.

independent of this constraint. To further understand the analog of the classical first order constraint equation of General Relativity it is useful construct the Hamiltonian described by the path integral (4.7), which we do in the next section.

Let us now discuss the invariance of the quantum dynamics under a more general gauge than the $\dot{N} = 0$ gauge. The gauge symmetry of General Relativity is general covariance *i.e.* the space-time manifold can be parameterized by any choice of coordinates and the underlying quantum dynamics should be invariant under such a reparameterization. In mini-superspace, this translates into the statement that we can take $t \to N(t)$ for arbitrary $N(t)$ and the quantum dynamics should still be invariant. Importantly, once we choose these coordinates, we have to perform the time evolution of the full quantum state using these coordinates. That is, if we have a quantum superposition, under a diffeomorphism, the time coordinate in the entire superposition is changed by the **same** function $N(t)$. The diffeomorphism, being a function on the manifold, does not allow us to choose different time parameterizations for different parts of a superposition. This has implications for certain conventionally used gauge choices in classical General Relativity that cannot be blindly applied at the quantum level.

In classical General Relativity, we are only interested in describing the behavior of a single metric and thus it is convenient to choose various gauges that depend on the metric itself - for *e.g.* one may take $N(t) = f(a(t))$. In quantum mechanics, we are required to describe the evolution of superpositions of metrics - indeed the path integral itself is a computation that specifies quantum evolution as a sum over many such superpositions. It is tempting to think that one could take the gauge $N(t) = f(a(t))$ in the path integral and integrate over the dynamical degree of freedom $a(t)$ while performing this path integral and demand that the final result be reparameterizaton invariant. But, this is incorrect. Such a procedure specifies a different parameterization of the time coordinate for each part of the quantum superposition and it will not give time reparameterization invariant results.

This is true even classically: one can choose a simple gauge $N(t) = 1$ and pick two different sets of initial values of fields and their cojugate momenta $(\phi_{1i}, \Pi_{1i}, a_{1i}, \Pi^a_{1i})$ and $(\phi_{2i}, \Pi_{2i}, a_{2i}, \Pi^a_{2i})$ on an initial time slice in the manifold. Time evolve this state to a final time where we have $(\phi_{1i}, \Pi_{1i}, a_{1i}, \Pi^a_{1i}) \rightarrow \left(\phi_{1f}, \Pi_{1f}, a_{1f}, \Pi^a_{1f}\right)$ and $(\phi_{2i}, \Pi_{2i}, a_{2i}, \Pi^a_{2i}) \rightarrow \left(\phi_{2f}, \Pi_{2f}, a_{2f}, \Pi^a_{2f}\right)$. Let us now pick a gauge of the form $N(t) = f(a(t))$ and perform the same time evolution by using the respective metrics $a_{1,2}$ in this lapse function.

One can check that classically when $(\phi_{1i}, \Pi_{1i}, a_{1i}, \Pi^a_{1i}) \rightarrow \left(\phi_{1f}, \Pi_{1f}, a_{1f}, \Pi^a_{1f}\right)$, we do **not** have $(\phi_{2i}, \Pi_{2i}, a_{2i}, \Pi^a_{2i}) \rightarrow \left(\phi_{2f}, \Pi_{2f}, a_{2f}, \Pi^a_{2f}\right)$ *i.e.* the relative evolution is not gauge invariant. But, this is not a surprise since the parameterization of time is being picked differently for each metric. What is true however is that we are free to choose a gauge of the form $N(t) = f(a_1(t))$ **or** $N(t) = f(a_2(t))$ and use the same gauge to perform both of these evolutions. In this case, we will get gauge invariant results.

In other words, the function $N(t)$ can be any arbitrary function of time (as demanded by general covariance) but it is the same function of time that has to be applied across the entire quantum superposition. One cannot have the dynamical degree of freedom appearing in $N(t)$ with this degree of freedom being integrated over in the path integral. It is straightforward to demonstrate gauge invariance of the physical evolution of the path integral parameterized by such an arbitrary function of time (that applies across the full quantum state) by suitably rescaling the time parameters as articulated in the discussion of the $\dot{N} = 0$ gauges.

4.4 Hamiltonian Construction

This path integral procedure sheds light on how one may canonically quantize gravity. When Dirac [207] tried to canonically quantize gravity, he ran into the following issue: in minisuperspace, the physical degrees of freedom are a and ϕ while N is a gauge degree of freedom.

To quantize the theory, it would seem like one has to decide what the N operator is supposed to be. Following the procedure in electromagnetism, Dirac first tried to solve for N by requiring the temporal Einstein equation $G_{00} + 8\pi G T_{00} = 0$ to hold at the operator level. But, since $H_N = -N\left(G_{00} + 8\pi G T_{00}\right)$, if $\left(G_{00} + 8\pi G T_{00}\right) = 0$, we also have $H_N = 0$ *i.e.* the Hamiltonian vanishes identically and the theory is trivial[6]. Instead, Dirac imposed the requirement that the physical states of the theory satisfy the temporal Einstein equation $\left(G_{00} + 8\pi G T_{00}\right)|\Psi\rangle = 0$, resulting in the Wheeler deWitt equation $H_N|\Psi\rangle = 0$.

While this procedure does not determine N, this restriction on the Hilbert space makes the quantum theory independent of N. This is similar to the procedure followed in gauge theories such as electromagnetism. In certain covariant gauges like the Lorenz gauge, the gauge redundancy is not fully removed and the Hamiltonian depends upon gauge degrees of freedom. But, by requiring physical states to obey certain constraint equations, one can prevent the gauge degrees of freedom from being physically relevant. It is thus tempting to attempt the same procedure in General Relativity since H_N depends on N. While the Hamiltonian H of this theory is now non-trivial, if $H_N|\Psi\rangle = 0$, then every physical state $|\Psi\rangle$ is required to be an energy eigenstate of H and thus the state has no evolutionary dynamics. Note that in this case, all the physical states have to have the same energy eigenvalue since if they did not, we could take a superposition of them which would then not be an energy eigenstate. This is the famous "problem of time" of quantum cosmology [208].

Let us see how the path integral formulation can be used to canonically quantize gravity. In this formulation, the meaning of N is clear - N defines co-ordinate time. Thus, one should not be "solving" for it - one simply chooses it. That is, N is not an operator, it is simply the number N_0 that was picked to define co-ordinate time in the path integral. One can now take the Lagrangian $\tilde{\mathcal{L}}$ obtained by gauge fixing and construct the canonical normal ordered Hamiltonian H_N from it. Quantum states will evolve as per the Schrodinger equation:

[6]The situation is different in electromagnetism where $(\nabla \cdot E)$ can be set to zero at the operator level and one can still obtain a non trivial Hamiltonian.

$$i\frac{\partial|\Psi\rangle}{\partial t_N} = H_N|\Psi\rangle \tag{4.14}$$

reproducing the dynamics of the path integral obtained from the gauge fixed Lagranian. Now, different values of N will yield different Hamiltonians H_N - but this is simply the statement that choosing different values of N corresponds to choosing different time co-ordinates t_N. Even though these Hamiltonians are different, just as in the case of the path integral, the evolution will preserve correlations between quantum states *i.e.* the physical meaning of "time evolution". We work this out explicitly in section 4.5. We see that the nature of the gauge symmetry in General Relativity is different from that of electromagnetism. In electromagnetism, one could solve for the gauge operators in terms of other physical operators. But, this is not true in General Relativity - N picks the time co-ordinate and the time reparameterization invariance of the theory guarantees that the underlying physics is gauge invariant.

Importantly, this quantization procedure does not require the Wheeler deWitt equation to hold *i.e.* physical states $|\Psi\rangle$ of the theory are not required to be annihilated by the Hamiltonian of General Relativity. With $H_N|\Psi\rangle \neq 0$, the quantum theory does not automatically satisfy the temporal Einstein equation $\frac{\partial\tilde{\mathcal{L}}}{\partial N}|\Psi\rangle = 0$ (where $\frac{\partial\tilde{\mathcal{L}}}{\partial N}$ is now an operator). But, the belief that the quantum theory should exactly satisfy the classical Einstein equation is incorrect. The quantum theory supersedes the classical equations of motion - instead of restricting the allowed quantum states, what we must do is to find the analog of the classical equations of motion that automatically arise from the quantum evolution.

Let us now discuss the analog of the first order constraint. Notice that any quantum state $|\Psi\rangle$ that satisfies (4.14) automatically satisfies:

$$\frac{d\langle\Psi|H_N|\Psi\rangle}{dt_N} = 0 \tag{4.15}$$

Thus, if we are given an initial condition that satisfies the constraint $\langle\Psi|H_N|\Psi\rangle = 0$, subsequent time evolution will automatically obey the first order Einstein constraint $\langle\Psi|\frac{\partial\tilde{\mathcal{L}}}{\partial N}|\Psi\rangle = 0$.

With this understanding, let us now understand why the classical evolution of General Relativity appears to obey the first order constraint. For classical cosmology, we need states $|\Psi_c\rangle$ that are coherent states of the theory (and not energy eigenstates as conventionally demanded). The construction of these coherent states in this non-linear theory is performed using the canonical creation and annihilation operators of the corresponding fields, as discussed in section 4.2. For these states, the expectation value $\langle\Psi|\frac{\partial\tilde{\mathcal{L}}}{\partial N}|\Psi\rangle$ reduces to the classical expression for $\frac{\partial\tilde{\mathcal{L}}}{\partial N}$ evaluated on the expectation values $\langle a\rangle$, $\langle\Pi_a\rangle$, $\langle\phi\rangle$ and $\langle\Pi\rangle$. If we choose a coherent state that obeys the Hamiltonian constraint $\langle\Psi_c|\frac{\delta\tilde{\mathcal{L}}}{\delta N}|\Psi_c\rangle = 0$, its subsequent time evolution will automatically obey the first order classical constraint of General Relativity. This procedure thus sheds light on the reason why classical General Relativity is able to solve the initial value problem. Quantum evolution is described by first order differential equations. Thus, given any initial state one can time evolve it. This is unlike the over constrained classical equations of General Relativity. But, the quantum equations guarantee that if we are given an initial state that obeys the first order constraint of classical General Relativity, the evolution will continue to preserve it. This is precisely the initial value problem of General Relativity and it is trivially proven using quantum dynamics.

What if we picked a coherent state that did not obey this constraint? Relaxation of this condition would imply that there would be coherent states of the theory that satisfy the dynamical Einstein equations (4.12) with $\langle\Psi|\frac{\partial\tilde{\mathcal{L}}}{\partial N}|\Psi\rangle \neq 0$, leading to the existence of classical

solutions that apparently violate the classical Einstein constraint. However, this does not seem to be an actual problem. When we have a coherent state with $\langle\Psi|\frac{\partial\tilde{\mathcal{L}}}{\partial N}|\Psi\rangle \neq 0$, this implies that the expectation value $\langle\Pi_a\rangle$ (*i.e.* the Hubble parameter) is not commensurate with the energy densities in the universe. But, the path integral allows us to time evolve this state. This time evolution is identical to that of a classical state with the same initial value $\langle\Pi_a\rangle$ and a new pressure-less "dark matter" component whose initial energy density is the amount necessary to enforce the constraint $\langle\Psi|\frac{\partial\tilde{\mathcal{L}}}{\partial N}|\Psi\rangle = 0$. This is because such a pressure-less dark matter component only affects the constraint equation but not the dynamical evolution equations for a and ϕ. In other words, the gravitational excitations that lead to $\langle\Psi|\frac{\partial\tilde{\mathcal{L}}}{\partial N}|\Psi\rangle \neq 0$ effectively act as an initial state with a component of dark matter.

4.5 Examples

Let us next see how to apply the above formalism in a cosmological model where the scalar field potential $V(\phi) = 0$. With the metric (4.4), the Lagrangian for this theory is $\mathcal{L} = \frac{M_{pl}^2}{2}\sqrt{-g}R + \sqrt{-g}\frac{g^{\mu\nu}\partial_\mu\phi\partial_\nu\phi}{2}$, yielding:

$$\mathcal{L} = 3M_{pl}^2\frac{a(t)\dot{a}(t)^2}{N(t)} - \frac{a(t)^3\dot{\phi}(t)^2}{2N(t)} \tag{4.16}$$

To proceed, we perform the gauge fixing procedure described in section 4.3 by taking $N(t) = \tilde{N}$, a constant, yielding:

$$\mathcal{L}_{\mathcal{F}} = \frac{\left(3M_{pl}^2 a(t)\dot{a}(t)^2 - \frac{a(t)^3\dot{\phi}(t)^2}{2}\right)}{\tilde{N}} \tag{4.17}$$

With this gauge fixed Lagrangian, we can compute the conjugate momenta $\Pi_a = \frac{\partial\mathcal{L}_{\mathcal{F}}}{\partial\dot{a}}$, $\Pi = \frac{\partial\mathcal{L}_{\mathcal{F}}}{\partial\dot{\phi}}$ and obtain the Hamiltonian $H = \Pi_a\dot{a} + \Pi\dot{\phi} - \mathcal{L}_{\mathcal{F}}$, yielding:

$$H_{\tilde{N}} = \tilde{N}\left(a^{-1}\frac{\Pi_a^2}{12M_{pl}^2} - a^{-3}\frac{\Pi^2}{2}\right) \tag{4.18}$$

upto ordering ambiguities that we will resolve below. The conjugate momentum Π_a satisfies the commutation relation $[a, \Pi_a] = i$ and thus in the "position" basis of the a operator, $\Pi_a = -i\frac{\partial}{\partial a}$. Time evolution is then determined using the Schrodinger equation with this Hamiltonian:

$$i\frac{\partial|\Psi\rangle}{\partial t_{\tilde{N}}} = \tilde{N}\left(a^{-1}\frac{\Pi_a^2}{12M_{pl}^2} - a^{-3}\frac{\Pi^2}{2}\right)|\Psi\rangle \tag{4.19}$$

When a different value of $\tilde{N}$ is picked, (4.19) makes it clear that it is simply just a reparameterizaton of the time coordinate. Physical correlations between states are determined by the time independent operators a, Π_a, Π and ϕ - these correlations will be maintained under reparameterization of the t coordinate.

Since a and Π_a do not commute, we can now see why there is a question about the order of the operators in (4.19) - should the kinetic term for a be $a^{-1}\Pi_a^2$ (as written) or some linear combination of $a^{-1}\Pi_a^2$, $\Pi_a a^{-1}\Pi_a$ and $\Pi_a^2 a^{-1}$? To answer this question, we resort to the physical requirement stated in section 4.2 - namely, we demand that the quantum evolution of coherent states $|\phi\Pi, a\Pi_a\rangle$ preserves the symmetries of the classical theory whose classical field values are given by the expectation values $\langle a\rangle = \langle\phi\Pi, a\Pi_a|a|\phi\Pi, a\Pi_a\rangle$, $\langle\Pi_a\rangle = \langle\phi\Pi, a\Pi_a|\Pi_a|\phi\Pi, a\Pi_a\rangle$, $\langle\phi\rangle = \langle\phi\Pi, a\Pi_a|\phi|\phi\Pi, a\Pi_a\rangle$ and $\langle\Pi\rangle = \langle\phi\Pi, a\Pi_a|\Pi|\phi\Pi, a\Pi_a\rangle$. In the absence of operators of the form a^{-1} and a^{-3} in (4.19), this requirement results in normal ordering the Hamiltonian as discussed in section 4.2. But, since (4.19) contains these inverse operators, the procedure is as follows. The correct operator that appears in (4.19) in place of $a^{-1}\Pi_a^2$ is the operator O for which the expectation value $\langle\phi\Pi, a\Pi_a|O|\phi\Pi, a\Pi_a\rangle$ is equal to the classical value $\langle\Pi_a\rangle^2/\langle a\rangle$. This specifies the diagonal matrix elements of O on any coherent

state. Since the coherent states are an overcomplete basis, it can be shown (for *e.g.* see [212]) that the specification of these diagonal matrix elements uniquely determines O. Thus, the operator O that appears in the Hamiltonian in place of $a^{-1}\Pi_a^2$ is uniquely determined. The same argument also applies for the operator that appears instead of $a^{-3}\Pi^2$.

4.6 Conclusions

In this chapter, we have shown that the quantum cosmology of mini-superspace can be defined unambiguously with a gauge-fixed path integral. This procedure yields finite transition amplitudes and it can be used to construct a non-trivial Hamiltonian. Classical evolution is described by coherent states of this theory. Since these are not energy eigenstates, the time evolution of this state is non-trivial. These states do not obey the Wheeler-DeWitt equation. That is, we have found that the typical Hamiltonian constraint that is imposed in classical General Relativity is not required in the quantum theory. When this condition is not imposed, the evolution of the universe can still be classical but with the additional gravitational excitations acting as a form of dark matter.

Our analysis focused on mini-superspace in order to simplify calculations and identify the key physical principles. It would be interesting to extend this analysis to more general cosmologies where one allows for inhomogeneous excitations. This would require gauge fixing components of the metric that mix time and space. Presumably, this gauge fixing procedure results in the identification of the foliation of the space-time manifold. The gauge fixed path integral should still yield finite transition matrix elements and this path integral can then be used to obtain a suitable Hamiltonian.

In linear quantum mechanics, due to decoherence, it is difficult to conceive of scenarios where a quantum description of gravitation is necessary to understand the dynamics of the universe.

The primary purpose of our work is to demonstrate that non-linear gravitational phenomena can be consistently described by quantum mechanics. The recognition that the classical states that do not satisfy the Hamiltonian constraint can be treated as classical states that obey the constraint but with additional dark matter may yield new phenomenology. The theoretical formalism developed in this chapter may be useful to understand stability issues in certain cosmologies where quantum tunneling could potentially be important [216, 217, 218, 219]. This formalism also permits a much wider class of quantum states that could describe the universe as opposed to the energy eigenstates that are allowed by the Wheeler-DeWitt equation. These may find use in describing the initial state of the universe emerging from the big bang singularity. Further, we also see that the quantum dynamics of coherent states is fully captured by the appropriate classical equations of motion. Since these states are a basis, understanding their classical behavior is tantamount to describing the actual quantum evolution of these systems.

The most phenomenologically interesting applications of this formalism are likely to be found in non-linear quantum mechanics where there can be macroscopic quantum mechanical phenomena that exist despite decoherence [220]. These phenomena exist when the universe is in a macroscopic superposition, as expected in conventional inflationary cosmology. The time evolution of such a state cannot be described by classical General Relativity. The formalism developed in this chapter can be applied to these non-linear quantum mechanical theories to obtain cosmological observables.

Acknowledgements and Author Contributions Statement

Thank you to Raman Sundrum, Steffen Gielen, and Shreya Shukla for discussions.

Using the CASRAI CRediT Contributor Roles Taxonomy: Conceptualization, A.K.B., D.E.K.,

T.M., S.R.; Formal analysis, A.K.B., D.E.K., T.M., S.R.; Funding acquisition, D.E.K., T.M., S.R.; Investigation, A.K.B., D.E.K., T.M., S.R.; Methodology, A.K.B., D.E.K., T.M., S.R.; Project administration, D.E.K., S.R.; Supervision, S.R.; Writing – original draft, A.K.B., D.E.K., T.M., S.R.; Writing – review and editing, A.K.B., D.E.K., T.M., S.R.

Chapter 5

PRyMordial: the first three minutes, within and beyond the standard model

This chapter is heavily based on work previously published in collaboration with Tim M.P. Tait and Mauro Valli [17].

5.1 Introduction

The snapshot of the universe approximately three minutes after the Big Bang [221] can be regarded as one of the most remarkable predictions of the Standard Model (SM) of Particle Physics in conjunction with the (so-called) concordance model of Cosmology, ΛCDM.

While a theory for the origin of chemical elements based on an epoch of high-energy densities and pressures was already formulated by Alpher, Bethe, and Gamow more than seventy years ago [222], the discovery of the quasi-black body spectrum of the Cosmic Microwave

Background (CMB) [223, 224] paved the road for the modern formulation of the theory of Big Bang Nucleosynthesis (BBN) [225]. Indeed, thanks to the CMB, we know today that the SM particle species were in a thermal state during an epoch dominated by radiation. Extrapolating this cosmological picture back in time when the universe was not yet transparent to light, within the standard lore of Cosmology and of Particle Physics we can accurately predict [226, 227, 228, 229, 230, 231]:

1) The evolution of the number of relativistic degrees of freedom until recombination, $N_{\rm eff}$;

2) The cosmological abundance of light nuclides synthesized from protons and neutrons, as a function of the number density of baryons relative to photons, $\eta_B \equiv n_B/n_\gamma$.

Regarding *1)*, given the current knowledge of neutrino oscillations [232], $N_{\rm eff}$ is predicted in the SM via solving a set of integro-differential equations for the neutrino density matrix at finite temperature [233], yielding $N_{\rm eff}^{\rm SM} = 3.044$ with an error estimated to be below the level of per mil [234, 235, 236].

Concerning *2)*, a detailed analysis of CMB anisotropies in temperature and polarization currently constrains η_B with 1% accuracy or better [237], anchoring the primordial asymmetry between baryons and anti-baryons to be $\mathcal{O}(10^{-10})$ [238]. Assuming no large asymmetry in the lepton sector as well, see e.g. [239], standard BBN turns into an extremely predictive theory, often dubbed "parameter free".

On the observational side, multi-wavelength astronomical campaigns have been able to provide rich spectroscopic information about emission and absorption lines of gas clouds in metal-poor extra-galactic environments, see e.g. [240, 241, 242, 243], bringing us today to a percent-level determination of the abundance of primordial deuterium and helium-4. Given the predictions of the standard theory and the precision of those measurements, together

with the strong constraints on the thermal history provided by the CMB [15, 244], the study of the early universe around the BBN epoch offers unique insight on New Physics (NP) [245, 246, 247, 248, 249, 250, 251, 252, 253, 22]. Looking at the exciting prospects of next-gen CMB experiments [254, 255, 256], and at the expected future sensitivity in the field of observational astronomy [257, 258], it is therefore very timely to have tools at our disposal that allow for numerically efficient, yet precise computations that test the SM in the early universe, and that are flexible enough to broadly explore NP scenarios.

A few packages have already been developed to accurately investigate the BBN era. A publicly available version of the historical code of Ref. [259] (whose most up-to-date version is currently adopted by the PDG [14]) is described in [260]. At the same time, publicly released codes dedicated to state-of-the-art BBN analyses are also available; in particular:

- `PArthENoPE` [261, 262, 263] is a code originally written in FORTRAN 77 that in its latest re-incarnation also enjoys a graphical user interface; it offers a very efficient evaluation of BBN light-element abundances based on fitting formulae worked out for both weak rates and nuclear cross sections.

- `PRIMAT` [18, 264] is an user-friendly Mathematica package containing all the inputs and ingredients for an ab-initio computation of neutron freeze-out and of weak rates; moreover, it has tabulated the largest nuclear network at hand in order to track the abundance of heavy nuclides as well.

Both codes include a few built-in options to account for the study of some specific NP scenarios. `AlterBBN` [265, 266] is a C++ open-source software developed for broad investigation of Physics Beyond the SM (BSM) in the BBN era. However, while allowing for fast numerical evaluations, `AlterBBN` does not implement the same level of detail and accuracy in its computation of light primordial abundances compared to `PArthENoPE` or `PRIMAT`. In fact,

these two packages may currently represent the best tools to perform precision cosmological analyses [15, 267].

While powerful and flexible, these public codes nevertheless suffer from a few limitations and/or missing features. A precision tool for Cosmology, able to handle BSM Particle Physics should:

- Allow for the evaluation of the physics of the thermal bath in a fast but precise way, following, e.g., the approach highlighted in [268, 269, 253], and implemented in the standalone code `NUDEC_BSM`;

- Interconnect a first-principle computation of the thermal background with an ab-initio precise calculation of the neutron-to-proton ($n \leftrightarrow p$) conversion, as the one implemented in `PRIMAT` [18];

- Render easily accessible exploration of the impact of the input parameters characterizing the BBN era and the uncertainties in the set of thermonuclear rates on the basis of more model-dependent/more data-driven approaches available in literature, see [270, 271, 22];

- Adopt a user-friendly, modern programming language compatible with numerical efficiency of the computations, while smoothly interfacing with standard libraries for statistically advanced analyses like Monte Carlo (MC) ones, see e.g. [16, 272].

In this work, we introduce `PRyMordial`: A new public tool for the community of Particle Physics and Cosmology that precisely aims at filling in the above gaps for precision studies on the physics of the early universe both within and beyond the SM. The package is written and runs entirely with Python 3. Moreover, for the most advanced users, the resolution of the set of stiff differential equations for the BBN nuclear-reaction network can be further

optimized with the optional switch to some routines of the SciML kit [273], the open-source software for scientific machine learning in Julia.

Our article is organized as follows: In section 5.2 we present all the key ingredients of the physics implemented in `PRyMordial`; In section 5.3 we discuss in detail how `PRyMordial` is structured and we provide several examples on the usage of the code; In section 5.4 we comment on future directions for further development of `PRyMordial` along with possible interesting applications. We finally collect in Appendix 5A a set of instructions for the installation of the package and its dependencies.

5.2 Physics in `PRyMordial`

In this section we present the key equations present in `PRyMordial`, which stand out as a reference for the physics implemented within the code as well as representing a guideline regarding its use (see section 5.3). We organize the presentation in three distinct topics: the thermodynamics of the plasma; the weak rates for $n \leftrightarrow p$ conversion; and the set of thermonuclear rates for the key reactions responsible of the non-zero primordial abundance of deuterium, helium-3 and -4, and lithium-7.

5.2.1 Thermodynamics with Non-instantaneous Decoupling

The description of the thermal background during the BBN era in ΛCDM follows from an isotropic, homogeneous universe modelled by the Einstein field equation:

$$H^2 \equiv \left(\frac{d\log a}{dt}\right)^2 = \frac{8\pi}{3M_{\rm Pl}^2}\,\rho_{\rm tot}\ , \tag{5.1}$$

where H is the Hubble rate of space-time expansion, a the scale factor of the Friedmann–Lemaître–Robertson–Walker metric, $\rho_{\rm tot}$ the total energy density present in the universe, and $M_{\rm Pl} \equiv 1/\sqrt{G_{\rm N}}$, with $G_{\rm N}$ the Newton gravitational constant.

Within an axiomatic characterization of the early universe provided by *local thermodynamic equilibrium* [274, 275], SM species are described according to the spin-statistics theorem and the temperature T_γ of the thermal bath (provided chemical potentials μ can be neglected, i.e., $\mu/T_\gamma \ll 1$). Standard BBN takes place during radiation domination, and thus features contributions to $\rho_{\rm tot}$ largely from relativistic species, i.e. $\rho_{\rm tot} \simeq \rho_{\rm rad} \propto T_\gamma^4$. This observation dramatically simplifies the investigation of BBN, allowing one to decouple the study of the thermal background from the nucleon dynamics. Indeed, after the QCD crossover takes place [276] protons and neutrons are already non-relativistic, i.e. they are highly Boltzmann-suppressed well before the MeV scale temperatures characteristic of the BBN era.

Hence, for temperatures $T_\gamma \lesssim \mathcal{O}(10)$ MeV, one can accurately describe $\rho_{\rm tot}$ in the SM as a sum of just three contributions:

$$\rho_\gamma = \frac{\pi^2}{15}\, T_\gamma^4 \quad , \quad \rho_{e^\pm} = \frac{2}{\pi^2} T_\gamma^4 \int_{x_e}^{\infty} d\tilde{x}\, \frac{\tilde{x}^2 \sqrt{\tilde{x}^2 - x_e^2}}{\exp(\tilde{x}+1)} \quad , \quad \rho_{\nu,{\rm tot}} = 3 \times \frac{7\pi^2}{120}\, T_\nu^4 \ , \tag{5.2}$$

where $x_e \equiv m_e/T_\gamma$ and we distinguish the temperature of the electron-positron-photon system, T_γ, from that of neutrinos, T_ν.[1] Indeed, while the initial condition $T_\nu = T_\gamma$ must hold at early times for the two systems to be in thermal (more precisely, in chemical and kinetic) equilibrium, around the MeV scale neutrinos are expected to freeze out from the thermal bath as weakly-interacting relativistic species [278]. Neglecting tiny departures from a Fermi-Dirac distribution in ν phase space, one can study the evolution of the two systems

[1] While $T_e = T_\gamma$ follows from $e^\pm$ being tightly coupled to photons via fast QED processes, the approximation underlying T_ν, namely $T_{\nu_e} \simeq T_{\nu_\mu} \simeq T_{\nu_\tau}$, can be motivated by the active flavor mixing of ν oscillations at T_γ of few MeV [277].

according to the momentum-integrated Boltzmann equations:

$$\begin{aligned}(\rho'_\gamma + \rho'_{e^\pm})\,\frac{dT_\gamma}{dt} &= -4H\,\rho_\gamma - 3H(\rho_{e^\pm} + p_{e^\pm}) + \delta C_{e^\pm}\ , \\ \rho'_{\nu,\mathrm{tot}}\,\frac{dT_\nu}{dt} &= -4\,H\,\rho_{\nu,\mathrm{tot}} + \delta C_\nu\ ,\end{aligned} \tag{5.3}$$

with $' \equiv d/dT$, p the pressure density (equal to $\rho/3$ for a relativistic species), δC the (momentum-integrated) collision term, and where we have conveniently traded energy densities for temperatures in light of Eq. (5.2). Due to energy-momentum conservation, the sum over all δCs must vanish, so that one recovers the continuity equation for the total energy density of the universe:

$$\frac{d\rho_{\mathrm{tot}}}{dt} + 3H(\rho_{\mathrm{tot}} + p_{\mathrm{tot}}) = 0\ . \tag{5.4}$$

In the SM, where Eq. (5.3) holds, such a constraint implies: $\delta C_\nu = -\delta C_{e^\pm}$. The collision term δC_ν has been evaluated in [278] under Maxwell-Boltzmann approximation, nicely refined in [268, 269] taking into account relativistic corrections as well as finite mass effects from $m_e \neq 0$, and more recently re-computed independently in [253]. Including finite temperature QED corrections to the electromagnetic plasma [279], one can solve the system of coupled differential equations in Eq. (5.3), to find $T_\gamma(t)$, $T_\nu(t)$, and, as a byproduct, $T_\nu(T_\gamma)$.[2] Such a treatment naturally includes non-instantaneous decoupling effects, and allows one to perform a numerically fast, but accurate prediction of the effective number of relativistic degrees of freedom from first principles, yielding (in the SM) at $T_\gamma \ll$ MeV:

$$N_{\mathrm{eff}} \equiv \frac{8}{7}\left(\frac{11}{4}\right)^{4/3}\left(\frac{\rho_{\mathrm{rad}} - \rho_\gamma}{\rho_\gamma}\right) = 3.044\ , \tag{5.5}$$

[2] In the current version of `PRyMordial` we adopt the computation of δC_ν as well as the next-to-leading (NLO) QED corrections to the electromagnetic pressure of the plasma directly from the numerical results tabulated in `NUDEC_BSM` [269].

while also opening up novel explorations of BSM physics in the early universe [269, 252, 253].[3]

Based on these results, one can also easily evaluate the relic density of neutrinos (neglecting phase space spectral distortions). From the CMB we know the photon temperature today is $T_{\gamma,0} = 0.2348$ meV; plugging this value into the solution of Eq. (5.3) yields the temperature $T_{\nu,0} = 0.1682$ meV, corresponding to the cosmological abundance of SM neutrinos:

$$\begin{aligned} \Omega_\nu^{(\mathrm{rel})} h^2 &= \left(\frac{7\pi^2}{120}\, T_{\nu,0}^4\right) \Big/ \left(\frac{3}{8\pi}\frac{M_{\mathrm{Pl}}^2 H_0^2}{h^2}\right) = 5.70 \times 10^{-6} \ , \\ \Omega_\nu^{(\mathrm{nr})} h^2 &= \left(\frac{3}{2}\frac{\zeta(3)}{\pi^2} T_{\nu,0}^3 \sum_i m_{\nu_i}\right) \Big/ \left(\frac{3}{8\pi}\frac{M_{\mathrm{Pl}}^2 H_0^2}{h^2}\right) = \sum_i \frac{m_{\nu_i}}{93.03\,\mathrm{eV}} \ , \end{aligned} \tag{5.6}$$

which reproduces the relic neutrino abundance computed, e.g., in Ref. [280] to the per mil level.

In order to obtain $T_\gamma(t)$ and $T_\nu(t)$ from Eq. (5.3), we have made use both of Eq. (5.1) together with Eq. (5.2). At this point, to complete the study of the thermodynamic background, we must extract the scale factor a as a function of time t and temperature T_γ. This can be accomplished by applying (again) the notion of local thermodynamic equilibrium, which allows one to introduce the entropy density for each species i as: $s_i = (\rho_i + p_i - \mu_i\, n_i)/T_i$, where n_i is the number density of the species with associated chemical potential μ_i.

For negligible chemical potentials, the total entropy density of the universe s_{tot} per comoving volume must be conserved as a consequence of energy-momentum conservation, Eq. (5.4). Then, during radiation domination s_{tot} roughly scales as T_γ^3, underlying the approximate relation $a \propto 1/T_\gamma$. Nevertheless, even under the assumption of $\mu_i/T_i \ll 1$, the entropy of each species is generally not separately conserved due to heat exchanges related to the

[3]Eq. (5.3) can be easily generalized to include new sectors. This contrasts with typical existing BBN codes which compute the thermodynamic background by interpolating the tabulated result of the (numerically intensive) integro-differential Boltzmann equation, solved for the neutrino phase-space density in the SM.

interactions with other species. The Boltzmann equation for s_i generally follows (see, e.g., the discussion in Refs. [281, 18]):

$$\frac{ds_i}{dt} + 3Hs_i = \frac{\delta C_i}{T_i} - \frac{\mu_i}{T_i}\left(\frac{dn_i}{dt} + 3Hn_i\right) \ , \tag{5.7}$$

where the first collision term (divided by the temperature) is the one appearing in the Boltzmann equation for the density ρ_i, while the second collision term has been rewritten using the Boltzmann equation for the number density n_i.[4] In the SM, in the limit[5] $\mu_e/T_\gamma \ll 1$, we use Eq. (5.7) for the electromagnetic bath to pin down the relation between a and T_γ; with $\bar{s}_{\rm pl} \equiv (s_\gamma + s_{e^\pm})/T_\gamma^3$, we get:

$$\frac{1}{(T_\gamma a)^3}\frac{d\left(\bar{s}_{\rm pl} T_\gamma^3 a^3\right)}{d\ln a} = -\frac{\delta C_\nu}{HT_\gamma^4} \equiv -\mathcal{N}_\nu \quad \Leftrightarrow \quad a(T_\gamma) = a_0 \exp\left(-\int_{T_{\gamma,0}}^{T_\gamma} \frac{dT}{T}\frac{3\bar{s}_{\rm pl} + T\,\bar{s}'_{\rm pl}}{3\bar{s}_{\rm pl} + \mathcal{N}_\nu}\right) \ . \tag{5.8}$$

Knowing all the thermodynamical quantities as a function of T_γ in the integrand above, Eq. (5.8) allows one to extract $a(T_\gamma)$ up to the scale-factor value of today, a_0, customarily defined as 1. Note that for $T_\gamma \lesssim m_e$ one has $\bar{s}'_{\rm pl} = 0$, and taking the limit $\mathcal{N}_\nu \to 0$, the expected scaling set by $d(s_\gamma a^3)/dt = 0$ is easily recovered. The solution in Eq. (5.8) precisely tracks the relation between the scale factor and T_γ in the case of non-instantaneous decoupling of neutrinos. While in the SM these effects are tiny (since $\mathcal{N}_\nu/3 \ll \bar{s}_{\rm pl}$), they could become non-negligible in a BSM scenario.

It is worth noting that given $T_\gamma(t)$ from the solution of Eq. (5.3) and $a(T_\gamma)$ from Eq. (5.8), one obtains $a(t)$ as a byproduct, which allows to assess the evolution of the number density of baryons in t or T_γ during the BBN era, since by definition: $n_B \propto 1/a^3$.

[4] Notice that in absence of interactions for the species i, entropy conservation can be guaranteed either by a negligible chemical potential, $\mu_i \ll T_i$ or by number density conservation per comoving volume, $d(n_i a^3)/dt = 0$.

[5] $\mu_e/T_\gamma \ll 1$ is justified in the SM by $\eta_B \sim \mathcal{O}(10^{-10})$ and the condition of electric charge neutrality in the early universe.

5.2.2 Neutron Freeze Out beyond the Born Approximation

Shortly after hadrons form, neutrons and protons are non-relativistic species that do not contribute appreciably to the total energy budget stored in the thermal bath. Nevertheless, their abundance is eventually responsible for the tiny fraction of light primordial elements relative to hydrogen which are observable today in pristine astrophysical environments.

According to local thermodynamic equilibrium, the relative number density of nucleons is initially given by the Maxwell-Boltzmann distribution:

$$\left(\frac{n_{\rm n}}{n_{\rm p}}\right)\Big|_{T_\gamma \gg \rm MeV} = \left(\frac{m_{\rm n}}{m_{\rm p}}\right)^{3/2} \exp\left(-\frac{\mathcal{Q}}{T_\gamma} - \frac{\mu_{\mathcal{Q}}}{T_\nu}\right) , \tag{5.9}$$

where $\mathcal{Q} = m_{\rm n} - m_{\rm p}$, $\mu_{\mathcal{Q}} = \mu_{\rm n} - \mu_{\rm p}$, $m_{\rm n,p}$ and $\mu_{\rm n,p}$ are the mass and chemical potential of neutrons and protons. For clarity, we have used $T_\nu = T_\gamma$ (valid for temperatures well above MeV) in the $\mathcal{Q}$ term, but retain T_ν explicitly in the $\mu_{\mathcal{Q}}$ term. Assuming $\mu_{\rm n} \simeq \mu_{\rm p}$ (e.g. a negligible contribution from lepton chemical potentials), Eq. (5.9) implies that at equilibrium $n_{\rm n} \simeq n_{\rm p}$. Indeed, fast electroweak processes efficiently convert $n \leftrightarrow p$:

$$\begin{aligned}
\Gamma_{\rm n\to p} &\equiv \Gamma(n\,e^+ \to p\,\bar\nu) + \Gamma(n\,\bar\nu \to p\,e^-) + \Gamma(n \to p\,e^-\,\bar\nu) \gg H\,, \\
\Gamma_{\rm p\to n} &\equiv \Gamma(p\,e^- \to n\,\bar\nu) + \Gamma(p\,\bar\nu \to n\,e^+) + \Gamma(p\,e^-\,\bar\nu \to n) \gg H\,,
\end{aligned}$$

and govern the Boltzmann equations for the nucleon yields $Y_{\rm n,p} \equiv n_{\rm n,p}\,/\,n_B = n_{\rm n,p}\,/\,(n_{\rm n}+n_{\rm p})$:

$$\begin{aligned}
\frac{dY_{\rm n}}{dt} &= \Gamma_{\rm p\to n}\,Y_{\rm p} - \Gamma_{\rm n\to p}\,Y_{\rm n}\ , \\
\frac{dY_{\rm p}}{dt} &= \Gamma_{\rm n\to p}\,Y_{\rm n} - \Gamma_{\rm p\to n}\,Y_{\rm p}\ ,
\end{aligned} \tag{5.10}$$

whose equilibrium solutions: $Y_{\rm n} = 1 - Y_{\rm p} = \Gamma_{\rm p\to n}/(\Gamma_{\rm p\to n} + \Gamma_{\rm n\to p}) \simeq 1/2$, are in agreement with Eq. (5.9). These reactions guarantee chemical equilibrium among the involved species, implying $\mu_{\mathcal{Q}} \simeq -\mu_\nu$. Eq. (5.9) thus demonstrates that a primordial non-zero lepton asymmetry in the neutrino sector [282, 283] can impact the initial conditions for BBN by altering the neutron-to-proton ratio, with notable cosmological consequences [22, 284].

At temperatures close to neutrino decoupling, $n \leftrightarrow p$ conversion falls out of equilibrium, freezing out the neutron-to-proton ratio to $\sim 1/6$ (in the SM), up to finite neutron lifetime effects [274, 275]. The weak rates for neutron freeze out require the evaluation of an involved multi-dimensional phase-space integral: e.g. for $n\, e^+ \to p\, \bar\nu$ (and similarly for the others) [285]:

$$Y_{\rm n}\, \Gamma(n\, e^+ \to p\, \bar\nu) = \frac{16\pi^4}{n_B} \int d\Pi_{\rm n} d\Pi_e d\Pi_{\rm p} d\Pi_\nu\, \delta^{(4)}(P_{\rm n} + P_e - P_{\rm p} - P_\nu)\, |\mathcal{M}|^2\, f_{\rm n} f_e (1 - f_{\rm p})(1 - f_\nu), \tag{5.11}$$

where $d\Pi_i$ and P_i are the Lorentz-invariant phase-space element and 4-momentum of the particle i, f_i is the relativistic thermal distribution of the species i in the rest frame of the thermal bath, and $\mathcal{M}$ is the full matrix element of the process summed over initial and final spins. The latter can be computed from the weak effective theory for β decay [286]:

$$\mathcal{L}_{\rm F} = -\frac{2G_{\rm F}}{\sqrt{2}}\, V_{\rm ud}\; \bar\nu(x)\, \gamma_\mu\, e_L(x) \left\{ \bar n(x) \gamma^\mu (1 - g_{\rm A}\, \gamma_5) p(x) + \frac{\kappa}{2m_{\rm N}} \partial_\nu \left[\bar n(x)\, \sigma^{\mu\nu}\, p(x) \right] \right\} + h.c.\,, \tag{5.12}$$

where $G_{\rm F}$ is the Fermi constant [14], $V_{\rm ud}$ corresponds to the Cabibbo angle [287], $g_{\rm A}$ and κ are the axial-current and weak-magnetism constant of the nucleon of mass $m_{\rm N}$ [288], and $\sigma_{\mu\nu} \equiv i\, (\gamma_\mu \gamma_\nu - \gamma_\nu \gamma_\mu)/2$. The computation of $|\mathcal{M}|^2$ can be found in detail in Appendix B of Ref. [18] (see also [289, 285]).

While expressions like Eq. (5.11) can be reduced to a five-dimensional integral in phase space by exploiting the symmetries of the problem, a dramatic simplification is obtained in the limit of infinite nucleon-mass at fixed $\mathcal{Q}$ [289, 285]. This is the so-called Born approximation, in which the kinetic energy of the 'infinitely' heavy neutrons and protons may be neglected, leading to the simplification: $|\mathcal{M}|^2 = 32\, G_{\rm F}^2 V_{\rm ud}^2 (1+3g_{\rm A}^2) E_e E_\nu E_{\rm p} E_{\rm n}$. In that limit the $n \leftrightarrow p$ rates read:

$$\begin{aligned}
\Gamma^{\infty}_{\rm n\to p} &= \widetilde{G}_{\rm F}^2 \int_0^\infty dE_e\, E_e \sqrt{E_e^2 - m_e^2}\, (E_\nu^-)^2 \left[f_\nu(E_\nu^-) f_e(-E_e) + f_\nu(-E_\nu^-) f_e(E_e) \right] \,, \\
\Gamma^{\infty}_{\rm p\to n} &= \widetilde{G}_{\rm F}^2 \int_0^\infty dE_e\, E_e \sqrt{E_e^2 - m_e^2}\, (E_\nu^+)^2 \left[f_\nu(E_\nu^+) f_e(-E_e) + f_\nu(-E_\nu^+) f_e(E_e) \right] \,,
\end{aligned} \tag{5.13}$$

where $\widetilde{G}_{\rm F} \equiv G_{\rm F} V_{\rm ud} \sqrt{(1+3g_{\rm A}^2)/(2\pi^3)}$ and $E_\nu^\pm = E_e \pm \mathcal{Q}$. The outcome of Eq. (5.13) are rates that generally depend on both background temperatures and chemical potentials (i.e. T_γ, T_ν and μ_ν). For $T_\nu = T_\gamma$ (and negligible chemical potentials) detailed balance follows as: $\Gamma^{\infty}_{\rm p\to n}/\Gamma^{\infty}_{\rm n\to p} = \exp(-\mathcal{Q}/T_\gamma)$. The dimensionful factor $\widetilde{G}_{\rm F}$ depends on $V_{\rm ud}$, $g_{\rm A}$, and $G_{\rm F}$, whose value is precisely determined by the muon lifetime. However, this factor is often more conveniently extracted from neutron decay in the vacuum, since in the SM:

$$\tau_{\rm n}^{-1} = \widetilde{G}_{\rm F}^2\, m_e^5\, \mathcal{F}_{\rm n} \,, \tag{5.14}$$

where $\mathcal{F}_{\rm n}$ incorporates a phase-space statistical factor for the neutron decay at zero temperature [290] plus electroweak radiative corrections [291]. For a precise calculation of $\mathcal{F}_{\rm n}$, see the very recent reassessment in Ref. [292] and references therein. This approach allows one to trade the combination $V_{ud}^2(1+3g_A^2)$ for the measured τ_n.[6] Using Eq. (5.14), in `PRyMordial` one can choose to adopt either a normalization of the weak rates based on the determination

[6] Any treatment must confront both the *neutron lifetime puzzle*, i.e. the tension between "bottle" [293] and "beam" [294] measurements of $\tau_{\rm n}$, see, e.g., [295]; and the *Cabibbo angle anomaly* [296], i.e. the extraction of $V_{\rm ud}$ from super-allowed β decays and $V_{\rm us}$ from semi-leptonic decays versus unitarity in the Cabibbo-Kobayashi-Maskawa matrix [287].

of the neutron lifetime, or one involving the knowledge of the modified Fermi constant $\widetilde{G}_{\rm F}$.

In the SM the Born approximation predicts a neutron freeze-out temperature of slightly below 1 MeV. At smaller temperatures, the neutron-to-proton ratio is still affected by β decay until the universe cools down sufficiently enough to preclude photo-dissociation of deuterium: for a binding energy $B_{\rm D} = 2.2$ MeV, this happens at temperatures around $B_{\rm D}/\log(1/\eta_B) \sim 0.1$ MeV [274, 275]. At that point, virtually all of the neutrons experience two-body nuclear reactions, ultimately resulting in their binding in helium-4, the most stable light element. As a result, the uncertainty on the Born-level theory prediction for helium-4 is only a few % (see Table 5 in [18]).

That said, the present percent-level inference of primordial helium-4 and deuterium [14] and the sub-percent target of future observational campaigns [257] demand the following refinements to Eq. (5.13):

- QED radiative corrections (in the vacuum) to the $n \leftrightarrow p$ amplitudes of order $\mathcal{O}(\alpha_{\rm em})$ via virtual- and real-photon emission [297, 298, 299, 300] must be computed;
- Finite nucleon-mass effects and non-zero weak magnetism, which induce relative shifts in the weak rates of $\Delta\Gamma/\Gamma \sim \mathcal{O}(10^{-2})$ [289, 285], must be taken into account;
- Finite-temperature effects [299, 301] must be evaluated for sub-percent accuracy.

`PRyMordial` implements all of these corrections, following the treatment in `PRIMAT` (see Appendix B of [18]), where particular care was taken to attempt to combine several existing state-of-the-art recipes for electroweak rates beyond the Born approximation.

It is worth noticing that in the context of the SM, the corrections to the Born rates due to the incomplete neutrino decoupling are only marginal [302, 303]. Nevertheless, NP could dramatically alter $T_\nu(T_\gamma)$, $a(T_\gamma)$ and $a(t)$, and the departure from the standard value for the

weak rates can impact the final BBN abundances in a non-negligible way [250, 252]. As a result, the approach undertaken in subsection 5.2.1 is particularly useful not only for the study of neutrino decoupling, but also for a careful assessment of the neutron-to-proton ratio in BSM scenarios.

5.2.3 BBN Thermonuclear Reactions

Local thermodynamical equilibrium implies that at temperatures above neutron decoupling, a nuclear species i of atomic number Z_i, mass number A_i, spin s_i, and binding energy B_i follows a Boltzmann distribution with internal degrees of freedom: $g_i = 2s_i + 1$; mass: $m_i = Z_i m_{\rm p} + (A_i - Z_i) m_{\rm n} - B_i$; and chemical potential: $\mu_i = Z_i \mu_{\rm p} + (A_i - Z_i)\mu_{\rm n}$. In terms of the yield $Y_i \equiv n_i/n_B$, this equilibrium distribution reads:

$$Y_i\big|_{T_\gamma \gtrsim \rm MeV} = g_i \, 2^{(3A_i-5)/2} \, \pi^{(1-A_i)/2} \, \left(\zeta(3)\,\eta_B\right)^{A_i-1} \left(\frac{m_i \, T_\gamma^{A_i-1}}{m_{\rm p}^{Z_i} m_{\rm n}^{A_i-Z_i}}\right)^{3/2} Y_{\rm p}^{Z_i} Y_{\rm n}^{A_i-Z_i} \exp\left(B_i/T_\gamma\right) \, , \tag{5.15}$$

where we made use of the relation: $n_B/\eta_B = 3\,\zeta(3)\,T_\gamma^3/(2\pi^2)$. This expression holds for the nucleons ($A_{\rm N} = 1$, $B_{\rm N} = 0$) themselves, and is consistent with Eq. (5.9). Importantly, it offers another handle on the estimate for the start of nucleosynthesis as the time in which the relative abundance of neutrons after freeze out becomes comparable to deuterium as dictated by Eq. (5.15), and pointing again to a temperature of about 0.1 MeV.

Starting from the initial conditions, abundances are determined by a network of Boltzmann equations that generalize Eq. (5.10) (see, e.g., Refs. [304, 305]) to include the relevant nuclei:

$$\frac{dY_i}{dt} = \sum_R \mathcal{S}_{i,R} \left[\Gamma^{(R)}_{\dots \to i \dots} \times \prod_j \left(\frac{Y_j^{\mathcal{S}_{j,R}}}{\mathcal{S}_{j,R}!}\right) - \Gamma^{(R)}_{i \dots \to \dots} \times \prod_k \left(\frac{Y_k^{\mathcal{S}_{k,R}}}{\mathcal{S}_{k,R}!}\right) \right] , \tag{5.16}$$

where the sum R is performed over all reactions involving the nuclear species i; $\mathcal{S}_{i,R}$ is the stoichiometric coefficient for the species i in the nuclear reaction R; and the products j and k run over all of the initial and final states of the reaction with nuclear rate $\Gamma^{(R)}_{\cdots\to i\,\cdots}$ or $\Gamma^{(R)}_{i\,\cdots\to\cdots}$.

Given the range of energies characterizing the BBN era, the nuclear reaction rates of interest can be measured in the laboratory, and are often tabulated as $\widetilde{\Gamma}_{i\ldots l\to j\ldots m} \equiv N_A^{\mathcal{S}_i\ldots\mathcal{S}_l-1}\langle\sigma_{i\ldots l\to j\ldots m}\,v\rangle$ [306], where N_A is Avogadro's number (typically expressed in units of mol^{-1}), and the velocity averaged cross section is obtained by weighting the appropriate cross section by the Maxwell-Boltzmann velocity distribution for the non-relativistic species (see e.g. Ref. [307] for a detailed description). By definition, for a given number-density rate $\langle\sigma^{(R)}_{i\cdots\to\cdots}v\rangle$, the corresponding abundance rate $\Gamma^{(R)}_{i\cdots\to\cdots}$ is:

$$\Gamma_{i\ldots l\to j\ldots m} = n_B^{\mathcal{S}_i\ldots\mathcal{S}_l-1}\langle\sigma_{i\ldots l\to j\ldots m}\,v\rangle = (n_B/N_A)^{\mathcal{S}_i\ldots\mathcal{S}_l-1}\,\widetilde{\Gamma}_{i\ldots l\to j\ldots m}\ . \tag{5.17}$$

A priori, Eq. (5.16) includes the rates of both forward and reverse reactions in the evolution of the abundance of the nuclear species i. Nevertheless detailed balance implies

$$\left(\frac{Y_j^{\mathcal{S}_j}\ldots Y_m^{\mathcal{S}_m}}{Y_i^{\mathcal{S}_i}\ldots Y_l^{\mathcal{S}_l}}\right)\Bigg|_{T_\gamma\gtrsim\mathrm{MeV}} = \frac{\langle\sigma_{i\ldots l\to j\ldots m}v\rangle/(\mathcal{S}_i!\ldots\mathcal{S}_l!)}{\langle\sigma_{j\ldots m\to i\ldots l}v\rangle/(\mathcal{S}_j!\ldots\mathcal{S}_m!)}\ , \tag{5.18}$$

since local thermodynamical equilibrium ensures that the forward and reverse reactions should balance. Thus, it is easy to evaluate the reverse reaction rates given the forward ones. It is customary to parameterize the relationship as:

$$\langle\sigma_{j\ldots m\to i\ldots l}v\rangle = \alpha_R\ T_9^{\beta_R}\ \exp(\gamma_R/T_9)\,\langle\sigma_{i\ldots l\to j\ldots m}v\rangle\ \ ,\ \text{with:}\ T_9\equiv T_\gamma/(10^9\,\mathrm{K})\,, \tag{5.19}$$

where the constants α_R, β_R, and γ_R for a given process R from e.g. the up-to-date nuclear database of Ref. [308] via Eq. (5.15).

`PRyMordial` solves the general system of equations Eq. (5.16) following the strategy of

Ref. [18] which conveniently breaks nucleosynthesis into three steps:

1) We analyze $n \leftrightarrow p$ conversion by solving Eq. (5.10) from an initial temperature of $\mathcal{O}(10)$ MeV (and initial conditions from Eq. (5.9)) down to standard neutron freeze out, around MeV;

2) We use the values of $Y_{\rm n,p}$ obtained from *1)* together with Eq. (5.15) and evolve with a network comprised of the 18 key thermonuclear rates for the abundance of n, p together with all of the nuclides up to $A = 8$ and $Z = 5$[7] down to the temperature where deuterium photo-dissociation becomes inefficient, around 0.1 MeV;

3) We further evolve the network with the full set of thermonuclear processes and with initial conditions given by the nuclide yields obtained in step *2)*, evolving the abundances of the aforementioned nuclides down to $\mathcal{O}$(keV) (i.e., well below $e^{\pm}$ annihilation), when BBN is over.

The output of Step *3)* is the abundances of the light-element originating from BBN. To compare with data, it is customary to quote helium-4 in terms of the primordial mass fraction:[8]

$$Y_P \equiv 4 \times Y_{^4\rm He} \simeq \rho_{^4\rm He}/\rho_B \,. \tag{5.20}$$

The other primordial elements under the lamppost of astrophysical observations are deuterium, helium-3 and lithium-7 (see, e.g., [231] for a recent report on the status of these measurements), which are usually quoted in terms of the relative number densities with

[7] In the current version of `PRyMordial` we include up to boron-8 in the nuclear chains, which is sufficient for an accurate prediction of lithium-7, likely the heaviest nuclide of interest when confronting BBN with observations [4]. For this purpose, the largest implemented set of thermonuclear rates comprises 63 reactions, see Appendix 5B.

[8] Notice that this definition differs at the sub-percent level from the helium mass fraction adopted in the context of the CMB [15]: $Y_P^{\rm CMB} \equiv (m_{^4\rm He}/4)\, Y_P/[(m_{^4\rm He}/4) Y_P + m_{\rm H}\,(1 - Y_P)]$, with $m_{\rm H,^4He}$ the atomic mass of hydrogen and helium.

respect to hydrogen:

$$i/\mathrm{H} \equiv Y_i/Y_\mathrm{p} = n_i/n_\mathrm{H} \quad , \text{ where } i = \mathrm{D},\ {}^3\mathrm{He},\ {}^7\mathrm{Li}\,. \tag{5.21}$$

Notice that the final yield of primordial helium-3 receives a contribution from unstable species such as tritium; likewise, the final amount of lithium-7 includes the decay of beryllium-7.

The literature contains several publicly accessible compilations of the thermonuclear rates relevant for BBN. It is important to note that there are several different parameterizations of these rates adopted in BBN studies, and they differ not only with respect to the theoretical approach, but also with respect to the measured nuclear reaction data included in fitting them. To highlight a few of the more important approaches:

- The NACRE II database [309] collects an extended evaluation of reaction rates of charged-particle induced reactions on target nuclides with mass number $A < 16$, adopting the so-called potential model [306] to describe nuclear cross sections in the energy range of interest.

- `PRIMAT` tabulates an extensive catalogue (comprising more than 400 reactions), characterized by several nuclear cross sections evaluated via refined statistical analyses within R-matrix theory [310, 311, 312, 313] or computed using dedicated numerical tools, e.g., the TALYS code [314].

- `PArthENoPE` implements semi-analytic expressions resulting from polynomial fits to nuclear data including theory modeling of screening and thermal effects [307, 315]; data-oriented analyses relevant for BBN rates can be also found in the work of Refs. [316, 317].

If one limits the scope to precise predictions of the helium-4 and deuterium abundances, the relevant portion of the nuclear network simplifies considerably, contracting to $\mathcal{O}(10)$

processes [318]. Thus, `PRyMordial` offers the option of restricting the BBN analysis to a small network of 12 key reactions [319], implemented according to two different sets of thermonuclear rates: the first is largely based on the NACRE II compilation, whereas the second is based on the tabulated rates in `PRIMAT`. These two sets differ marginally in their predictions for helium-4, but lead to relevant differences in the prediction for deuterium, as discussed at length in Ref. [270], after the important measurement carried out by the LUNA collaboration [320].[9] For the most precise prediction of lithium-7, `PRyMordial` offers the possibility to solve a nuclear network including the 51 additional reactions listed in Appendix 5B, by adopting part of the network in Ref. [314] included in the `PRIMAT` database.

`PRyMordial` handles uncertainties on the tabulated thermonuclear rates $\widetilde{\Gamma}^{(R)}$ by providing (for each forward[10] nuclear reaction) a set of median values, $\langle\widetilde{\Gamma}^{(R)}\rangle$ together with an uncertainty factor $\Delta\widetilde{\Gamma}^{(R)}$, corresponding to a sample of temperatures. Following the method outlined in Refs. [321, 322], to perform a MC analysis with `PRyMordial` one should treat the provided thermonuclear rates as log-normal distributed, implying that for each nuclear process R a random realization of the thermonuclear rate will be:

$$\log\widetilde{\Gamma}^{(R)} = \log\langle\widetilde{\Gamma}^{(R)}\rangle + p^{(R)}\log\Delta\widetilde{\Gamma}^{(R)} \ , \tag{5.22}$$

where $p^{(R)}$ is a temperature-independent coefficient following a normal distribution [323]. Hence, in order to properly take into account the uncertainties of the thermonuclear rates in a MC analysis of BBN, one should independently vary the nuisance parameters $p^{(R)}$ for all the reactions R included in the study, see, e.g., the work carried out in Ref. [22] and the MC examples presented in section 5.3.

[9] This fact has been more quantitatively acknowledged in Ref. [22] which used a beta version of `PRyMordial`.

[10] The corresponding reverse reactions are obtained via Eq. (5.19) from the interpolated forward rates.

5.3 How to Use PRyMordial

In this section we provide some example code that demonstrates the use of PRyMordial. We start by detailing the modules of the code including their inputs and key parameters. We show how to implement a state-of-the-art analysis of the BBN era within the SM. Finally, we provide a concise description on how to use the code for the study of NP, and discuss how to implement and analyze generic BSM scenarios.

5.3.1 Structure of the Code and Hello, World!

PRyMordial is a numerical tool dedicated to efficiently and accurately evaluate in the SM and beyond all the key observables related to the BBN era, discussed in section 5.2, namely:

- The number of effective relativistic degrees of freedom, $N_{\rm eff}$, Eq. (5.5) ;
- The cosmic neutrino abundance today, $\Omega_\nu h^2$, Eq. (5.6) ;
- The helium-4 mass fraction (both for BBN and CMB), Y_P, Eq. (5.20) ;
- The relative number density of deuterium, helium-3 and lithium-7, Eq. (5.21) .

In contrast to other BBN codes available, PRyMordial begins by computing the thermal background from first principles. As a byproduct of the determination of $N_{\rm eff}$ and $\Omega_\nu h^2$, the relationship between time, scale factor and temperature of relativistic species is determined precisely, including effects from non-instantaneous decoupling within and beyond the Standard Model.

Next, PRyMordial evaluates the weak rates for neutron freeze out via a state-of-the-art implementation that includes nucleon finite-mass effects, one-loop QED corrections and finite-temperature effects. While the latter are typically negligible within current observational

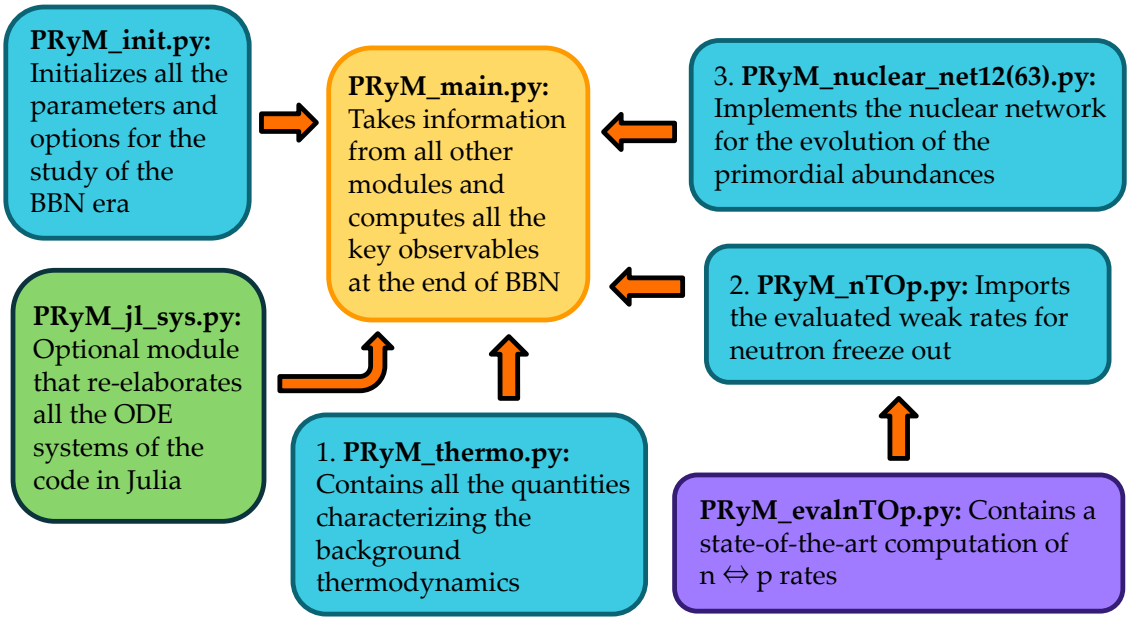

Figure 5.1: `PRyMordial` in a nutshell: Schematic of the modules making it up and their inter-relations.

precision and can be conveniently stored between runs, the remainder are generally recomputed for each iteration of a generic BBN analysis.

Finally, `PRyMordial` solves a network of nuclide reactions for their yields within three different physical regimes: *i)* a high-temperature era in which one can restrict the study to nucleons with an initial temperature of $\mathcal{O}(10)$ MeV and a final temperature close to neutrino decoupling; *ii)* a mid-temperature era from $\mathcal{O}(1)$ MeV down to $\mathcal{O}(0.1)$ MeV, during which photo-dissociation of nuclear bound states is relevant; *iii)* and a low temperature era starting at $\mathcal{O}(0.1)$ MeV during which `PRyMordial` follows all of the nuclear species of interest, which ends at a temperature well below $e^{\pm}$ heating of the thermal bath, i.e. down to $\mathcal{O}(1)$ keV. Local thermal equilibrium sets the initial nuclide abundances and detailed balance determines all of the reverse reactions included in the chosen set of nuclear reactions. These three regimes are matched such that the solution for each one provides the initial conditions for the successive period.

`PRyMordial` is a Python package with optional dependencies which allow more advanced users to speed up execution by exploiting the Julia programming language. The recommended libraries and general requirements are tabulated in Appendix 5A. As highlighted in Figure 5.1, `PRyMordial` is organized in five primary modules:

- `PRyM_init.py` is an initialization module where physical constants and Boolean flags for user-controlled options are defined; in particular, three main blocks for input parameters are found:
  - ⋆ Fundamental constants, masses (in natural units), initialized according to the PDG [14];[11]
  - ⋆ Additional parameters needed for the evaluation of the $n \leftrightarrow p$ rates beyond the Born level;
  - ⋆ Cosmological inputs including the CMB temperature and the abundance of baryonic matter [15].

  Boolean flags allow the user to switch on/off the following options:
  - ◦ `verbose_flag`: Allows the user to run the code with all of the internal messages enabled;
  - ◦ `numba_flag`: If `True`, speeds up some numerical integrations, if the `Numba` library is installed;
  - ◦ `numdiff_flag`: If `True`, performs numerical derivatives using `Numdifftools` library;
  - ◦ `aTid_flag`: Controls the inclusion of incomplete-decoupling effects in the determination of the scale factor as a function of time and temperature;

[11] For the electroweak sector we adopt $\{\alpha_{\rm em}, G_{\rm F}, M_{\rm Z}\}$ as inputs and derive the rest via tree-level relations.

- `compute_bckg_flag`: If `True`, recomputes the thermodynamical background as presented in subsection 5.2.1 (via `save_bckg_flag` the outcome can be stored in a file for future runs);
- `NP_thermo_flag`: If `True`, includes the contribution(s) of new (interacting) species to the dynamics of the thermal bath (by default, one must also provide a NP temperature);
- `NP_nu_flag`: If `True`, includes new species thermalized with the neutrino bath;
- `NP_e_flag`: If `True`, includes new species thermalized with the plasma;
- `compute_nTOp_flag`: If `True`, recomputes weak rates beyond Born as discussed in subsection 5.2.2 (via `save_nTOp_flag` the outcome can be stored in a file for future runs);
- `nTOpBorn_flag`: If `True`, adopts the Born approximation for the neutron freeze out;
- `compute_nTOp_thermal_flag`: If `True`, recomputes thermal corrections to $n \leftrightarrow p$ rates via `Vegas` (since this is numerically intensive, we recommend `save_nTOp_thermal_flag = True`);
- `tau_n_flag`: If `True`, uses the neutron lifetime to normalize the weak rates, see subsection 5.2.2;
- `NP_nTOp_flag`: If `True`, includes NP affecting $n \leftrightarrow p$ rates in units of the Born rates;
- `smallnet_flag`: If `True`, restricts the nuclear network to the set of 12 key nuclear processes collected in Table 5.1 of Appendix 5B;
- `nacreii_flag`: If `True`, the key nuclear rates adopted in `PRyMordial` will be mostly based on NACRE II compilation rather than those of `PRIMAT`, see subsection 5.2.3;

- `NP_nuclear_flag`: If `True`, shifts the nuclear rates due to NP in units of the standard ones;
- `julia_flag`: If `True`, solves all of the systems of ordinary differential equations using routines in the SciML kit [273] developed for the Julia programming language; the optional dependencies described in Appendix 5A are then required.

This module also loads the tabulated nuclear rates (as well as the coefficients of Eq. (5.19)).

- `PRyM_thermo.py` is the module where all of the thermodynamical quantities for the species contributing to the expansion of the universe during radiation domination are defined, together with all the collision terms that enter in Eq. (5.3) and Eq. (5.7).

- `PRyM_nTOp.py` is the module which imports the weak rates for $n \leftrightarrow p$ conversion described in subsection 5.2.2, either relying on the additional module `PRyM_evalnTOp.py` – where the actual computation of the rates is performed from scratch – or by loading pre-stored rates from a file.

- `PRyM_nuclear_net12.py` and `PRyM_nuclear_net63.py` are the modules which set up the systems of ordinary differential equations – see Eq. (5.16) – involving the nuclear rates loaded by `PRyM_init.py`. The Boolean flag `smallnet_flag` controls whether `PRyMordial` sets up and solves the smaller network of 12 key reactions or the full set of 63 nuclear processes.

- `PRyM_main.py` is the main module, which calls the other modules to solve for the thermodynamical background, compute $N_{\rm eff}$ and the cosmic neutrino abundance, and solve for the nuclide yields. It contains the Python class `PRyMclass()`, designated to return all the cosmological observables implemented in the package.

- `PRyM_jl_sys.py` is an optional module which allows the user to solve all of the systems of ordinary differential equations in `PRyM_main.py` by taking advantage of the

numerically efficient routines that are part of the SciML kit [273] developed in Julia. In some cases, this significantly speed up the execution time of the code (to a degree depending on both the adopted precision of the computation as well as the specific choice of differential-equation solver).

After downloading `PRyMordial`, the code can be used immediately. To run a `Hello, World!`-style example, the user would enter the package folder, start an interactive Python session, and type:

```
# Hello, World! of PRyMordial
import PRyM.PRyM_main as PRyMmain
res = PRyMmain.PRyMclass().PRyMresults()
```

which executes a BBN computation and fills the array `res` with the values of:

$$\left[\, N_{\rm eff}, \Omega_\nu h^2 \times 10^6 \ \text{(rel)}, \sum m_\nu/\Omega_\nu h^2 [\text{eV}], Y_P^{(\text{CMB})}, Y_P^{(\text{BBN})}, D/H \times 10^5, {}^3\text{He/H} \times 10^5, {}^7\text{Li/H} \times 10^{10} \,\right]$$

Located in the same folder are:

- a folder `PRyM` in which all of the modules described above reside;
- a folder `PRyMrates` in which all the essential thermal, weak and nuclear rates are present, and where new evaluations of them can be stored;
- a script named `runPryM_julia.py` that provides a simple example for the user as to how to use the package, with execution-time benchmarking in both standard and Julia modes.

In the following subsections we present more sophisticated examples illustrating some of `PRyMordial`'s capabilities.

5.3.2 SM examples: the PDG Plot and Monte Carlo Analysis

In an interactive session in Python, any default value in `PRyM_init.py` can be changed using the syntax:

```
import PRyM.PRyM_init as PRyMini
# New assignment x for parameter X
PRyMini.X = x
```

This includes the Boolean flags listed in the previous subsection. Hence – to perform a run with: *i)* the computation of the thermal background from scratch, including non-instantaneous decoupling effects; *ii)* the ab-initio evaluation of the weak rates for neutron freeze out; and *iii)* the inclusion of key nuclear processes based on the tabulated rates of the NACRE II compilation – one should type:

```
import PRyM.PRyM_init as PRyMini
# Include incomplete decoupling in a(T)
aTid_flag = True
# Recompute the background from scratch
PRyMini.compute_bckg_flag = True
# Save the background in PRyMrates/thermo
PRyMini.save_bckg_flag = True
# Recompute n <--> p rates from scratch
PRyMini.compute_nTOp_flag = True
# Save n <--> p rates in PRyMrates/nTOp
PRyMini.save_nTOp_flag = True
# Include only key rates in nuclear network
PRyMini.smallnet_flag = True
```

```
# NACRE II compilation for key rates
PRyMini.nacreii_flag = True
# Compute PRyMordial observables
import PRyM.PRyM_main as PRyMmain
res = PRyMmain.PRyMclass().PRyMresults()
```

The array `res` is assigned the same values as in the `Hello, World!` example, above. This code also stores the results for the thermal background and $n \leftrightarrow p$ rates for future runs. Consequently, a subsequent call with the same setup can be made faster:

```
import PRyM.PRyM_init as PRyMini
# No need to recompute background since stored
PRyMini.compute_bckg_flag = False
PRyMini.save_bckg_flag = False
# No need to recompute n <--> p  rates as well
PRyMini.compute_nTOp_flag = False
PRyMini.save_nTOp_flag = False
# Compute PRyMordial observables: now faster!
import PRyM.PRyM_main as PRyMmain
res = PRyMmain.PRyMclass().PRyMresults()
```

While it may be necessary in general to recompute the thermal background and/or the rates for neutron freeze out, there are cases for which storing the outcome of these computations can be computationally advantageous. An example is the classic PDG review BBN plot of the primordial abundances as a function of the baryon-to-photon ratio η_B [14]. Once thermal background and weak rates have been stored, the behaviour of the abundances in the PDG Figure 24.1 can be reproduced with `PRyMordial`:

```
# PDG plot
npoints = 50
import numpy as np
etabvec = np.logspace(-10,-9,npoints)
# Initialization of array of observables
YP_vec, DoH_vec, He3oH_vec, Li7oH_vec = np.zeros((4,npoints))
for i in range(npoints):
    # Update value of baryon-to-photon ratio and store new obs
    PRyMini.eta0b = etabvec[i]
    YP_vec[i], DoH_vec[i], He3oH_vec[i], Li7oH_vec[i] =
    PRyMmain.PRyMclass().PRyMresults()[4:8]
```

The outcome of this code is illustrated in Figure 5.2, which adopts the largest nuclear network for the most accurate prediction of the relative abundance of lithium-7. It is worth noting that the BBN prediction for deuterium matches observations of quasar absorption systems, and is also in line with the cosmological abundance of baryons independently determined from the CMB (without a BBN prior). As pointed out in Ref. [270] and further scrutinized in Ref. [22], this test of concordance would fail if the `PRIMAT` rates were to be adopted, i.e. `nacreii_flag = False`.

To perform a Monte Carlo analysis of the SM predictions taking into account uncertainties (similar to the one presented in Ref. [22]):

```
# SM MC run
num_it = 10000 # number of iterations
import numpy as np
Yp_vec, YDoH_vec, YHe3oH_vec, YLi7oH_vec = np.zeros((4,num_it))
# Import PRyM modules
```

```
import PRyM.PRyM_init as PRyMini
import PRyM.PRyM_main as PRyMmain
# Baryon eta from Planck 18 (no BBN prior)
mean_eta0b = PRyMini.eta0b
std_Omegabh2 = 2*1.e-4
std_eta0b = PRyMini.Omegabh2_to_eta0b*std_Omegabh2
# Neutron lifetime from PDG 2023
mean_tau_n = PRyMini.tau_n
std_tau_n = 0.5

# Compute primordial abundances at each iteration
def ComputeAbundances(i):
    # Settings to speed up the SM MC
    PRyMini.recompute_bckg = False
    PRyMini.recompute_nTOp_rates = False
    # Large network for nuclear rates
    PRyMini.smallnet_flag = False
    # Gaussian prior on baryon-to-photon ratio
    PRyMini.eta0b = np.random.normal(mean_eta0b,std_eta0b)
    # Gaussian prior on neutron lifetime
    PRyMini.tau_n = np.random.normal(mean_tau_n,std_tau_n)
    # Log-normal prior on nuclear rates
    PRyMini.p_npdg,PRyMini.p_dpHe3g,PRyMini.p_ddHe3n,
    ... # for the sake of brevity not listing all 63 process
    PRyMini.p_ppndp, PRyMini.p_Li7taann = np.random.normal(0,1,PRyMini.num_reactions)
    # NACRE II compilation for key rates
    PRyMini.nacreii_flag = True
```

```
    PRyMini.ReloadKeyRates()
    return PRyMmain.PRyMclass().PRyMresults()[4:8]

# Parallelizing w/ joblib + multiprocessing
from joblib import Parallel, delayed
import multiprocessing
num_cpu = int(multiprocessing.cpu_count())
FinalAbundances = Parallel(n_jobs = num_cpu)(delayed(ComputeAbundances)((i))
for i in range(num_it))
Yp_vec,YDoH_vec,YHe3oH_vec,YLi7oH_vec = np.array(FinalAbundances).transpose()
```

The output maps out the probability distributions, shown in Figure 5.3, where the light elements at the end of the BBN era are predicted within the SM via a MC analysis that involves: *i)* a cosmological prior on the cosmic baryon abundance; *ii)* a particle-physics measurement prior on the neutron lifetime; and *iii)* a dedicated treatment of the uncertainties in the rates of the nuclear processes. Figure 5.3 displays the "deuterium anomaly" present for the `PRIMAT` compilation of the key nuclear rates, and further shows that it is completely washed out when one employs the NACRE II database[12].

Figure 5.3 suggests that the "primordial lithium problem" stands out as statistically significant, regardless of the approach undertaken for the nuclear network. However, the up-to-date analysis of the lithium problem in Ref. [4] points out that the predicted primordial abundance of lithium-7 could be depleted via stellar (and cosmic-ray) nucleosynthesis. Given this argument, the observational inference of Figure 5.2 and Figure 5.3, in which the observations lie below the theoretical prediction for primordial lithium-7, are consistent with a resolution for this long-standing puzzle.

[12]The results in Figure 5.3 slightly differ from Ref. [22] due to an update on the Gaussian prior for the neutron lifetime and the different choice for the cosmological baryon abundance adopted in that study.

5.3.3 NP examples: New Interacting Sectors and BBN

`PRyMordial` allows the user to perform state-of-the-art analyses for Physics beyond the SM in the early universe. A few options already built-in to the current release include:

- additional relativistic degrees of freedom contributing to the expansion rate of the universe in the form of a shift of $N_{\rm eff}$, see Eq. (5.5);
- a non-zero chemical potential for neutrinos, influencing both the cosmological expansion rate as well as the equilibrium distributions in the weak processes for neutron-to-proton conversion;
- Boolean flags specific to the study of new species interacting with the plasma and/or neutrino bath, as well as flags implementing a new entire sector with temperature $T_{\rm NP} \neq T_{\gamma,\nu}$;
- a Boolean flag and a dedicated parameter encoding NP effects as a phenomenological modification of $n \leftrightarrow p$ conversion rates (in units of the Born rates);
- a set of parameters that allow one to similarly investigate NP effects in the nuclear processes as a simple shift in terms of the median rate of each process.

The first two have been extensively investigated in Ref [22], and thus we focus here on the others. The following is code demonstrating how to implement an electrophilic species in thermal equilibrium with the SM bath during BBN:

```
import PRyM.PRyM_init as PRyMini
# Electrophilic
PRyMini.NP_e_flag = True
import numpy as np
```

```
from scipy.integrate import quad
# Scalar with mass mX = 5 MeV
gX = 1; mX = 5.;
def rho_NP(T_NP):
    if T_NP < mX/30.: return 0.
    else:
        res_int = quad(lambda E: E**2*(E**2-(mX/T_NP)**2)**0.5
        /(np.exp(E)-1.) ,mX/T_NP,100.,epsrel=1e-9,epsabs=1e-12)[0]
        return gX/(2*np.pi**2)*T_NP**4*res_int
def p_NP(T_NP):
    if T_NP < mX/30.: return 0.
    else:
        res_int = quad(lambda E: (E**2-(mX/T_NP)**2)**1.5
        /(np.exp(E)-1.) ,mX/T_NP,100.,epsabs=1e-9,epsrel=1e-12)[0]
        return gX/(6*np.pi**2)*T_NP**4*res_int
def drho_NP_dT(T_NP):
    if T_NP < mX/30.: return 0.
    else:
        res_int = quad(lambda E: 0.25*E**3*(E**2-(mX/T_NP)**2)**0.5*
        np.sinh(E/2.0)**-2 ,mX/T_NP,100,epsabs=1e-9,epsrel=1e-12)[0]
        return gX/(2*np.pi**2)*T_NP**3*res_int
import PRyM.PRyM_main as PRyMmain
res = PRyMmain.PRyMclass(rho_NP,p_NP,drho_NP_dT).PRyMresults()
```

One can similarly evaluate a neutrinophilic species thermalized with the SM bath by replacing the Boolean flag at the top of the script with: `PRyMini.NP_nu_flag = True`.

In Figure 5.4 we present the results for NP scenarios of this type, reproducing the qualitative

features already well-discussed, e.g., in Ref. [250]. In particular, we observe three primary NP effects: *i)* a change in the cosmological expansion rate, affecting the time-temperature relation; *ii)* an impact on the evolution of the neutrino-to-photon temperature ratio, relevant for both neutrino and neutron decoupling; and *iii)* additional entropy released in the plasma, altering the number of baryons per a given baryon-to-photon ratio. Note that in Figure 5.4 we use the set of nuclear reactions from `PRIMAT` (`nacreii_flag = False`) and as a result a neutrinophilic species around ~ 10 MeV in mass appears to be favored by current observations of primordial D/H while remaining compatible with the other cosmological NP probes based on helium-4 and $N_{\rm eff}$.

In contrast to the previous scripts, this code calls `PRyMclass()` with three functions (of temperature) as arguments: the contribution to the energy density, its derivative, and the pressure of the new species added to the bath. More generally, one can include a new interacting sector with its own temperature $T_{\rm NP}$ and non-trivial collision term $\delta C_{\rm NP}$ along the lines of the recent work in Ref. [253]. In `PRyMordial` one may study such "dark sectors" consistently by generalizing the set of equations in Eq. (5.3) to follow $T_{\rm NP}$ together with $T_{\gamma,\nu}$, and solving for the entropy density involved in Eq (5.8) taking into account the effect of the NP. To do this, one switches on the Boolean flag `NP_thermo_flag` and codes all of the relevant contributions to the energy density, its derivative (which can optionally be evaluated numerically via `Numdifftools`), pressure and collision term for the NP sector, and passes them to `PRyMresults`.

One can also study NP resulting in changes to the weak rates for neutron freeze out and/or any of the implemented thermonuclear rates. To modify the weak rates, one sets the Boolean flag `NP_nTOp_flag = True` and change the parameter `NP_delta_nTOp` from its default of zero. Analogously, for the nuclear rates one switches on the flag `NP_nuclear_flag` and modifies the value of `NP_delta_R` with `R` being the reaction of interest.

As an example, we consider NP which results in a small change to the $n \leftrightarrow p$ conversion

rates. We perform a Bayesian fit to Y_P and D/H (as quoted by the PDG [14]) and allowing $\tau_{\rm n}$, $\Omega_B h^2$, and the other key nuclear rates to vary within their uncertainties (in line with the SM MC analysis of the previous subsection):

```
# Bayesian analysis w/ PRyMordial and emcee
import emcee
# BBN measurements from PDG 2023
YP_ave = 0.245; YP_std = 0.003;
DoH_ave = 2.547; DoH_std = 0.025;
# Mean and standard deviation on neutron lifetime [s]
mean_tau_n = PRyMini.tau_n
std_tau_n = 0.5
# Mean and standard deviation on cosmic baryonic abundance
mean_Omegabh2 = PRyMini.Omegabh2
std_Omegabh2 =  2*1.e-4
# Test statistic for the fit
def log_L(theta):
    delta_nTOp = theta
    PRyMini.NP_delta_nTOp = delta_nTOp
    # Gaussian extraction of neutron lifetime
    PRyMini.tau_n = np.random.normal(mean_tau_n,std_tau_n)
    # Gaussian extraction of cosmic baryonic abundance
    PRyMini.Omegabh2 = np.random.normal(mean_Omegabh2,std_Omegabh2)
    # IMPORTANT: Assign etab after updating Omegab (or directly vary etab)
    PRyMini.etaOb =  PRyMini.Omegabh2_to_etaOb*PRyMini.Omegabh2
    # Gaussian weights for log-normal nuclear rates
    PRyMini.p_npdg,PRyMini.p_dpHe3g,PRyMini.p_ddHe3n,PRyMini.p_ddtp,
```

```
    PRyMini.p_tpag, PRyMini.p_tdan,PRyMini.p_taLi7g,PRyMini.p_He3ntp,
    PRyMini.p_He3dap, PRyMini.p_He3aBe7g, PRyMini.p_Be7nLi7p,PRyMini.p_Li7paa
    = np.random.normal(0,1,12)
    YPth, DoHth = PRyMmain.PRyMclass().PRyMresults()[4:6]
    m2LogL = (YPth-YP_ave)**2/(YP_std**2) + (DoHth-DoH_ave)**2/(DoH_std**2)
    return -0.5*m2LogL
def log_prior(theta):
    delta_nTOp = theta
    if -0.3 < delta_nTOp < 0.3:
        return 0.0
    return -np.inf
def log_prob(theta):
    lp = log_prior(theta)
    if not np.isfinite(lp):
        return -np.inf
    ll = log_L(theta)
    return lp + ll

if __name__ == '__main__' :
    # Total number of steps x walker
    nsteps = 2100
    # Guess on burn-in steps
    discsteps = int(nsteps/3.)
    nwalkers = 6
    ndim = 1
    pos = np.array([0.]) + [1e-2]*np.random.randn(nwalkers,ndim)
    def RunMCMCserial(i):
```

```
        import PRyM.PRyM_init as PRyMini
        PRyMini.smallnet_flag = True
        PRyMini.nacreii_flag = True
        PRyMini.ReloadKeyRates()
        PRyMini.NP_nTOp_flag = True
        sampler = emcee.EnsembleSampler(nwalkers, ndim, log_prob)
        sampler.run_mcmc(pos, nsteps, progress = True)
        all_samples = sampler.get_chain(discard=discsteps,flat=True)
        return all_samples
    from joblib import Parallel, delayed
    import multiprocessing
    num_cpu = int(multiprocessing.cpu_count())
    start = time.time()
    FinalRes = Parallel(n_jobs = num_cpu)(delayed(RunMCMCserial)((i))
    for i in range(num_cpu))
    my_samples_1,my_samples_2,my_samples_3,my_samples_4,
    my_samples_5,my_samples_6,my_samples_7,my_samples_8 = FinalRes
    # Collecting the samples all together
    final_samples = np.concatenate((my_samples_1,my_samples_2,my_samples_3,
    my_samples_4,my_samples_5,my_samples_6,my_samples_7,my_samples_8))
```

This code can be simply generalized to modify any of the other nuclear reactions.

Figure 5.5 shows the resulting 2D joint (68% and 95%) probability regions for `NP_delta_nTOp` correlated with the measurements of primordial helium-4 and deuterium. To perform the statistical analysis, we adopt the `emcee` package [16]. For the sake of computational efficiency, we restrict the analysis to the network of 12 key reactions (with `nacreii_flag = True`), as is sufficient given the focus on helium-4 and deuterium. Figure 5.5 indicates that BBN is

consistent with NP in the $n \leftrightarrow p$ conversion rates at the level of at most a few percent relative to the standard Born rates. The tight correlation with Y_P illustrates the importance of neutron freeze out in determining the primordial helium-4 abundance.

5.4 Outlook

In this work we have presented `PRyMordial`: A new tool to explore the physics of BBN in great detail, with an unprecedented eye toward applications for physics beyond the SM. The package also allows for fast, user-friendly precision analyses of the BBN era within the SM of Particle Physics, reaching the same level of accuracy as the state-of-the-art codes already publicly available.

In section 5.2 we have provided in some detail a review of the BBN era, highlighting the physics implemented in the code. The main novelties in `PRyMordial` are that it is:

- A package entirely written in Python, easy to install, run and modify, efficient in the evaluation of the key quantities for the study of BBN; moreover, an optional dependence on Julia allows the user to make the code run even faster;
- A computation of the thermal background based on the Boltzmann equations governing the evolution of the relativistic species present at that time. This allows for an accurate prediction of $N_{\rm eff}$ from first principles and opens up new avenues for the study of BSM Physics;
- A fast and accurate evaluation of the weak rates including QED, nucleon-finite mass and thermal corrections for a prediction of the neutron-to-proton ratio that confronts the precision of current and next-generation measurements;
- A BBN code that easily allows exploration of uncertainties and changes in all of the

input parameters and most importantly, includes by default different treatments for the nuclear rates in order to give to the user a better handle on the overall theoretical systematics.

In section 5.3 we describe the structure of the code and provide several examples of its usage within the Standard Model and for a few interesting scenarios of NP.

There are many directions that can be pursued in the future to make `PRyMordial` an even more compelling and flexible tool for the community. One important aspect we plan to expand upon is the characterization of the thermal background. At the moment, only a single common temperature for neutrinos is considered and no evolution equation for primordial chemical potentials is given by default. All of these can be easily implemented along the lines of Ref. [269].

Also relevant for precision studies would be an approach to efficiently include effects from phase-space spectral distortions of relativistic species. In this regard, we plan to further enrich the physics in `PRyMordial` with a dedicated framework for neutrino decoupling that includes effects from oscillations at non-zero lepton chemical potentials, see Ref. [324].

It would be a very interesting (though formidable) task to further improve the current next-to-leading order computation of neutron freeze out in the early universe, filling in the gaps of some of the approximations undertaken in the literature (see Appendix B of [325] as well as the improvements brought by the recent effective-field-theory study at zero temperature of Ref. [292]). We would also eventually like to include higher-order QED corrections such as the ones available in Refs [279] and [326], as well as the NLO QED corrections to $e^+e^- \leftrightarrow \nu\bar{\nu}$ matrix elements recently inspected in Ref. [327].

Finally, in the future we would like to enlarge the nuclear network beyond the 63 nuclear reactions currently implemented, which encode all of the processes involving nuclides up to

boron-8 in atomic and mass number (needed for an accurate prediction of lithium-7 in the Standard Model).

With the public release of `PRyMordial` we hope to provide to the community an important new tool to address fundamental questions about the early universe, whose study remains central to further progress in our understanding of Nature. In the wise words of a giant of our time [221]:

> *"[Human beings] are not content to comfort themselves with tales of gods and giants, or to confine their thoughts to the daily affairs of life; they also build telescopes and satellites and accelerators, and sit at their desks for endless hours working out the meaning of the data they gather. The effort to understand the universe is one of the very few things that lifts human life a little above the level of farce, and gives it some of the grace of tragedy."*

Note about referencing: `PRyMordial` makes use of previous work in the literature. When using it, please make certain to appropriately reference the original literature as well as `PRyMordial` itself.

Acknowledgements and Author Contributions Statement

We are grateful to Cara Giovanetti and Federico Bianchini for providing us valuable feedback for the present release after β-testing `PRyMordial`. We acknowledge Kevork Abazajian, Kim Berghaus, Federico Bianchini, Miguel Escudero, Rouven Essig, Cara Giovanetti, Seyda Ipek, Mariangela Lisanti, Hongwan Liu, Jessie Shelton for discussion. We are in debt to all of the authors of `AlterBBN`, `NUDEC_BSM`, `PArthENoPE`, and `PRIMAT` for making their codes publicly accessible: The present work and the release of `PRyMordial` greatly benefited from the

open-source community.

Using the CASRAI CRediT Contributor Roles Taxonomy: Conceptualization, A.K.B., T.M.P.T., M.V.; Data curation, A.K.B., M.V.; Formal analysis, A.K.B., T.M.P.T., M.V.; Funding acquisition, T.M.P.T., M.V.; Investigation, A.K.B., T.M.P.T., M.V.; Methodology, A.K.B., T.M.P.T., M.V.; Project administration, T.M.P.T., M.V.; Software, A.K.B., M.V.; Supervision, T.M.P.T.; Validation, A.K.B., M.V.; Visualization, A.K.B., M.V.; Writing – original draft, A.K.B., T.M.P.T., M.V.; Writing – review and editing, A.K.B., T.M.P.T., M.V.

Appendix 5A: How to Install `PRyMordial`

`PRyMordial` is publicly released on GitHub. Once in the desired directory, from your terminal type:

```
git clone https://github.com/vallima/PRyMordial
```

The code requires a modern distribution of Python (Python 3 recommended) in order to properly run, and features only a couple of standard libraries as mandatory dependencies:

- NumPy (mandatory) – pip install numpy;
- SciPy (mandatory) – pip install scipy;
- Vegas (mandatory) – pip install vegas;
- Numba (recommended) – pip install numba;
- Numdifftools (recommended) – pip install numdifftools;
- PyJulia (optional) – pip install julia;

- diffeqpy (optional) – pip install diffeqpy.

Indeed, the code can easily avoid dependencies on Numba and Numdifftools. Nevertheless, giving up on Numba will slightly slow down a few routines in `PRyM_thermo.py` which involve SciPy integration. Also, the installation of Vegas library is required only in the case where thermal corrections to the weak rates governing neutron freeze out have to be recomputed. This is usually not the case, since those are already tiny effects in the SM and can be reasonably neglected in studies of NP during BBN.

The optional dependencies above require the Julia programming language to be installed. It can be downloaded at https://julialang.org. Once Julia is installed, it is recommended to create a soft link from the terminal typing something like:

```
ln -s path-where-/bin/julia-is /usr/local/bin/julia
```

Then, launch Julia and install `DifferentialEquations.jl` of the SciML kit (with Sundials wrapper):

```
using Pkg;
Pkg.add("DifferentialEquations");
Pkg.add("Sundials");
```

After a successful installation of the package, one needs to open a Python shell and type:

```
import julia
julia.install()
import diffeqpy
diffeqpy.install()
```

At this point the user will be able to exploit the SciML routines developed in Julia to solve the nuclear-reaction network in `PRyMordial`, speeding up the execution of time by a factor of two or more, and with the possibility of cherry-picking from a large collection of differential-equation solvers built-in in the package, see the documentation at https://docs.sciml.ai/DiffEqDocs/stable/

To use the SciML routines, the user must set the flag `PRyM_init.flag_julia = True`. In some systems, the very first call of `PRyM_main.PRyMresults()` might need to be in Python and therefore requires initially `PRyM_init.flag_julia = False`. Also, the first call in Julia will inevitably be slow, since it will compile `PRyM_jl_sys.py`. As a concise example of the dedicated script `runPRyM_julia.py` coming with the present release, here below is how things should work in the Julia mode:

```
import PRyM.PRyM_init as PRyMini
import PRyM.PRyM_main as PRyMmain
# Initialization call in Python:
PRyMini.julia_flag = False
res = PRyMmain.PRyMclass().PRyMresults()
# First call in Julia will be slow:
PRyMini.julia_flag = True
res = PRyMmain.PRyMclass().PRyMresults()
# From here on, any call will be fast!
```

Appendix 5B: Nuclear Processes in `PRyMordial`

In this appendix we collect the 12 key reactions necessary to accurately predict helium-4 and deuterium, see Table 5.1, as well as the 51 additional reactions comprising the full set recommended for a more robust prediction of lithium-7, Table 5.2. For the general aspects

of the evaluation of the nuclear rates in the early universe as well as the theoretical and statistical details behind the compilation of the nuclear rates present in `PRyMordial`, we refer the interested reader to Ref. [307] and Refs. [321, 322].

Nuclear Reaction	Ref.	Ref.	**Nuclear Reaction**	Ref.	Ref.
n+p $\rightarrow$ D+γ	[328]	[328]	D+p $\rightarrow$ ^{3}He+γ	[320]	[320]
D+D $\rightarrow$ ^{3}He+n	[312]	[329]	D+D $\rightarrow$ ^{3}H+p	[312]	[329]
^{3}H+p $\rightarrow$ ^{4}He+γ	[307]	[307]	^{3}H+D $\rightarrow$ ^{4}He+n	[310]	[329]
^{3}H+^{4}He $\rightarrow$ ^{7}Li+γ	[310]	[329]	^{3}He+n $\rightarrow$ ^{3}H+p	[310]	[316]
^{3}He+D $\rightarrow$ ^{4}He+p	[310]	[329]	^{3}He+^{4}He $\rightarrow$ ^{7}Be+γ	[312]	[329]
^{7}Be+n $\rightarrow$ ^{7}Li+p	[310]	[317]	^{7}Li+p $\rightarrow$ ^{4}He+^{4}He	[310]	[329]

Table 5.1: The key nuclear reactions adopted in `PRyMordial`, with corresponding references. The red (blue) column refers to the option `nacreii_flag = True (False)`, see subsection 5.2.3 for further details. Notice that the compilation of the blue column is present also in the code `PRIMAT` [18].

Nuclear Reaction	Ref.	**Nuclear Reaction**	Ref.
^{7}Li+p $\rightarrow$ ^{4}He+^{4}He+γ	[329]	^{7}Be+n $\rightarrow$ ^{4}He+^{4}He	[330]
^{7}Be+D $\rightarrow$ ^{4}He+^{4}He+p	[331]	D+^{4}He $\rightarrow$ ^{6}Li+γ	[332]
^{6}Li+p $\rightarrow$ ^{7}Be+γ	[329]	^{6}Li+p $\rightarrow$ ^{3}He+^{4}He	[329]
^{8}B+n $\rightarrow$ ^{4}He+^{4}He+p	[333]	^{6}Li+^{3}He $\rightarrow$ ^{4}He+^{4}He+p	[333]
^{6}Li+^{3}H $\rightarrow$ ^{4}He+^{4}He+n	[333]	^{6}Li+^{3}H $\rightarrow$ ^{8}Li+p	[333]
^{7}Li+^{3}He $\rightarrow$ ^{6}Li+^{4}He	[333]	^{8}Li+^{3}He $\rightarrow$ ^{7}Li+^{4}He	[333]
^{7}Be+^{3}H $\rightarrow$ ^{6}Li+^{4}He	[333]	^{8}B+^{3}H $\rightarrow$ ^{7}Be+^{4}He	[333]
^{8}B+n $\rightarrow$ ^{6}Li+^{3}He	[333]	^{8}B+n $\rightarrow$ ^{7}Be+D	[333]
^{6}Li+^{3}H $\rightarrow$ ^{7}Li+D	[333]	^{6}Li+^{3}He $\rightarrow$ ^{7}Be+D	[333]
^{7}Li+^{3}He $\rightarrow$ ^{4}He+^{4}He+D	[333]	^{8}Li+^{3}He $\rightarrow$ ^{4}He+^{4}He+^{3}H	[333]
^{7}Be+^{3}H $\rightarrow$ ^{4}He+^{4}He+D	[333]	^{7}Be+^{3}H $\rightarrow$ ^{7}Li+^{3}He	[333]
^{8}B+D $\rightarrow$ ^{7}Be+^{3}He	[333]	^{8}B+^{3}H $\rightarrow$ ^{4}He+^{4}He+^{3}He	[333]
^{7}Be+^{3}He $\rightarrow$ p+p+^{4}He+^{4}He	[333]	D+D $\rightarrow$ ^{4}He+γ	[329]
^{3}He+^{3}He $\rightarrow$ ^{4}He+p+p	[329]	^{7}Be+p $\rightarrow$ ^{8}B+γ	[329]
^{7}Li+D $\rightarrow$ ^{4}He+^{4}He+n	[334]	D+n $\rightarrow$ ^{3}H+γ	[335]
^{3}H+^{3}H $\rightarrow$ ^{4}He+n+n	[335]	^{3}He+n $\rightarrow$ ^{4}He+γ	[305]
^{3}He+^{3}H $\rightarrow$ ^{4}He+D	[331]	^{3}He+^{3}H $\rightarrow$ ^{4}He+n+p	[331]
^{7}Li+^{3}H $\rightarrow$ ^{4}He+^{4}He+n+n	[331], [336]	^{7}Li+^{3}He $\rightarrow$ ^{4}He+^{4}He+n+p	[331], [336]
^{8}Li+D $\rightarrow$ ^{7}Li+^{3}H	[337]	^{7}Be+^{3}H $\rightarrow$ ^{4}He+^{4}He+n+p	[331], [336]
^{7}Be+^{3}He $\rightarrow$ ^{4}He+^{4}He+p+p	[331], [336]	^{6}Li+n $\rightarrow$ ^{3}H+^{4}He	[331]
^{3}He+^{3}H $\rightarrow$ ^{6}Li+γ	[338]	^{4}He+n+p $\rightarrow$ ^{6}Li+γ	[331]
^{6}Li+n $\rightarrow$ ^{7}Li+γ	[336]	^{6}Li+D $\rightarrow$ ^{7}Li+p	[336]
^{6}Li+D $\rightarrow$ ^{7}Be+n	[336]	^{7}Li+n $\rightarrow$ ^{8}Li+γ	[336], [339]
^{7}Li+D $\rightarrow$ ^{8}Li+p	[336]	^{8}Li+p $\rightarrow$ ^{4}He+^{4}He+n	[340]
^{4}He+n+n $\rightarrow$ ^{6}He+γ	[341]	p+p+n $\rightarrow$ D+p	[331]
^{7}Li+^{3}H $\rightarrow$ ^{4}He+^{4}He+n+n	[331], [336]		

Table 5.2: Nuclear processes beyond the key ones implemented in the package `PRyMordial`, with related references. Those processes are particularly needed for a precise prediction of the primordial abundance of lithium-7. Notice that the compilation above is part of the larger one present in the code `PRIMAT` *[18].*

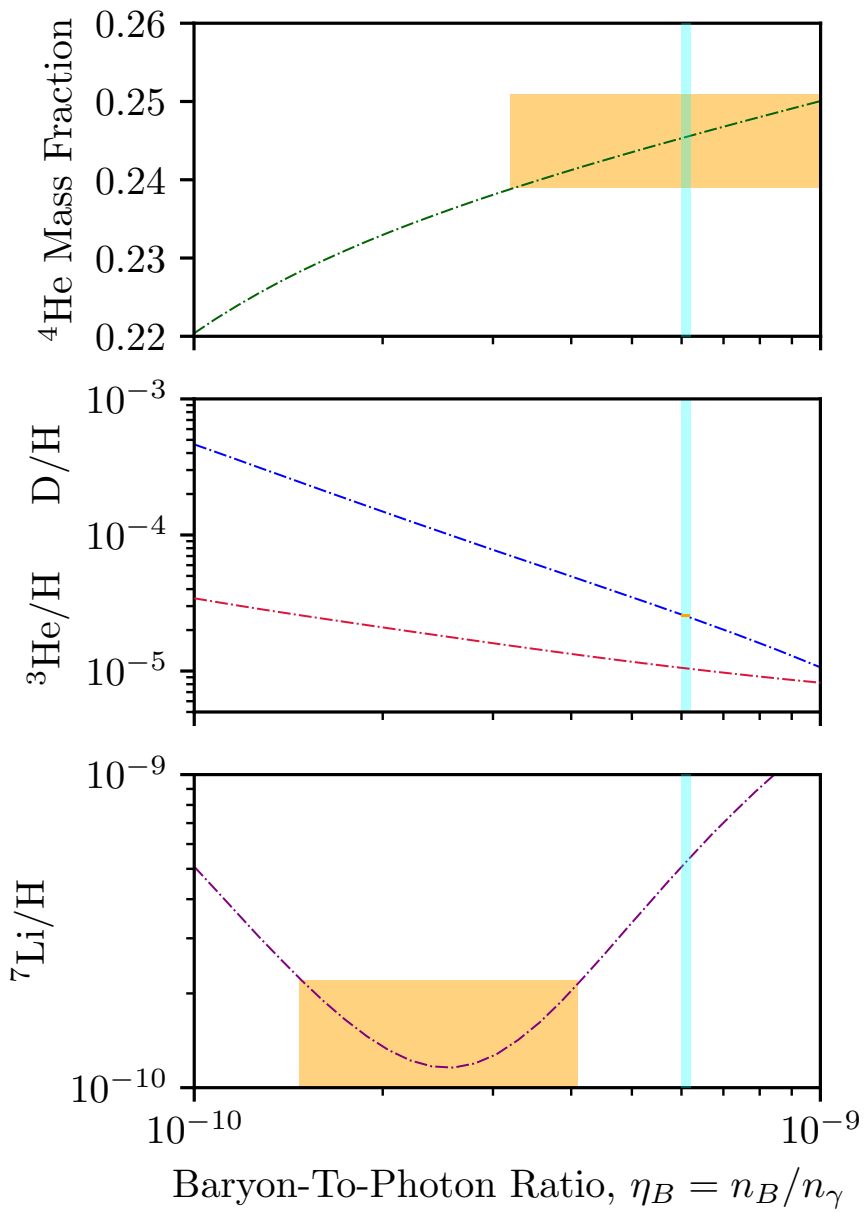

Figure 5.2: Primordial abundances of helium-4, deuterium, helium-3, and lithium-7 as predicted by `PRyMordial` within the SM, as a function of the cosmic baryon density. Central predictions are shown without theory uncertainties (i.e. using the nominal nuclear rates for the largest set implemented in the package with the NACRE II compilation for the key processes) and at the central values of all of the inputs. Measurements of light-element abundances (orange) as well as the CMB constraint on the baryon-to-photon ratio (cyan) follow from Figure 24.1 of the PDG [14].

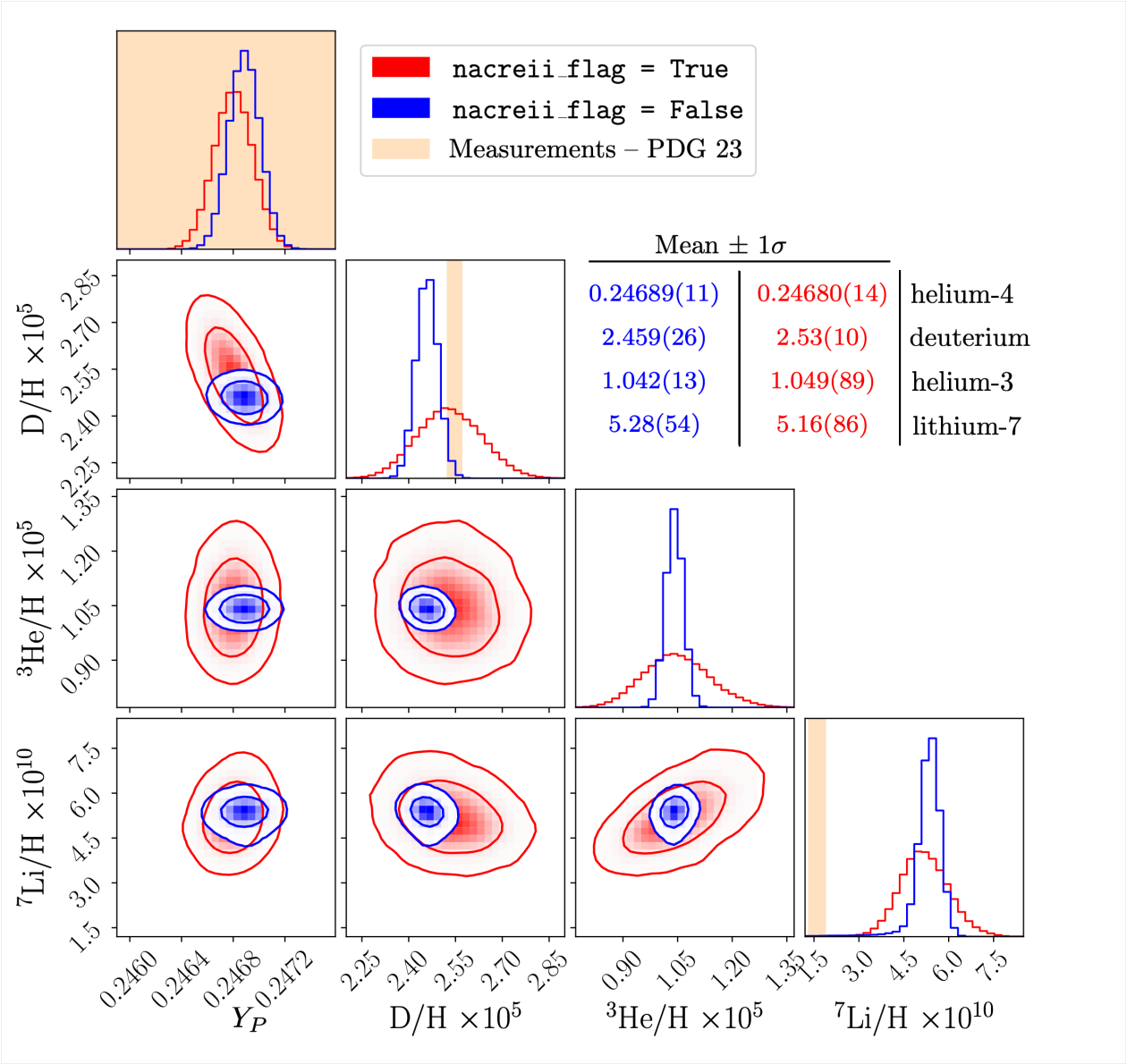

Figure 5.3: 1D probability distributions (and 2D joint 68% and 95% probability regions) for the light primordial abundances predicted in the SM with `PRyMordial`. Predictions are obtained using a Gaussian prior for the neutron lifetime $\tau_n = 878.4 \pm 0.5$ s (comprising the eight best measurements from ultra-cold neutron experiments combined in Ref. [14]), and the cosmic baryon density, $\Omega_B h^2 = 0.02230 \pm 0.00020$ (from Table 5 of Ref. [15] for the analysis with an uninformative Y_P prior). The large network of nuclear reactions has been used, implying an additional 63 nuisance parameters varied with a log-normal distribution. Two different sets of key nuclear rates have been considered on the basis of the Boolean flag `nacreii_flag` , and the statistics of the marginalized distributions for each case is presented.

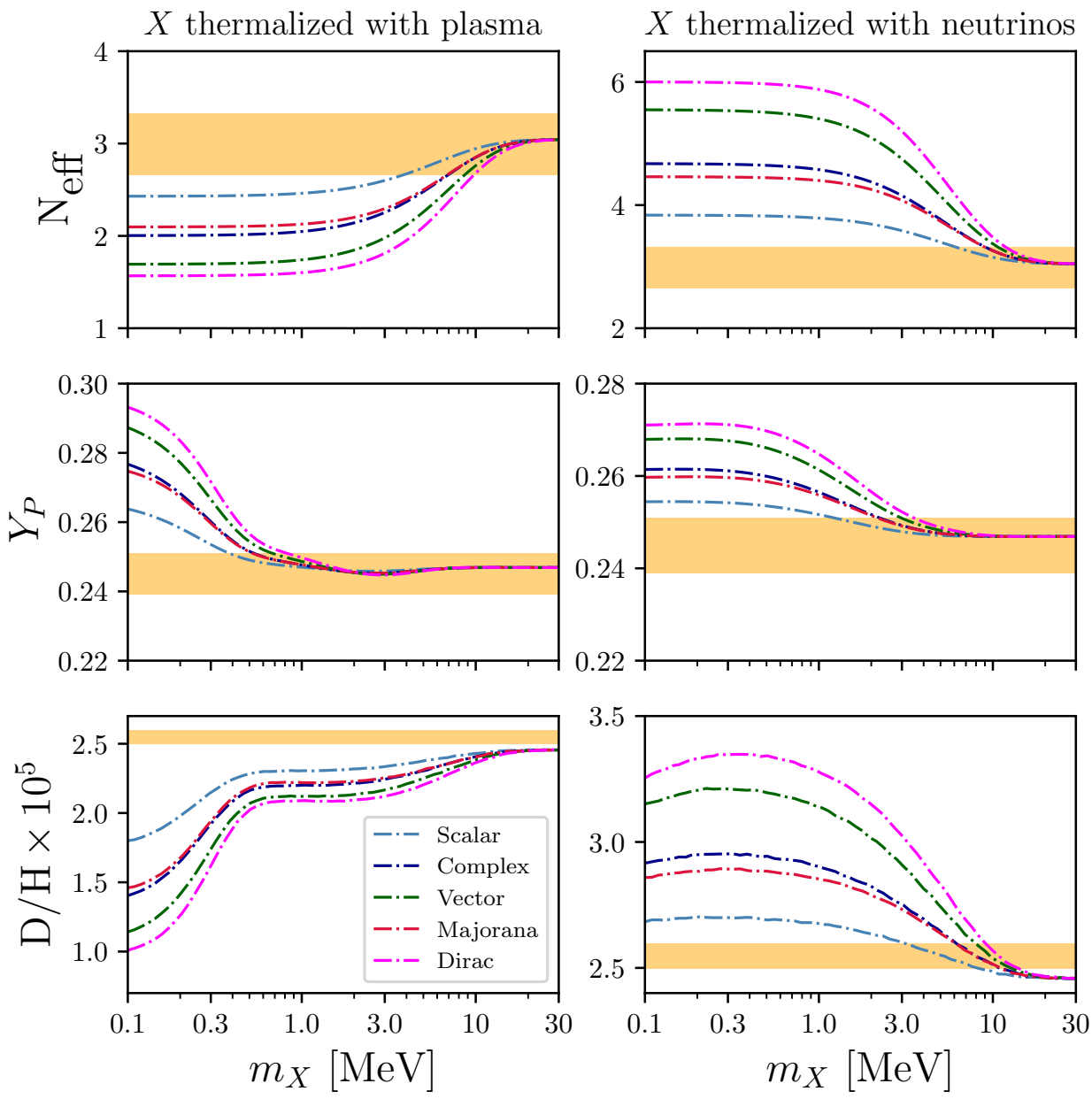

Figure 5.4: Investigation of the cosmological impact at the end of the BBN era from a new relativistic species X with degrees of freedom corresponding to a real / complex scalar (light / dark-blue lines), a real massive vector (magenta), or a Majorana / Dirac fermion (red / green); X is assumed to be in thermal equilibrium with either the electron-positron-photon plasma (left panels) or with the SM neutrino thermal bath (right panels). The orange bands represent the observational constraints at the 2σ level from Refs. [15, 14]. Predictions with `PRyMordial` are obtained at nominal inputs and rates.

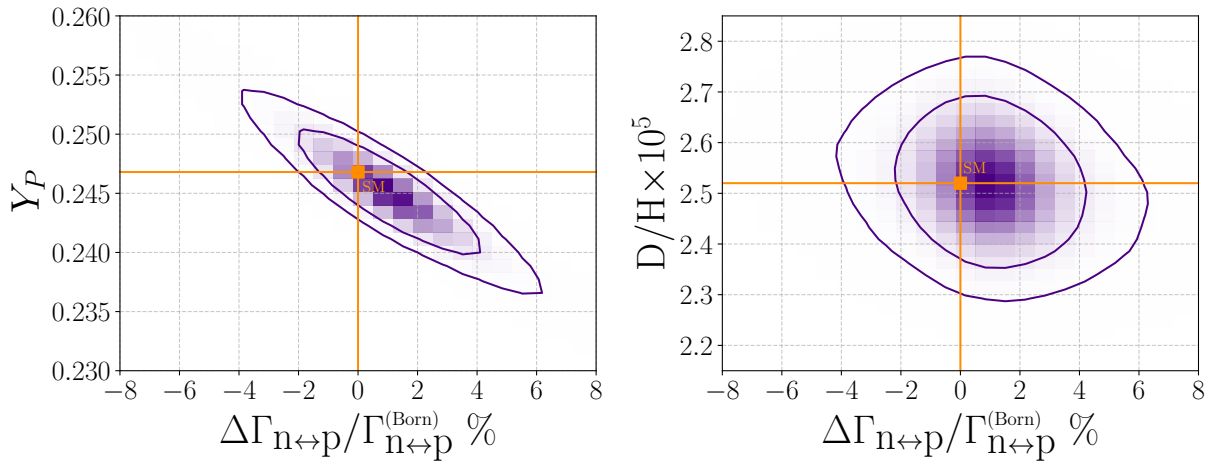

Figure 5.5: Constraint on a relative change of the weak $n \leftrightarrow p$ conversion rates from NP, based on a Bayesian fit performed with `PRyMordial` with the use of the `emcee` [16]package. Gaussian priors on the neutron lifetime and the cosmic baryon abundance are assumed (as for Figure 5.3) and flags `smallnet_flag` and `nacreii_flag` are both switched on. Helium-4, deuterium measurements correspond to the recommended values from the PDG [14].

Chapter 6

Indications for a Nonzero Lepton Asymmetry from Extremely Metal-Poor Galaxies

This chapter is heavily based on work previously published in collaboration with Tim M.P. Tait and Mauro Valli [22].

6.1 Introduction

Cosmological observations from the early universe provide an invaluable probe of Physics Beyond the Standard Model (BSM). Observations of the Cosmic Microwave Background (CMB), epitomized by the Planck mission [342] and further developed e.g. by the ACT [343] and SPT [344] collaborations, paint a picture of a universe dominated by non-baryonic dark energy and dark matter, well-described by the ΛCDM model [345, 346, 347]. Equipped with the CMB inference of the small cosmological baryonic abundance, $\Omega_B \sim 4\%$, the theory

of Big Bang Nucleosynthesis (BBN) within the Standard Model (SM) of Particle Physics is highly predictive, and confronted with accurate measurements of primeval elements such as the mass density fraction of helium-4, Y_P, and the relative abundance of deuterium to hydrogen, D/H, offers important constraints on New Physics (NP) [226, 228, 348, 229] active during the first few minutes of the universe [349, 350, 250, 351].

At present, measurements of deuterium in quasar absorption spectra provide the best proxy for the determination of a primordial abundance. The most recent measurements from damped Lyman-α systems achieve better than 1% precision [352, 353, 241], yielding a weighted average of $\mathrm{D/H} \times 10^5 = 2.547 \pm 0.025$ [354]. This remarkable precision appears to be in tension with the SM at about the 2σ level [264], although this remains under debate [315, 355] in light of the uncertainties on the key nuclear reactions involved. This highlights the primary importance to assess the impact of uncertainties in the nuclear network rates on the predictions from BBN [270]. A notable recent advance in this direction is the improved determination of the $\mathrm{D}(p,\gamma)^3\mathrm{He}$ rate by the LUNA collaboration [320], which has an important impact on BBN constraints from primordial deuterium on various NP scenarios [271].

The recent near-infrared observation of 10 extremely metal-poor galaxies (EMPGs) by the Subaru Survey [356] points to even more puzzling mysteries. Spectroscopic observations of EMPGs provide a crucial input to the inference of Y_P, because they host the gas of nebulae resembling extraordinarily pristine environments which allow for a more accurate extrapolation of the helium density to zero metallicity. Combined with the pre-existing data from 3 EMPGs and 51 metal-poor galaxies [357] and measurements of the He λ10830 infrared emission line (relevant for parameter-degeneracy breaking [41]), 5 (out of 10) Subaru EMPGs yield a determination of primordial helium-4 of $Y_P = 0.2370^{+0.0034}_{-0.0033}$, in sharp contrast with the PDG value $Y_P = 0.245 \pm 0.003$ [354], and well below the SM prediction [264, 315, 355], naively a 3σ-level discrepancy.

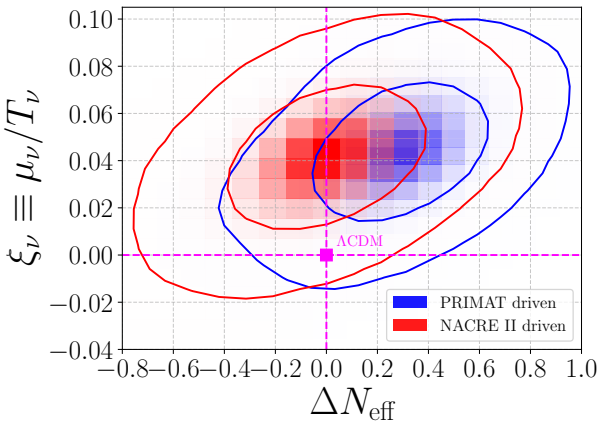

Figure 6.1: 68% and 95% two-dimensional probability distribution of the primordial chemical potential of neutrinos, μ_ν, normalized to the neutrino temperature T_ν, and the number of extra relativistic degrees of freedom in the early universe, $\Delta N_{\rm eff}$, from a state-of-the-art analysis of BBN and CMB data. The red and blue contours indicate the results for two different sets of nuclear uncertainties; magenta lines the ΛCDM prediction.

Ref. [356] took the first steps toward an interpretation of this *helium anomaly* in terms of a BSM fit where the standard theory has been extended by extra-relativistic degrees of freedom, $\Delta N_{\rm eff}$, as well as a nonzero electron neutrino asymmetry, ξ_{ν_e}, while simply anchoring $\Omega_B h^2$ to the most precise determination derived by Planck [342].

In this *Letter* we revise the inference of a lepton asymmetry ξ_ν in the early universe, as well as on $\Delta N_{\rm eff}$ (defined at the last scattering), paying attention to the details of a joint likelihood analysis of BBN and CMB data as recently carefully formulated in [250, 351]. Our key result is given in Figure 6.1 [1]. We perform a Bayesian analysis taking into account the theory uncertainties pivotal for unbiased conclusions based on the use of the new public code for state-of-the-art investigations of (BSM) physics in the early universe – `PRyMordial` – presented in a companion paper [358].

[1] While the methodology developed in this work stands out as a robust recipe for an advanced statistical analysis of early universe data, the measurement published in [356], focus of the present study, strongly depends on the emission-line data modeling. Further scrutiny on the corresponding systematics of the measurement is warranted for the future.

6.2 Primordial Lepton Asymmetries

Electric charge neutrality of the early universe does not allow for a large primordial asymmetry in the charged lepton sector, which is constrained to be (at most) of the order of the baryon-to-photon ratio $\eta_B \equiv n_B/n_\gamma \sim \mathcal{O}(10^{-10})$ [274, 275]. Nevertheless, a large cosmic asymmetry can be hidden in the neutrino sector [359]:

$$\eta_L \equiv \frac{1}{n_\gamma} \sum_{i=e,\mu,\tau} (n_{\nu_i} - n_{\bar{\nu}_i}) \simeq \frac{\pi^2}{33\zeta(3)} (\xi_{\nu_e} + \xi_{\nu_\mu} + \xi_{\nu_\tau}) \ , \tag{6.1}$$

where n_γ is the photon number density, n_{ν_i} the flavor i neutrino density, and $\xi_{\nu_i} \equiv \mu_{\nu_i}/T_{\nu_i}$ are the *degeneracy parameters* defined as the chemical potential for each neutrino normalized to its temperature, which encode the relevant lepton asymmetries today. Eq. (6.1) assumes $T_{\nu_i}/T_\gamma = (4/11)^{1/3}$, which is a good approximation given the modest impact of non-instantaneous neutrino decoupling and tiny departures from the Fermi-Dirac distributions in relativistic freeze-out [360, 235, 234]. It is further relevant that nonzero neutrino chemical potentials play a marginal role in SM neutrino decoupling [302, 361].

Eq. (6.1) further implements the condition $|\xi_{\nu_i}| < 1$, as $\mathcal{O}(1)$ degeneracy parameters were probed by early-stage CMB observations about two decades ago [362, 363], and now are robustly [364, 365, 366] ruled out (irrespective of the lepton flavor [367, 368]). In fact, a nonzero chemical potential for the i-flavored neutrino would yield a contribution to the total radiation density (relative to photons) of

$$\frac{\Delta\rho_{\rm rad}}{\rho_\gamma} \simeq \frac{15}{4\pi^2} \left(\frac{4}{11}\right)^{4/3} \xi_{\nu_i}^2 \ , \tag{6.2}$$

and would increase the expansion rate of the universe, resulting in a positive shift of $N_{\rm eff}$ that would delay the time of matter-radiation equality which is tightly constrained by the CMB acoustic peaks.

From the Planck constraint on $N_{\rm eff}$ adopting the likelihood analysis including TTTEEE and low-ℓ measurements, as well as baryonic acoustic oscillations (BAO) and lensing data, and assuming a flat prior on $\mathrm{Y_P}$, one may derive a simple upper-bound on the degeneracy parameters purely driven by the CMB. In particular, for $N_{\rm eff} = 2.97 \pm 0.29$ (68% probability interval) [342, 369], considering the SM prediction $N_{\rm eff} = 3.044$ (known better than the per-mille level) [360, 235, 234], the 1σ upper-bound is:

$$\xi^2_{\nu_e} + \xi^2_{\nu_\mu} + \xi^2_{\nu_\tau} \lesssim 0.5 \ , \tag{6.3}$$

implying the conservative constraint $|\xi_{\nu_i}| \lesssim 0.71$, valid for each flavor individually (see also Ref. [370]). Since the onset of neutrino oscillations is expected to occur around $T_\nu \sim 10$ MeV, flavor equilibration in the muon-tau sector is predicted to be complete by the time of neutrino decoupling ($T_\nu \sim 2$ MeV) [277, 371], and the conservative CMB bound of Eq. (6.3) becomes slightly tighter for the $2^{\rm nd}$ and $3^{\rm rd}$ generation ν asymmetries:

$$|\xi_{\nu_{\mu,\tau}}| \lesssim 0.5 \ . \tag{6.4}$$

BBN can place stronger constraints on the electron-neutrino asymmetry (by about an order of magnitude [359, 317]) largely because an electron-neutrino asymmetry at the time of BBN affects the β equilibrium of weak interactions controlling the neutron-proton conversion [372]. A positive (negative) value of ξ_{ν_e} acts through the equilibrium reactions $n\,\nu_e \leftrightarrow p\,e^-$, $p\,\bar{\nu}_e \leftrightarrow n\,e^+$ and neutron decay to reduce (enhance) the neutron-to-proton ratio:

$$(n_n/n_p)\big|_{\rm eq.} \simeq \exp\left(-\mathcal{Q}/T_\gamma - \xi_{\nu_e}\right) \ , \tag{6.5}$$

where $\mathcal{Q} \equiv m_n - m_p = 1.293$ MeV is the neutron-proton mass difference. While light primordial abundances like deuterium are particularly sensitive to Ω_B, from Eq. (6.5) it follows that helium-4 – which depends crucially on the amount of neutrons at the time

where deuterium is no longer photo-dissociated [274, 275] – can be regarded as a sensitive *primordial leptometer*.

In Ref. [18] a combined analysis of the helium and deuterium PDG values together with a Gaussian prior on $\Omega_B h^2$ from the CMB yields the precise determination: $\xi_\nu = 0.001 \pm 0.016$, consistent with zero. By assuming full equilibration of lepton flavor asymmetries due to neutrino oscillations, this inference is more stringent than the bound outlined in Eq. (6.4). Nevertheless, a recent state-of-the-art investigation in Ref. [373] indicates that the degree to which full flavor equilibration is realized during the BBN era sensitively depends on the PMNS mixing angle θ_{13} and on the initially generated values of the degeneracy parameters. In the following, we revisit the determination of ξ_ν in light of the newly measured helium-4 mass fraction from EMPGs as reported in Ref. [356]. While $\xi_\nu = \xi_{\nu_{e,\mu,\tau}}$ may be achieved in the early universe, one should bear in mind that the conservative interpretation of our main finding in Fig. 6.1 applies only to $\xi_\nu = \xi_{\nu_e}$, i.e. the primordial electron-neutrino asymmetry probed by BBN via β equilibrium, Eq. (6.5).

6.3 Methodology

Our computation of BBN abundances via the `PRyMordial` [358] code, proceeds through 3 main steps:

1) Solving for the thermal background;

2) Computing neutron-proton conversion;

3) Evaluating the final primordial abundances.

For *1)* we base our computation on the approach proposed in [374] and further developed in [361] (see also [253]). It consists in solving the Boltzmann equations for the electron-

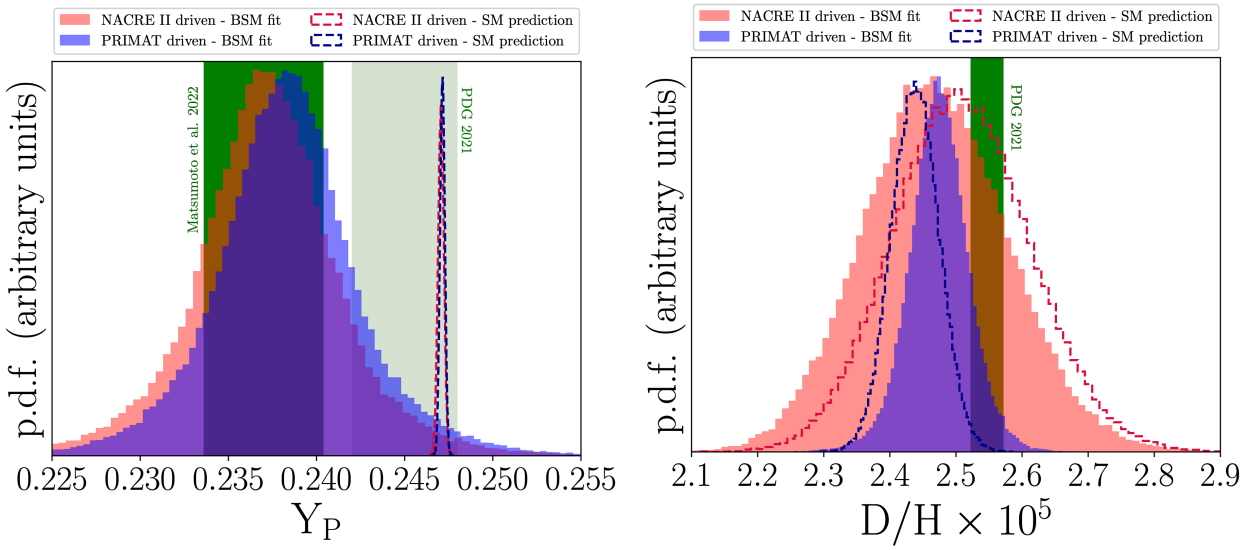

Figure 6.2: Probability density function (p.d.f.) for the primordial light elements analyzed in this study. In the left panel, the p.d.f. for helium-4, Y_P, as precisely predicted in the SM according to two different set of nuclear uncertainties and adopting the determination of the cosmological baryon-to-photon ratio from the fit of CMB data within ΛCDM (color code similar to Figure 6.1). In the same panel, the outcome from the joint fit to BBN and CMB likelihoods in the BSM scenario where ξ_ν and $\Delta N_{\rm eff}$ are consistently allowed to differ from their ΛCDM limit. In the right panel, the same set of p.d.f.s is shown for the deuterium. In both panels, vertical dark green bands correspond to the 1σ interval for the BBN measurements employed in the analysis. In the left one, the PDG 2021 recommended value for helium-4 is also reported, in agreement with the SM prediction.

photon plasma and neutrinos assuming a thermal distribution for the species, including NLO QED corrections for the plasma [279] as well as non-instantaneous decoupling effects for the neutrino sector [361]. For our purposes, it suffices to describe the neutrino sector by a common temperature T_ν, yielding the SM prediction $N_{\rm eff} = 3.045$, differing from the most refined prediction in [360, 235, 234] only at the per-mille level, well within current and future observational sensitivity [375, 376, 377]. A nonzero chemical potential for neutrinos would influence our analysis of the thermal background via Eq. (6.2). If full neutrino equilibration is achieved, we find a-posteriori a contribution to the radiation density that would be totally negligible. Nevertheless, in our BSM analysis we also account for the possibility of a nonzero lepton asymmetry $|\xi_{\nu_{\mu,\tau}}| \gg |\xi_{\nu_e}|$ by varying $\Delta N_{\rm eff}$ (a valid interpretation of $\Delta N_{\rm eff}$ in the scenario where such a shift is mainly driven by a non-vanishing muon-tau chemical potential).

Note that from our bound in Eq. (6.4), a muon-tau neutrino asymmetry can induce a maximal shift $\Delta N_{\rm eff} \sim 0.1$.

Moving to *2)*, we compute $n \leftrightarrow p$ matrix elements beyond the Born approximation [297], namely including isospin-breaking contributions like finite-mass [301] and QED [378, 379] corrections, as well as finite-temperature effects [285], following the implementation carried out in [18]. Most importantly, we evaluate weak-interaction rates integrating over nucleon thermal distributions with chemical potential $\mu_{\mathcal{Q}} \equiv \mu_n - \mu_p = -\mu_{\nu_e} \neq 0$.

Finally, regarding *3)*, we proceed evolving the abundances according to the network of thermonuclear reactions comprising the main processes listed in **Table 1** of Ref. [318] (plus $^3\mathrm{He}(p,\gamma)^4\mathrm{He}$, taken from [307]), yielding state-of-the-art predictions for $Y_{\rm P}$ and D/H. In particular, for the radiative neutron capture rate we adopt the MCMC result of Ref. [380], while in the treatment of the other 10 key reactions we distinguish two approaches:

- PRIMAT driven: Nuclear rates are implemented according to the statistical determination of Refs [381, 382, 383, 384, 385, 386], i.e. following theoretical ab-initio energy modeling tuned to datasets for which an estimate of systematic errors is available [18, 264, 270].
- NACRE II driven: Nuclear rates are interpolated from the updated NACRE compilation [309], comprising charged-particle-induced reactions [2]; for $\mathrm{D}(p,\gamma)^3\mathrm{He}$ we use the LUNA result reported in [320]; for $^7\mathrm{Be}(n,p)^7\mathrm{Li}$ we adopt the baseline of Ref. [317].

We perform a Bayesian analysis of early universe data constructing the cosmological test statistic:

$$\mathrm{TS}_{\rm cosmo} \equiv -2(\log \mathcal{L}_{\rm CMB} + \log \mathcal{L}_{\rm BBN}) \ ; \tag{6.6}$$

[2] In particular, for the key reactions $\mathrm{D}(d,n)^3\mathrm{He}$ and $\mathrm{D}(d,p)^3\mathrm{H}$ we either interpolate rates and corresponding uncertainties from the NACRE II numerical database or from the outcome of the Bayesian analysis of Ref. [382].

the CMB likelihood explicitly reads:

$$\log \mathcal{L}_{\rm CMB} = -\frac{1}{2}\Delta\vec{v}^{\,T}\,\mathcal{C}_{\rm CMB}^{-1}\,\Delta\vec{v}\ , \tag{6.7}$$

with $\Delta\vec{v} \equiv \vec{v}^{\,\rm th} - \vec{v}$, $\vec{v} = (\mathrm{Y_P}, \Omega_B h^2, N_{\rm eff})^T$, using mean and standard-deviation values from the TTTEEE + low-ℓ + BAO + lensing Planck run varying also $\mathrm{Y_P}$, $N_{\rm eff}$ [342, 369] and also retrieving correlations in $\mathcal{C}_{\rm CMB}$ from [387]. The BBN likelihood of our study corresponds to:

$$\log \mathcal{L}_{\rm BBN} = -\frac{1}{2}\sum_X \left(\frac{X^{\rm th} - X}{\sigma_X}\right)^2\ , \tag{6.8}$$

where $X = \{\mathrm{Y_P}, \mathrm{D/H}\}$, and we use the measurements: $\mathrm{Y_P} = 0.2370(34)$ [356], $\mathrm{D/H} = 0.00002547(25)$ [354].

The parameters we infer are varied according to uniform priors: $-2 \leq \Delta N_{\rm eff} \leq 2$, $-0.2 \leq \xi_\nu \leq 0.2$, $1 \leq (\eta_B \times 10^{10}) \leq 10$ (using $\eta_B \times 10^{10} \simeq 273.748\ \Omega_B h^2$). We marginalize over the neutron lifetime and the adopted nuclear uncertainties. From the PDG analysis [354] we assign the Gaussian prior: $\tau_n = (879.4 \pm 0.6)$ s to the neutron lifetime. For the uncertainties in the nuclear rates, we assign log-normal distributions following the method detailed in Ref. [322], varying a total of 12 additional nuisance parameters.

We perform an MCMC analysis via the `emcee` [388] package, using 60 walkers with 2100 steps each, discarding the first 700 steps of each walker as burn-in. From the best-fit values minimizing $\mathrm{TS_{cosmo}}$ we also compute for each scenario the Information Criterion [389, 390] $IC \equiv -2\log\hat{\mathcal{L}}_{\rm BBN} + 2(k-1)$, k being the number of BSM parameters and accounting for the CMB information as an extra constraint in the fit. Then, we evaluate the IC difference with respect to the SM prediction of the primordial light abundances within a given approach: $\Delta IC \sim \mathcal{O}(1)$ ($\sim \mathcal{O}(10)$) provides positive (strong) support in favor of NP beyond ΛCDM according to the canonical scales of evidence [391].

6.4 Results

Scenario	Approach	Y_P	$D/H \times 10^5$	ΔN_{eff}	ξ_ν	$\eta_B \times 10^{10}$	ΔIC
SM prediction	PRIMAT driven	0.24715(14)	2.439(36)	–	–	6.137(38)	–
	NACRE II driven	0.24706(16)	2.51(10)	–	–	6.137(38)	–
ΔN_{eff} *BSM fit*	PRIMAT driven	0.2472(13)	2.472(45)	0.02(20)	–	6.091(66)	2
	NACRE II driven	0.2455(15)	2.46(11)	-0.26(23)	–	6.093(67)	0
$(\Delta N_{eff}, \xi_\nu)$ *BSM fit*	PRIMAT driven	0.2383(42)	2.474(46)	0.29(23)	0.044(20)	6.119(65)	8
	NACRE II driven	0.2372(43)	2.47(11)	0.00(23)	0.041(21)	6.114(68)	5

Table 6.1: 68% probability interval for the posterior distribution of the main observables and parameters in the scenarios considered in this work. For the BSM fits, improvement with respect to the SM is given by $\Delta IC > 0$, see text for more details.

In Figure 6.1 we report the main result of our study: the 68% and 95% probability region for the primordial lepton asymmetry ξ_ν and the extra-relativistic degrees of freedom ΔN_{eff} as determined by TS_{cosmo}, Eq. (6.6), corresponding to the two approaches to thermonuclear rates described in the previous section. From the ΛCDM limit highlighted in the same figure, we can conclude that a BSM fit to a dataset that includes the newly measured EMPGS by Subaru [356] favors at present a non-vanishing asymmetry in the neutrino sector.

In Figure 6.1 we also observe that, dependent on the approach to nuclear uncertainties, a shift of N_{eff} of $\mathcal{O}(1)$ can be simultaneously favored by current cosmological data. Note that the size of the shift in the number of relativistic degrees of freedom can be interpreted within the 68% probability region as the result of a large neutrino asymmetry in the muon-tau sector in case flavor equilibration has not been fully realized.

To further investigate the different outcome from each approach, we show in Figure 6.2 the posterior probability density function (p.d.f.) for the BBN observables Y_P and D/H. We report both the result from the BSM fit varying both ξ_ν and N_{eff} as well as the one from the SM prediction, obtained fixing the BSM parameters to 0 and replacing the CMB likelihood with the Gaussian prior: $\Omega_B h^2 = 0.02242 \pm 0.00014$, from the ΛCDM Planck

analysis (TTTEEE + low-ℓ + BAO + lensing) [342, 369]. In the same figure, we also highlight with vertical dark green bands the measurements adopted in our BBN analysis via Eq. (6.8), and report the PDG 2021 value $\mathrm{Y_P} = 0.245(3)$ [354], in optimal agreement with the analysis of Ref. [309] that comprises the set studied also in [356] without the new EMPGs from Subaru.

Figure 6.2 neatly highlights two tensions in the limit where BSM physics is not accounted for:

- A discrepancy at the 3σ level between the SM prediction of $\mathrm{Y_P}$ and the newly inferred helium-4 mass-fraction value, regardless of the approach taken for the thermonuclear reactions; the tension is fully driven by the new measurement delivered by Ref. [356], while the overall significance also depends on the precision obtained for the inference of the cosmological baryon abundance within ΛCDM;
- A tension of about 2σ significance between the SM prediction of D/H and the PDG 2021 recommended measurement [354] when the PRIMAT driven approach is taken for the analysis of the key thermonuclear reactions involved, in line with recent discussions in the literature [270].

From Figure 6.2, it is clear that a shift of ΔN_{eff} is required together with $\xi_\nu \neq 0$ only when the PRIMAT driven approach is considered, in order to address the discrepancy consequently present in the fit in relation to the observed primordial deuterium abundance. In the same figure it is also evident how the PDG 2021 recommended measurement of the helium-4 mass fraction is in perfect agreement with the SM prediction, and our inference for a nonzero degeneracy parameter ξ_ν is the consequence of adopting the new $\mathrm{Y_P}$ measurement [356].

We report in Table 6.1 the 68% probability interval for the scenarios discussed so far as well as the one for the BSM fit where only ΔN_{eff} is considered. Looking at the ΔIC values, we

conclude that a joint analysis of BBN + CMB data provides mild to strong evidence for a scenario with non-vanishing lepton asymmetry. Moreover, within the NACRE II approach no notable support from data is found for the presence of extra relativistic degrees of freedom in the early universe, whereas a scenario where only $\Delta N_{\rm eff}$ is varied may be slightly preferred by data over the SM in the case of the PRIMAT driven approach, partially ameliorating a potential *deuterium anomaly*.

6.5 Discussion and outlook

Our study based on the addition of the newly observed EMPGs [356] to the original sample of ref. [357] suggests that today's total lepton asymmetry, Eq. (6.1), is large, $\eta_L \gg \eta_B$, ranging from $\sim 10^{-2}$ to $\sim 1/4$, depending on the details of the neutrino sector.

There are common factors that any successful explanation of a large η_L must share. At temperatures above the scale of electroweak symmetry restoration, electroweak sphalerons equilibrate $B + L$ such that the final total lepton and baryon asymmetries differ by a $\mathcal{O}(1)$ factor [392, 393]. Thus, for a difference of orders of magnitude between η_L and η_B to persist, it must either be generated after the sphalerons become inactive (in the SM, at the electroweak phase transition around temperatures of order 100 GeV) or the individual flavor asymmetries must be distributed such that the net L is much smaller than the individual asymmetries [282]. The latter scenario would point to flavor-dependent NP in the lepton sector, with possible interesting implications for the smallness of η_B as well, see for instance [394, 282, 395, 396].

Because equilibration of neutrino species depends both on imprecisely determined mixing parameters and the assumed initial asymmetry in each flavor [373], mapping the inferred neutrino asymmetries during BBN into the space of consistent initial conditions at some

earlier time is an interesting inverse problem; it requires also assumptions on the interpretation of the inference carried out here for $\Delta N_{\rm eff}$, and it is beyond the scope of this work. Several examples of theories capable of generating a sufficiently large and persistent lepton-flavored neutrino asymmetry via variations of the Affleck-Dine mechanism [397] exist in the literature [398, 399, 282, 283].

Acknowledgements and Author Contributions Statement

We thank Federico Bianchini, Kevork Abazajian, Manoj Kaplinghat, Rouven Essig and Peizhi Du for discussion.

Using the CASRAI CRediT Contributor Roles Taxonomy: Conceptualization, A.K.B., T.M.P.T., M.V.; Data curation, A.K.B., M.V.; Formal analysis, A.K.B., T.M.P.T., M.V.; Funding acquisition, T.M.P.T., M.V.; Investigation, A.K.B., T.M.P.T., M.V.; Methodology, A.K.B., T.M.P.T., M.V.; Project administration, T.M.P.T., M.V.; Software, A.K.B., M.V.; Supervision, T.M.P.T.; Validation, A.K.B., M.V.; Visualization, A.K.B., M.V.; Writing – original draft, A.K.B., T.M.P.T., M.V.; Writing – review and editing, A.K.B., T.M.P.T., M.V.

Chapter 7

Constraints on Variation of the Weak Scale from Big Bang Nucleosynthesis

This chapter is heavily based on work previously published in collaboration with Venus Keus, Marc Sher, and Tim M.P. Tait [23].

7.1 Introduction

The ΛCDM model has been extraordinarily successful in describing the cosmological history and evolution of the universe. However, there are some anomalies in the model. The most well-known is the Hubble tension, in which the value of the Hubble parameter measured from the cosmic microwave background (CMB) by Planck [342], $H_0 = 67.4 \pm 0.5$ km/s/Mpc, differs by 5σ from the measurement of Cepheids and Type-Ia supernovae by the SH0ES collaboration[400], $H_0 = 73.0 \pm 1.0$ km/s/Mpc. There have been numerous studies trying to explain this discrepancy (see Ref. [401] for an extensive review). Another anomaly concerns the ^{4}He abundance, Y_p, from Big Bang Nucleosynthesis (BBN). A recent report

by EMPRESS [356] adds measurements from 10 additional extremely metal-poor galaxies which, combined with the previously existing dataset, results in a fit to $Y_p = 0.2370 \pm 0.0033$ which differs from the value obtained based only the pre-existing data [402, 403, 404]. This has led to several studies, such as the implications of the result for the lepton asymmetry [283, 22, 405, 284].

The variation of fundamental constants is a subject that has been around since Dirac's large number hypothesis [207]. Most work in the past has focused on variation in the fine-structure constant [406, 407, 408] and the electron mass [409, 410] and both have been used to study the above anomalies. Variation of the fine-structure constant to solve the Hubble tension was proposed in a mirror dark sector model recently [411]. Variation of the electron mass [409] has also been proposed as a solution to the Hubble tension in Ref. [412] in which they also studied the effects on Big Bang Nucleosynthesis; a mechanism for such a variation was proposed in Ref. [413]. A detailed series of papers studying variation of both the fine-structure constant and the electron mass is by Hart and Chluba [414, 415, 416]. The helium anomaly is more recent. It was shown by Seto, Takahashi and Toda [417] that a variation in the fine-structure constant alone would be sufficient to explain the Y_p anomaly.

While one can consider variation of the fine-structure constant and the electron mass, we feel that it would be more reasonable to consider variation in the vacuum expectation value (vev) of the Higgs field (or, equivalently, the Higgs mass term). The vev is the only dimensionful parameter in the Standard Model, and it is also the most mysterious, in the sense that its value is many, many orders of magnitude smaller that one would naturally expect. In addition, the Standard Model vev is cosmologically dynamical, and is predicted to vary substantially during the electroweak phase transition. At high temperature, the gauge symmetry is restored [418, 419] and the vev is zero. As the universe cools, a transition occurs and the vev increases to the low temperature value observed today. Thus, it would seem to be more reasonable to consider variations in the vev rather than in one of the many dimen-

sionless parameters. For example, one can imagine an extended model in which the Higgs vev slowly rolls to its current value but has not quite reached it at the MeV temperature scale. One might wonder if that might affect later observables such as the CMB, but that occurs at the ∼eV temperature scale and we presume that the slow roll would have essentially completed by then.

The possible effects of a changing vev on BBN was first discussed in 1988 by Dixit and Sher [420], but this was a crude calculation that only considered the ^{4}He abundance. There have since been several studies [421, 422, 423, 424] of BBN due to a changing vev and other studies [425, 426] on the effects of changing many parameters, including the vev. These papers all include the effects not only on the electron mass but also on quark masses, which subsequently affect the pion and other meson masses and thus the strong force (leading, for example, to changes in the deuteron binding energy). Other works did not directly discuss modifying the vev, but only Λ_{QCD} [427], the deuteron binding energy [428] and quark masses [429]. Finally, there has also been work done looking at the effect of changing the strength of the weak interaction at late times [430]. Like these works, our approach is phenomenological and we will not present a specific model with a changing vev at the time of BBN. A recent paper [431] did present a model in which the Higgs field may not achieve a thermal spectrum at the time of nucleosynthesis - the effects on the vev are unclear. Further investigation of this model would be interesting.

However, these works did not include the effects of a changing Higgs vev on the value of Λ_{QCD}, which clearly will affect strong interaction dynamics. As noted by Agrawal, *et al.* [432, 433], a variation in the Higgs vev will modify all of the quark masses and this in turn will impact the running of the strong coupling constant through the quark thresholds. The effect is somewhat smaller (they find Λ_{QCD} varying by roughly $(v/v_0)^{0.25}$)), but can still be substantial. These effects were included in Ref. [434] which was an anthropic principle based study of the triple alpha process in stars, but have not been included in analyses of

BBN.

Since these above works, we have learned much more about the current baryon-photon ratio, the nuclear abundances and have better codes [17]. One such code, PRyMordial was created to fill several gaps that currently exist in the landscape of publicly available BBN codes. Namely, the code allows for easy and flexible exploration of a variety of new physics models, including the investigation of varying input parameters on both N_{eff} and the final abundance values. PRyMordial also allows users to examine the uncertainties in different sets of thermonuclear reaction rates and to scale these chosen reaction rates as desired. In addition, PRyMordial calculates the thermodynamics of the plasma from first principles, the results of which serve as the initial conditions for the full calculation of neutron to proton conversion. Unlike other codes, PRyMordial is written in `Python`, allowing its users to perform Monte Carlo (MC) analyses with ease by interfacing with standard MC libraries. In order to maximize efficiency, the code also has an option to use `Julia` to speed up the computation. PRyMordial has already been used by several groups to study the effects of a variety of new physics scenarios on BBN [22, 435, 436, 437, 438, 439, 295]. In this paper, using PRyMordial, we will calculate the abundances of light nuclei as a function of the Higgs vev including all of these effects and in light of the EMPRESS result.

7.2 BBN as a Function of the Higgs vev

In looking at the effect of changing the Higgs vev on the production of light elements, there are several important parameters that determine the abundance of these light elements: the neutron-proton mass difference, the deuteron binding energy, and the rates of several key thermonuclear reactions involving light nuclei. In this section, we consider how each of these vary with the Higgs vev, in turn.

7.2.1 Neutron-Proton Mass Difference

In order to calculate the way in which the neutron-proton mass difference changes with a changing vev, we first considered the change in the masses of their constituent quarks. When the vev is varied, the quark masses receive fractional corrections of $\delta v/v$. While the bulk of the neutron and proton masses are the result of confinement, their masses, and most importantly their mass difference, is sensitive to the change in quark masses. As is well known, the down quark is roughly 2.5 MeV heavier than the up quark, but the neutron is only 1.293 MeV heavier than the proton. The discrepancy is due to the electromagnetic energy of the up quarks within the proton, which is thus approximately 1.2 MeV, independent of the Higgs vev. As a result, we take the neutron-proton mass difference in MeV to be

$$\frac{m_n - m_p}{\text{MeV}} = 2.493\ (1 + \frac{\delta v}{v}) - 1.2\ . \tag{7.1}$$

This mass difference has a direct impact on the rate of the neutron-proton inter-conversion which occurs via six reactions which, along with protons and neutrons, also involves electrons and electron neutrinos. At temperatures above about 1 MeV, these reactions were in chemical equilibrium and conversion happened freely and regularly. In his 1972 book, Weinberg [440] lists the reaction rates for these six processes and one can see that both the variation in the neutron-proton mass difference and the electron mass, which varies as $\delta v/v$ like the quarks, will suffice to determine the variation in these processes. By including information about the neutron lifetime, the final ratio of the number of neutrons to the number of protons at the beginning of BBN can be determined. Because almost all of the neutrons end up in ^{4}He, this ratio allows us to crudely calculate the ^{4}He abundance. However, to more precisely calculate the ^{4}He abundance, along with the abundances of deuterium, tritium and ^{3}He nuclei, it is necessary to include in the calculation at least twelve thermonuclear reactions, all of which play essential roles in the formation of nuclei during BBN.

7.2.2 $n \leftrightarrow p$ Conversion Rates

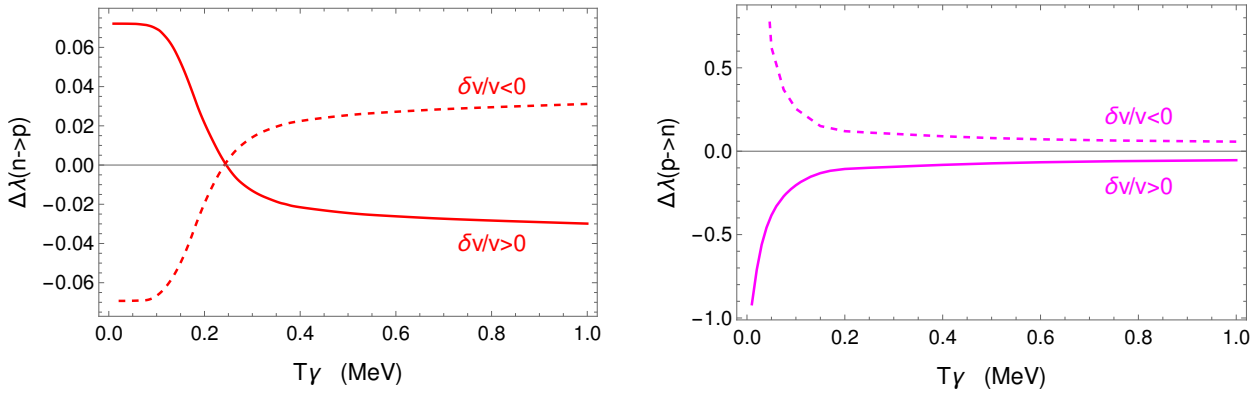

Figure 7.1: The fractional change in the $\lambda(n \to p)$ and $\lambda(p \to n)$ rates for $d \equiv |\delta v/v| = 0.01$. Note that the fractional change in $\lambda(p \to n)$ gets very large at low temperatures since the rate itself vanishes at low temperature. For each rate, we include a factor of $1/(1+d)^4$ coming from the shift in the W mass.

The theoretical expressions for the total $n \to p$ and $p \to n$ conversion rates are given in Weinberg [440]. Using Eq. (7.1) for the neutron-proton mass difference and scaling the electron mass fractionally as $\delta v/v$, the relationship between the electron and neutrino temperatures is slightly modified. Putting these effects together with the factor of $1/(1+\delta v/v)^4$ coming from the shift in the W boson mass, the resulting fractional change for the $n \to p$ and $p \to n$ conversion rates as a function of T_γ, the radiation temperature, for $d \equiv |\delta v/v| = 0.01$, are shown in Figure 1. The fractional changes in the rates scale approximately linearly with δv.

7.2.3 Deuteron Binding Energy

In addition to these thermonuclear reaction rates, the binding energy of the deuteron is an important component of the calculation. Its relatively low value leads to the well-known deuterium bottleneck, which refers to the time period during which nucleosynthesis had begun, but the average temperature of photons in the bath was higher than the deuterium binding energy. As a result, almost immediately after deuterium formed in the aforemen-

tioned process, it would photo-disassociate, and until the photon bath had cooled below this value, BBN was unable to proceed.

In order to understand the way in which the deuteron binding energy varies with a changing vev, we first compute the way in which the pion mass varies. The pion mass in QCD is given by $m_\pi^2 \simeq (m_u + m_d) f_\pi$. While the quark masses scale linearly with δv, the value of f_π is proportional to Λ_{QCD}. As noted earlier, this will scale differently from the quark masses and will depend on the vev through mass thresholds. In Appendix A, we show that Λ_{QCD} scales as $(\delta v)^{0.25}$, and thus, the pion mass scales as $(\delta v)^{1.25/2}$.

We now turn to the deuteron binding energy itself. Since we are interested in the impact of a small change in the vev, high precision in the standard calculation is not necessary. We model the nucleon-nucleon potential for the deuteron as an exchange of pion, σ and ω mesons as discussed in the review article by Meissner [441]. The pion mass, as discussed above, scales as $(\delta v/v)^{1.25/2}$. The ω mass comes primarily from QCD and so scales as $(\delta v/v)^{0.25}$. The σ is believed to be a two-pion correlated state. Lin and Serot [442] calculated the σ mass in terms of the pion-nucleon coupling, the pion mass and the nucleon mass. Varying the masses in their expressions, we find that the σ mass is insensitive to the pion mass, scaling as Λ_{QCD}.

The net result of π, ω, and σ exchange results in a potential energy function for the binding of a neutron and a proton which can be modelled as the sum of three Yukawa potentials - repulsive from the ω and attractive from σ and π. Each potential has a corresponding coupling constant indicated by g_π, g_σ and g_ω. These couplings are in principle determined by QCD, but cannot be computed in perturbation theory, and so we constrain them by requiring that the resulting binding energy of the deuteron matches its experimentally determined value of 2.2 MeV at $d \equiv |\delta v/v| = 0$. This selects families of viable parameters which can be found for $d = 0$ by adjusting these three parameters such that the solution to the Schrödinger equation gives a binding energy of 2.2 MeV. One such solution[1], for example,

[1]We have examined other values of g_π, g_σ and g_ω which give the correct $d = 0$ binding energy of 2.2 MeV,

has $g_\pi = 11.97$, $g_\sigma = 8.46$, $g_\omega = 21.19$. These are dimensionless parameters and are not expected to change much in response to small changes in the vev. Results for small $d \neq 0$ are obtained by adjusting the meson masses for the particular d of interest as described above, and recalculating the binding energy. The resulting binding energies are presented in Figure 7.2 for positive and negative values of $\delta v/v$. Values of $|\delta v/v| > 0.1$ lead to either very large binding energies or an unbounded deuteron for positive and negative values, respectively. Since both very large binding energies and an unbounded deuteron, lead to predictions for the light elements abundances very far outside of what has been observed, we find it unnecessary to consider values of $\delta v/v$ outside of this range.

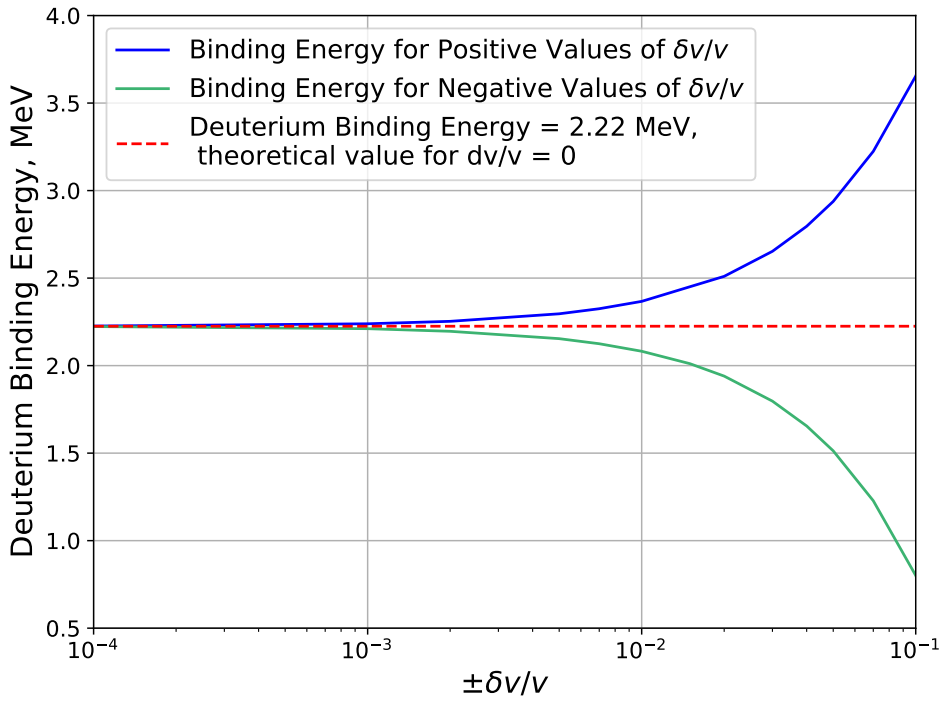

Figure 7.2: Value of the deuterium binding energy with varied Higgs vev for positive and negative values of $\delta v/v$.

and find that they make very similar predictions for small d to the ones we have chosen.

7.2.4 Thermonuclear Reaction Rates

With the change in the $n \leftrightarrow p$ processes and the deuteron binding energy in hand, we turn to the other nuclear processes in BBN. There are 12 key reactions which are needed to predict deuterium and helium abundances and an additional 51 reactions to accurately predict the lithium abundance which involve the binding energies and matrix elements of heavier nuclei.

These reaction rates are typically determined empirically, making it difficult to predict their dependence on the vev from first principles. However, they do not involve the weak interactions and are not as sensitive to the pion mass and thus on dimensional grounds, we assume their rates vary as Λ_{QCD}, or $v^{0.25}$, which is expected to be a decent approximation since the pion interactions are long-range.

7.3 Primordial Abdundances

Assembling all of the changes in the inputs to BBN described above, we implement them in PRyMordial to determine the abundances of primordial helium and deuterium as a function of $\delta v/v$. Starting from a calculated set of initial conditions, including the ratio of photon to neutrino temperatures, the light element abundances are determined via a network of Boltzmann equations. This system of equations is solved in three steps. First, the neutron to proton ratio at the temperature of neutron freeze out is determined by analyzing the neutron to proton conversion rates.[2] Next, using the calculated abundance values of protons and neutrons, the network of Boltzmann equations using 18 of the 63 thermonuclear rates is evolved down to the temperature of deuterium photo-disassociation. Finally, the network is further evolved down to temperatures of $\mathcal{O}(\text{keV})$ to determine the final primordial abundance values of each light element.

[2]For explicit formulas, please see equations 15.7.14 and 15.7.15 in Weinberg's book *Gravitation and Cosmology: Principles and Applications of the General Theory of Relativity* [440].

The result for Y_p, which characterizes the abundance of ^{4}He, is shown in Figure 3 for both positive and negative values of $\delta v/v$. The blue and green lines correspond to the predicted

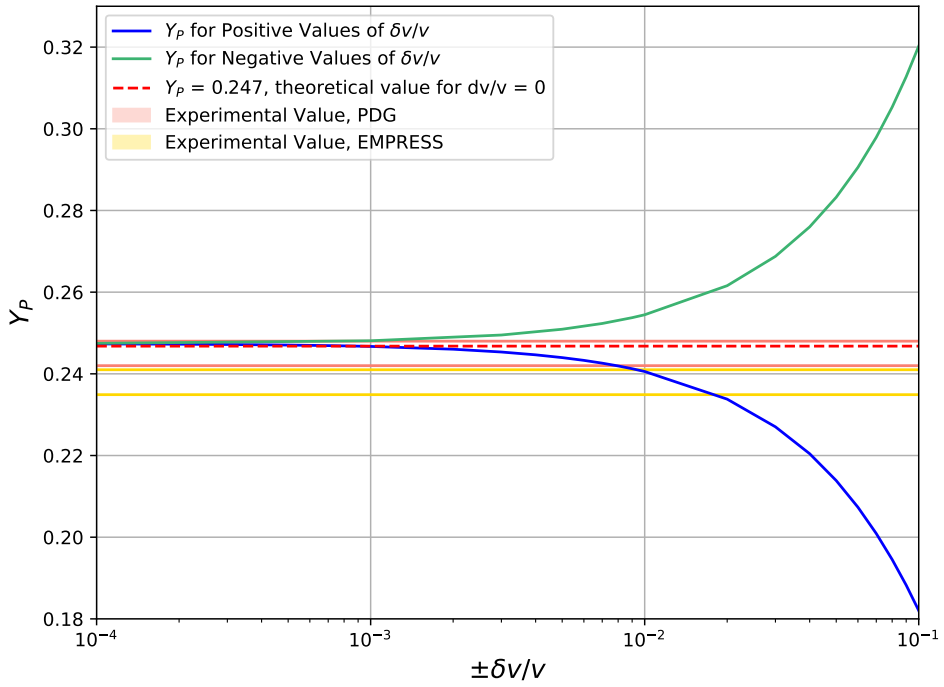

Figure 7.3: Value of the abundance of ^{4}He, Y_p, with varying Higgs vev for positive and negative values of $\delta v/v$. The red dashed line is the standard result without a change in the Higgs vev and the blue and green lines are the results with the change. The coral and gold boxes give the experimental values from the Particle Data Group and from the recent EMPRESS experiment.

^{4}He abundance from PRyMordial for positive and negative values of $\delta v/v$, respectively. The uncertainty for Y_p is negligible. The experimental value from Refs. [402, 403] (as listed in the Particle Data Group [443] summary) and the 2σ uncertainties are shown in shaded pink, and the recent result from EMPRESS [356] in shaded yellow. For negative $\delta v/v$, the 2σ upper bound on the magnitude is approximately 0.001, whereas for positive $\delta v/v$, the magnitude must be less than 0.008 based on the PDG result and less than 0.02 using the EMPRESS result. If the EMPRESS result turns out to be correct, $\delta v = 0$ would be mildly excluded, and δv between 0.008 and 0.02 would be able to explain the ^{4}He abundance.

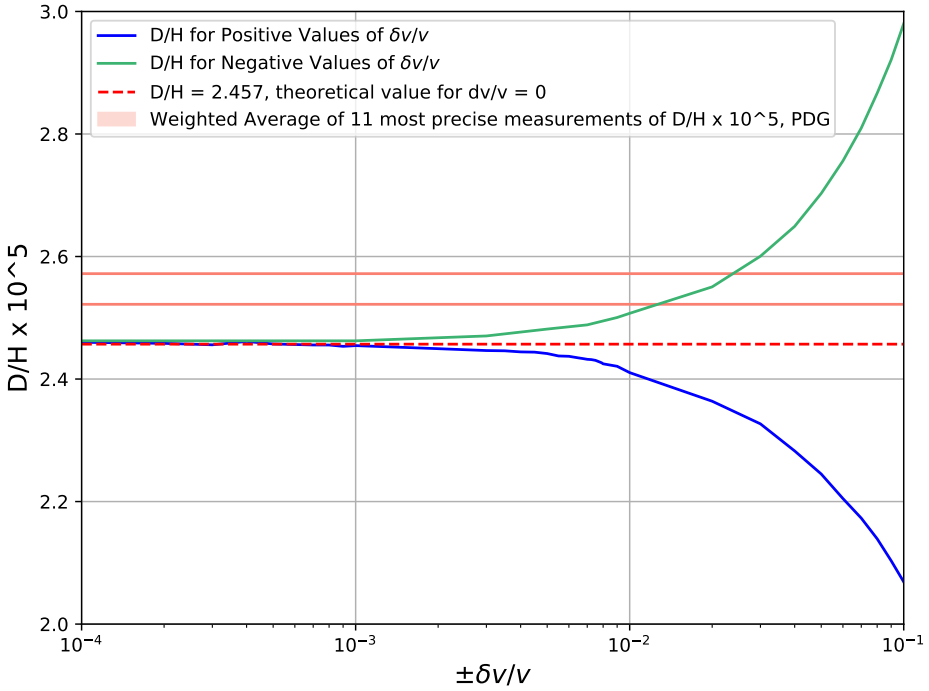

Figure 7.4: Value of the abundance of deuterium with varying Higgs vev for positive and negative values of $\delta v/v$. The red dashed line is the standard result without a change in the Higgs vev and the blue and green lines are the results with the change. The coral box gives the experimental values from the Particle Data Group. The error in the theoretical curves are similar to the error in the experimental values, as discussed in the text.

In Figure 4, we show the results for the deuterium abundance. Here, the theoretical calculation of the abundance has an uncertainty of 0.05, which is similar to the error in the experimental value [443, 444]. Thus, the $\delta v = 0$ limit has roughly a 2σ discrepancy between the theoretical and experimental values. For negative values of $\delta v/v$, we see that the magnitude of $\delta v/v$ must be less than approximately 0.025, but for positive $\delta v/v$ the magnitude must be substantially smaller. This is somewhat unfortunate since positive $\delta v/v$ is needed to explain the EMPRESS result for Y_p, but that would make the discrepancy with deuterium much worse. Thus changing the vev can explain one, but not both, of the anomalies.

7.4 Conclusions

Originally motivated by anthropic arguments, many have studied the possibility that some of the constants of nature are time-dependent. Astrophysical studies have bounded some parameters as have some cosmological studies. Recently, the EMPRESS collaboration reported a measurement of the primordial ^{4}He abundance which is somewhat over 3σ from the theoretical value. There is also a small 2σ discrepancy in the deuterium abundance. In this paper, we have considered the possibility that a difference in the Higgs vev between the time of BBN and the present could be responsible for one or both of these discrepancies. We choose the Higgs vev to vary because it is the only dimensionful parameter of the Standard Model and is already known to vary during the earlier electroweak phase transition.

This was studied some time ago, but previous authors did not include the fact that the QCD scale will also vary if the quark masses vary, due to threshold effects. They also did not use the latest BBN codes, which are more accurate than previous ones. The varying quark masses and QCD scale will have a substantial effect on all nuclear reaction rates as well as the binding energy of the deuteron.

We find that the ^{4}He abundance can be noticeably affected if the change in the Higgs vev is a few parts per thousand or more. If $\delta v/v$ is between 0.008 and 0.02, then the prediction fits well within the EMPRESS calculation error bars. If one instead uses the older PDG results, then one must (at 2σ) have $\delta v/v$ less than 0.008 and greater than -0.001.

The deuterium abundance is also affected. Here, a positive value of $\delta v/v$ makes the discrepancy with the theoretical prediction worse. A negative value will fit within 2σ as long as its magnitude is less then 0.025. Together, we see that no value will be able to explain both the EMPRESS and deuterium anomalies, but can certainly explain either one. Clearly, more experimental results for the ^{4}He abundance are needed as are more theoretical studies of the deuterium abundance.

Acknowledgements and Author Contributions Statement

We are very grateful for conversations with Meyer and Meißner related to their Ref. [445], which revealed a coding error in our earlier results but confirmed our over-all conclusions. We thank Albert Stadler for discussions. AKB and TMPT thank Mauro Valli for previous collaboration on PRyMordial.

Using the CASRAI CRediT Contributor Roles Taxonomy: Conceptualization, A.K.B., V.K., M.S., T.M.P.T.; Data curation, A.K.B.; Formal analysis, A.K.B., V.K., M.S.; Funding acquisition, V.K., M.S., T.M.P.T.; Investigation, A.K.B., V.K., M.S., T.M.P.T.; Methodology, A.K.B., V.K., M.S., T.M.P.T.; Project administration, M.S.; Software, A.K.B., T.M.P.T.; Supervision, V.K., M.S., T.M.P.T.; Validation, A.K.B., V.K., M.S., T.M.P.T.; Visualization, A.K.B., V.K., M.S.; Writing – original draft, A.K.B., V.K., M.S., T.M.P.T.; Writing – review and editing, A.K.B., V.K., M.S., T.M.P.T.

Appendix 7A: The evolution of the strong coupling constant

A crude approximation to the scaling is obtained by integrating the one-loop renormalization group equations for the strong coupling constant from a scale well above the top quark mass down to somewhat below the charm quark mass and then using the standard formula to deduce Λ_{QCD}. Using a mass-independent renormalization scheme at one-loop, for Q much larger than $2m_t$, one has

$$\frac{1}{\alpha(1\text{ GeV})^2} - \frac{1}{\alpha(Q^2)} = \frac{1}{12\pi}(21\log 4m_t/Q^2 + 23\log m_b^2/m_t^2 + 25\log m_c^2/m_b^2 + 27\log 1\text{ GeV}^2/m_c^2)$$

Now, if one multiplies all of the quark masses by $1 + \delta v/v$, one finds that

$$\frac{1}{\alpha_{new}(1\text{ GeV})^2} - \frac{1}{\alpha_{old}(1\text{ GeV})^2} = \frac{1}{12\pi}(21-27)*2\frac{\delta v}{v} = -\frac{1}{\pi}\frac{\delta v}{v},$$

and plugging this into the standard one-loop formula for Λ_{QCD},

$$\Lambda^2 \equiv \mu^2 e^{-\frac{4\pi}{\beta_0 \alpha_s(\mu^2)}}, \tag{7.2}$$

one finds that

$$\Lambda_{new} = \mu\ \exp\frac{-6\pi}{27\alpha_{new}} = \mu\ \exp\left(\frac{-6\pi}{27\alpha_{old}} + \frac{6}{27}\frac{\delta v}{v}\right) = \Lambda_{old}(1 + \frac{2}{9}\frac{\delta v}{v}), \tag{7.3}$$

which is close to the results in [432, 433]. Thus, our crude approximation yields Λ_{QCD} scaling as $(\delta v/v)^{2/9}$

To be more precise, we integrate the 2 loop renormalization group equations. The scale dependence of the strong coupling constant is controlled by the β-function which can be expressed as a perturbative series:

$$Q^2\frac{\partial}{\partial Q^2}\frac{\alpha_s}{4\pi} \quad = \beta(\alpha_s) = -\left(\tfrac{\alpha_s}{4\pi}\right)^2 \sum_{n=0}\left(\tfrac{\alpha_s}{4\pi}\right)^n \beta_n. \tag{7.4}$$

The values of the first terms of the β-series are:

$$\beta_0 = 11 - \frac{2}{3}n_f, \tag{7.5}$$

at 1-loop level and

$$\beta_1 = 102 - \frac{38}{3}n_f, \tag{7.6}$$

at 2-loop level with n_f the number of quark flavors active at the scale Q^2.

The exact analytical solution to Eq. (7.4) is known only to β_0 order, and thus we integrate numerically, defining Λ_{QCD} to be the scale at which α_s diverges. We find that Λ_{QCD} scales as $(\delta v/v)^{0.25}$, with the exponent varying from 0.245 to 0.255 over the entire possible range of Λ_{QCD}. Thus, we use 0.25 as the exponent.

Chapter 8

Conclusions and Outlook

In this thesis we have detailed several ways to explore unanswered questions relating to the nature of the universe using cosmology and astro-particle physics. We did this through a diverse range of methodologies, including developing models of DM to explain a potential indirect detection signal, using the path integral formalism to understand the way in which time evolves in quantum cosmology, and via BBN studies.

In Chapter 2 we discussed the presence of an excess γ-ray signal toward the GC. Leading explanations for the signal include mismodeling of the Galactic diffuse emission along the line of sight, an unresolved population of millisecond pulsars, and/or the annihilation of DM. Recently, evidence for another excess γ-ray signal has been reported toward the outer halo of M31. We interpreted the excess signals from both the GC and outer halo of M31 in the framework of DM annihilation, and showed that the two spectra are consistent with a DM origin once J-factors are taken into account. We further compared the excesses to models of DM annihilation, and determined the corresponding best-fit parameters. We found good fits to the spectrum both in two body and four body annihilation modes.

In Chapter 3 we further explored the excess γ-ray signal toward the outer halo of M31. As

already established in Chapter 2, although other explanations are plausible, the possibility that the signal arises from DM annihilation is valid. In this chapter we interpreted the excess using one representative case: WIMP DM annihilating to bottom quarks, and we performed a detailed study of the systematic uncertainty in the J-factor for the M31 field. We found that the signal favors a DM particle with a mass of ∼45-72 GeV. While the mass is well constrained, the systematic uncertainty in the cross section spans 3 orders of magnitude, ranging from $\sim 5 \times 10^{-27}$ to 5×10^{-24} cm^{3}s^{-1}. This high uncertainty is due to two main factors: an uncertainty in the substructure nature and geometry of the DM halos for both M31 and the MW, and correspondingly, an uncertainty in the contribution to the signal from the MW's DM halo along the line of sight. However, under the conditions that the minimum subhalo mass is $\leq 10^{-6}$ times the mass of the sun and the actual contribution from the MW's DM halo along the line of sight is at least ∼30% of its total value, we showed that there is a large overlap with the DM interpretations of both the GC excess and the antiproton excess, while also being compatible with the limits for the MW dwarf spheroidals. In addition, we summarized the results from numerous complementary DM searches in the energy range 10 GeV – 300 GeV corresponding to the GC excess and identified a region in parameter space that still remains viable for discovery of the DM particle.

In Chapter 4 we showed, in the simplified setting of mini-superspace, that time evolution of cosmological space-time can be obtained using a gauge fixed path integral, as long as we do not integrate over proper time. Using this gauge fixed action we constructed a Hamiltonian in the coherent - or classical - state basis. We showed that by construction the coherent states satisfy the classical dynamical equations of General Relativity. However, they do not satisfy the Hamiltonian constraint. A consequence of this is that the Wheeler-DeWitt equation should not be satisfied in quantum gravity. Classical states have a natural non-trivial time evolution since they are not eigenstates of the Hamiltonian. A general feature of the unconstrained quantum theory of gravity is the prediction of a pressureless dark matter component of either sign energy density in the classical universe which may lead to novel

phenomenology, which deserves further exploration.

In Chapter 5 we presented PRyMordial: A package dedicated to efficient computations of observables in the early universe with the focus on the cosmological era of Big Bang Nucleosynthesis (BBN). The code offers fast and precise evaluation of BBN light-element abundances together with the effective number of relativistic degrees of freedom, including non-instantaneous decoupling effects. PRyMordial is suitable for state-of-the-art analyses in the Standard Model as well as for general investigations into New Physics active during BBN. After reviewing the physics implemented in PRyMordial, we provided a short guide on how to use the code for applications in the Standard Model and beyond. The package is written in Python, but more advanced users can optionally take advantage of the open-source community for Julia.

In Chapter 6 we explored the recent measurement of helium-4 from the near-infrared spectroscopy of extremely metal-poor galaxies by the Subaru Survey. We exploited this new helium measurement together with the percent-level determination of primordial deuterium, to assess indications for a nonvanishing lepton asymmetry during the BBN era, paying particular attention to the role of uncertainties in the nuclear reaction network. A cutting-edge Bayesian analysis focused on the role of the newly measured extremely metal-poor galaxies, jointly with information from the cosmic microwave background, suggested the existence of a nonzero lepton asymmetry at around the 2σ level, providing a hint for cosmology beyond lambda cold dark matter. To conclude, we briefly discussed conditions for a large total lepton asymmetry to be consistently realized in the early universe.

Finally, in Chapter 7 we further explored data on primordial ^{4}He from the EMPRESS collaboration. In this chapter we attempted to explain this the apparent anomaly by variation of fundamental constants between the time of BBN and the present. Since the Higgs vev is the only dimensionful parameter of the Standard Model and it is already known to vary during the electroweak phase transition, we considered the possibility that the vev is slightly

different during BBN compared to its present value. A modification of the vev changes not only particle masses but also affects, through mass thresholds, the QCD confinement scale. We used PRyMordial to study this variation and its impact on the ^{4}He and deuterium abundances. We find that bounds on $|\delta v/v|$ are approximately 0.01, and that the EMPRESS result can be explained within 2σ if $0.008 < \delta v/v < 0.02$, but at the cost of worsening the current 2σ discrepancy in the deuterium abundance to over 3σ.

End note: Throughout the course of my PhD, I have often reflected on the indulgent nature of studying theoretical cosmology and particle physics. Unlike my friend Kerin who passionately advocates for justice as a public defender, or my sister Josephine who is training to detect signs of oral cancer in dental school, or my friend Holly whose research is dedicated to studying and protecting an endangered species, my pursuits are distant from immediate societal challenges. So what's the point? Why does it matter whether or not we discover the nature of dark matter or determine a complete theory of quantum gravity?

My answers to these questions are personal and subjective. I believe that the pursuit of knowledge and understanding has inherent value, and that learning paves the way for compassion. I believe that advancing scientific knowledge of all kinds is essential for the positive growth and development of our culture. I believe in the importance of making science accessible to all people, particularly those in marginalized groups. By breaking down barriers and fostering inclusivity in science, we not only expand opportunities for individuals but also enrich our collective understanding and appreciation of the universe. As scientists working in a field that has historically excluded women, people of color, and queer folks, we have the opportunity to be role models in the explicit pursuit of inclusion. I believe that if we are dedicated, these efforts will catalyze positive change that will ripple out and impact culture beyond the realm of physics.

I'll end with a quote from Carl Sagan, whose TV show, *Cosmos*, played a significant role in shaping the career trajectory I'm on today.

It has been said that astronomy is a humbling and character-building experience. There is perhaps no better demonstration of the folly of human conceits than this distant image of our tiny world. To me, it underscores our responsibility to deal more kindly with one another, and to preserve and cherish the pale blue dot, the only home we've ever known. - Carl Sagan

Bibliography

[1] Julien Billard et al. Direct detection of dark matter—APPEC committee report*. *Rept. Prog. Phys.*, 85(5):056201, 2022.

[2] Henso Abreu et al. Search for dark photons with the FASER detector at the LHC. *Phys. Lett. B*, 848:138378, 2024.

[3] Doojin Kim, Jong-Chul Park, and Seodong Shin. Dark matter "transporting" mechanism explaining positron excesses. *JHEP*, 04:093, 2018.

[4] Brian D. Fields and Keith A. Olive. Implications of the non-observation of ^{6}Li in halo stars for the primordial ^{7}Li problem. *JCAP*, 10:078, 2022.

[5] M. Ajello et al. Fermi-LAT Observations of High-Energy γ-Ray Emission Toward the Galactic Center. *Astrophys. J.*, 819(1):44, 2016.

[6] Christopher M. Karwin, Simona Murgia, Sheldon Campbell, and Igor V. Moskalenko. Fermi-LAT Observations of γ-Ray Emission toward the Outer Halo of M31. , 880(2):95, August 2019.

[7] Ángeles Moliné, Miguel A Sánchez-Conde, Sergio Palomares-Ruiz, and Francisco Prada. Characterization of subhalo structural properties and implications for dark matter annihilation signals. *Mon. Not. Roy. Astron. Soc.*, 466(4):4974–4990, 2017.

[8] Tomoaki Ishiyama and Shin'ichiro Ando. The abundance and structure of subhaloes near the free streaming scale and their impact on indirect dark matter searches. *arXiv preprint arXiv:1907.03642*, 2019.

[9] Miguel A Sánchez-Conde and Francisco Prada. The flattening of the concentration–mass relation towards low halo masses and its implications for the annihilation signal boost. *Mon. Not. Roy. Astron. Soc.*, 442(3):2271–2277, 2014.

[10] James S. Bullock, Tsafrir S. Kolatt, Yair Sigad, Rachel S. Somerville, Andrey V. Kravtsov, Anatoly A. Klypin, Joel R. Primack, and Avishai Dekel. Profiles of dark haloes. Evolution, scatter, and environment. *Mon. Not. Roy. Astron. Soc.*, 321:559–575, 2001.

[11] Jie Wang, Sownak Bose, Carlos S. Frenk, Liang Gao, Adrian Jenkins, Volker Springel, and Simon D. M. White. Universality in the structure of dark matter haloes over twenty

orders of magnitude in halo mass. *arXiv e-prints*, page arXiv:1911.09720, November 2019.

[12] Christopher M Karwin, Simona Murgia, Sheldon Campbell, and Igor V Moskalenko. Fermi-lat observations of γ-ray emission toward the outer halo of m31. *Astrophys. J.*, 880(2):95, 2019.

[13] Mattia Di Mauro, Xian Hou, Christopher Eckner, Gabrijela Zaharijas, and Eric Charles. Search for γ-ray emission from dark matter particle interactions from Andromeda and Triangulum Galaxies with the Fermi Large Area Telescope. *Phys. Rev.*, D99(12):123027, 2019.

[14] R. L. Workman et al. Review of Particle Physics. *PTEP*, 2022:083C01, 2022.

[15] N. Aghanim et al. Planck 2018 results. VI. Cosmological parameters. *Astron. Astrophys.*, 641:A6, 2020. [Erratum: Astron.Astrophys. 652, C4 (2021)].

[16] Daniel Foreman-Mackey, David W. Hogg, Dustin Lang, and Jonathan Goodman. emcee: The MCMC Hammer. , 125(925):306, March 2013.

[17] Anne-Katherine Burns, Tim M. P. Tait, and Mauro Valli. PRyMordial: the first three minutes, within and beyond the standard model. *Eur. Phys. J. C*, 84(1):86, 2024.

[18] Cyril Pitrou, Alain Coc, Jean-Philippe Uzan, and Elisabeth Vangioni. Precision big bang nucleosynthesis with improved Helium-4 predictions. *Phys. Rept.*, 754:1–66, 2018.

[19] Anne-Katherine Burns, Max Fieg, Christopher M. Karwin, and Arvind Rajaraman. Dark matter explanations of the gamma-ray excesses from the Galactic Center and M31. *Phys. Rev. D*, 103(6):063023, 2021.

[20] Chris Karwin, Simona Murgia, Igor Moskalenko, Sean Fillingham, Anne-Katherine Burns, and Max Fieg. Dark Matter Interpretation of the Fermi-LAT Observations Toward the Outer Halo of M31. 10 2020.

[21] Anne-Katherine Burns, David E. Kaplan, Tom Melia, and Surjeet Rajendran. Time Evolution in Quantum Cosmology. 4 2022.

[22] Anne-Katherine Burns, Tim M. P. Tait, and Mauro Valli. Indications for a Nonzero Lepton Asymmetry from Extremely Metal-Poor Galaxies. *Phys. Rev. Lett.*, 130(13):131001, 2023.

[23] Anne-Katherine Burns, Venus Keus, Marc Sher, and Tim M. P. Tait. Constraints on variation of the weak scale from big bang nucleosynthesis. *Phys. Rev. D*, 109(12):123506, 2024.

[24] Antony Lewis and Sarah Bridle. Cosmological parameters from CMB and other data: A Monte Carlo approach. , 66:103511, 2002.

[25] J. Aalbers et al. First Dark Matter Search Results from the LUX-ZEPLIN (LZ) Experiment. *Phys. Rev. Lett.*, 131(4):041002, 2023.

[26] E. Aprile et al. First Dark Matter Search with Nuclear Recoils from the XENONnT Experiment. *Phys. Rev. Lett.*, 131(4):041003, 2023.

[27] Ciaran A. J. O'Hare. New Definition of the Neutrino Floor for Direct Dark Matter Searches. *Phys. Rev. Lett.*, 127(25):251802, 2021.

[28] M. Aguilar, G. Alberti, B. Alpat, A. Alvino, G. Ambrosi, K. Andeen, H. Anderhub, L. Arruda, P. Azzarello, A. Bachlechner, F. Barao, B. Baret, A. Barrau, L. Barrin, A. Bartoloni, L. Basara, A. Basili, L. Batalha, J. Bates, R. Battiston, J. Bazo, R. Becker, U. Becker, M. Behlmann, B. Beischer, J. Berdugo, P. Berges, B. Bertucci, G. Bigongiari, A. Biland, V. Bindi, S. Bizzaglia, G. Boella, W. de Boer, K. Bollweg, J. Bolmont, B. Borgia, S. Borsini, M. J. Boschini, G. Boudoul, M. Bourquin, P. Brun, M. Buénerd, J. Burger, W. Burger, F. Cadoux, X. D. Cai, M. Capell, D. Casadei, J. Casaus, V. Cascioli, G. Castellini, I. Cernuda, F. Cervelli, M. J. Chae, Y. H. Chang, A. I. Chen, C. R. Chen, H. Chen, G. M. Cheng, H. S. Chen, L. Cheng, N. Chernoplyiokov, A. Chikanian, E. Choumilov, V. Choutko, C. H. Chung, C. Clark, R. Clavero, G. Coignet, V. Commichau, C. Consolandi, A. Contin, C. Corti, M. T. Costado Dios, B. Coste, D. Crespo, Z. Cui, M. Dai, C. Delgado, S. Della Torre, B. Demirkoz, P. Dennett, L. Derome, S. Di Falco, X. H. Diao, A. Diago, L. Djambazov, C. Díaz, P. von Doetinchem, W. J. Du, J. M. Dubois, R. Duperay, M. Duranti, D. D'Urso, A. Egorov, A. Eline, F. J. Eppling, T. Eronen, J. van Es, H. Esser, A. Falvard, E. Fiandrini, A. Fiasson, E. Finch, P. Fisher, K. Flood, R. Foglio, M. Fohey, S. Fopp, N. Fouque, Y. Galaktionov, M. Gallilee, L. Gallin-Martel, G. Gallucci, B. García, J. García, R. García-López, L. García-Tabares, C. Gargiulo, H. Gast, I. Gebauer, S. Gentile, M. Gervasi, W. Gillard, F. Giovacchini, L. Girard, P. Goglov, J. Gong, C. Goy-Henningsen, D. Grandi, M. Graziani, A. Grechko, A. Gross, I. Guerri, C. de la Guía, K. H. Guo, M. Habiby, S. Haino, F. Hauler, Z. H. He, M. Heil, J. Heilig, R. Hermel, H. Hofer, Z. C. Huang, W. Hungerford, M. Incagli, M. Ionica, A. Jacholkowska, W. Y. Jang, H. Jinchi, M. Jongmanns, L. Journet, L. Jungermann, W. Karpinski, G. N. Kim, K. S. Kim, Th. Kirn, R. Kossakowski, A. Koulemzine, O. Kounina, A. Kounine, V. Koutsenko, M. S. Krafczyk, E. Laudi, G. Laurenti, C. Lauritzen, A. Lebedev, M. W. Lee, S. C. Lee, C. Leluc, H. León Vargas, V. Lepareur, J. Q. Li, Q. Li, T. X. Li, W. Li, Z. H. Li, P. Lipari, C. H. Lin, D. Liu, H. Liu, T. Lomtadze, Y. S. Lu, S. Lucidi, K. Lübelsmeyer, J. Z. Luo, W. Lustermann, S. Lv, J. Madsen, R. Majka, A. Malinin, C. Mañá, J. Marín, T. Martin, G. Martínez, F. Masciocchi, N. Masi, D. Maurin, A. McInturff, P. McIntyre, A. Menchaca-Rocha, Q. Meng, M. Menichelli, I. Mereu, M. Millinger, D. C. Mo, M. Molina, P. Mott, A. Mujunen, S. Natale, P. Nemeth, J. Q. Ni, N. Nikonov, F. Nozzoli, P. Nunes, A. Obermeier, S. Oh, A. Oliva, F. Palmonari, C. Palomares, M. Paniccia, A. Papi, W. H. Park, M. Pauluzzi, F. Pauss, A. Pauw, E. Pedreschi, S. Pensotti, R. Pereira, E. Perrin, G. Pessina, G. Pierschel, F. Pilo, A. Piluso, C. Pizzolotto, V. Plyaskin, J. Pochon, M. Pohl, V. Poireau, S. Porter, J. Pouxe, A. Putze, L. Quadrani, X. N. Qi, P. G. Rancoita, D. Rapin, Z. L. Ren, J. S. Ricol, E. Riihonen, I. Rodríguez, U. Roeser, S. Rosier-Lees, L. Rossi, A. Rozhkov, D. Rozza, A. Sabellek, R. Sagdeev, J. Sandweiss, B. Santos, P. Saouter, M. Sarchioni, S. Schael, D. Schinzel, M. Schmanau, G. Schw-

ering, A. Schulz von Dratzig, G. Scolieri, E. S. Seo, B. S. Shan, J. Y. Shi, Y. M. Shi, T. Siedenburg, R. Siedling, D. Son, F. Spada, F. Spinella, M. Steuer, K. Stiff, W. Sun, W. H. Sun, X. H. Sun, M. Tacconi, C. P. Tang, X. W. Tang, Z. C. Tang, L. Tao, J. Tassan-Viol, Samuel C. C. Ting, S. M. Ting, C. Titus, N. Tomassetti, F. Toral, J. Torsti, J. R. Tsai, J. C. Tutt, J. Ulbricht, T. Urban, V. Vagelli, E. Valente, C. Vannini, E. Valtonen, M. Vargas Trevino, S. Vaurynovich, M. Vecchi, M. Vergain, B. Verlaat, C. Vescovi, J. P. Vialle, G. Viertel, G. Volpini, D. Wang, N. H. Wang, Q. L. Wang, R. S. Wang, X. Wang, Z. X. Wang, W. Wallraff, Z. L. Weng, M. Willenbrock, M. Wlochal, H. Wu, K. Y. Wu, Z. S. Wu, W. J. Xiao, S. Xie, R. Q. Xiong, G. M. Xin, N. S. Xu, W. Xu, Q. Yan, J. Yang, M. Yang, Q. H. Ye, H. Yi, Y. J. Yu, Z. Q. Yu, S. Zeissler, J. G. Zhang, Z. Zhang, M. M. Zhang, Z. M. Zheng, H. L. Zhuang, V. Zhukov, A. Zichichi, P. Zuccon, and C. Zurbach. First result from the alpha magnetic spectrometer on the international space station: Precision measurement of the positron fraction in primary cosmic rays of 0.5–350 gev. *Phys. Rev. Lett.*, 110:141102, Apr 2013.

[29] Tracy R. Slatyer. Les Houches Lectures on Indirect Detection of Dark Matter. *SciPost Phys. Lect. Notes*, 53:1, 2022.

[30] Oscar Adriani et al. An anomalous positron abundance in cosmic rays with energies 1.5-100 GeV. *Nature*, 458:607–609, 2009.

[31] Stefano Profumo. Dissecting cosmic-ray electron-positron data with Occam's Razor: the role of known Pulsars. *Central Eur. J. Phys.*, 10:1–31, 2011.

[32] Ming-Yang Cui, Qiang Yuan, Yue-Lin Sming Tsai, and Yi-Zhong Fan. Possible dark matter annihilation signal in the ams-02 antiproton data. *Phys. Rev. Lett.*, 118:191101, May 2017.

[33] Martin Wolfgang Winkler and Tim Linden. Dark matter annihilation can produce a detectable antihelium flux through $\overline{\Lambda}_b$ decays. *Phys. Rev. Lett.*, 126:101101, Mar 2021.

[34] Esra Bulbul, Maxim Markevitch, Adam Foster, Randall K. Smith, Michael Loewenstein, and Scott W. Randall. Detection of An Unidentified Emission Line in the Stacked X-ray spectrum of Galaxy Clusters. *Astrophys. J.*, 789:13, 2014.

[35] Judd D. Bowman, Alan E. E. Rogers, Raul A. Monsalve, Thomas J. Mozdzen, and Nivedita Mahesh. An absorption profile centred at 78 megahertz in the sky-averaged spectrum. *Nature*, 555(7694):67–70, 2018.

[36] Lisa Goodenough and Dan Hooper. Possible Evidence For Dark Matter Annihilation In The Inner Milky Way From The Fermi Gamma Ray Space Telescope. *arXiv preprint*, 2009.

[37] Robert H. Kraichnan. Special-relativistic derivation of generally covariant gravitation theory. *Phys. Rev.*, 98:1118–1122, May 1955.

[38] P. J. E. Peebles. Primeval helium abundance and the primeval fireball. *Phys. Rev. Lett.*, 16:410–413, Mar 1966.

[39] Scott Burles and David Tytler. Cosmological deuterium abundance and the baryon density of the universe. 3 1996.

[40] Particle Data Group, P A Zyla, R M Barnett, J Beringer, O Dahl, D A Dwyer, D E Groom, C J Lin, K S Lugovsky, E Pianori, D J Robinson, C G Wohl, W M Yao, K Agashe, G Aielli, B C Allanach, C Amsler, M Antonelli, E C Aschenauer, D M Asner, H Baer, Sw Banerjee, L Baudis, C W Bauer, J J Beatty, V I Belousov, S Bethke, A Bettini, O Biebel, K M Black, E Blucher, O Buchmuller, V Burkert, M A Bychkov, R N Cahn, M Carena, A Ceccucci, A Cerri, D Chakraborty, R Sekhar Chivukula, G Cowan, G D'Ambrosio, T Damour, D de Florian, A de Gouvêa, T DeGrand, P de Jong, G Dissertori, B A Dobrescu, M D'Onofrio, M Doser, M Drees, H K Dreiner, P Eerola, U Egede, S Eidelman, J Ellis, J Erler, V V Ezhela, W Fetscher, B D Fields, B Foster, A Freitas, H Gallagher, L Garren, H J Gerber, G Gerbier, T Gershon, Y Gershtein, T Gherghetta, A A Godizov, M C Gonzalez-Garcia, M Goodman, C Grab, A V Gritsan, C Grojean, M Grünewald, A Gurtu, T Gutsche, H E Haber, C Hanhart, S Hashimoto, Y Hayato, A Hebecker, S Heinemeyer, B Heltsley, J J Hernández-Rey, K Hikasa, J Hisano, A Höcker, J Holder, A Holtkamp, J Huston, T Hyodo, K F Johnson, M Kado, M Karliner, U F Katz, M Kenzie, V A Khoze, S R Klein, E Klempt, R V Kowalewski, F Krauss, M Kreps, B Krusche, Y Kwon, O Lahav, J Laiho, L P Lellouch, J Lesgourgues, A R Liddle, Z Ligeti, C Lippmann, T M Liss, L Littenberg, C Lourengo, S B Lugovsky, A Lusiani, Y Makida, F Maltoni, T Mannel, A V Manohar, W J Marciano, A Masoni, J Matthews, U G Meißner, M Mikhasenko, D J Miller, D Milstead, R E Mitchell, K Mönig, P Molaro, F Moortgat, M Moskovic, K Nakamura, M Narain, P Nason, S Navas, M Neubert, P Nevski, Y Nir, K A Olive, C Patrignani, J A Peacock, S T Petcov, V A Petrov, A Pich, A Piepke, A Pomarol, S Profumo, A Quadt, K Rabbertz, J Rademacker, G Raffelt, H Ramani, M Ramsey-Musolf, B N Ratcliff, P Richardson, A Ringwald, S Roesler, S Rolli, A Romaniouk, L J Rosenberg, J L Rosner, G Rybka, M Ryskin, R A Ryutin, Y Sakai, G P Salam, S Sarkar, F Sauli, O Schneider, K Scholberg, A J Schwartz, J Schwiening, D Scott, V Sharma, S R Sharpe, T Shutt, M Silari, T Sjöstrand, P Skands, T Skwarnicki, G F Smoot, A Soffer, M S Sozzi, S Spanier, C Spiering, A Stahl, S L Stone, Y Sumino, T Sumiyoshi, M J Syphers, F Takahashi, M Tanabashi, J Tanaka, M Taševský, K Terashi, J Terning, U Thoma, R S Thorne, L Tiator, M Titov, N P Tkachenko, D R Tovey, K Trabelsi, P Urquijo, G Valencia, R Van de Water, N Varelas, G Venanzoni, L Verde, M G Vincter, P Vogel, W Vogelsang, A Vogt, V Vorobyev, S P Wakely, W Walkowiak, C W Walter, D Wands, M O Wascko, D H Weinberg, E J Weinberg, M White, L R Wiencke, S Willocq, C L Woody, R L Workman, M Yokoyama, R Yoshida, G Zanderighi, G P Zeller, O V Zenin, R Y Zhu, S L Zhu, F Zimmermann, J Anderson, T Basaglia, V S Lugovsky, P Schaffner, and W Zheng. Review of Particle Physics. *Progress of Theoretical and Experimental Physics*, 2020(8):083C01, 08 2020.

[41] Erik Aver, Keith A. Olive, and Evan D. Skillman. The effects of He I λ10830 on helium abundance determinations. *JCAP*, 07:011, 2015.

[42] Akinori Matsumoto et al. EMPRESS. VIII. A New Determination of Primordial He Abundance with Extremely Metal-Poor Galaxies: A Suggestion of the Lepton Asymmetry and Implications for the Hubble Tension. 3 2022.

[43] Dana S. Balser and T. M. Bania. Green bank telescope observations of 3he+: H ii regions. *The Astronomical Journal*, 156(6):280, November 2018.

[44] David S. Aguado, Jonay I. González Hernández, Carlos Allende Prieto, and Rafael Rebolo. Back to the Lithium Plateau with J0023+0307 with [Fe/H]<-6. *Astrophys. J. Lett.*, 874:L21, 2019.

[45] Ella Xi Wang, Thomas Nordlander, Martin Asplund, Karin Lind, Yixiao Zhou, and Henrique Reggiani. Non-detection of 6li in spite plateau stars with espresso. *Monthly Notices of the Royal Astronomical Society*, 509(1):1521–1535, October 2021.

[46] Adam G. Riess et al. Observational evidence from supernovae for an accelerating universe and a cosmological constant. *Astron. J.*, 116:1009–1038, 1998.

[47] Saul Perlmutter, G Aldering, G Goldhaber, RA Knop, P Nugent, PG Castro, S Deustua, S Fabbro, A Goobar, DE Groom, et al. Measurements of ω and λ from 42 high-redshift supernovae. *Astrophys. J.*, 517(2):565, 1999.

[48] Douglas Clowe, Marusa Bradac, Anthony H. Gonzalez, Maxim Markevitch, Scott W. Randall, Christine Jones, and Dennis Zaritsky. A direct empirical proof of the existence of dark matter. *Astrophys. J.*, 648:L109–L113, 2006.

[49] G. Hinshaw et al. Nine-Year Wilkinson Microwave Anisotropy Probe (WMAP) Observations: Cosmological Parameter Results. *Astrophys. J. Suppl. Ser.*, 208:19, 2013.

[50] P. A. R. Ade et al. Planck 2015 results. XIII. Cosmological parameters. *A&A*, 594:A13, 2016.

[51] Daniel J. Eisenstein et al. Detection of the Baryon Acoustic Peak in the Large-Scale Correlation Function of SDSS Luminous Red Galaxies. *Astrophys. J.*, 633:560–574, 2005.

[52] Lauren Anderson et al. The clustering of galaxies in the SDSS-III Baryon Oscillation Spectroscopic Survey: baryon acoustic oscillations in the Data Releases 10 and 11 Galaxy samples. *Mon. Not. Roy. Astron. Soc.*, 441(1):24–62, 2014.

[53] M. Tanabashi et al. Review of Particle Physics. *Phys. Rev. D*, 98(3):030001, 2018.

[54] John A. Peacock et al. A Measurement of the cosmological mass density from clustering in the 2dF Galaxy Redshift Survey. *Natur*, 410:169–173, 2001.

[55] Lisa Goodenough and Dan Hooper. Possible Evidence For Dark Matter Annihilation In The Inner Milky Way From The Fermi Gamma Ray Space Telescope. *arXiv e-prints*, page arXiv:0910.2998, October 2009.

[56] Dan Hooper and Lisa Goodenough. Dark matter annihilation in the Galactic Center as seen by the Fermi Gamma Ray Space Telescope. *Physics Letters B*, 697(5):412–428, March 2011.

[57] Dan Hooper and Tim Linden. Origin of the gamma rays from the Galactic Center. , 84(12):123005, December 2011.

[58] Kevork N. Abazajian and Manoj Kaplinghat. Detection of a gamma-ray source in the Galactic Center consistent with extended emission from dark matter annihilation and concentrated astrophysical emission. , 86(8):083511, October 2012.

[59] Dan Hooper and Tracy R. Slatyer. Two emission mechanisms in the Fermi Bubbles: A possible signal of annihilating dark matter. *Physics of the Dark Universe*, 2(3):118–138, September 2013.

[60] Chris Gordon and Oscar Macías. Dark matter and pulsar model constraints from Galactic Center Fermi-LAT gamma-ray observations. , 88(8):083521, October 2013.

[61] Wei-Chih Huang, Alfredo Urbano, and Wei Xue. Fermi Bubbles under Dark Matter Scrutiny. Part I: Astrophysical Analysis. *arXiv e-prints*, page arXiv:1307.6862, July 2013.

[62] Tansu Daylan, Douglas P. Finkbeiner, Dan Hooper, Tim Linden, Stephen K. N. Portillo, Nicholas L. Rodd, and Tracy R. Slatyer. The characterization of the gamma-ray signal from the central Milky Way: A case for annihilating dark matter. *Physics of the Dark Universe*, 12:1–23, June 2016.

[63] Kevork N. Abazajian, Nicolas Canac, Shunsaku Horiuchi, and Manoj Kaplinghat. Astrophysical and dark matter interpretations of extended gamma-ray emission from the Galactic Center. , 90(2):023526, July 2014.

[64] Bei Zhou, Yun-Feng Liang, Xiaoyuan Huang, Xiang Li, Yi-Zhong Fan, Lei Feng, and Jin Chang. GeV excess in the Milky Way: The role of diffuse galactic gamma-ray emission templates. , 91(12):123010, June 2015.

[65] Francesca Calore, Ilias Cholis, and Christoph Weniger. Background model systematics for the Fermi GeV excess. *JCAP*, 2015(3):038, March 2015.

[66] Kevork N. Abazajian, Nicolas Canac, Shunsaku Horiuchi, Manoj Kaplinghat, and Anna Kwa. Discovery of a new galactic center excess consistent with upscattered starlight. *JCAP*, 2015(7):013, July 2015.

[67] Francesca Calore, Ilias Cholis, Christopher McCabe, and Christoph Weniger. A tale of tails: Dark matter interpretations of the Fermi GeV excess in light of background model systematics. , 91(6):063003, March 2015.

[68] Eric Carlson, Tim Linden, and Stefano Profumo. Improved cosmic-ray injection models and the Galactic Center gamma-ray excess. , 94(6):063504, September 2016.

[69] Anirban Das and Basudeb Dasgupta. Selection rule for enhanced dark matter annihilation. *Physical Review Letters*, 118(25), Jun 2017.

[70] Bhaskaran Balaji, Ilias Cholis, Patrick J. Fox, and Samuel D. McDermott. Analyzing the gamma-ray sky with wavelets. *Physical Review D*, 98(4), Aug 2018.

[71] Richard Bartels, Emma Storm, Christoph Weniger, and Francesca Calore. The fermi-lat gev excess as a tracer of stellar mass in the galactic bulge. *Nature Astronomy*, 2(10):819–828, Aug 2018.

[72] Florian List, Nicholas L. Rodd, Geraint F. Lewis, and Ishaan Bhat. The GCE in a New Light: Disentangling the γ-ray Sky with Bayesian Graph Convolutional Neural Networks. 6 2020.

[73] Giacomo Fragione, Fabio Antonini, and Oleg Y. Gnedin. Millisecond Pulsars and the Gamma-Ray Excess in Andromeda. *Astrophys. J.*, 871(1):L8, January 2019.

[74] Giacomo Fragione, Fabio Antonini, and Oleg Y. Gnedin. Disrupted globular clusters and the gamma-ray excess in the Galactic Centre. *MNRAS*, 475(4):5313–5321, April 2018.

[75] Richard Bartels, Suraj Krishnamurthy, and Christoph Weniger. Strong support for the millisecond pulsar origin of the galactic center gev excess. *Physical Review Letters*, 116(5), Feb 2016.

[76] Yi-Ming Zhong, Samuel D. McDermott, Ilias Cholis, and Patrick J. Fox. Testing the sensitivity of the galactic center excess to the point source mask. *Physical Review Letters*, 124(23), Jun 2020.

[77] M. Ackermann et al. Searching for Dark Matter Annihilation from Milky Way Dwarf Spheroidal Galaxies with Six Years of Fermi Large Area Telescope Data. *Phys. Rev. Lett.*, 115(23):231301, 2015.

[78] A. Albert et al. Searching for Dark Matter Annihilation in Recently Discovered Milky Way Satellites with Fermi-LAT. *Astrophys. J.*, 834(2):110, 2017.

[79] Shin'ichiro Ando, Alex Geringer-Sameth, Nagisa Hiroshima, Sebastian Hoof, Roberto Trotta, and Matthew G. Walker. Structure Formation Models Weaken Limits on WIMP Dark Matter from Dwarf Spheroidal Galaxies. *arXiv e-prints*, page arXiv:2002.11956, February 2020.

[80] V. Bonnivard, C. Combet, D. Maurin, and M.G. Walker. Spherical Jeans analysis for dark matter indirect detection in dwarf spheroidal galaxies - Impact of physical parameters and triaxiality. *Mon. Not. Roy. Astron. Soc.*, 446:3002–3021, 2015.

[81] Niki Klop, Fabio Zandanel, Kohei Hayashi, and Shin'ichiro Ando. Impact of axisymmetric mass models for dwarf spheroidal galaxies on indirect dark matter searches. *Phys. Rev. D*, 95:123012, Jun 2017.

[82] Mariangela Lisanti, Siddharth Mishra-Sharma, Nicholas L Rodd, and Benjamin R Safdi. Search for dark matter annihilation in galaxy groups. *Phys. Rev. Lett.*, 120(10):101101, 2018.

[83] Mariangela Lisanti, Siddharth Mishra-Sharma, Nicholas L Rodd, Benjamin R Safdi, and Risa H Wechsler. Mapping extragalactic dark matter annihilation with galaxy surveys: A systematic study of stacked group searches. *PhRvD*, 97(6):063005, 2018.

[84] Christopher Karwin, Simona Murgia, Tim MP Tait, Troy A Porter, and Philip Tanedo. Dark matter interpretation of the fermi-lat observation toward the galactic center. *Physical Review D*, 95(10):103005, 2017.

[85] Miguel Escudero, Dan Hooper, and Samuel J Witte. Updated collider and direct detection constraints on dark matter models for the galactic center gamma-ray excess. *Journal of Cosmology and Astroparticle Physics*, 2017(02):038, 2017.

[86] Mohammad Abdullah, Anthony DiFranzo, Arvind Rajaraman, Tim M. P. Tait, Philip Tanedo, and Alexander M. Wijangco. Hidden on-shell mediators for the Galactic Center γ-ray excess. *PhRvD*, 90:035004, 2014.

[87] Arvind Rajaraman, Jordan Smolinsky, and Philip Tanedo. On-Shell Mediators and Top-Charm Dark Matter Models for the Fermi-LAT Galactic Center Excess. 3 2015.

[88] I. V. Moskalenko and A. W. Strong. Production and Propagation of Cosmic-Ray Positrons and Electrons. , 493(2):694–707, January 1998.

[89] Igor V. Moskalenko and Andrew W. Strong. Anisotropic Inverse Compton Scattering in the Galaxy. , 528(1):357–367, January 2000.

[90] Andrew W. Strong and Igor V. Moskalenko. Propagation of Cosmic-Ray Nucleons in the Galaxy. , 509(1):212–228, December 1998.

[91] Andrew W. Strong, Igor V. Moskalenko, and Olaf Reimer. Diffuse Continuum Gamma Rays from the Galaxy. , 537(2):763–784, July 2000.

[92] Vladimir S. Ptuskin, Igor V. Moskalenko, Frank C. Jones, Andrew W. Strong, and Vladimir N. Zirakashvili. Dissipation of Magnetohydrodynamic Waves on Energetic Particles: Impact on Interstellar Turbulence and Cosmic-Ray Transport. , 642(2):902–916, May 2006.

[93] Andrew W. Strong, Igor V. Moskalenko, and Vladimir S. Ptuskin. Cosmic-Ray Propagation and Interactions in the Galaxy. *Annual Review of Nuclear and Particle Science*, 57(1):285–327, November 2007.

[94] A. E. Vladimirov, S. W. Digel, G. Jóhannesson, P. F. Michelson, I. V. Moskalenko, P. L. Nolan, E. Orland o, T. A. Porter, and A. W. Strong. GALPROP WebRun: An internet-based service for calculating galactic cosmic ray propagation and associated photon emissions. *Computer Physics Communications*, 182(5):1156–1161, May 2011.

[95] G. Jóhannesson, R. Ruiz de Austri, A. C. Vincent, I. V. Moskalenko, E. Orlando, T. A. Porter, A. W. Strong, R. Trotta, F. Feroz, P. Graff, and M. P. Hobson. Bayesian Analysis of Cosmic Ray Propagation: Evidence against Homogeneous Diffusion. , 824(1):16, June 2016.

[96] Gulaugur Jóhannesson, Troy A. Porter, and Igor V. Moskalenko. The Three-dimensional Spatial Distribution of Interstellar Gas in the Milky Way: Implications for Cosmic Rays and High-energy Gamma-ray Emissions. , 856(1):45, March 2018.

[97] T. A. Porter, G. Jóhannesson, and I. V. Moskalenko. High-energy Gamma Rays from the Milky Way: Three-dimensional Spatial Models for the Cosmic-Ray and Radiation Field Densities in the Interstellar Medium. , 846(1):67, September 2017.

[98] Yoann Génolini, David Maurin, Igor V. Moskalenko, and Michael Unger. Current status and desired precision of the isotopic production cross sections relevant to astrophysics of cosmic rays: Li, Be, B, C, and N. , 98(3):034611, September 2018.

[99] A.A. Abdo et al. Fermi Large Area Telescope observations of Local Group galaxies: Detection of M31 and search for M33. *A&A*, 523:L2, 2010.

[100] M. S. Pshirkov, V. V. Vasiliev, and K. A. Postnov. Evidence of Fermi bubbles around M31. *Mon. Not. Roy. Astron. Soc.*, 459(1):L76–L80, 2016.

[101] M. Ackermann et al. Observations of M31 and M33 with the Fermi Large Area Telescope: A Galactic Center Excess in Andromeda? *Astrophys. J.*, 836(2):208, 2017.

[102] Marco Cirelli, Gennaro Corcella, Andi Hektor, Gert Hutsi, Mario Kadastik, Paolo Panci, Martti Raidal, Filippo Sala, and Alessandro Strumia. PPPC 4 DM ID: A Poor Particle Physicist Cookbook for Dark Matter Indirect Detection. *J. COSMOL. ASTROPART. P.*, 1103:051, 2011. [Erratum: JCAP1210,E01(2012)].

[103] Jianwei Lyu, G. H. Rieke, and Stacey Alberts. THE CONTRIBUTION OF HOST GALAXIES TO THE INFRARED ENERGY OUTPUT OFz$\gtrsim$ 5.0 QUASARS. *The Astrophysical Journal*, 816(2):85, jan 2016.

[104] T. Isobe, E. D. Feigelson, and P. I. Nelson. Statistical Methods for Astronomical Data with Upper Limits. II. Correlation and Regression. , 306:490, July 1986.

[105] Francesca Calore, Ilias Cholis, and Christoph Weniger. Background Model Systematics for the Fermi GeV Excess. *J. COSMOL. ASTROPART. P.*, 1503:038, 2015.

[106] Shunsaku Horiuchi, Manoj Kaplinghat, and Anna Kwa. Investigating the Uniformity of the Excess Gamma rays towards the Galactic Center Region. 2016.

[107] Tim Linden, Nicholas L. Rodd, Benjamin R. Safdi, and Tracy R. Slatyer. The High-Energy Tail of the Galactic Center Gamma-Ray Excess. 2016.

[108] Marco Cirelli, Gennaro Corcella, Andi Hektor, Gert Hutsi, Mario Kadastik, Paolo Panci, Martti Raidal, Filippo Sala, and Alessandro Strumia. PPPC 4 DM ID: A Poor Particle Physicist Cookbook for Dark Matter Indirect Detection. *JCAP*, 03:051, 2011. [Erratum: JCAP 10, E01 (2012)].

[109] Neil D. Christensen and Claude Duhr. FeynRules - Feynman rules made easy. *Comput. Phys. Commun.*, 180:1614–1641, 2009.

[110] J. Alwall, R. Frederix, S. Frixione, V. Hirschi, F. Maltoni, O. Mattelaer, H. S. Shao, T. Stelzer, P. Torrielli, and M. Zaro. The automated computation of tree-level and next-to-leading order differential cross sections, and their matching to parton shower simulations. *JHEP*, 07:079, 2014.

[111] Torbjorn Sjostrand, Stephen Mrenna, and Peter Z. Skands. A Brief Introduction to PYTHIA 8.1. *Comput. Phys. Commun.*, 178:852–867, 2008.

[112] M. Aguilar et al. Precision measurement of the boron to carbon flux ratio in cosmic rays from 1.9 gv to 2.6 tv with the alpha magnetic spectrometer on the international space station. *Phys. Rev. Lett.*, 117:231102, Nov 2016.

[113] Alessandro Cuoco, Jan Heisig, Lukas Klamt, Michael Korsmeier, and Michael Krämer. Scrutinizing the evidence for dark matter in cosmic-ray antiprotons. *Phys. Rev. D*, 99(10):103014, 2019.

[114] Ilias Cholis, Tim Linden, and Dan Hooper. A robust excess in the cosmic-ray antiproton spectrum: Implications for annihilating dark matter. *Phys. Rev. D*, 99:103026, May 2019.

[115] Annika Reinert and Martin Wolfgang Winkler. A precision search for WIMPs with charged cosmic rays. *Journal of Cosmology and Astroparticle Physics*, 2018(01):055–055, jan 2018.

[116] Horace W Babcock. The rotation of the Andromeda Nebula. *Lick Observatory Bulletin*, 19:41–51, 1939.

[117] Vera C. Rubin and W. Kent Ford, Jr. Rotation of the Andromeda Nebula from a Spectroscopic Survey of Emission Regions. *Astrophys. J.*, 159:379–403, 1970.

[118] Morton S Roberts and Robert N Whitehurst. The rotation curve and geometry of M31 at large galactocentric distances. *Astrophys. J.*, 201:327–346, 1975.

[119] Claude Carignan, Laurent Chemin, Walter K Huchtmeier, and Felix J Lockman. The extended hi rotation curve and mass distribution of m31. *ApJ Letters*, 641(2):L109, 2006.

[120] E. Corbelli, S. Lorenzoni, R. Walterbos, R. Braun, and D. Thilker. A wide-field H I mosaic of Messier 31. II. The disk warp, rotation, and the dark matter halo. *A&A*, 511:A89, February 2010.

[121] Marc Kamionkowski and Ali Kinkhabwala. Galactic halo models and particle dark matter detection. *PhRvD*, 57:3256–3263, 1998.

[122] R. Braun and W. B. Burton. The kinematic and spatial deployment of compact, isolated high-velocity clouds. *A&A*, 341:437, 1999.

[123] Leo Blitz, David N Spergel, Peter J Teuben, Dap Hartmann, and W Butler Burton. High-velocity clouds: Building blocks of the local group. *Astrophys. J.*, 514(2):818, 1999.

[124] V. de Heij, Robert Braun, and W. B. Burton. An all-sky study of compact, isolated high velocity clouds. *A&A*, 392:417, 2002.

[125] Robert Braun and David Thilker. The WSRT wide- field HI survey: 2. Local Group features. *A&A*, 417:421–435, 2004.

[126] Amina Helmi. Is the dark halo of our galaxy spherical? *Mon. Not. Roy. Astron. Soc.*, 351:643, 2004.

[127] Jeremy Bailin and Matthias Steinmetz. Internal and external alignment of the shapes and angular momenta of lambda-CDM halos. *Astrophys. J.*, 627:647–665, 2005.

[128] Brandon Allgood, Ricardo A. Flores, Joel R. Primack, Andrey V. Kravtsov, Risa H. Wechsler, Andreas Faltenbacher, and James S. Bullock. The shape of dark matter halos: dependence on mass, redshift, radius, and formation. *Mon. Not. Roy. Astron. Soc.*, 367:1781–1796, 2006.

[129] Philip Bett, Vincent Eke, Carlos S. Frenk, Adrian Jenkins, John Helly, and Julio Navarro. The spin and shape of dark matter haloes in the Millennium simulation of a lambda-CDM universe. *Mon. Not. Roy. Astron. Soc.*, 376:215–232, 2007.

[130] E. Hayashi, J. F. Navarro, and V. Springel. The Shape of the Gravitational Potential in Cold Dark Matter Halos. *Mon. Not. Roy. Astron. Soc.*, 377:50–62, 2007.

[131] M. Kuhlen, J. Diemand, and P. Madau. The shapes, orientation, and alignment of Galactic dark matter subhalos. *Astrophys. J.*, 671:1135, 2007.

[132] Arunima Banerjee and Chanda J. Jog. The Flattened Dark Matter Halo of M31 as Deduced from the Observed HI Scale Heights. *Astrophys. J.*, 685:254, 2008.

[133] Volker Springel, Jie Wang, Mark Vogelsberger, Aaron Ludlow, Adrian Jenkins, Amina Helmi, Julio F. Navarro, Carlos S. Frenk, and Simon D. M. White. The Aquarius Project: the subhalos of galactic halos. *Mon. Not. Roy. Astron. Soc.*, 391:1685–1711, 2008.

[134] Jürg Diemand, Michael Kuhlen, Piero Madau, M Zemp, Ben Moore, D Potter, and J Stadel. Clumps and streams in the local dark matter distribution. *Nature*, 454(7205):735–738, 2008.

[135] Marcel Zemp, Jurg Diemand, Michael Kuhlen, Piero Madau, Ben Moore, Doug Potter, Joachim Stadel, and Lawrence Widrow. The Graininess of Dark Matter Haloes. *Mon. Not. Roy. Astron. Soc.*, 394:641–659, 2009.

[136] Kanak Saha, Evan S. Levine, Chanda J. Jog, and Leo Blitz. The Milky Way's dark matter halo appears to be lopsided. *Astrophys. J.*, 697:2015–2029, 2009.

[137] David R. Law, Steven R. Majewski, and Kathryn V. Johnston. Evidence for a Triaxial Milky Way Dark Matter Halo from the Sagittarius Stellar Tidal Stream. *Astrophys. J.*, 703:L67–L71, 2009.

[138] Arunima Banerjee and Chanda J. Jog. Progressively more prolate dark matter halo in the outer Galaxy as traced by flaring HI gas. *Astrophys. J.*, 732:L8, 2011.

[139] L. Gao, C. S. Frenk, A. Jenkins, V. Springel, and S. D. M. White. Where will supersymmetric dark matter first be seen? *Mon. Not. Roy. Astron. Soc.*, 419:1721, 2012.

[140] Tomoaki Ishiyama. Hierarchical Formation of Dark Matter Halos and the Free Streaming Scale. *Astrophys. J.*, 788:27, 2014.

[141] Shea Garrison-Kimmel, Michael Boylan-Kolchin, James S Bullock, and Kyle Lee. Elvis: Exploring the local volume in simulations. *Mon. Not. Roy. Astron. Soc.*, 438(3):2578–2596, 2014.

[142] Marco Velliscig et al. The alignment and shape of dark matter, stellar, and hot gas distributions in the EAGLE and cosmo-OWLS simulations. *Mon. Not. Roy. Astron. Soc.*, 453(1):721–738, 2015.

[143] Nicolás Bernal, Lina Necib, and Tracy R. Slatyer. Spherical Cows in Dark Matter Indirect Detection. *J. COSMOL. ASTROPART. P.*, 1612(12):030, 2016.

[144] Shea Garrison-Kimmel, Andrew Wetzel, James S Bullock, Philip F Hopkins, Michael Boylan-Kolchin, Claude-André Faucher-Giguère, Dušan Kereš, Eliot Quataert, Robyn E Sanderson, Andrew S Graus, et al. Not so lumpy after all: modelling the depletion of dark matter subhaloes by milky way-like galaxies. *Mon. Not. Roy. Astron. Soc.*, 471(2):1709–1727, 2017.

[145] A. Falvard et al. Supersymmetric dark matter in m31: can one see neutralino annihilation with celeste? *Astropart. Phys.*, 20:467–484, 2004.

[146] N. Fornengo, L. Pieri, and S. Scopel. Neutralino annihilation into gamma-rays in the Milky Way and in external galaxies. *PhRvD*, 70:103529, 2004.

[147] Gregory D. Mack, Thomas D. Jacques, John F. Beacom, Nicole F. Bell, and Hasan Yuksel. Conservative Constraints on Dark Matter Annihilation into Gamma Rays. *PhRvD*, 78:063542, 2008.

[148] Leanna Dugger, Tesla E. Jeltema, and Stefano Profumo. Constraints on Decaying Dark Matter from Fermi Observations of Nearby Galaxies and Clusters. *J. COSMOL. ASTROPART. P.*, 1012:015, 2010.

[149] Jan Conrad, Johann Cohen-Tanugi, and Louis E. Strigari. WIMP searches with gamma rays in the Fermi era: challenges, methods and results. *J. Exp. Theor. Phys.*, 121(6):1104–1135, 2015. [Zh. Eksp. Teor. Fiz.148,no.6,1257(2015)].

[150] Jennifer M. Gaskins. A review of indirect searches for particle dark matter. *ConPh*, 57(4):496–525, 2016.

[151] Yi Zhang, Ruo-Yu Liu, Hui Li, Shi Shao, Huirong Yan, Xiang-Yu Wang, and Xiao-Na Sun. Measuring the Mass of Missing Baryons in the Halo of Andromeda Galaxy with Gamma-Ray Observations. *arXiv e-prints*, page arXiv:2010.15477, October 2020.

[152] Christopher Eckner, Xian Hou, Pasquale D Serpico, Miles Winter, Gabrijela Zaharijas, Pierrick Martin, Mattia di Mauro, Nestor Mirabal, Jovana Petrovic, Tijana Prodanovic, et al. Millisecond pulsar origin of the galactic center excess and extended gamma-ray emission from andromeda: A closer look. *Astrophys. J.*, 862(1):79, 2018.

[153] Alex McDaniel, Tesla Jeltema, and Stefano Profumo. Multiwavelength analysis of annihilating dark matter as the origin of the gamma-ray emission from m31. *PRD*, 97(10):103021, 2018.

[154] Alex McDaniel, Tesla Jeltema, and Stefano Profumo. Exploring a cosmic-ray origin of the multiwavelength emission in M31. *Phys. Rev.*, D100(2):023014, 2019.

[155] M. Ajello, M. Di Mauro, V. S. Paliya, and S. Garrappa. The γ-Ray Emission of Star-forming Galaxies. *Astrophys. J.*, 894(2):88, May 2020.

[156] Zhijie Qu, Rui Huang, Joel N. Bregman, and Jiang-Tao Li. An X-ray and SZ bright diffuse source toward M31: a Local Hot Bridge. *arXiv e-prints*, page arXiv:2011.02125, November 2020.

[157] Pavel Kroupa, Christian Theis, and Christian M. Boily. The Great disk of Milky Way satellites and cosmological sub-structures. *A&A*, 431:517–521, 2005.

[158] M. S. Pawlowski, J. Pflamm-Altenburg, and P. Kroupa. The VPOS: a vast polar structure of satellite galaxies, globular clusters and streams around the Milky Way. *Mon. Not. Roy. Astron. Soc.*, 423:1109, 2012.

[159] Anthony R. Conn et al. The Three-Dimensional Structure of the M31 Satellite System: Strong Evidence for an Inhomogeneous Distribution of Satellites. *Astrophys. J.*, 766:120, 2013.

[160] Rodrigo A. Ibata et al. A Vast Thin Plane of Co-rotating Dwarf Galaxies Orbiting the Andromeda Galaxy. *Natur*, 493:62–65, 2013.

[161] Marcel S. Pawlowski, Pavel Kroupa, and Helmut Jerjen. Dwarf Galaxy Planes: the discovery of symmetric structures in the Local Group. *Mon. Not. Roy. Astron. Soc.*, 435:1928, 2013.

[162] François Hammer, Yanbin Yang, Sylvain Fouquet, Marcel S. Pawlowski, Pavel Kroupa, Mathieu Puech, Hector Flores, and Jianling Wang. The vast thin plane of M31 co-rotating dwarfs: an additional fossil signature of the M31 merger and of its considerable impact in the whole Local Group. *Mon. Not. Roy. Astron. Soc.*, 431:3543, 2013.

[163] Marcel S. Pawlowski. The Planes of Satellite Galaxies Problem, Suggested Solutions, and Open Questions. *MPLA*, A33(06):1830004, 2018.

[164] Marcel S Pawlowski, Rodrigo A Ibata, and James S Bullock. The lopsidedness of satellite galaxy systems in λcdm simulations. *Astrophys. J.*, 850(2):132, 2017.

[165] Aad NM Hulsbosch. Studies on high-velocity clouds of neutral hydrogen. *A&A*, 40:1–25, 1975.

[166] Felix J. Lockman. High velocity cloud complex H: A Satellite of the Milky Way in a retrograde orbit? *ApJ Letters*, 591:L33–L36, 2003.

[167] Joshua D. Simon, Leo Blitz, Andrew A. Cole, Martin D. Weinberg, and Martin Cohen. The cosmological significance of high-velocity cloud complex h. *Astrophys. J.*, 640:270–281, 2006.

[168] J Kerp, PMW Kalberla, N Ben Bekhti, L Flöer, D Lenz, and B Winkel. A survey of hi gas toward the andromeda galaxy. *A&A*, 589:A120, 2016.

[169] N Ben Bekhti, L Flöer, R Keller, J Kerp, D Lenz, B Winkel, J Bailin, MR Calabretta, L Dedes, HA Ford, et al. Hi4pi: a full-sky h i survey based on ebhis and gass. *A&A*, 594:A116, 2016.

[170] M. Ajello, M. Di Mauro, V. S. Paliya, and S. Garrappa. The γ-Ray Emission of Star-forming Galaxies. , 894(2):88, May 2020.

[171] Shao-Qiang Xi, Hai-Ming Zhang, Ruo-Yu Liu, and Xiang-Yu Wang. GeV γ-ray emission from M33 and Arp˜299. *arXiv e-prints*, page arXiv:2003.07830, March 2020.

[172] MCH Wright. The tail of m33 and the adjacent hydrogen cloud. *Astrophys. J.*, 233:35–38, 1979.

[173] OC Keenan, Jonathan Ivor Davies, Rhys Taylor, and RF Minchin. The arecibo galaxy environment survey–x. the structure of halo gas around m33. *Mon. Not. Roy. Astron. Soc.*, 456(1):951–960, 2015.

[174] David A Thilker, Robert Braun, and RAM Walterbos. A high-resolution mosaic of hi in m33. In *Seeing Through the Dust: The Detection of HI and the Exploration of the ISM in Galaxies*, volume 276, page 370, 2002.

[175] Paolo Ciafaloni, Denis Comelli, Antonio Riotto, Filippo Sala, Alessandro Strumia, and Alfredo Urbano. Weak Corrections are Relevant for Dark Matter Indirect Detection. *J. Cosmol. Astropart. P.*, 1103:019, 2011.

[176] Jianwei Lyu, G. H. Rieke, and Stacey Alberts. The Contribution of Host Galaxies to the Infrared Energy Output of z $\gtrsim$ 5.0 Quasars. , 816(2):85, January 2016.

[177] Aldée Charbonnier, Céline Combet, and David Maurin. Clumpy: A code for γ-ray signals from dark matter structures. *Computer Physics Communications*, 183(3):656–668, 2012.

[178] Vincent Bonnivard, Moritz Hütten, Emmanuel Nezri, Aldée Charbonnier, Céline Combet, and David Maurin. Clumpy: Jeans analysis, γ-ray and ν fluxes from dark matter (sub-) structures. *Computer physics communications*, 200:336–349, 2016.

[179] Moritz Hütten, Céline Combet, and David Maurin. Clumpy v3: γ-ray and ν signals from dark matter at all scales. *Computer Physics Communications*, 235:336–345, 2019.

[180] Anne M. Green, Stefan Hofmann, and Dominik J. Schwarz. The power spectrum of SUSY - CDM on sub-galactic scales. *Mon. Not. Roy. Astron. Soc.*, 353:L23, 2004.

[181] Jurg Diemand, Michael Kuhlen, and Piero Madau. Dark matter substructure and gamma-ray annihilation in the Milky Way halo. *Astrophys. J.*, 657:262–270, 2007.

[182] A Tamm, E Tempel, P Tenjes, O Tihhonova, and T Tuvikene. Stellar mass map and dark matter distribution in M 31. *A&A*, 546:A4, 2012.

[183] Christopher Wegg, Ortwin Gerhard, and Marie Bieth. The gravitational force field of the Galaxy measured from the kinematics of RR Lyrae in Gaia. *Mon. Not. R. Astron. Soc.*, 485(3):3296–3316, May 2019.

[184] A. Bowden, N. W. Evans, and A. A. Williams. Is the dark halo of the milky way prolate? *Mon. Not. R. Astron. Soc.*, 460(1):329–337, Apr 2016.

[185] Lorenzo Posti and Amina Helmi. Mass and shape of the Milky Way's dark matter halo with globular clusters from Gaia and Hubble. *Astron. Astrophys.*, 621:A56, January 2019.

[186] Sarah R. Loebman, Željko Ivezić, Thomas R. Quinn, Jo Bovy, Charlotte R. Christensen, Mario Jurić, Rok Roškar, Alyson M. Brooks, and Fabio Governato. The Milky Way Tomography with Sloan Digital Sky Survey. V. Mapping the Dark Matter Halo. , 794(2):151, October 2014.

[187] Giuliano Iorio and Vasily Belokurov. The shape of the Galactic halo with Gaia DR2 RR Lyrae. Anatomy of an ancient major merger. *Mon. Not. R. Astron. Soc.*, 482(3):3868–3879, January 2019.

[188] N. Wyn Evans, Ciaran A.J. O'Hare, and Christopher McCabe. Refinement of the standard halo model for dark matter searches in light of the Gaia Sausage. *Phys. Rev. D*, 99(2):023012, 2019.

[189] Razieh Emami, Shy Genel, Lars Hernquist, Charles Alcock, Sownak Bose, Rainer Weinberger, Mark Vogelsberger, Federico Marinacci, Abraham Loeb, Paul Torrey, and John C. Forbes. DM halo morphological types of MW-like galaxies in the TNG50 simulation: Simple, Twisted, or Stretched. *arXiv e-prints*, page arXiv:2009.09220, September 2020.

[190] Eugene Vasiliev, Vasily Belokurov, and Denis Erkal. Tango for three: Sagittarius, LMC, and the Milky Way. *arXiv e-prints*, page arXiv:2009.10726, September 2020.

[191] Kevork N. Abazajian and Ryan E. Keeley. Bright gamma-ray Galactic Center excess and dark dwarfs: Strong tension for dark matter annihilation despite Milky Way halo profile and diffuse emission uncertainties. *PhRvD*, 93(8):083514, 2016.

[192] Alessandro Cuoco, Michael Krämer, and Michael Korsmeier. Novel Dark Matter Constraints from Antiprotons in Light of AMS-02. , 118(19):191102, May 2017.

[193] Ilias Cholis, Tim Linden, and Dan Hooper. A robust excess in the cosmic-ray antiproton spectrum: Implications for annihilating dark matter. , 99(10):103026, May 2019.

[194] Annika Reinert and Martin Wolfgang Winkler. A precision search for wimps with charged cosmic rays. *J. Cosmol. Astropart. P.*, 2018(01):055, 2018.

[195] Christopher Karwin, Simona Murgia, Tim M. P. Tait, Troy A. Porter, and Philip Tanedo. Dark Matter Interpretation of the Fermi-LAT Observation Toward the Galactic Center. *PhRvD*, 95(10):103005, 2017.

[196] Kevork N. Abazajian, Nicolas Canac, Shunsaku Horiuchi, and Manoj Kaplinghat. Astrophysical and Dark Matter Interpretations of Extended Gamma-Ray Emission from the Galactic Center. *PhRvD*, 90(2):023526, 2014.

[197] Tansu Daylan, Douglas P. Finkbeiner, Dan Hooper, Tim Linden, Stephen K. N. Portillo, Nicholas L. Rodd, and Tracy R. Slatyer. The characterization of the gamma-ray signal from the central Milky Way: A case for annihilating dark matter. *PDU*, 12:1–23, 2016.

[198] Chris Gordon and Oscar Macias. Dark Matter and Pulsar Model Constraints from Galactic Center Fermi-LAT Gamma Ray Observations. *PhRvD*, 88(8):083521, 2013. [Erratum: PhRvD 89,no.4,049901(2014)].

[199] Matthew R. Buckley, Eric Charles, Jennifer M. Gaskins, Alyson M. Brooks, Alex Drlica-Wagner, Pierrick Martin, and Geng Zhao. Search for Gamma-ray Emission from Dark Matter Annihilation in the Large Magellanic Cloud with the Fermi Large Area Telescope. *Phys. Rev.*, D91(10):102001, 2015.

[200] Regina Caputo, Matthew R. Buckley, Pierrick Martin, Eric Charles, Alyson M. Brooks, Alex Drlica-Wagner, Jennifer M. Gaskins, and Matthew Wood. Search for Gamma-ray Emission from Dark Matter Annihilation in the Small Magellanic Cloud with the Fermi Large Area Telescope. *Phys. Rev.*, D93(6):062004, 2016.

[201] M. Ajello et al. The Origin of the Extragalactic Gamma-Ray Background and Implications for Dark-Matter Annihilation. *Astrophys. J.*, 800(2):L27, 2015.

[202] M. Ackermann et al. Constraints on the Galactic Halo Dark Matter from Fermi-LAT Diffuse Measurements. *Astrophys. J.*, 761:91, 2012.

[203] Dan Hooper and Samuel J Witte. Gamma rays from dark matter subhalos revisited: refining the predictions and constraints. *Journal of Cosmology and Astroparticle Physics*, 2017(04):018, 2017.

[204] I. Cholis, D. Hooper, and T. Linden. A critical reevaluation of radio constraints on annihilating dark matter. *PhRvD*, 91(8):083507, April 2015.

[205] A. E. Egorov and E. Pierpaoli. Constraints on dark matter annihilation by radio observations of M31. *Phys. Rev.*, D88(2):023504, 2013.

[206] John F. Donoghue. General relativity as an effective field theory: The leading quantum corrections. *Phys. Rev. D*, 50:3874–3888, 1994.

[207] Paul Adrien Maurice Dirac. The theory of gravitation in hamiltonian form. *Proceedings of the Royal Society A*, 246, Aug 1958.

[208] Bryce S. DeWitt. Quantum theory of gravity. i. the canonical theory. *Phys. Rev.*, 160:1113–1148, Aug 1967.

[209] Don N. Page and William K. Wootters. Evolution Without Evolution: Dynamics Described by Stationary Observables. *Phys. Rev. D*, 27:2885, 1983.

[210] William G. Unruh and Robert M. Wald. What happens when an accelerating observer detects a Rindler particle. *Phys. Rev. D*, 29:1047–1056, 1984.

[211] Jonathan J. Halliwell. Derivation of the Wheeler-De Witt Equation from a Path Integral for Minisuperspace Models. *Phys. Rev. D*, 38:2468, 1988.

[212] Christopher Gerry and Peter Knight. Introductory Quantum Optics. *Cambridge University Press*, 2004.

[213] John R. Klauder. Using Coherent States to Make Physically Correct Classical-to-Quantum Procedures that Help Resolve Nonrenomalizable Fields Including Einstein's Gravity. 4 2021.

[214] Wei-Min Zhang. Coherent states in field theory. pages 297–323, 8 1999.

[215] Jordan Cotler and Kristan Jensen. Gravitational Constrained Instantons. *Phys. Rev. D*, 104:081501, 2021.

[216] Peter W. Graham, Bart Horn, Surjeet Rajendran, and Gonzalo Torroba. Exploring eternal stability with the simple harmonic universe. *JHEP*, 08:163, 2014.

[217] Peter W. Graham, Bart Horn, Shamit Kachru, Surjeet Rajendran, and Gonzalo Torroba. A Simple Harmonic Universe. *JHEP*, 02:029, 2014.

[218] Audrey T. Mithani and Alexander Vilenkin. Collapse of simple harmonic universe. *JCAP*, 01:028, 2012.

[219] Audrey T. Mithani and Alexander Vilenkin. Stabilizing oscillating universes against quantum decay. *JCAP*, 07:010, 2015.

[220] David E. Kaplan and Surjeet Rajendran. Causal framework for nonlinear quantum mechanics. *Phys. Rev. D*, 105(5):055002, 2022.

[221] Steven Weinberg. *The First Three Minutes. A Modern View of the Origin of the Universe*. Basic Books, 1977.

[222] R. A. Alpher, H. Bethe, and G. Gamow. The origin of chemical elements. *Phys. Rev.*, 73:803–804, Apr 1948.

[223] A. A. Penzias and R. W. Wilson. A Measurement of Excess Antenna Temperature at 4080 Mc/s. , 142:419–421, July 1965.

[224] R. H. Dicke, P. J. E. Peebles, P. G. Roll, and D. T. Wilkinson. Cosmic Black-Body Radiation. , 142:414–419, July 1965.

[225] D N Schramm and R V Wagoner. Element production in the early universe. *Annual Review of Nuclear Science*, 27(1):37–74, 1977.

[226] Subir Sarkar. Big bang nucleosynthesis and physics beyond the standard model. *Rept. Prog. Phys.*, 59:1493–1610, 1996.

[227] Keith A. Olive, Gary Steigman, and Terry P. Walker. Primordial nucleosynthesis: Theory and observations. *Phys. Rept.*, 333:389–407, 2000.

[228] Gary Steigman. Primordial Nucleosynthesis in the Precision Cosmology Era. *Ann. Rev. Nucl. Part. Sci.*, 57:463–491, 2007.

[229] Maxim Pospelov and Josef Pradler. Big Bang Nucleosynthesis as a Probe of New Physics. *Ann. Rev. Nucl. Part. Sci.*, 60:539–568, 2010.

[230] Richard H. Cyburt, Brian D. Fields, Keith A. Olive, and Tsung-Han Yeh. Big Bang Nucleosynthesis: 2015. *Rev. Mod. Phys.*, 88:015004, 2016.

[231] Evan Grohs and George M. Fuller. Big Bang Nucleosynthesis. 1 2023.

[232] Ivan Esteban, M. C. Gonzalez-Garcia, Michele Maltoni, Thomas Schwetz, and Albert Zhou. The fate of hints: updated global analysis of three-flavor neutrino oscillations. *JHEP*, 09:178, 2020.

[233] Kensuke Akita and Masahide Yamaguchi. A Review of Neutrino Decoupling from the Early Universe to the Current Universe. *Universe*, 8(11):552, 2022.

[234] Jack J. Bennett, Gilles Buldgen, Pablo F. De Salas, Marco Drewes, Stefano Gariazzo, Sergio Pastor, and Yvonne Y. Y. Wong. Towards a precision calculation of $N_{\rm eff}$ in the Standard Model II: Neutrino decoupling in the presence of flavour oscillations and finite-temperature QED. *JCAP*, 04:073, 2021.

[235] Julien Froustey, Cyril Pitrou, and Maria Cristina Volpe. Neutrino decoupling including flavour oscillations and primordial nucleosynthesis. *JCAP*, 12:015, 2020.

[236] Kensuke Akita and Masahide Yamaguchi. A precision calculation of relic neutrino decoupling. *JCAP*, 08:012, 2020.

[237] Planck Collaboration, Ade, P. A. R., Aghanim, N., Arnaud, M., Ashdown, M., Aumont, J., Baccigalupi, C., Banday, A. J., Barreiro, R. B., Bartlett, J. G., Bartolo, N., Battaner, E., Battye, R., Benabed, K., Benoît, A., Benoit-Lévy, A., Bernard, J.-P., Bersanelli, M., Bielewicz, P., Bock, J. J., Bonaldi, A., Bonavera, L., Bond, J. R., Borrill, J., Bouchet, F. R., Boulanger, F., Bucher, M., Burigana, C., Butler, R. C., Calabrese, E., Cardoso, J.-F., Catalano, A., Challinor, A., Chamballu, A., Chary, R.-R., Chiang, H. C., Chluba, J., Christensen, P. R., Church, S., Clements, D. L., Colombi, S., Colombo, L. P. L., Combet, C., Coulais, A., Crill, B. P., Curto, A., Cuttaia, F., Danese, L., Davies, R. D., Davis, R. J., de Bernardis, P., de Rosa, A., de Zotti, G., Delabrouille, J., Désert, F.-X., Di Valentino, E., Dickinson, C., Diego, J. M., Dolag, K., Dole, H., Donzelli, S., Doré, O., Douspis, M., Ducout, A., Dunkley, J., Dupac, X., Efstathiou, G., Elsner, F., Enßlin, T. A., Eriksen, H. K., Farhang, M., Fergusson, J., Finelli, F., Forni, O., Frailis, M., Fraisse, A. A., Franceschi, E., Frejsel, A., Galeotta, S., Galli, S., Ganga, K., Gauthier, C., Gerbino, M., Ghosh, T., Giard, M., Giraud-Héraud, Y., Giusarma, E., Gjerløw, E., González-Nuevo, J., Górski, K. M., Gratton, S., Gregorio, A., Gruppuso, A., Gudmundsson, J. E., Hamann, J., Hansen, F. K., Hanson, D., Harrison, D. L., Helou, G., Henrot-Versillé, S., Hernández-Monteagudo, C., Herranz, D., Hildebrandt, S. R., Hivon, E., Hobson, M., Holmes, W. A., Hornstrup, A., Hovest, W., Huang, Z., Huffenberger, K. M., Hurier, G., Jaffe, A. H., Jaffe, T. R., Jones, W. C., Juvela, M., Keihänen, E., Keskitalo, R., Kisner, T. S., Kneissl, R., Knoche, J., Knox, L., Kunz, M., Kurki-Suonio, H., Lagache, G., Lähteenmäki, A., Lamarre, J.-M., Lasenby, A., Lattanzi, M., Lawrence, C. R., Leahy, J. P., Leonardi, R., Lesgourgues, J., Levrier, F., Lewis, A., Liguori, M., Lilje, P. B., Linden-Vørnle, M., López-Caniego, M., Lubin, P. M., Macías-Pérez, J. F., Maggio, G., Maino, D., Mandolesi, N., Mangilli, A., Marchini, A., Maris, M., Martin, P. G., Martinelli, M., Martínez-González, E., Masi, S., Matarrese, S., McGehee, P., Meinhold, P. R., Melchiorri, A., Melin, J.-B., Mendes, L., Mennella, A., Migliaccio, M., Millea, M., Mitra, S., Miville-Deschênes, M.-A., Moneti, A., Montier, L., Morgante, G., Mortlock, D., Moss, A., Munshi, D., Murphy, J. A., Naselsky, P., Nati, F., Natoli, P., Netterfield, C. B., Nørgaard-Nielsen, H. U., Noviello, F., Novikov, D., Novikov, I., Oxborrow, C. A., Paci, F., Pagano, L., Pajot, F., Paladini, R., Paoletti, D., Partridge, B., Pasian, F., Patanchon, G., Pearson, T. J., Perdereau, O., Perotto, L., Perrotta, F., Pettorino, V., Piacentini, F., Piat, M., Pierpaoli, E., Pietrobon, D., Plaszczynski, S., Pointecouteau, E., Polenta, G., Popa, L., Pratt, G. W., Prézeau, G., Prunet, S., Puget, J.-L., Rachen, J. P., Reach, W. T., Rebolo, R., Reinecke, M., Remazeilles, M., Renault, C., Renzi,

A., Ristorcelli, I., Rocha, G., Rosset, C., Rossetti, M., Roudier, G., Rouillé d´Orfeuil, B., Rowan-Robinson, M., Rubiño-Martín, J. A., Rusholme, B., Said, N., Salvatelli, V., Salvati, L., Sandri, M., Santos, D., Savelainen, M., Savini, G., Scott, D., Seiffert, M. D., Serra, P., Shellard, E. P. S., Spencer, L. D., Spinelli, M., Stolyarov, V., Stompor, R., Sudiwala, R., Sunyaev, R., Sutton, D., Suur-Uski, A.-S., Sygnet, J.-F., Tauber, J. A., Terenzi, L., Toffolatti, L., Tomasi, M., Tristram, M., Trombetti, T., Tucci, M., Tuovinen, J., Türler, M., Umana, G., Valenziano, L., Valiviita, J., Van Tent, F., Vielva, P., Villa, F., Wade, L. A., Wandelt, B. D., Wehus, I. K., White, M., White, S. D. M., Wilkinson, A., Yvon, D., Zacchei, A., and Zonca, A. Planck 2015 results - xiii. cosmological parameters. *A&A*, 594:A13, 2016.

[238] Laurent Canetti, Marco Drewes, and Mikhail Shaposhnikov. Matter and Antimatter in the Universe. *New J. Phys.*, 14:095012, 2012.

[239] Pasquale D. Serpico and Georg G. Raffelt. Lepton asymmetry and primordial nucleosynthesis in the era of precision cosmology. *Phys. Rev. D*, 71:127301, 2005.

[240] Signe Riemer-Sørensen and Espen Sem Jenssen. Nucleosynthesis Predictions and High-Precision Deuterium Measurements. *Universe*, 3(2):44, 2017.

[241] Ryan J. Cooke, Max Pettini, and Charles C. Steidel. One Percent Determination of the Primordial Deuterium Abundance. *Astrophys. J.*, 855(2):102, 2018.

[242] Tiffany Hsyu, Ryan J. Cooke, J. Xavier Prochaska, and Michael Bolte. The PHLEK Survey: A New Determination of the Primordial Helium Abundance. , 896(1):77, June 2020.

[243] Erik Aver, Danielle A. Berg, Keith A. Olive, Richard W. Pogge, John J. Salzer, and Evan D. Skillman. Improving helium abundance determinations with Leo P as a case study. *JCAP*, 03:027, 2021.

[244] Tsung-Han Yeh, Jessie Shelton, Keith A. Olive, and Brian D. Fields. Probing physics beyond the standard model: limits from BBN and the CMB independently and combined. *JCAP*, 10:046, 2022.

[245] Céline Boehm, Matthew J. Dolan, and Christopher McCabe. A Lower Bound on the Mass of Cold Thermal Dark Matter from Planck. *JCAP*, 08:041, 2013.

[246] Edward Hardy, Robert Lasenby, John March-Russell, and Stephen M. West. Big Bang Synthesis of Nuclear Dark Matter. *JHEP*, 06:011, 2015.

[247] James Alvey, Nashwan Sabti, Miguel Escudero, and Malcolm Fairbairn. Improved BBN Constraints on the Variation of the Gravitational Constant. *Eur. Phys. J. C*, 80(2):148, 2020.

[248] Sergey Sibiryakov, Philip Sørensen, and Tien-Tien Yu. BBN constraints on universally-coupled ultralight scalar dark matter. *JHEP*, 12:075, 2020.

[249] Rakhi Mahbubani, Michele Redi, and Andrea Tesi. Dark Nucleosynthesis: Cross-sections and Astrophysical Signals. *JCAP*, 02:039, 2021.

[250] Nashwan Sabti, James Alvey, Miguel Escudero, Malcolm Fairbairn, and Diego Blas. Refined Bounds on MeV-scale Thermal Dark Sectors from BBN and the CMB. *JCAP*, 01:004, 2020.

[251] Paul Frederik Depta, Marco Hufnagel, and Kai Schmidt-Hoberg. Updated BBN constraints on electromagnetic decays of MeV-scale particles. *JCAP*, 04:011, 2021.

[252] Cara Giovanetti, Mariangela Lisanti, Hongwan Liu, and Joshua T. Ruderman. Joint Cosmic Microwave Background and Big Bang Nucleosynthesis Constraints on Light Dark Sectors with Dark Radiation. *Phys. Rev. Lett.*, 129(2):021302, 2022.

[253] Xiaoyong Chu, Jui-Lin Kuo, and Josef Pradler. Toward a full description of MeV dark matter decoupling: A self-consistent determination of relic abundance and Neff. *Phys. Rev. D*, 106(5):055022, 2022.

[254] Kevork Abazajian, Graeme Addison, Peter Adshead, Zeeshan Ahmed, Steven W. Allen, David Alonso, Marcelo Alvarez, Adam Anderson, Kam S. Arnold, Carlo Baccigalupi, Kathy Bailey, Denis Barkats, Darcy Barron, Peter S. Barry, James G. Bartlett, Ritoban Basu Thakur, Nicholas Battaglia, Eric Baxter, Rachel Bean, Chris Bebek, Amy N. Bender, Bradford A. Benson, Edo Berger, Sanah Bhimani, Colin A. Bischoff, Lindsey Bleem, Sebastian Bocquet, Kimberly Boddy, Matteo Bonato, J. Richard Bond, Julian Borrill, François R. Bouchet, Michael L. Brown, Sean Bryan, Blakesley Burkhart, Victor Buza, Karen Byrum, Erminia Calabrese, Victoria Calafut, Robert Caldwell, John E. Carlstrom, Julien Carron, Thomas Cecil, Anthony Challinor, Clarence L. Chang, Yuji Chinone, Hsiao-Mei Sherry Cho, Asantha Cooray, Thomas M. Crawford, Abigail Crites, Ari Cukierman, Francis-Yan Cyr-Racine, Tijmen de Haan, Gianfranco de Zotti, Jacques Delabrouille, Marcel Demarteau, Mark Devlin, Eleonora Di Valentino, Matt Dobbs, Shannon Duff, Adriaan Duivenvoorden, Cora Dvorkin, William Edwards, Joseph Eimer, Josquin Errard, Thomas Essinger-Hileman, Giulio Fabbian, Chang Feng, Simone Ferraro, Jeffrey P. Filippini, Raphael Flauger, Brenna Flaugher, Aurelien A. Fraisse, Andrei Frolov, Nicholas Galitzki, Silvia Galli, Ken Ganga, Martina Gerbino, Murdock Gilchriese, Vera Gluscevic, Daniel Green, Daniel Grin, Evan Grohs, Riccardo Gualtieri, Victor Guarino, Jon E. Gudmundsson, Salman Habib, Gunther Haller, Mark Halpern, Nils W. Halverson, Shaul Hanany, Kathleen Harrington, Masaya Hasegawa, Matthew Hasselfield, Masashi Hazumi, Katrin Heitmann, Shawn Henderson, Jason W. Henning, J. Colin Hill, Renée Hlozek, Gil Holder, William Holzapfel, Johannes Hubmayr, Kevin M. Huffenberger, Michael Huffer, Howard Hui, Kent Irwin, Bradley R. Johnson, Doug Johnstone, William C. Jones, Kirit Karkare, Nobuhiko Katayama, James Kerby, Sarah Kernovsky, Reijo Keskitalo, Theodore Kisner, Lloyd Knox, Arthur Kosowsky, John Kovac, Ely D. Kovetz, Steve Kuhlmann, Chao-lin Kuo, Nadine Kurita, Akito Kusaka, Anne Lahteenmaki, Charles R. Lawrence, Adrian T. Lee, Antony Lewis, Dale Li, Eric Linder, Marilena Loverde, Amy Lowitz, Mathew S. Madhavacheril, Adam Mantz, Frederick

Matsuda, Philip Mauskopf, Jeff McMahon, Matthew McQuinn, P. Daniel Meerburg, Jean-Baptiste Melin, Joel Meyers, Marius Millea, Joseph Mohr, Lorenzo Moncelsi, Tony Mroczkowski, Suvodip Mukherjee, Moritz Münchmeyer, Daisuke Nagai, Johanna Nagy, Toshiya Namikawa, Federico Nati, Tyler Natoli, Mattia Negrello, Laura Newburgh, Michael D. Niemack, Haruki Nishino, Martin Nordby, Valentine Novosad, Paul O'Connor, Georges Obied, Stephen Padin, Shivam Pandey, Bruce Partridge, Elena Pierpaoli, Levon Pogosian, Clement Pryke, Giuseppe Puglisi, Benjamin Racine, Srinivasan Raghunathan, Alexandra Rahlin, Srini Rajagopalan, Marco Raveri, Mark Reichanadter, Christian L. Reichardt, Mathieu Remazeilles, Graca Rocha, Natalie A. Roe, Anirban Roy, John Ruhl, Maria Salatino, Benjamin Saliwanchik, Emmanuel Schaan, Alessandro Schillaci, Marcel M. Schmittfull, Douglas Scott, Neelima Sehgal, Sarah Shandera, Christopher Sheehy, Blake D. Sherwin, Erik Shirokoff, Sara M. Simon, Anze Slosar, Rachel Somerville, David Spergel, Suzanne T. Staggs, Antony Stark, Radek Stompor, Kyle T. Story, Chris Stoughton, Aritoki Suzuki, Osamu Tajima, Grant P. Teply, Keith Thompson, Peter Timbie, Maurizio Tomasi, Jesse I. Treu, Matthieu Tristram, Gregory Tucker, Caterina Umiltà, Alexander van Engelen, Joaquin D. Vieira, Abigail G. Vieregg, Mark Vogelsberger, Gensheng Wang, Scott Watson, Martin White, Nathan Whitehorn, Edward J. Wollack, W. L. Kimmy Wu, Zhilei Xu, Siavash Yasini, James Yeck, Ki Won Yoon, Edward Young, and Andrea Zonca. CMB-S4 Science Case, Reference Design, and Project Plan. *arXiv e-prints*, page arXiv:1907.04473, July 2019.

[255] Adrian Lee, Maximilian H. Abitbol, Shunsuke Adachi, Peter Ade, James Aguirre, Zeeshan Ahmed, Simone Aiola, Aamir Ali, David Alonso, Marcelo A. Alvarez, Kam Arnold, Peter Ashton, Zachary Atkins, Jason Austermann, Humna Awan, Carlo Baccigalupi, Taylor Baildon, Anton Baleato Lizancos, Darcy Barron, Nick Battaglia, Richard Battye, Eric Baxter, Andrew Bazarko, James A. Beall, Rachel Bean, Dominic Beck, Shawn Beckman, Benjamin Beringue, Tanay Bhandarkar, Sanah Bhimani, Federico Bianchini, Steven Boada, David Boettger, Boris Bolliet, J. Richard Bond, Julian Borrill, Michael L. Brown, Sarah Marie Bruno, Sean Bryan, Erminia Calabrese, Victoria Calafut, Paolo Calisse, Julien Carron, Fred. M. Carl, Juan Cayuso, Anthony Challinor, Grace Chesmore, Yuji Chinone, Jens Chluba, Hsiao-Mei Sherry Cho, Steve Choi, Susan Clark, Philip Clarke, Carlo Contaldi, Gabriele Coppi, Nicholas F. Cothard, Kevin Coughlin, Will Coulton, Devin Crichton, Kevin D. Crowley, Kevin T. Crowley, Ari Cukierman, John M. D'Ewart, Rolando Dünner, Tijmen de Haan, Mark Devlin, Simon Dicker, Bradley Dober, Cody J. Duell, Shannon Duff, Adri Duivenvoorden, Jo Dunkley, Hamza El Bouhargani, Josquin Errard, Giulio Fabbian, Stephen Feeney, James Fergusson, Simone Ferraro, Pedro Fluxa, Katherine Freese, Josef C. Frisch, Andrei Frolov, George Fuller, Nicholas Galitzki, Patricio A. Gallardo, Jose Tomas Galvez Ghersi, Jiansong Gao, Eric Gawiser, Martina Gerbino, Vera Gluscevic, Neil Goeckner-Wald, Joseph Golec, Sam Gordon, Megan Gralla, Daniel Green, Arpi Grigorian, John Groh, Chris Groppi, Yilun Guan, Jon E. Gudmundsson, Mark Halpern, Dongwon Han, Peter Hargrave, Kathleen Harrington, Masaya Hasegawa, Matthew Hasselfield, Makoto Hattori, Victor Haynes, Masashi Hazumi, Erin Healy, Shawn W. Henderson, Brandon Hensley, Carlos Hervias-Caimapo, Charles A. Hill, J. Colin Hill,

Gene Hilton, Matt Hilton, Adam D. Hincks, Gary Hinshaw, Renee Hložek, Shirley Ho, Shuay-Pwu Patty Ho, Thuong D. Hoang, Jonathan Hoh, Selim C. Hotinli, Zhiqi Huang, Johannes Hubmayr, Kevin Huffenberger, John P. Hughes, Anna Ijjas, Margaret Ikape, Kent Irwin, Andrew H. Jaffe, Bhuvnesh Jain, Oliver Jeong, Matthew Johnson, Daisuke Kaneko, Ethan D. Karpel, Nobuhiko Katayama, Brian Keating, Reijo Keskitalo, Theodore Kisner, Kenji Kiuchi, Jeff Klein, Kenda Knowles, Anna Kofman, Brian Koopman, Arthur Kosowsky, Nicoletta Krachmalnicoff, Akito Kusaka, Paul La Plante, Jacob Lashner, Adrian Lee, Eunseong Lee, Antony Lewis, Yaqiong Li, Zack Li, Michele Limon, Eric Linder, Jia Liu, Carlos Lopez-Caraballo, Thibaut Louis, Marius Lungu, Mathew Madhavacheril, Daisy Mak, Felipe Maldonado, Hamdi Mani, Ben Mates, Frederick Matsuda, Loïc Maurin, Phil Mauskopf, Andrew May, Nialh McCallum, Heather McCarrick, Chris McKenney, Jeff McMahon, P. Daniel Meerburg, James Mertens, Joel Meyers, Amber Miller, Mark Mirmelstein, Kavilan Moodley, Jenna Moore, Moritz Munchmeyer, Charles Munson, Masaaki Murata, Sigurd Naess, Toshiya Namikawa, Federico Nati, Martin Navaroli, Laura Newburgh, Ho Nam Nguyen, Andrina Nicola, Mike Niemack, Haruki Nishino, Yume Nishinomiya, John Orlowski-Scherer, Luca Pagano, Bruce Partridge, Francesca Perrotta, Phumlani Phakathi, Lucio Piccirillo, Elena Pierpaoli, Giampaolo Pisano, Davide Poletti, Roberto Puddu, Giuseppe Puglisi, Chris Raum, Christian L. Reichardt, Mathieu Remazeilles, Yoel Rephaeli, Dominik Riechers, Felipe Rojas, Aditya Rotti, Anirban Roy, Sharon Sadeh, Yuki Sakurai, Maria Salatino, Mayuri Sathyanarayana Rao, Lauren Saunders, Emmanuel Schaan, Marcel Schmittfull, Neelima Sehgal, Joseph Seibert, Uros Seljak, Paul Shellard, Blake Sherwin, Meir Shimon, Carlos Sierra, Jonathan Sievers, Cristobal Sifon, Precious Sikhosana, Maximiliano Silva-Feaver, Sara M. Simon, Adrian Sinclair, Kendrick Smith, Wuhyun Sohn, Rita Sonka, David Spergel, Jacob Spisak, Suzanne T. Staggs, George Stein, Jason R. Stevens, Radek Stompor, Aritoki Suzuki, Osamu Tajima, Satoru Takakura, Grant Teply, Daniel B. Thomas, Ben Thorne, Robert Thornton, Hy Trac, Jesse Treu, Calvin Tsai, Carole Tucker, Joel Ullom, Sunny Vagnozzi, Alexander van Engelen, Jeff Van Lanen, Daniel D. Van Winkle, Eve M. Vavagiakis, Clara Vergès, Michael Vissers, Kasey Wagoner, Samantha Walker, Yuhan Wang, Jon Ward, Ben Westbrook, Nathan Whitehorn, Jason Williams, Joel Williams, Edward Wollack, Zhilei Xu, Siavash Yasini, Edward Young, Byeonghee Yu, Cyndia Yu, Fernando Zago, Mario Zannoni, Hezi Zhang, Kaiwen Zheng, Ningfeng Zhu, and Andrea Zonca. The Simons Observatory. In *Bulletin of the American Astronomical Society*, volume 51, page 147, September 2019.

[256] Neelima Sehgal, Simone Aiola, Yashar Akrami, Kaustuv Basu, Michael Boylan-Kolchin, Sean Bryan, Sébastien Clesse, Francis-Yan Cyr-Racine, Luca Di Mascolo, Simon Dicker, Thomas Essinger-Hileman, Simone Ferraro, George Fuller, Dongwon Han, Matthew Hasselfield, Gil Holder, Bhuvnesh Jain, Bradley R. Johnson, Matthew Johnson, Pamela Klaassen, Mathew Madhavacheril, Philip Mauskopf, Daan Meerburg, Joel Meyers, Tony Mroczkowski, Moritz Münchmeyer, Sigurd Kirkevold Naess, Daisuke Nagai, Toshiya Namikawa, Laura Newburgh, Nam Nguyen, Michael Niemack, Benjamin D. Oppenheimer, Elena Pierpaoli, Emmanuel Schaan, Anže Slosar, David Spergel, Eric Switzer, Alexander van Engelen, and Edward Wollack. CMB-HD: An

Ultra-Deep, High-Resolution Millimeter-Wave Survey Over Half the Sky. In *Bulletin of the American Astronomical Society*, volume 51, page 6, September 2019.

[257] Evan B. Grohs, J. Richard Bond, Ryan J. Cooke, George M. Fuller, Joel Meyers, and Mark W. Paris. Big Bang Nucleosynthesis and Neutrino Cosmology. 4 2019.

[258] Alex Laguë and Joel Meyers. Prospects and Limitations for Constraining Light Relics with Primordial Abundance Measurements. *Phys. Rev. D*, 101(4):043509, 2020.

[259] Robert V. Wagoner, William A. Fowler, and Fred Hoyle. On the Synthesis of elements at very high temperatures. *Astrophys. J.*, 148:3–49, 1967.

[260] Lawrence Kawano. Let's go: Early universe 2. Primordial nucleosynthesis the computer way, January 1992.

[261] O. Pisanti, A. Cirillo, S. Esposito, F. Iocco, G. Mangano, G. Miele, and P. D. Serpico. PArthENoPE: Public Algorithm Evaluating the Nucleosynthesis of Primordial Elements. *Comput. Phys. Commun.*, 178:956–971, 2008.

[262] R. Consiglio, P. F. de Salas, G. Mangano, G. Miele, S. Pastor, and O. Pisanti. PArthENoPE reloaded. *Comput. Phys. Commun.*, 233:237–242, 2018.

[263] S. Gariazzo, P. F. de Salas, O. Pisanti, and R. Consiglio. PArthENoPE revolutions. *Comput. Phys. Commun.*, 271:108205, 2022.

[264] Cyril Pitrou, Alain Coc, Jean-Philippe Uzan, and Elisabeth Vangioni. A new tension in the cosmological model from primordial deuterium? *Mon. Not. Roy. Astron. Soc.*, 502(2):2474–2481, 2021.

[265] Alexandre Arbey. AlterBBN: A program for calculating the BBN abundances of the elements in alternative cosmologies. *Comput. Phys. Commun.*, 183:1822–1831, 2012.

[266] A. Arbey, J. Auffinger, K. P. Hickerson, and E. S. Jenssen. AlterBBN v2: A public code for calculating Big-Bang nucleosynthesis constraints in alternative cosmologies. *Comput. Phys. Commun.*, 248:106982, 2020.

[267] Mathew S. Madhavacheril et al. The Atacama Cosmology Telescope: DR6 Gravitational Lensing Map and Cosmological Parameters. 4 2023.

[268] Miguel Escudero. Neutrino decoupling beyond the Standard Model: CMB constraints on the Dark Matter mass with a fast and precise $N_{\rm eff}$ evaluation. *JCAP*, 02:007, 2019.

[269] Miguel Escudero Abenza. Precision early universe thermodynamics made simple: $N_{\rm eff}$ and neutrino decoupling in the Standard Model and beyond. *JCAP*, 05:048, 2020.

[270] Cyril Pitrou, Alain Coc, Jean-Philippe Uzan, and Elisabeth Vangioni. Resolving conclusions about the early Universe requires accurate nuclear measurements. *Nature Rev. Phys.*, 3(4):231–232, 2021.

[271] Nashwan Sabti, James Alvey, Miguel Escudero, Malcolm Fairbairn, and Diego Blas. Addendum: Refined bounds on MeV-scale thermal dark sectors from BBN and the CMB. *JCAP*, 08:A01, 2021.

[272] Oliver Schulz, Frederik Beaujean, Allen Caldwell, Cornelius Grunwald, Vasyl Hafych, Kevin Kröninger, Salvatore La Cagnina, Lars Röhrig, and Lolian Shtembari. Bat.jl: A julia-based tool for bayesian inference. *SN Computer Science*, 2(3):210, Apr 2021.

[273] Christopher Rackauckas and Qing Nie. Differentialequations.jl–a performant and feature-rich ecosystem for solving differential equations in julia. *Journal of Open Research Software*, 5(1):15, 2017.

[274] Edward W. Kolb and Michael S. Turner. *The Early Universe*, volume 69. CRC Press, 1990.

[275] Valery A. Rubakov and Dmitry S. Gorbunov. *Introduction to the Theory of the Early Universe: Hot big bang theory*. World Scientific, Singapore, 2017.

[276] Sz. Borsanyi et al. Calculation of the axion mass based on high-temperature lattice quantum chromodynamics. *Nature*, 539(7627):69–71, 2016.

[277] A. D. Dolgov, S. H. Hansen, S. Pastor, S. T. Petcov, G. G. Raffelt, and D. V. Semikoz. Cosmological bounds on neutrino degeneracy improved by flavor oscillations. *Nucl. Phys. B*, 632:363–382, 2002.

[278] A. D. Dolgov. Neutrinos in cosmology. *Phys. Rept.*, 370:333–535, 2002.

[279] Jack J. Bennett, Gilles Buldgen, Marco Drewes, and Yvonne Y. Y. Wong. Towards a precision calculation of the effective number of neutrinos $N_{\rm eff}$ in the Standard Model I: the QED equation of state. *JCAP*, 03:003, 2020. [Addendum: JCAP 03, A01 (2021)].

[280] Gianpiero Mangano, Gennaro Miele, Sergio Pastor, Teguayco Pinto, Ofelia Pisanti, and Pasquale D. Serpico. Relic neutrino decoupling including flavor oscillations. *Nucl. Phys. B*, 729:221–234, 2005.

[281] E. Grohs, G. M. Fuller, C. T. Kishimoto, M. W. Paris, and A. Vlasenko. Neutrino energy transport in weak decoupling and big bang nucleosynthesis. *Phys. Rev. D*, 93:083522, Apr 2016.

[282] John March-Russell, Hitoshi Murayama, and Antonio Riotto. The Small observed baryon asymmetry from a large lepton asymmetry. *JHEP*, 11:015, 1999.

[283] Masahiro Kawasaki and Kai Murai. Lepton asymmetric universe. *JCAP*, 08(08):041, 2022.

[284] Miguel Escudero, Alejandro Ibarra, and Victor Maura. Primordial lepton asymmetries in the precision cosmology era: Current status and future sensitivities from BBN and the CMB. *Phys. Rev. D*, 107(3):035024, 2023.

[285] Robert E. Lopez, Michael S. Turner, and Geza Gyuk. Effect of finite nucleon mass on primordial nucleosynthesis. *Phys. Rev. D*, 56:3191–3197, 1997.

[286] John F. Donoghue, Eugene Golowich, and Barry R. Holstein. *Dynamics of the Standard Model : Second edition*, volume 2. Oxford University Press, 2014.

[287] Marcella Bona et al. New UTfit Analysis of the Unitarity Triangle in the Cabibbo-Kobayashi-Maskawa scheme. *Rend. Lincei Sci. Fis. Nat.*, 34:37–57, 2023.

[288] A. N. Ivanov, M. Pitschmann, and N. I. Troitskaya. Neutron β^- decay as a laboratory for testing the standard model. *Phys. Rev. D*, 88:073002, Oct 2013.

[289] David Seckel. Nucleon mass corrections to the p <—> n rates during big bang nucleosynthesis. 6 1993.

[290] Denys H. Wilkinson. ANALYSIS OF NEUTRON BETA DECAY. *Nucl. Phys. A*, 377:474–504, 1982.

[291] William J. Marciano and Alberto Sirlin. Improved calculation of electroweak radiative corrections and the value of V(ud). *Phys. Rev. Lett.*, 96:032002, 2006.

[292] Vincenzo Cirigliano, Wouter Dekens, Emanuele Mereghetti, and Oleksandr Tomalak. Effective field theory for radiative corrections to charged-current processes I: Vector coupling. 6 2023.

[293] F. M. Gonzalez et al. Improved neutron lifetime measurement with UCNτ. *Phys. Rev. Lett.*, 127(16):162501, 2021.

[294] A. T. Yue, M. S. Dewey, D. M. Gilliam, G. L. Greene, A. B. Laptev, J. S. Nico, W. M. Snow, and F. E. Wietfeldt. Improved Determination of the Neutron Lifetime. *Phys. Rev. Lett.*, 111(22):222501, 2013.

[295] Tammi Chowdhury and Seyda Ipek. Neutron Lifetime Anomaly and Big Bang Nucleosynthesis. 10 2022.

[296] Vincenzo Cirigliano, Andreas Crivellin, Martin Hoferichter, and Matthew Moulson. Scrutinizing CKM unitarity with a new measurement of the Kμ3/Kμ2 branching fraction. *Phys. Lett. B*, 838:137748, 2023.

[297] A. Sirlin. General Properties of the Electromagnetic Corrections to the Beta Decay of a Physical Nucleon. *Phys. Rev.*, 164:1767–1775, 1967.

[298] Ernest S. Abers, Duane A. Dicus, Richard E. Norton, and Helen R. Quinn. Radiative Corrections to the Fermi Part of Strangeness-Conserving beta Decay. *Phys. Rev.*, 167:1461–1478, 1968.

[299] Duane A. Dicus, Edward W. Kolb, A. M. Gleeson, E. C. G. Sudarshan, Vigdor L. Teplitz, and Michael S. Turner. Primordial Nucleosynthesis Including Radiative, Coulomb, and Finite Temperature Corrections to Weak Rates. *Phys. Rev. D*, 26:2694, 1982.

[300] A. N. Ivanov, M. Pitschmann, and N. I. Troitskaya. Neutron β^-decay as a laboratory for testing the standard model. *Phys. Rev. D*, 88(7):073002, 2013.

[301] Lowell S. Brown and R. F. Sawyer. Finite temperature corrections to weak rates prior to nucleosynthesis. *Phys. Rev. D*, 63:083503, 2001.

[302] E. Grohs, G. M. Fuller, C. T. Kishimoto, M. W. Paris, and A. Vlasenko. Neutrino energy transport in weak decoupling and big bang nucleosynthesis. *Phys. Rev. D*, 93(8):083522, 2016.

[303] Julien Froustey and Cyril Pitrou. Incomplete neutrino decoupling effect on big bang nucleosynthesis. *Phys. Rev. D*, 101(4):043524, 2020.

[304] W. A. Fowler, G. R. Caughlan, and B. A. Zimmerman. Thermonuclear reaction rates. *Ann. Rev. Astron. Astrophys.*, 5:525–570, 1967.

[305] R V Wagoner. Synthesis of the elements within objects exploding from very high temperatures. *Astrophys. J., 18: Suppl. Ser., 162, 247-95(June 1969).*, 18, 1 1969.

[306] C. Angulo et al. A compilation of charged-particle induced thermonuclear reaction rates. *Nucl. Phys. A*, 656:3–183, 1999.

[307] Pasquale Dario Serpico, S. Esposito, F. Iocco, G. Mangano, G. Miele, and O. Pisanti. Nuclear reaction network for primordial nucleosynthesis: A Detailed analysis of rates, uncertainties and light nuclei yields. *JCAP*, 12:010, 2004.

[308] F. G. Kondev, M. Wang, W. J. Huang, S. Naimi, and G. Audi. The NUBASE2020 evaluation of nuclear physics properties. *Chin. Phys. C*, 45(3):030001, 2021.

[309] Yi Xu, Kohji Takahashi, Stephane Goriely, Marcel Arnould, Masahisa Ohta, and Hiroaki Utsunomiya. NACRE II: an update of the NACRE compilation of charged-particle-induced thermonuclear reaction rates for nuclei with mass number $A < 16$. *Nucl. Phys. A*, 918:61–169, 2013.

[310] Pierre Descouvemont, Abderrahim Adahchour, Carmen Angulo, Alain Coc, and Elisabeth Vangioni-Flam. Compilation and r-matrix analysis of big bang nuclear reaction rates. *Atomic Data and Nuclear Data Tables*, 88(1):203–236, Sep 2004.

[311] R. Longland, C. Iliadis, A.E. Champagne, J.R. Newton, C. Ugalde, A. Coc, and R. Fitzgerald. Charged-particle thermonuclear reaction rates: I. monte carlo method and statistical distributions. *Nuclear Physics A*, 841(1):1–30, 2010. The 2010 Evaluation of Monte Carlo based Thermonuclear Reaction Rates.

[312] C. Iliadis, K. S. Anderson, A. Coc, F. X. Timmes, and S. Starrfield. Bayesian estimation of thermonuclear reaction rates. *The Astrophysical Journal*, 831(1):107, Oct 2016.

[313] Á . Gómez Iñesta, C. Iliadis, and A. Coc. Bayesian estimation of thermonuclear reaction rates for deuterium+deuterium reactions. *The Astrophysical Journal*, 849(2):134, nov 2017.

[314] Alain Coc, Stephane Goriely, Yi Xu, Matthias Saimpert, and Elisabeth Vangioni. Standard Big-Bang Nucleosynthesis up to CNO with an improved extended nuclear network. *Astrophys. J.*, 744:158, 2012.

[315] Ofelia Pisanti, Gianpiero Mangano, Gennaro Miele, and Pierpaolo Mazzella. Primordial Deuterium after LUNA: concordances and error budget. *JCAP*, 04:020, 2021.

[316] Richard H. Cyburt. Primordial nucleosynthesis for the new cosmology: Determining uncertainties and examining concordance. *Phys. Rev. D*, 70:023505, 2004.

[317] Brian D. Fields, Keith A. Olive, Tsung-Han Yeh, and Charles Young. Big-Bang Nucleosynthesis after Planck. *JCAP*, 03:010, 2020. [Erratum: JCAP 11, E02 (2020)].

[318] Christian Iliadis and Alain Coc. Thermonuclear reaction rates and primordial nucleosynthesis. *Astrophys. J.*, 901(2):127, 2020.

[319] Alain Coc and Elisabeth Vangioni. Big-Bang nucleosynthesis with updated nuclear data. *J. Phys. Conf. Ser.*, 202:012001, 2010.

[320] V. Mossa et al. The baryon density of the Universe from an improved rate of deuterium burning. *Nature*, 587(7833):210–213, 2020.

[321] Richard Longland, Christian Iliadis, Art Champagne, Joe Newton, Claudio Ugalde, Alain Coc, and Ryan Fitzgerald. Charged-Particle Thermonuclear Reaction Rates: I. Monte Carlo Method and Statistical Distributions. *Nucl. Phys. A*, 841:1–30, 2010.

[322] Alain Coc, Jean-Philippe Uzan, and Elisabeth Vangioni. Standard big bang nucleosynthesis and primordial CNO Abundances after Planck. *JCAP*, 10:050, 2014.

[323] A. L. Sallaska, C. Iliadis, A. E. Champagne, S. Goriely, S. Starrfield, and F. X. Timmes. STARLIB: A Next-Generation Reaction-Rate Library for Nuclear Astrophysics. *Astrophys. J. Suppl.*, 207:18, 2013.

[324] Julien Froustey. *The Universe at the MeV era : neutrino evolution and cosmological observables*. PhD thesis, Institut d'Astrophysique de Paris, France, Paris, Inst. Astrophys., 2022.

[325] Cyril Pitrou, Alain Coc, Jean-Philippe Uzan, and Elisabeth Vangioni. Precision big bang nucleosynthesis with improved helium-4 predictions. *Physics Reports*, 754:1–66, Sep 2018.

[326] Cyril Pitrou and Maxim Pospelov. QED corrections to Big-Bang nucleosynthesis reaction rates. *Phys. Rev. C*, 102(1):015803, 2020.

[327] Mattia Cielo, Miguel Escudero, Gianpiero Mangano, and Ofelia Pisanti. Neff in the Standard Model at NLO is 3.043. 6 2023.

[328] S. Ando, R. H. Cyburt, S. W. Hong, and C. H. Hyun. Radiative neutron capture on a proton at BBN energies. *Phys. Rev. C*, 74:025809, 2006.

[329] Yi Xu, Kohji Takahashi, Stephane Goriely, Marcel Arnould, Masahisa Ohta, and Hiroaki Utsunomiya. NACRE II: an update of the NACRE compilation of charged-particle-induced thermonuclear reaction rates for nuclei with mass number $A < 16$. *Nucl. Phys. A*, 918:61–169, 2013.

[330] M. Barbagallo et al. ^{7}Be$(n,\alpha)^{4}$He Reaction and the Cosmological Lithium Problem: Measurement of the Cross Section in a Wide Energy Range at n_TOF at CERN. *Phys. Rev. Lett.*, 117(15):152701, 2016.

[331] Georgeanne R. Caughlan and William A. Fowler. Thermonuclear reaction rates v. *Atomic Data and Nuclear Data Tables*, 40(2):283–334, 1988.

[332] F. Hammache et al. High-energy break-up of 6Li as a tool to study the Big-Bang nucleosynthesis reaction 2H(alpha,gamma)6Li. *Phys. Rev. C*, 82:065803, 2010.

[333] S. Goriely, S. Hilaire, and A. J. Koning. Improved predictions of nuclear reaction rates with the TALYS reaction code for astrophysical applications. *Astron. Astrophys.*, 487:767, 2008.

[334] Alain Coc, Stephane Goriely, Yi Xu, Matthias Saimpert, and Elisabeth Vangioni. Standard Big-Bang Nucleosynthesis up to CNO with an improved extended nuclear network. *Astrophys. J.*, 744:158, 2012.

[335] Y. Nagai et al. Measurement of the H-2(n, gamma)H-3 reaction cross section between 10-keV and 550-keV. *Phys. Rev. C*, 74:025804, 2006.

[336] Robert A. Malaney and William A. Fowler. On Nuclear Reactions and 9Be Production in Inhomogeneous Cosmologies. , 345:L5, October 1989.

[337] T. Hashimoto et al. A new measurement of the astrophysical Li-8(d,t) Li-7 reaction. *Phys. Lett. B*, 674:276–280, 2009.

[338] M. Fukugita and T. Kajino. Contribution of the ^{3}He$(t,\gamma)^{6}$Li reaction to ^{6}Li production in primordial nucleosynthesis. *Phys. Rev. D*, 42:4251–4253, Dec 1990.

[339] W. Heil, J. Ahrens, H.G. Andresen, A. Bornheimer, D. Conrath, K.-J. Dietz, W. Gasteyer, H.-J. Gessinger, W. Hartmann, J. Jethwa, H.-J. Kluge, H. Kessler, T. Kettner, L. Koch, F. Neugebauer, R. Neuhausen, E.W. Otten, E. Reichert, F.P. Schäfer, and B. Wagner. Improved limits on the weak, neutral, hadronic axial vector coupling constants from quasielastic scattering of polarized electrons. *Nuclear Physics B*, 327(1):1–31, 1989.

[340] D. R. Mendes, A. Lépine-Szily, P. Descouvemont, R. Lichtenthäler, V. Guimarães, P. N. de Faria, A. Barioni, K. C. C. Pires, V. Morcelle, R. Pampa Condori, M. C. Morais, E. Leistenschneider, C. E. F. Lima, J. C. Zamora, J. A. Alcantara, V. Zagatto, M. Assun ç ao, and J. M. B. Shorto. Erratum: The ^{8}Li$(p,\alpha)^{5}$He reaction at low energies, and ^{9}Be spectroscopy around the proton threshold [phys. rev. c 86, 064321 (2012)]. *Phys. Rev. C*, 98:069901, Dec 2018.

[341] V. Efros, Werner Balogh, H. Herndl, R. Hofinger, and H. Oberhummer. Reaction rate for two-neutron capture by4he. *Zeitschrift für Physik A Hadrons and Nuclei*, 355:101–105, 01 1996.

[342] N. Aghanim et al. Planck 2018 results. VI. Cosmological parameters. *Astron. Astrophys.*, 641:A6, 2020. [Erratum: Astron.Astrophys. 652, C4 (2021)].

[343] Simone Aiola et al. The Atacama Cosmology Telescope: DR4 Maps and Cosmological Parameters. *JCAP*, 12:047, 2020.

[344] D. Dutcher et al. Measurements of the E-mode polarization and temperature-E-mode correlation of the CMB from SPT-3G 2018 data. *Phys. Rev. D*, 104(2):022003, 2021.

[345] Daniel Baumann, Daniel Green, Joel Meyers, and Benjamin Wallisch. Phases of New Physics in the CMB. *JCAP*, 01:007, 2016.

[346] Eiichiro Komatsu. New physics from the polarised light of the cosmic microwave background. 2 2022.

[347] Clarence L. Chang et al. Snowmass2021 Cosmic Frontier: Cosmic Microwave Background Measurements White Paper. 3 2022.

[348] Fabio Iocco, Gianpiero Mangano, Gennaro Miele, Ofelia Pisanti, and Pasquale D. Serpico. Primordial Nucleosynthesis: from precision cosmology to fundamental physics. *Phys. Rept.*, 472:1–76, 2009.

[349] Pasquale Dario Serpico and Georg G. Raffelt. MeV-mass dark matter and primordial nucleosynthesis. *Phys. Rev. D*, 70:043526, 2004.

[350] Céline Boehm, Matthew J. Dolan, and Christopher McCabe. A Lower Bound on the Mass of Cold Thermal Dark Matter from Planck. *JCAP*, 08:041, 2013.

[351] Cara Giovanetti, Mariangela Lisanti, Hongwan Liu, and Joshua T. Ruderman. Joint CMB and BBN Constraints on Light Dark Sectors with Dark Radiation. 9 2021.

[352] Ryan J. Cooke, Max Pettini, Kenneth M. Nollett, and Regina Jorgenson. The primordial deuterium abundance of the most metal-poor damped Lyα system. *Astrophys. J.*, 830(2):148, 2016.

[353] S. Riemer-Sørensen, S. Kotuš, J. K. Webb, K. Ali, V. Dumont, M. T. Murphy, and R. F. Carswell. A precise deuterium abundance: remeasurement of the z = 3.572 absorption system towards the quasar PKS1937–101. *Mon. Not. Roy. Astron. Soc.*, 468(3):3239–3250, 2017.

[354] P.A. Zyla et al. Review of Particle Physics. *PTEP*, 2020(8):083C01, 2020. and 2021 update.

[355] Tsung-Han Yeh, Keith A. Olive, and Brian D. Fields. The impact of new $d(p, \gamma)3$ rates on Big Bang Nucleosynthesis. *JCAP*, 03:046, 2021.

[356] Akinori Matsumoto et al. EMPRESS. VIII. A New Determination of Primordial He Abundance with Extremely Metal-poor Galaxies: A Suggestion of the Lepton Asymmetry and Implications for the Hubble Tension. *Astrophys. J.*, 941(2):167, 2022.

[357] Tiffany Hsyu, Ryan J. Cooke, J. Xavier Prochaska, and Michael Bolte. The PHLEK Survey: A New Determination of the Primordial Helium Abundance. , 896(1):77, June 2020.

[358] A.-K. Burns, T. M.P. Tait, and M. Valli. `PRyMordial`: The first minutes beyond the Standard Model in a few seconds. *in preparation*.

[359] Vimal Simha and Gary Steigman. Constraining The Universal Lepton Asymmetry. *JCAP*, 08:011, 2008.

[360] Kensuke Akita and Masahide Yamaguchi. A precision calculation of relic neutrino decoupling. *JCAP*, 08:012, 2020.

[361] Miguel Escudero Abenza. Precision early universe thermodynamics made simple: $N_{\rm eff}$ and neutrino decoupling in the Standard Model and beyond. *JCAP*, 05:048, 2020.

[362] William H. Kinney and Antonio Riotto. Measuring the cosmological lepton asymmetry through the CMB anisotropy. *Phys. Rev. Lett.*, 83:3366–3369, 1999.

[363] Julien Lesgourgues and Sergio Pastor. Cosmological implications of a relic neutrino asymmetry. *Phys. Rev. D*, 60:103521, 1999.

[364] Isabel M. Oldengott and Dominik J. Schwarz. Improved constraints on lepton asymmetry from the cosmic microwave background. *EPL*, 119(2):29001, 2017.

[365] Alexander Bonilla, Rafael C. Nunes, and Everton M. C. Abreu. Forecast on lepton asymmetry from future CMB experiments. *Mon. Not. Roy. Astron. Soc.*, 485(2):2486–2491, 2019.

[366] Suresh Kumar, Rafael C. Nunes, and Priya Yadav. Updating non-standard neutrinos properties with Planck-CMB data and full-shape analysis of BOSS and eBOSS galaxies. 5 2022.

[367] Kevork N. Abazajian, John F. Beacom, and Nicole F. Bell. Stringent Constraints on Cosmological Neutrino Antineutrino Asymmetries from Synchronized Flavor Transformation. *Phys. Rev. D*, 66:013008, 2002.

[368] Emanuele Castorina, Urbano Franca, Massimiliano Lattanzi, Julien Lesgourgues, Gianpiero Mangano, Alessandro Melchiorri, and Sergio Pastor. Cosmological lepton asymmetry with a nonzero mixing angle θ_{13}. *Phys. Rev. D*, 86:023517, 2012.

[369] N. Aghanim et al. `https://wiki.cosmos.esa.int/planck-legacy-archive/images/4/43/Baseline_params_table_2018_68pc_v2.pdf`, 2019.

[370] Gabriela Barenboim, William H. Kinney, and Wan-Il Park. Flavor versus mass eigenstates in neutrino asymmetries: implications for cosmology. *Eur. Phys. J. C*, 77(9):590, 2017.

[371] Sergio Pastor, Teguayco Pinto, and Georg G. Raffelt. Relic density of neutrinos with primordial asymmetries. *Phys. Rev. Lett.*, 102:241302, 2009.

[372] Kazunori Kohri, M. Kawasaki, and Katsuhiko Sato. Big bang nucleosynthesis and lepton number asymmetry in the universe. *Astrophys. J.*, 490:72–75, 1997.

[373] Julien Froustey and Cyril Pitrou. Primordial neutrino asymmetry evolution with full mean-field effects and collisions. *JCAP*, 03(03):065, 2022.

[374] Miguel Escudero. Neutrino decoupling beyond the Standard Model: CMB constraints on the Dark Matter mass with a fast and precise $N_{\rm eff}$ evaluation. *JCAP*, 02:007, 2019.

[375] Peter Ade et al. The Simons Observatory: Science goals and forecasts. *JCAP*, 02:056, 2019.

[376] Kevork Abazajian et al. Snowmass 2021 CMB-S4 White Paper. In *2022 Snowmass Summer Study*, 3 2022.

[377] Simone Aiola et al. Snowmass2021 CMB-HD White Paper. 3 2022.

[378] Andrzej Czarnecki, William J. Marciano, and Alberto Sirlin. Precision measurements and CKM unitarity. *Phys. Rev. D*, 70:093006, 2004.

[379] A. N. Ivanov, R. Höllwieser, N. I. Troitskaya, M. Wellenzohn, and Ya. A. Berdnikov. Precision Theoretical Analysis of Neutron Radiative Beta Decay. *Phys. Rev. D*, 95(3):033007, 2017.

[380] S. Ando, R. H. Cyburt, S. W. Hong, and C. H. Hyun. Radiative neutron capture on a proton at BBN energies. *Phys. Rev. C*, 74:025809, 2006.

[381] Pierre Descouvemont, Abderrahim Adahchour, Carmen Angulo, Alain Coc, and Elisabeth Vangioni-Flam. Compilation and R-matrix analysis of Big Bang nuclear reaction rates. *Atom. Data Nucl. Data Tabl.*, 88:203–236, 2004.

[382] Christian Iliadis, Kevin Anderson, Alain Coc, Frank Timmes, and Sumner Starrfield. Bayesian Estimation of Thermonuclear Reaction Rates. *Astrophys. J.*, 831(1):107, 2016.

[383] Á. Iñesta Gómez, C. Iliadis, and A. Coc. Bayesian estimation of thermonuclear reaction rates for deuterium+deuterium reactions. *Astrophys. J.*, 849(2):134, 2017.

[384] Rafael S. de Souza, Christian Iliadis, and Alain Coc. Astrophysical S-factors, Thermonuclear Rates, and Electron Screening Potential for the ^{3}He(d,p)^{4}He Big Bang Reaction via a Hierarchical Bayesian Model. *Astrophys. J.*, 872(1):75, 2019.

[385] Rafael S. de Souza, S. Reece Boston, Alain Coc, and Christian Iliadis. Thermonuclear fusion rates for tritium + deuterium using Bayesian methods. *Phys. Rev. C*, 99(1):014619, 2019.

[386] Joseph Moscoso, Rafael S. de Souza, Alain Coc, and Christian Iliadis. Bayesian Estimation of the D(p,γ)^{3}He Thermonuclear Reaction Rate. *Astrophys. J.*, 923(1):49, 2021.

[387] N. Aghanim et al. `https://wiki.cosmos.esa.int/planck-legacy-archive/index.php/Cosmological_Parameters`, 2019.

[388] Daniel Foreman-Mackey, David W. Hogg, Dustin Lang, and Jonathan Goodman. emcee: The MCMC Hammer. *PASP*, 125(925):306, March 2013.

[389] H. Akaike. A new look at the statistical model identification. *IEEE Transactions on Automatic Control*, 19(6):716–723, December 1974.

[390] Andrew Gelman, Jessica Hwang, and Aki Vehtari. Understanding predictive information criteria for Bayesian models. *arXiv e-prints*, page arXiv:1307.5928, Jul 2013.

[391] Robert E. Kass and Adrian E. Raftery. Bayes factors. *Journal of the American Statistical Association*, 90(430):773–795, 1995. `http://dx.doi.org/10.1080/01621459.1995.10476572`.

[392] S. Yu. Khlebnikov and M. E. Shaposhnikov. The Statistical Theory of Anomalous Fermion Number Nonconservation. *Nucl. Phys. B*, 308:885–912, 1988.

[393] Jeffrey A. Harvey and Michael S. Turner. Cosmological baryon and lepton number in the presence of electroweak fermion number violation. *Phys. Rev. D*, 42:3344–3349, 1990.

[394] Herbert K. Dreiner and Graham G. Ross. Sphaleron erasure of primordial baryogenesis. *Nucl. Phys. B*, 410:188–216, 1993.

[395] Jing Shu, Timothy M. P. Tait, and Carlos E. M. Wagner. Baryogenesis from an Earlier Phase Transition. *Phys. Rev. D*, 75:063510, 2007.

[396] Pei-Hong Gu. Large Lepton Asymmetry for Small Baryon Asymmetry and Warm Dark Matter. *Phys. Rev. D*, 82:093009, 2010.

[397] Ian Affleck and Michael Dine. A New Mechanism for Baryogenesis. *Nucl. Phys. B*, 249:361–380, 1985.

[398] Alberto Casas, Wai Yan Cheng, and Graciela Gelmini. Generation of large lepton asymmetries. *Nucl. Phys. B*, 538:297–308, 1999.

[399] John McDonald. Naturally large cosmological neutrino asymmetries in the MSSM. *Phys. Rev. Lett.*, 84:4798–4801, 2000.

[400] A. G. Riess, W. Yuan, L. M. Macri, D. Scolnic, D. Brout, S. Casertano, D. O. Jones, Y. Murakami, L. Breuval, T. G. Brink, and et al. A Comprehensive Measurement of the Local Value of the Hubble Constant with 1 km/s/Mpc Uncertainty from the Hubble Space Telescope and the SH0ES Team. *Astrophys. J. Lett.*, 934(1):L7, 2022.

[401] M. Dainotti, B. De Simone, G. Montani, T. Schiavone, and G. Lambiase. The Hubble constant tension: current status and future perspectives through new cosmological probes.

[402] O. A. Kurichin, P. A. Kislitsyn, V. V. Klimenko, S. A. Balashev, and A. V. Ivanchik. A new determination of the primordial helium abundance using the analyses of H II region spectra from SDSS. *Mon. Not. Roy. Astron. Soc.*, 502(2):3045–3056, 2021.

[403] T. Hsyu, R. J. Cooke, J. X. Prochaska, and M. Bolte. The PHLEK Survey: A New Determination of the Primordial Helium Abundance. *Astrophys. J.*, 896(1):77, 2020.

[404] E. Aver, D. A. Berg, A. S. Hirschauer, K. A. Olive, R. W. Pogge, N. S. J. Rogers, J. J. Salzer, and E. D. Skillman. A comprehensive chemical abundance analysis of metal-poor stars using SDSS/APOGEE spectra: implications for the universality of the -process. *Mon. Not. Roy. Astron. Soc.*, 505(3):4159–4175, 2021.

[405] D. Borah and A. Dasgupta. Large neutrino asymmetry from tev scale leptogenesis. *Phys. Rev. D*, 108(3):035015, 2023.

[406] L. Bergstrom, S. Iguri, and H. Rubinstein. Constraints on the variation of the fine structure constant from big bang nucleosynthesis. *Phys. Rev. D*, 60:045005, 1999.

[407] K. M. Nollett and R. E. Lopez. Primordial nucleosynthesis with a varying fine structure constant: An Improved estimate. *Phys. Rev. D*, 66:063507, 2002.

[408] M. E. Mosquera, C. G. Scoccola, S. J. Landau, and H. Vucetich. Time variation of the fine structure constant in the early universe and the Bekenstein model. *Astron. Astrophys.*, 478:675, 2008.

[409] J. D. Barrow and J. Magueijo. Cosmological constraints on a dynamical electron mass. *Phys. Rev. D*, 72:043521, 2005.

[410] C. G. Scoccola, M. E. Mosquera, S. J. Landau, and H. Vucetich. Time variation of the electron mass in the early universe and the Barrow-Magueijo model. *Astrophys. J.*, 681:737, 2008.

[411] J. Zhang and J. A. Frieman. Mirror dark sector solution of the Hubble tension with time-varying fine-structure constant. *Phys. Rev. D*, 107:043529, 2023.

[412] O. Seto and Y. Toda. Big bang nucleosynthesis constraints on varying electron mass solution to the Hubble tension. *Phys. Rev. D*, 107:083512, 2023.

[413] R. Solomon, G. Agarwal, and D. Stojkovic. Environment dependent electron mass and the Hubble constant tension. *Phys. Rev. D*, 105:103536, 2022.

[414] L. Hart and J. Chluba. New constraints on time-dependent variations of fundamental constants using Planck data. *Mon. Not. Roy. Astron. Soc.*, 474:1850–1861, 2018.

[415] L. Hart and J. Chluba. Updated fundamental constant constraints from Planck 2018 data and possible relations to the Hubble tension. *Mon. Not. Roy. Astron. Soc.*, 493:3255–3263, 2020.

[416] L. Hart and J. Chluba. Varying fundamental constants principal component analysis: additional hints about the Hubble tension. *Mon. Not. Roy. Astron. Soc.*, 510:2206–2227, 2022.

[417] O. Seto, T. Takahashi, and Y. Toda. Variation of the fine structure constant in light of recent helium abundance measurement. *Phys. Rev. D*, 108:023525, 2023.

[418] L. Dolan and R. Jackiw. Symmetry Behavior at Finite Temperature. *Phys. Rev. D*, 9:3320–3341, 1974.

[419] S. Weinberg. Gauge and Global Symmetries at High Temperature. *Phys. Rev. D*, 9:3357–3378, 1974.

[420] V. V. Dixit and M. Sher. Variation of the Fermi Constant and Primordial Nucleosynthesis. *Phys. Rev. D*, 37:1097, 1988.

[421] J. Yoo and R. J. Scherrer. Big bang nucleosynthesis and cosmic microwave background constraints on the time variation of the Higgs vacuum expectation value. *Phys. Rev. D*, 67:043517, 2003.

[422] N. Chamoun, S. J. Landau, M. E. Mosquera, and H. Vucetich. Helium and deuterium abundances as a test for the time variation of the fine structure constant and the higgs vacuum expectation value. *J. Phys. G*, 34:163–176, 2007.

[423] J. M. Gassner and H. Lesch. Constraining the Spatial and Time Variation of the Higgs Vacuum Expectation Value by the Primordial He-4 Abundance. *Int. J. Theor. Phys.*, 47:438–445, 2008.

[424] S. J. Landau, M. E. Mosquera, C. G. Scoccola, and H. Vucetich. Early Universe Constraints on Time Variation of Fundamental Constants. *Phys. Rev. D*, 78:083527, 2008.

[425] C. M. Muller, G. Schafer, and C. Wetterich. Nucleosynthesis and the variation of fundamental couplings. *Phys. Rev. D*, 70:083504, 2004.

[426] A. Coc, N. J. Nunes, K. A. Olive, J. P. Uzan, and E. Vangioni. Coupled Variations of Fundamental Couplings and Primordial Nucleosynthesis. *Phys. Rev. D*, 76:023511, 2007.

[427] J. P. Kneller and G. C. McLaughlin. BBN and Lambda(QCD). *Phys. Rev. D*, 68:103508, 2003.

[428] V. F. Dmitriev, V. V. Flambaum, and J. K. Webb. Cosmological variation of deuteron binding energy, strong interaction and quark masses from big bang nucleosynthesis. *Phys. Rev. D*, 69:063506, 2004.

[429] P. F. Bedaque, T. Luu, and L. Platter. Quark mass variation constraints from Big Bang nucleosynthesis. *Phys. Rev. C*, 83:045803, 2011.

[430] A. Ferrero and B. Altschul. Limits on the Time Variation of the Fermi Constant G_F Based on Type Ia Supernova Observations. *Phys. Rev. D*, 82:123002, 2010.

[431] G. Laverda and J. Rubio. The Rise and Fall of the Standard-Model Higgs: Electroweak Vacuum Stability during Kination.

[432] V. Agrawal, S. M. Barr, J. F. Donoghue, and D. Seckel. Viable range of the mass scale of the standard model. *Phys. Rev. D*, 57:5480–5492, 1998.

[433] V. Agrawal, S. M. Barr, J. F. Donoghue, and D. Seckel. Anthropic considerations in multiple domain theories and the scale of electroweak symmetry breaking. *Phys. Rev. Lett.*, 80:1822–1825, 1998.

[434] T. E. Jeltema and M. Sher. The Triple alpha process and the anthropically allowed values of the weak scale. *Phys. Rev. D*, 61:017301, 2000.

[435] U. G. Meißner, B. C. Metsch, and H. Meyer. The electromagnetic fine-structure constant in primordial nucleosynthesis revisited. *Eur. Phys. J. A*, 59(10):223, 2023.

[436] N. Schoneberg. The 2024 BBN baryon abundance update.

[437] A. Giri and R. J. Scherrer. Big bang nucleosynthesis with rapidly varying G.

[438] H. Hong, U. Min, M. Son, and T. You. A Cosmic Window on the Dark Axion Portal.

[439] F. Bianchini, G. G. di Cortona, and M. Valli. The QCD Axion: Some Like It Hot.

[440] S. Weinberg. *Gravitation and Cosmology: Principles and Applications of the General Theory of Relativity*. John Wiley and Sons, 1972.

[441] U. G. Meissner. Low-Energy Hadron Physics from Effective Chiral Lagrangians with Vector Mesons. *Phys. Rept.*, 161:213, 1988.

[442] W. Lin and B. D. Serot. Mid range nucleon nucleon interaction in the linear sigma model. *Nucl. Phys. A*, 512:637–668, 1990.

[443] R. L. Workman et al. (Particle Data Group). Review of Particle Physics. *PTEP*, 2022:083C01, 2022.

[444] P. A. Kislitsyn, S. A. Balashev, M. T. Murphy, C. Ledoux, P. Noterdaeme, and A. V. Ivanchik. A new precise determination of the primordial abundance of deuterium: measurement in the metal-poor sub-DLA system at z = 3.42 towards quasar J 1332+0052. *Mon. Not. Roy. Astron. Soc.*, 528(3):4068–4081, 2024.

[445] H. Meyer and U. G. Meißner. Improved Constraints on the Variation of the Weak Scale from Big Bang Nucleosynthesis.